Numerical Simulation of Combustion Instability

Flame Thickening and Boundary Conditions

Omer Rathore

Department of Mechanical Engineering
Imperial College London

This dissertation is submitted for the degree of
Doctor of Philosophy

July 2023

For Naureen, Ali and Saadat Rathore

Declaration

I hereby declare that except where specific reference is made to the work of others, the contents of this dissertation are original and my own work.

The copyright of this thesis rests with the author. Unless otherwise indicated, its contents are licensed under a Creative Commons Attribution-NonCommercial 4.0 International Licence (CC BY-NC).

Under this licence, you may copy and redistribute the material in any medium or format. You may also create and distribute modified versions of the work. This is on the condition that: you credit the author and do not use it, or any derivative works, for a commercial purpose.

When reusing or sharing this work, ensure you make the licence terms clear to others by naming the licence and linking to the licence text. Where a work has been adapted, you should indicate that the work has been changed and describe those changes.

Please seek permission from the copyright holder for uses of this work that are not included in this licence or permitted under UK Copyright Law.

Omer Rathore
July 2023

Acknowledgements

I would like to thank my supervisor, Dr. Salvador Navarro-Martinez for his guidance, support, fascinating conversations and immense patience. This journey has been very enjoyable due to his candid demeanour, excellent mentoring and good humour.

To my mother, words cannot do justice to the sacrifices, commitment, effort and sheer time she has devoted to me, I would not be where I am today without her. My brother has my deepest gratitude for his unconditional support, willingness to help and always being there for me. Thanks ask well to my nieces for consistently being a genuine source of joy.

To my friends who have supported me along the way, you all share credit in ensuring I made it so far, thank you to all of you. In particular to Aakeen and Rik for making Imperial feel like a second home, Dom for bearing with my whinging and Stephen for his many subjective views that always kept me entertained. Finally, to Fiona Boyce I am sincerely grateful for being a better friend than I could have possibly asked for.

Abstract

Combustion-driven instabilities are a significant barrier for progress for many avenues of immense practical relevance in engineering devices, such as next generation gas turbines geared towards minimising pollutant emissions being susceptible to thermoacoustic instabilities. Numerical simulations of such reactive systems must try to balance a dynamic interplay between cost, complexity, and retention of system physics. As such, new computational tools of relevance to Large Eddy Simulation (LES) of compressible, reactive flows are proposed and evaluated.

High order flow solvers are susceptible to spurious noise generation at boundaries which can be very detrimental for combustion simulations. Therefore Navier-Stokes Characteristic Boundary conditions are also reviewed and an extension to axisymmetric configurations proposed. Limitations and lingering open questions in the field are highlighted.

A modified Artificially Thickened Flame (ATF) model coupled with a novel dynamic formulation is shown to preserve flame-turbulence interaction across a wide range of canonical configurations. The approach does not require efficiency functions which can be difficult to determine, impact accuracy and have limited regimes of validity. The method is supplemented with novel reverse transforms and scaling laws for relevant post-processing from the thickened to unthickened state. This is implemented into a wider Adaptive Mesh Refinement (AMR) context to deliver a unified LES-AMR-ATF framework. The model is validated in a range of test case showing noticeable improvements over conventional LES alternatives.

The proposed modifications allow meaningful inferences about flame structure that conventionally may have been restricted to the domain of Direct Numerical Simulation. This allows studying the changes in small-scale flow and scalar topologies during flame-flame interaction. The approach is applied to a dual flame burner setup, where simulations show inclusion of a neighbouring burner increases compressive flow topologies as compared to a lone flame. This may lead to favouring convex scalar structures that are potentially responsible for the increase in counter-normal flame-flame interactions observed in experiments.

Table of contents

List of figures **xv**

List of tables **xxi**

1 Introduction **1**
1.1 Background and Motivation 1
1.2 Combustion Instability 3
1.2.1 Flame-Flame Interaction 5
1.2.2 Modelling Approaches 8
1.3 Objectives and Thesis Structure 10

2 Theoretical Formulation **13**
2.1 Governing Equations 14
2.1.1 Thermodynamic Relations 14
2.1.2 Physical Conservation Laws 15
2.1.3 Diffusion and Mass Conservation 17
2.2 Large Eddy Simulation 18
2.2.1 Filtering Operation 18
2.2.2 Filtered Balance Equations 19
2.2.3 SGS Modelling 20
2.2.4 Closed Filtered Transport Equations 25
2.2.5 Implicit and Explicit Filtering 25
2.3 Combustion Modelling 27
2.3.1 Thickened Flame Model 27
2.3.2 Modified Thickened Flame Model 31
2.3.3 Dynamic Formulation 34
2.4 Small-Scale Scalar Structures 36
2.5 Local Flow Topology 39

2.6 Summary . . . 46

3 Numerical Implementation 47
3.1 Inviscid Flux . . . 47
3.1.1 Riemann Formulation . . . 48
3.1.2 Hybrid Formulation . . . 49
3.1.3 Skew-symmetric Formulation . . . 51
3.2 Artificial Flux . . . 54
3.2.1 Additional Considerations . . . 56
3.3 Chemical Source Term . . . 60
3.3.1 Reaction Kinetics . . . 60
3.3.2 Reduced Reaction Schemes . . . 61
3.3.3 Time Integration . . . 62
3.4 Mesh Generation . . . 64
3.4.1 Grid Stretching . . . 65
3.4.2 Adaptive Mesh Refinement . . . 67
3.5 Summary . . . 71

4 Navier-Stokes Characteristic Boundary Conditions 73
4.1 Mathematical Background . . . 74
4.1.1 Characteristic Equations . . . 74
4.1.2 Non-reflective Outflow . . . 76
4.1.3 Non-reflective Inflow . . . 77
4.1.4 Rebuilding Governing Equations . . . 77
4.1.5 Corner Treatments . . . 79
4.2 Results . . . 81
4.2.1 Vortex Convection . . . 81
4.2.2 Corner Collisions . . . 86
4.2.3 Reactive Systems . . . 89
4.2.4 Extension to Axisymmetric Flows . . . 94
4.2.5 Remaining Challenges . . . 98
4.3 Summary . . . 101

5 Model Validation and Evaluation 103
5.1 Flame-Vortex Interaction . . . 104
5.1.1 Computational Setup . . . 104
5.1.2 Small to Moderate Thickening . . . 105

5.1.3 Large Thickening . . . 113
5.1.4 Varying Vortex Induced Strain . . . 126
5.2 Acoustically Forced Flames . . . 132
5.2.1 Computational Setup . . . 133
5.2.2 Results . . . 135
5.2.3 Reverse Transform . . . 145
5.3 Non-reactive Turbulent Subsonic Jet . . . 148
5.3.1 Computational Setup . . . 149
5.3.2 Results . . . 153
5.4 Turbulent Bunsen Flame . . . 165
5.4.1 Computational Setup . . . 165
5.4.2 Results . . . 168
5.5 Summary . . . 178

6 Flame-Flame Interaction 181
6.1 Simulation of Experimental Slot Flame . . . 182
6.1.1 Computational Setup . . . 183
6.1.2 Results . . . 184
6.1.3 Curvature . . . 191
6.2 Dual Flames . . . 193
6.2.1 Computational Setup . . . 193
6.2.2 Results . . . 196
6.3 Summary . . . 204

7 Conclusions 207
7.1 Development of an in-house flow solver . . . 207
7.2 Combustion Modelling . . . 208
7.3 Flame-Flame interaction . . . 210
7.4 Outlook . . . 211

References 213

Appendix A Conservative and Primitive Forms 241

Appendix B Scaling of Curvatures 245

Appendix C Dimensionality of Curvature Data 247

Appendix D Slot Curvatures **249**

List of figures

1.1 Underlying coupling that drives thermoacoustic instabilities. 4
1.2 Topology of flame-flame interaction sub-types, denoting reactants (R) and products (P): a) Tunnel formation b) Tunnel closure c) Pocket event. Adapted from Dunstan et al. (2013a). 7

2.1 Classical ATF. Only the flame is thickened while turbulence is unaffected by the transformation. 28
2.2 Modified ATF model. By thickening turbulent scales as well it preserves flame/turbulence interaction within the reaction zone ($\Omega > 0$) 32
2.3 Structure of the "classical" flame sensor of Durand and Polifke (2007) and the proposed asymmetric modification for which both regression data points and polynomial fit are displayed. 35
2.4 Classification of small scale structures in terms of their mean and Gaussian curvatures. Red arrows indicate surface normal and point towards the fresh mixture. 39
2.5 Flow patterns on the $\mathcal{Q} - \mathcal{R}$ plane for different signs of $\mathcal{P}$. Adapted from Suman and Girimaji (2010). 43

3.1 Illustration of numerical techniques for dealing with discontinuities using canonical Sod's shock tube configuration. 58
3.2 Effects of numerical damping illustrated on vortex convection. 59
3.3 Illustration of the effects of stretching metrics applied in the axial direction. 66
3.4 Patch structure: sample grid with two levels of refinement. Base grid covers the entire domain and higher levels are properly nested. Source Bell et al. (2012). 67
3.5 Impact of AMR on the relevant integration range for ATF with no level interface (Case 1) and a level interface but larger filter width (case 2) or intermediate filter width (Case 3) . Source Mehl et al. (2018). 70

4.1 Evolution of normalised pressure (P^*) during vortex-boundary interaction for LODI-NSCBCs (left) and NSCBCs with transverse terms (right). Increasing time from top to bottom. 83
4.2 Evolution of transverse velocity contours during vortex-boundary interaction for LODI-NSCBCs (left) and NSCBCs with transverse terms (right). Increasing time from top to bottom. 84
4.3 Implications of choice of velocity used to evaluate transverse terms for the case of non-orthogonal mean flows. Illustrated using the time evolution of maximums in the normalised pressure field. 85
4.4 Impact of choice of relaxation parameter on an outward expanding 2D pressure wave. 87
4.5 Pressure isolines from 100500 to 101325Pa at increasing times from top to bottom for transverse terms evaluated using original (left) and corrected (right) velocities. 88
4.6 Impact of treating the chemical source term on the solution during flame-boundary interaction. Source Sutherland and Kennedy (2003). 89
4.7 Time evolution of 1D flame simulation for source terms omitted (top) and retained (bottom) in the boundary cells. 90
4.8 Domain configuration for flame-vortex-boundary interaction. Initial one dimensional flame thickness illustrated in orange, downstream of a pair of counter-rotating vortices. 91
4.9 Mass fraction of H at increasing times from left to right. R= reference, C=chemical source terms retained, NC= no chemical source terms 92
4.10 Off-centered pressure pulse: using pressure as primitive variable 93
4.11 Off-centered pressure pulse: using temperature as primitive variable 94
4.12 Pulsating vortex ring with standard NSCBCs. 96
4.13 Pulsating vortex ring with standard NSCBCs and proposed axisymmetric correction. 97
4.14 General configuration for indirect noise generation by convection of compositional inhomgeneities (green) injected upstream of a nozzle. 99
4.15 Pressure evolution for either side of the nozzle prior to injection. 100
4.16 Generation of strong vortices at the nozzle (shaded white) illustrated using axial velocity distribution 100

5.1 Evolution of the progress variable iso-contours (0.1 and 0.9) in time during flame-vortex interaction for DNS (black), $\mathcal{F} = 2$ (blue) and $\mathcal{F} = 4$ (red). . . 107

5.2 Evolution of the progress variable iso-contours (0.1 and 0.9) in time during pocket formation and burnout for DNS (black), $\mathcal{F} = 2$ (blue) and $\mathcal{F} = 4$ (red). 108
5.3 Total non-dimensional heat release plotted against non-dimensional flame time. 110
5.4 Curvature distributions at moment of max flame wrinkling. 110
5.5 Temporal evolution of curvature distribution across the flame front (i.e. progress variables $0.1 - 0.9$) for DNS (left) and $\mathcal{F} = 4$ (right) demarcated by sign. Blue represents positive and red is negative. 112
5.6 Non-dimensional heat release against non-dimensional flame time. Dotted black lines encompass the region of time 10.5-11.1 113
5.7 Evolution of progress variable distribution through times $10.5 - 11.1$ (as marked on Figure 5.6 earlier) for DNS (left) and $\mathcal{F} = 20$ (right). 115
5.8 Non-dimensional heat release rate conditioned on progress variable just after plateau region i.e. at time 10.8 shown on Figure 5.6 earlier. 117
5.9 Non-dimensional heat release rate against non-dimensional flame time. For original and clipped at progress variable < 0.9 solutions. 117
5.10 Non-dimensional reaction rates for $\mathcal{F} = 15$ compared with DNS. 119
5.11 Evolution of heat release for DNS and two sensor implementations coupled with $\mathcal{F} = 6$. 121
5.12 Non-dimensional heat release against non-dimensional flame time for classical ATF (CATF), proposed modifications and DNS. 121
5.13 Temporal evolution of flame structure displayed using progress variable, during pinch off for asymmetric (left) and symmetric (right) sensors in the modified ATF model with $\mathcal{F} = 6$. 122
5.14 Temporal evolution of flame structure displayed using progress variable, during pinch off for DNS (left) and CATF with $\mathcal{F} = 6$ (right). 123
5.15 Non-dimensional reaction rates for classical ATF with $\mathcal{F} = 6$ compared with DNS 125
5.16 Non-dimensional heat release and flame time for Vortex B. 128
5.17 Non-dimensional heat release and flame time for Vortex C. 128
5.18 Progress variable iso-contours $(0.1 - 0.9)$ for Vortex B, shown for DNS (black) and CATF (blue)/MATF(red) with a thickening factor of 6. 130
5.19 Progress variable iso-contours $(0.1 - 0.9)$ for Vortex C, shown for DNS (black) and CATF (blue)/MATF(red) with a thickening factor of 6. 131
5.20 General domain configuration with revolved flame solution showing cusping (A) and necking prior to pocket pinch off (B) during acoustic cycle. 134

5.21 Computational domain for simulated flame. Grid remains uniform in the near field prior to progressive stretching downstream towards the outlet . . 134
5.22 Instantaneous flame positions during one entire acoustic forcing cycle. DNS (black), MATF on a fine mesh (blue), MATF on a course mesh (red) and NM on a course mesh (brown) are superposed. 137
5.23 Flame shapes during acoustic cycle. Comparison between DNS (black), MATF (blue) and CATF (Orange). 138
5.24 Integrated heat release in the domain during acoustic forcing. Comparison between modified ATF (MATF) and no model (NM). 140
5.25 Integrated heat release in the domain during acoustic forcing. Comparison between modified ATF (MATF) and classical ATF (CATF). 140
5.26 Velocity vector map superimposed onto contours showing flame position for DNS. 142
5.27 Velocity vector map superimposed onto contours showing flame position for MATF with $\mathcal{F} = 6$. 143
5.28 Velocity vector map superimposed onto contours showing flame position for CATF with $\mathcal{F} = 6$. 144
5.29 Illustration of the reverse transform technique from a thickened to unthickened solution shown using different views of the progress variable. 147
5.30 Schematic of jet configuration including iso-contours of density. 151
5.31 Four level, nested mesh hierarchy with early truncation of finest level at $x \approx 0.7m$. 151
5.32 Time averaged mean velocity profile along jet center line. 154
5.33 Time averaged velocity fluctuation profile along jet center line. 154
5.34 Instantaneous dilatation field for Case A (i.e. $\tilde{\Delta} = h^{coarse}$) 158
5.35 Instantaneous dilatation field for Case E (i.e. $\tilde{\Delta} = h^{local}$) 158
5.36 Line-out of instantaneous dilatation sampled along the center line. 159
5.37 Instantaneous vorticity field for Case E (i.e. $\tilde{\Delta} = h^{local}$) 160
5.38 Instantaneous Q-criterion iso-surfaces. From bottom to top: decreasing filter width culminating in the local approach (i.e.Vertically ascending as per Case A $\rightarrow$ Case B $\rightarrow$ Case C $\rightarrow$ Case D $\rightarrow$ Case E) 161
5.39 Time averaged mean velocity profiles along the center line. 164
5.40 Time averaged velocity fluctuation profiles along the center line. 164
5.41 Time averaged mean velocity profiles along the lip-line. 164

5.42 Domain configuration for lean Bunsen flame. Flame surface iso-contours shown in red are encapsulated by AMR boxes at the finest level at all times. With blue arrows indicating the co-flow of hot products surrounding the central region. 166
5.43 Instantaneous progress variable for test cases described in Table 5.6. 170
5.44 Instantaneous 3D progress variable for test cases described in Table 5.6. . . 171
5.45 Time averaged distribution of progress variable iso-contour of 0.5 for MATF. Experiment sourced from Hernández-Pérez et al. (2011). 172
5.46 Time averaged distribution of progress variable iso-contour of 0.5 for conventional LES methodologies. Adapted from Hernández-Pérez et al. (2011). 172
5.47 Mean curvature distributions at progress variable of 0.5. Raw and filtered experimental data sourced from Yuen (2009) and Hernández-Pérez et al. (2011) respectively. 174
5.48 Mean curvature distribution at progress variable of 0.1. Raw and filtered experimental data sourced from Yuen (2009) and Hernández-Pérez et al. (2011) respectively. 175
5.49 Mean curvature distributions for different LES methodologies. Adapted from Hernández-Pérez et al. (2011). 175
5.50 A comparison between induced thickening for the case of MATF, no model (NM) and no model but inclusion of diffusive flux terms (NM+DF). 177

6.1 Illustration of experimental test rig for dual slot flames. Green arrows represent fresh mixture while red arrows stand for hot co-flow products used to stabilise the flame. Adapted from Tyagi et al. (2019a). 183
6.2 General computational domain configuration for isolated slot flame. Red iso-surface of progress variable illustrates instantaneous flame wrinkling and blue arrows refer to coflows. 185
6.3 Grid stretching progressively coarsens mesh away from the flame zone. Overlay of instantaneous velocity field and flame position (blue contours) are included. 185
6.4 **Normal flame-flame** interaction with dotted line indicating interaction zone. Experiments (top) use black for reactants and white for products with a red line to show flame surface (Tyagi et al., 2019b). Simulations (bottom) use blue for reactants, red for products and a color scale for the resolved flame structure. 187

6.5 **Counter-normal** flame-flame interaction with dotted line indicating interaction zone. Experiments (top) use black for reactants and white for products with a red line to show flame surface (Tyagi et al., 2019b). Simulations (bottom) use blue for reactants, red for products and a color scale for the resolved flame structure. 188
6.6 Vector overlay of the velocity field during a counter-normal interaction as the flow pushes one flame fold into another due to local turbulence. 189
6.7 Illustration of the three dimensional structure of both flame folds and the underlying flow field. Interaction events do not always occur in the same plane. 189
6.8 Focus view near the flame tip illustrating a highly broken flame front with significant out of plane interaction. Tunnel closure (A) leading to subsequent pocket formation and tunnel formation (B) leading to a broken flame front are readily identified. The region is a complex mixture of flame surface annihilation and generation events. 190
6.9 Curvature statistics samples in the field of view close to the inlet. 192
6.10 Curvature statistics sampled in the field of view downstream. 192
6.11 Curvature statistics sampled in the field of view downstream 193
6.12 Flame iso-surface illustrated using progress variable for different burner spacing. Blue arrows indicate coflows of burnt products. 195
6.13 Curvature distributions for the model case compared with the experimental configuration. 197
6.14 Scalar topology distributions mapped in curvature space. 198
6.15 Scalar topology distributions mapped in curvature space. 200
6.16 Local flow topologies within the flame zone. Split in terms of progress variable to highlight impact of flame front. 201
6.17 Case B- Dual Flame 203
6.18 Local flow topologies conditioned on type of scalar structure. 203
6.19 Local flow topologies conditioned on type of convex structure. 204

C.1 Comparison between 2D and 3D curvatures for lean turbulent Bunsen flame. 248

D.1 Impact of different degrees of unsteadiness in the artificial turbulent generator on flame curvature 250
D.2 Impact of different degrees of uncertainties in coflow on flame curvature. . 250

List of tables

1.1 Interaction characteristics prior to flame merging. 8

2.1 Indices and Acronyms for the different flow topologies being considered. . 41

3.1 Comprehensive mechanism for Hydrogen oxidation. Sourced from Yetter et al. (1991). M refers to a third body. 63
3.2 Jones-Lindstedt mechanism for methane oxidation. Sourced from Jones and Lindstedt (1988) 63
3.3 BFER mechanism for methane oxidation. Sourced from Franzelli et al. (2010) 63

5.1 Vortex characteristic size (estimated from separation distance) and velocities considered during flame-vortex interaction. 105
5.2 Mesh resolution in near field of acoustically modulated flame simulations. 134
5.3 Simulation parameters and filter width choices for subsonic jet. 150
5.4 Simulation parameters and filter width approaches for non-reactive jet case. 152
5.5 Turbulence Characteristics for lean methane-air Bunsen flame. Source Yuen (2009). 167
5.6 Simulation parameters for lean premixed methane-air Bunsen flame. 168
5.7 AMR grid spacing at coarsest/finest levels and approximate flame resolution. 168

6.1 Turbulence characteristics for experimental slot flame. Source Tyagi et al. (2019b) 184
6.2 Parameters for model dual flame simulations. 194

Chapter 1

Introduction

This chapter introduces the topic of combustion instabilities and highlights their significance across a wide range of practical applications. Current state of the art methods and associated challenges are briefly highlighted to lay a foundation for the research endeavours carried out in this work. Thereafter motivation for the particular avenues investigated here are discussed and potential implications made clear. Finally the structure for the remainder of this thesis is presented along with a selection of research objectives.

1.1 Background and Motivation

Provision of a reliable but also environmentally friendly energy supply continues to be one of the most prominent challenges faced by society, particularly so in light of ever growing populations yet ever dwindling supplies of fossil fuels. Coupled with a wider paradigm shift in industry and societal views on sustainable power generation this has led to significant reform in government policies (Koplow and Dernbach, 2001). A large proportion of which is targeted towards shifting away from fossil fuels by introducing restrictions on pollutants and noise emissions or subsidies towards new greener alternative technologies.

Even with substantial investment geared towards making use of renewable sources, there remains such a heavy reliance on fossil fuels (Heinberg, 2015) that it is difficult to phase out their use unilaterally or even imminently. Inevitably this has motivated a strong research effort in tandem with alternatives that looks at better optimising existing combustion systems to reduce fuel consumption and pollutant emissions while still retaining performance. However in order to achieve such ambition goals there is much left to still understand regarding the fundamentals and modelling of turbulent combustion systems.

An important example is the evolution in design of gas turbines which have long been a key component of aviation and power generation. In theory when run in a combined cycle

configuration, gas turbines form the core of the cleanest possible fossil fuel burning systems (Global, 2020). Despite their many advantages over renewable alternatives which can suffer from intermittency, the continued use of gas turbines in the scope of a low carbon vision has been contingent on technological innovation to meet changing requirements. Trends include looking towards pure hydrogen combustion Beita et al. (2021), changes to cooling systems (Xu et al., 2015) or premixing techniques (Cohen et al., 2011; Moore, 1997) to burn under desired combustion regimes.

However these very changes aimed towards improving environmental impact give rise to new difficulties such as the matter of thermoacoustic instability. The latter is the result of coupling between unsteady heat release and pressure waves which can lead to a positive feedback loop, potentially causing fatigue failure of turbine blades, cracks in the combustor wall, flame flashback or general system failure (Christodoulou et al., 2016; Giacomazzi et al., 2014; Zhou et al., 2021). Indeed the challenges regarding combustion stability in the context of gas turbines have evolved dramatically with the progression from conventional diffusion burners to lean, premixed, low NOx alternatives. The liner cooling systems of previous combustors were excellent attenuators of sound and mitigated thermoacoustic instability but do very little in current configurations (Keller, 1995). The introduction of hydrogen or ammonia as opposed to methane into the fuel stream to reduce pollutants can also exasperate thermoacoustic instability (Moëll et al., 2015, 2018; Valera-Medina et al., 2017, 2015). Even the use of annular configurations for the purposes of increased efficiency opened the door to the previously neglected but dynamically rich field of azimuthal instabilities (Noiray et al., 2011; Noiray and Schuermans, 2013).

In summary it can be said that the barriers towards continued innovation have changed over the last decade in conjunction with evolving technology. However in doing so this has opened new avenues for research with much to still be understood in terms of flame behaviour in order to deliver improved operating systems. As such demonstrating how the field of research remains ever evolving and even when motivated by environmental concerns, continued progress at its core depends on a better understanding of combustion fundamentals.

One of the major contributions of this work was the development, implementation and verification of computational tools to facilitate study of these phenomena. Whereas experiments will always remain a key component of any field they can be costly, require multiple prototypes and do not always provide the desired output data. Not to mention high operating temperatures and pressures, limited optical access, difficulty in specifying proper acoustic boundary conditions and significant experimental uncertainties are only some of factors that increase complexity while potentially affecting accuracy of experimental measurements. As such computational methods that can reliably and efficiently simulate

these systems play an invaluable role in trying to reduce lead time and production costs for industrial applications, while also shedding light on the underlying physics in academic applications.

1.2 Combustion Instability

Ever since they were first encountered in liquid rocket engines Crocco (1969); Crocco and Cheng (1956), combustion-instabilities have become a focal point for continued and targeted research. Recently the topic has grown in importance as next generation gas turbines designed under stringent environmental considerations have become known to be susceptible to self-excited thermoacoustic instabilities (Lefebvre and Ballal, 2010; Lieuwen and Yang, 2005). Typically in the past this susceptibility has only been identified late in the design process. Thereafter triggering a costly retesting process across multiple prototypes, or even *a posteriori* installation of preventive, retrofit measures albeit often at the cost of system efficiency Fredrich (2019); Sengupta et al. (2021).

Early works (Dowling, 1997, 1999; Fleifil et al., 1996) investigated these combustion-driven instabilities in simplified geometries for laminar premixed flames. It was shown that the driving force is a two way coupling between acoustic waves and unsteady heat release. This coupling in turn can depend on a complex combination of factors such as compositional inhomogeneities, vorticity waves, equivalence ratio or upstream velocity oscillations etc. A simplified mechanism can be interpreted as a small perturbation in the flow dynamics leading to a modulation of flame surface area and in turn heat release. The unsteady heat release results in volumetric expansion/contraction leading to generation of pressure fluctuations which propagate as acoustic waves. Some of these waves may be reflected by domain boundaries and arrive back at the flame prior to causing further perturbations of flame surface. Many studies have focused particularly on the nature of the latter interaction and various mechanisms such as equivalence ratio fluctuations (Ćosić et al., 2015; Stöhr et al., 2017) or hydrodynamic (Candel et al., 2014; Kim et al., 2010) interactions have been identified.

For now it is sufficient to take the simplified perspective of Figure 1.1 and appreciate that for certain conditions a resonant feedback loop may manifest, leading to self-sustained growth of oscillations. Even if this growth rate eventually dwindles as the system saturates and approaches a limit cycle, the magnitude of oscillations in this regime is usually very detrimental and at the very least completely impractical for routine operation.

A minimum condition for this positive feedback is the well known Rayleigh criterion (Rayleigh, 1877, 1878) stating the time and volume integral of pressure multiplied by heat release rate represents total energy generated by flame-acoustic interaction and must exceed

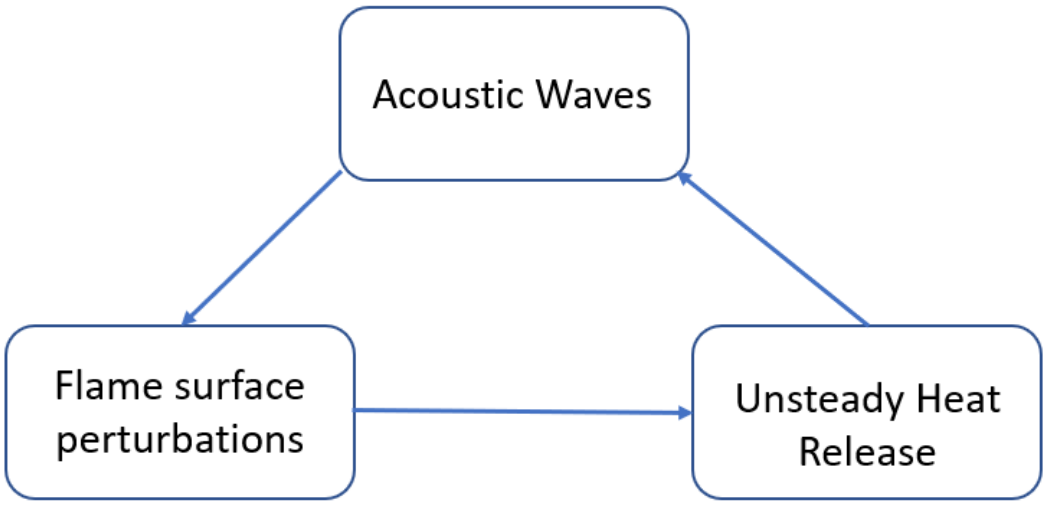

Fig. 1.1 Underlying coupling that drives thermoacoustic instabilities.

total energy dissipation as shown in Equation 1.1. Where p' is the pressure fluctuation, $\dot{q}'$ the volumetric heat release rate fluctuation, and T a sufficiently long time interval (usually taken to be the wave period), across a domain of volume and surface area of $\mathcal{V}$ and $\mathcal{A}$ respectively . The first term on the right hand side denotes the loss of acoustic energy at domain boundaries while the second refers to all other forms of dissipation and transmission (Lieuwen et al., 1998).

$$\int_0^T \int_V p(\boldsymbol{x},t)'\dot{q}(\boldsymbol{x},t)d\mathcal{V}dt > \int_0^T \int_A p(\boldsymbol{x},t)(\boldsymbol{u'}.\boldsymbol{n})d\mathcal{A}dt + \int_0^T \int_V \sum_i L_i(\boldsymbol{x},t)d\mathcal{V}dt \tag{1.1}$$

However extending and applying these fundamentals in the context of real gas turbines in all their glorious complexity remains a challenging task. Significant progress has been made over the years (Bauerheim et al., 2016; Candel et al., 2012), but there remain many open questions that are still active fields of research. Examples include the influence of transverse instabilities (Lee and Kim, 2022), complex hydrodynamic interactions (Kasthuri et al., 2022), influence of boundary conditions both in terms of reflection coefficients (Ozturkmen and Ozyoruk, 2022) but also wall heat transfers (Agostinelli et al., 2021) among others. Of particular note are the many peculiarities unique to annular combustion which facilitate the manifestation of azimuthal unstable modes (Ahn et al., 2022; Kim et al., 2022). These can be standing, spinning or mixed modes and indeed mode bifurcation in time has been observed

in experiments and remains a difficult phenomena to fully understand (Fang et al., 2021; Indlekofer et al., 2021).

One of the main questions to address in order to better understand the above phenomena revolves around the interaction between neighbouring burners. Indeed even from a purely numerical perspective if the influence between neighbouring burners can be explicitly described than only a partial segment needs to be resolved rather than the full annular combustor (Gicquel et al., 2012; Wolf et al., 2009), while much of the existing physical insight obtained from single, isolated flames can be readily extended to real applications. Burner interaction has been suggested to be the root cause for a large host of nonlinear mechanisms of interest for global system stability (Farisco et al., 2017; von Saldern et al., 2021; Yoon, 2021, 2022). One of the goals in this work was to add to this pool of knowledge by looking at the problem from a more fundamental perspective of flame-flame interaction and its associated nature.

1.2.1 Flame-Flame Interaction

There exist several examples in literature of how profound an effect having a neighbouring flame can have as opposed to an isolated one. Worth and Dawson (2012a) conducted an experimental investigation into a pair of bluff body stabilised flames and gradually reduced their separation distance. Finding that as the distance between flames grew smaller and jet merging took place, the acoustic response changed drastically due to the altered shear layer affecting large scale vortex roll up. Furthermore this creates a large degree of asymmetry in the heat release rate response which can have important implications if incorporated into a practical combustor geometry. Complementary to the study of interaction shear layers there have been several studies (Smith et al., 2018) on the interaction between neighbouring jets with varying levels of importance given to flow-flow interaction.

Flame-flame interaction can also affect flammability limits (Sohrab et al., 1985) or be an intense source of noise generation (Brouzet et al., 2019; Candel et al., 2004) directly as flame elements self-annihilate or break away. The merging of flame elements leads to rapid changes in local heat release rate and has been identified to be a leading source of combustion generated noise for both laminar (Schuller et al., 2002b; Talei et al., 2012) and turbulent (Balachandran et al., 2005) premixed configurations. Which could have a drastic impact on global system stability under the appropriate conditions. During these interaction events the flame behaves neither as a continuous and unbroken flame front, nor as a perfectly stirred homogeneous reacting mixture therefore a thorough understanding of underlying dynamics is necessary for developing combustion models capable of spanning multiple regimes.

Broadly speaking premixed *flame-flame interaction* can be classified as either **normal** or **counter-normal** interactions, where the normal is defined as positive in the direction of

fresh gases i.e. direction of flame propagation. Sometimes in literature these have also been referred to as upstream/reactant-side or downstream/product-side interactions respectively. **Normal** interactions describe the situation when two flame elements approach each other from the fresh gas side and is characterised by an initial acceleration as the preheat layers merge, followed by cusp formation with extreme negative values of local curvature. Following this the cusp recovery stage involve a rapid loss of flame surface area as the cusp retracts into the fresh mixture Dunstan et al. (2013a). This phenomena was the focus of both theoretical (Kollmann and Chen, 1998) and numerical studies (Chen and Sohrab, 1995; Chen et al., 1999) in the past and forms a key part of modern classification of flame-flame interaction.

Alternatively **counter-normal** interactions are the result of surrounding turbulence bringing together flame elements against their normal direction of propagation, or due to counter-normal flame propagation in areas of high positive curvature in thermo-diffusively stable flames (Gran et al., 1996). Several experimental and numerical campaigns have helped shed light on their behaviour (Hawkes and Chen, 2004; Kostiuk et al., 1993) and in general they occur over longer time scales due to the absence of an initial acceleration as well as slower cusp recovery (Dunstan et al., 2013a).

These broad categories can be further classified into several sub-types identifying particular interaction structures. Griffiths et al. (2015) propose a method based on eigenvalues of the scalar Hessian and a pair of shape factors to characterise all possible interaction topologies. Thereafter applying the methodology to a DNS data set of freely propagating hydrogen-air flames undergoing intense shear-generated turbulence to find that cylindrical structures are favoured over spherical ones and that most interaction occurs at either the leading or trailing edges of a flame front as opposed to the center of the flame brush.

Dunstan et al. (2013b) suggest an automatic feature extraction imaging technique to identify and track interaction evens before considering a twin V-flame configuration. Characteristic time and length scales were identified and effects of non-unity Lewis number later investigated as well (Dunstan et al., 2013a). Brouzet et al. (2019) use the method of Griffiths et al. (2015) to show how these interaction events can also occur for a single flame as the folds meld into each other, corroborating the earlier importance given to turbulent advection of the flame front (Dunstan et al., 2013a). These self-flame-flame interactions were studied in the context of annihilation events as a source of sound and shown to be responsible for much of the broadband noise generation due to modulations of unsteady heat release.

In essence three different canonical interaction sub-types are readily identified as shown in Figure 1.2 for normal interactions with the topologies remaining identical but with reactants and products switched for counter-normal interactions. Tunnel formation refers to when a hole appears in the iso-surface of progress variable as two flame elements meet while tunnel

closure manifests from the pinching off of a pocket of fresh gas from the flame leading to two distinct unburnt zones. Lastly pocket burnout is evidently the case of a pocket of fresh gas encompassed by a flame propagating inwards, with the converse being a region of burnt products and the flame propagating outwards.

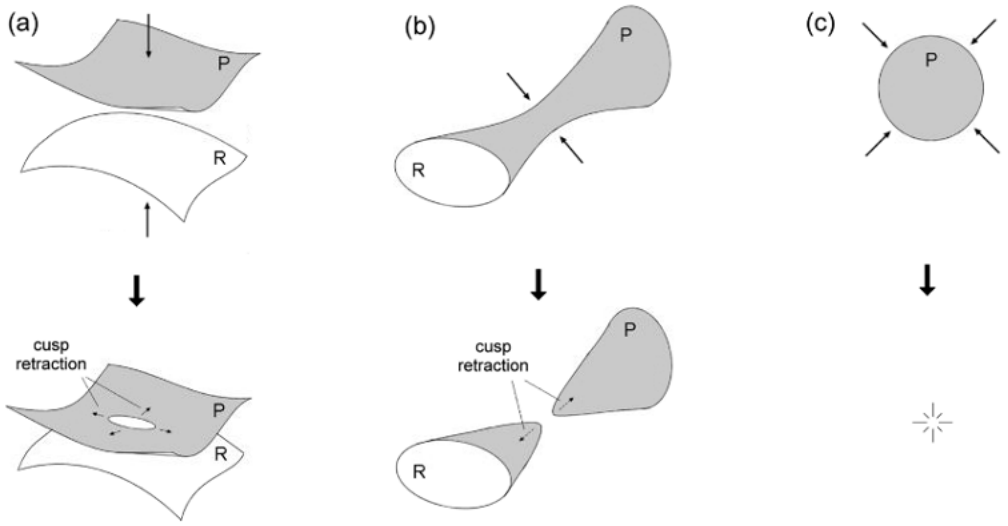

Fig. 1.2 Topology of flame-flame interaction sub-types, denoting reactants (R) and products (P): a) Tunnel formation b) Tunnel closure c) Pocket event. Adapted from Dunstan et al. (2013a).

The above differentiation of interaction sub-types is strongly motivated by an appreciation of how the total stretch rate is a leading order parameter in determining displacement speed of a flame element. As total stretch rate can be decomposed into curvature and tangential strain rate, it is convenient to have a system of classification that reflects underlying differences in these parameters. Moreover it can be deduced from Figure 1.2 that each interaction type can be associated with distinct principal curvature characteristics prior to merger. This is discussed in more detail by Dunstan et al. (2013b) but is briefly summarised in Table 1.1 below.

Therefore curvature is clearly an important parameter at all stages of interaction in determining changes to the local flame surface, which is why this classification system provides a simple way to interpret its effects without needing to locally resolve the actual values. To better understand this phenomena Chapter 6 aims to complement this approach to interaction events by looking at both flow and scalar topologies at the small scale and how they relate to experimental observations. For completeness it should be noted that in realistic systems these sub-types usually do not only manifest independently or distinctly, leading to

Table 1.1 Interaction characteristics prior to flame merging.

Type	Principal Curvature	Note
Tunnel Formation (Normal)	+ve,+ve	Quasi-1D. Both curvature and tangential straining can be important
Tunnel Formation (Counter-normal)	-ve,-ve	Quasi-1D. Weak/weakly negative curvatures due to kinematic restoration. Tangential straining dominant.
Tunnel Closure	+ve,-ve or ≈ 0	Quasi-2D. Increasing negative first curvature dominates early stretch rate.
Pocket Burnout	-ve,-ve	Fully 3D. Increasing negative curvatures dominate stretch rate prior to merging.

mixed modes which offer considerable increases in complexity and are discussed in Brouzet et al. (2019).

1.2.2 Modelling Approaches

The particular choice of approach is largely dictated by desired output which is a complex blend of different motivations. Low order network models (Han et al., 2015; Stow and Dowling, 2004; Xia et al., 2017) for example have had tremendous success in predicting thermoacoustic instability for realistic gas turbines and from a design point of view are an invaluable tool. The excellent balance between computational complexity to accommodate general geometries but computational simplicity in incorporating flame dynamics offers a very large scope for potential applications. However the reliance on external data for flame transfer functions precludes their use in the fundamental combustion studies envisioned here.

As such the basis for these activities is Direct Numerical Simulation (DNS) which involves discretising and solving the general conservation laws for fluid flows directly. Despite the immense benefit of being model-free, this approach requires resolution of all turbulent scales. Even in light of the ever growing capabilities of modern high performance computing facilities, the latter limits the approach to mostly simplified configurations and relatively low Reynolds numbers. In order to extract meaningful conclusions from the higher Reynolds number cases found in practical applications, Reynolds Averages Naveier Stokes (RANS) methods were introduced and quickly became the industry standard. Based on a decomposition of flow quantities into the time averaged mean and their statistical deviations prior to reinsertion into the governing equations, the approach outperforms DNS in terms of speed by replacing the need for resolution of scales with models. However the predictive

abilities are unquestionably inferior due to the additional averaging and approximations introduced into the system.

Large Eddy Simulation (LES) offers a blend of the two where some of the scales are resolved, but the prohibitively expensive small scales are modelled. Thus extending the range of application to many flows of practical interest while retaining much of the inherent physics. This is the approach taken in this work in order to meet desired objectives. Naturally one of the aforementioned objectives was development of appropriate models for the LES framework to be applied in the desired context. To this end a modified Artificially Thickened Flame (ATF) is proposed as detailed in Chapter 2, that best delivers intended results while offering very general functionality of wider relevance. ATF methods have already been applied to a large variety of cases in literature, and indeed even in a very recent comparative study (Kuhlmann et al., 2022) were seen to perform better than a common LES alternative in predicting flame dynamics and overall system stability. Moreover it is argued that the proposed modifications offer significant advantages, the least of which is how the topology analysis conducted later would not have been possible with current state of the art LES alternatives.

In addition to modelling of unclosed terms in the LES transport equations, care is warranted in implementing boundary treatments. Simplified approaches such as directly fixing variables at the inlet or extrapolating at the outlet to have zero gradient outflows although convenient can lead to spurious noise generation. This noise is a numerical artifact with no physical basis and can propagate upstream at the speed of sound. Although for supersonic applications this may be of little relevance, for the low Mach number simulations considered here this can taint the acoustic field in the domain. A contaminated solution such as this is undesirable in general as well but particularly so for any thermoacoustic or combustion instability application where pressure waves have significant impact. Moreover the proper transmission of waves at boundaries is imperative not only to eliminate undue numerical interference with the solution, but also to allow for early truncation of the domain. Rather than having an elongated outflow region to translate spurious noise generation away from the region of interest, appropriate boundary treatments allow the use of smaller domains and with it important savings in computational cost.

Generally treatments geared towards non-reflecting boundaries can be classified into one of three categories (Manco and de Mendonca, 2019) and still remain an active field of research (Du and Cai, 2022; Jacques and Wilk, 2021; Marchner et al., 2022; Shehadi and van der Weide, 2021). The first depends on asymptotic solutions of the governing equations in the far field (Bayliss and Turkel, 1982; Hagstrom et al., 2003) where the flow is uniform or simpler. This approach offers notable accuracy however requires boundaries

to be placed sufficiently far which can quickly accrue undue computational cost. More importantly, asymptotic solutions are not always available for complex, nonlinear problems hereby severely limiting generality. The second family of methods is based on damping zones (Colonius et al., 1993; Wasistho et al., 1997) where the computational domain is extended to include a region in which filtering, damping, stretching or a combination of which is employed. The ease of implementation here is a considerable advantage however effectiveness depends on the size of the zone, choice of parameters and which choice of damping method is employed (Manco and de Mendonca, 2019).

The final group of methods relies on characteristic decomposition of the governing equations to better understand behaviour of its wave solutions (Giles, 1990; Thompson, 1990). In theory this would provide a very accurate remedy as the waves can be directly controlled at boundaries. However in practise factors such as generalisation to multi-dimensions, uncertainties at the inflow, waves impinging on the boundary at an angle or locally reversed flow creates significant challenges. Yet the approach holds the potential to facilitate much smaller domains while retaining a large degree of generality. Which is why it was chosen for further work here, both in terms of implementation and incorporation into a cohesive research software tool but also for further evaluation of its shortcomings and potential solutions as discussed in Chapter 4.

1.3 Objectives and Thesis Structure

This research endeavour has been diverse in scope and ranged from extensive software development, combustion modelling and its subsequent validation as well as practical application. In summary the selection of outcomes presented here can be said to have been motivated by three primary objectives:

- Development and delivery of a fully compressible, LES research software tool geared towards turbulent reactive flow simulations. This includes implementation and evaluation of appropriate boundary conditions and numerical discretisation schemes, incorporating adaptive mesh refinement functionality, interfacing reduced chemical schemes and extensive code evolution overall.

- Modifications to the conventional ATF approach and investigating impact on flame-turbulence interaction. Evaluating advantages and disadvantages of the method and demonstrating the ability to make valuable inferences on small scale structures which would not be possible otherwise with standard LES alternatives. This also includes

proposal of novel scaling laws and incorporation of the modified combustion model into a wider unified ATF-LES-AMR framework.

- Application of the method to study flame-flame interaction in the presence of multiple flames which has been identified as a fundamental configuration of importance to thermoacoustic applications, as well as combustion modelling in general. This involves attempting to characterise the interaction using statistical knowledge of scalar and flow structures at the small scales and relating conclusions to large scale observations.

To highlight achievements made in these areas the rest of this thesis is structured as follows: Chapter 2 covers the theoretical foundation used to built later ideas. This includes a discussion of conventional and the novel ATF approaches proposed as well as a mathematical basis for characterisation of coherent small scale structures. Chapter 3 provides a brief description of certain facets of numerical implementation into an in-house research code named CompReal. This excludes the topic of boundary treatments which is discussed in more detail in Chapter 4. Following this Chapter 5 contains an extensive validation campaign for a modified combustion model across a range of canonical configurations as well as testing in a combined framework with AMR and LES. Lastly Chapter 6 directs application of the method to an experimental campaign targeting the nature of flame-flame interaction for multi-burner scenarios. Inferences based on small scale structures, which so far have been limited to mostly DNS studies, are used to help explain system behaviour.

Chapter 2

Theoretical Formulation

The complexity of coupling between turbulence, chemistry and flow features makes numerical simulation of combustion an inherently challenging endeavour. The computational burden grows in thermoacoustic scenarios where there is a large disparity between the small scales associated with the flame and the much larger acoustic scales. Recent reviews such as Beita et al. (2021); Giusti and Mastorakos (2019); Juniper and Sujith (2018) among many others describe some of the challenges faced in the field.

Direct Numerical Simulation of the governing equations have the potential to shed light on inherent physics by correctly capturing system behaviour. As such DNS has long since been a very useful tool in turbulence research for both reactive (Vervisch and Poinsot, 1998) and nonreactive applications (Moin and Mahesh, 1998). The requirement of DNS to resolve all scales for both the reactive flame front and turbulence all the way down to the Kolomogorov scale is simultaneously its biggest strength but also largest drawback. While on the one hand this opens the door to a wide avenue of potential investigative approaches - see for example the book of Pitsch and Attili (2020) - the computational burden can quickly become intractable for many practical configurations.

Large Eddy Simulation provides an attractive solution to mitigating this prohibitive computational cost, by limiting the resolved range of turbulence to the larger energy containing scales and filtering out smaller ones. Albeit straightforward in principle, many open questions remain (Pope, 2004), with the main difficulty stemming from having to replace filtered scales with appropriate models that often still remain elusive. Turbulent combustion poses additional challenges, for example at high Reynolds and Damköhler numbers, the dominant rate controlling processes of molecular mixing and chemical reactions occur below the filter width (Peters, 2001). Hence a complex and non-linear turbulence-chemistry interaction must be accounted for at the filtered level. Despite this a large selection of models have been developed over the years with their respective advantages and disadvantages (Pitsch, 2006),

along with a diligent framework to determine quality metrics and meshing guidelines (Chow and Moin, 2003; Freitag and Klein, 2006; Geurts and Fröhlich, 2002).

The focus here will be on particular class of methods named Artificially Thickened Flame (ATF) models for the chemical closure along with the use of the classical Smagorinsky model for the momentum equations. This chapter first presents the governing equations in the context of a single phase, reacting system before discussing the filtering operation and relevant closures for LES. The mathematical background for some of the post processing conducted later such as identification of coherent scalar and flow structures is also reviewed.

2.1 Governing Equations

Computational endeavours in the realm of thermo-fluids aim to predict the evolution of a given fluid flow in time. This phenomena and its many layers of associated inherent physics are acutely described by a set of coupled non-linear partial differential equations (PDEs) based on laws of conservation. Despite being very general in their their original form, a large proportion of the ongoing research effort is focused on changing the governing equations to a more tractable form. Nevertheless they form the basis for all that will follow and are a good starting point. Note that in the context of reactive flows the set of PDEs must be supplemented by a series of thermodynamic relations.

2.1.1 Thermodynamic Relations

For multi-component mixtures it is convenient to define a dimensionless mass fraction Y_k for each of the N chemical species present, where m_k is the mass of species k:

$$Y_k = \frac{m_k}{\sum_{k=1}^{N} m_k} \tag{2.1}$$

Division by the corresponding molar mass (W_k) results in the specific mole number n_k which leads to the definition of the mole fraction, X_k:

$$X_k = \frac{n_k}{n} = \frac{n_k}{\sum_{k=1}^{N} n_k}, \quad Y_k = n_k W_k \tag{2.2}$$

For subsonic flows it is usually common practice to consider each species component as an ideal gas, which allows application of the ideal gas law:

$$p = \rho R T = \rho \frac{\overline{R}}{W} T \tag{2.3}$$

Where the pressure (p) is related to the density (ρ) and temperature (T) via the specific gas constant (R), which is the ratio between the universal gas constant ($\overline{R}$) and mean molecular weight of the mixture($\overline{W}$). With the latter being obtained from a summation of specific mole numbers for all species:

$$W = \frac{1}{\sum_{k=1}^{N} n_k} \tag{2.4}$$

The static enthalpy of a system is defined as the sum of the sensible enthalpy and chemical enthalpy of formation. Where C_p is the mean heat capacity at constant pressure and h_k^0 is the enthalpy of formation at species k at the reference temperature:

$$h = \int_{T_0}^{T} C_p dT + \sum_{k=1}^{N} \Delta h_k^0 Y_k \tag{2.5}$$

The above combination along with C_p and other quantities discussed later such as Gibbs free energy can be approximated using the JANAF polynomials (Stull, 1965).

2.1.2 Physical Conservation Laws

There is a degree of variability in choice of primitive variables, in particular some implementations may choose to use pressure or temperature or enthalpy instead of energy. However the governing equations being considered here are shown in Equations 2.6-2.9 (Kuo, 1986; Williams, 2018) and stem from the universal laws of conservation of mass, momentum and total energy (internal, kinetic and chemical energy) . Unless otherwise stated repeated indices are subject to the Einstein summation convention.

$$\frac{\partial \rho}{\partial t} + \frac{\partial \rho u_i}{\partial x_i} = 0 \tag{2.6}$$

$$\frac{\partial \rho u_i}{\partial t} + \frac{\partial \rho u_i u_j}{\partial x_j} = -\frac{\partial p}{\partial x_i} + \frac{\partial \tau_{ij}}{\partial x_i} + \rho \sum_{k=1}^{N} Y_k f_{k,i}, \;\; i = [i, j, k] \tag{2.7}$$

$$\frac{\partial \rho e_t}{\partial t} + \frac{\partial \rho u_i e_t}{\partial x_i} = -\frac{\partial q_i}{\partial x_i} - \frac{\partial p u_i}{\partial x_i} + \frac{\partial \tau_{ij} u_j}{\partial x_i} + \rho \sum_{k=1}^{N} Y_k f_{k,i}(u_i + V_{k,i}) + \dot{Q} \tag{2.8}$$

$$\frac{\partial \rho Y_k}{\partial t} + \frac{\partial \rho u_i Y_k}{\partial x_i} + \frac{\partial \rho V_{k,i} Y_k}{\partial x_i} = \dot{\omega}, \;\; k = [1, ..., N] \tag{2.9}$$

Where ρ is the density, u_i is the velocity component in the i-th direction, p is the thermodynamic pressure, τ_{ij} is the viscous stress tensor, e_t is the total energy, q_i is the heat flux vector and $\dot{Q}$ is an external heat source while $f_{k,i}$ describes any relevant body force (such as gravity). The external heat source and effect of body forces will henceforth be neglected. Meanwhile Y_k,$V_{k,i}$ and $\dot{\omega}$ denote the mass fraction, diffusion velocity and reaction rate respectively of species k.

The viscous stress tensor for a Newtonian fluid can be expressed as Equation 2.10, where μ is the dynamic viscosity and δ_{ij} is the Kronecker delta.

$$\tau_{ij} = \left(\mu_b - \frac{2}{3}\mu\right)\frac{\partial u_k}{\partial x_k}\delta_{ij} + \mu\left(\frac{\partial u_i}{\partial x_j} + \frac{\partial u_j}{\partial x_i}\right) \tag{2.10}$$

The bulk velocity (μ_b) above is taken to be negligible in accordance with Stokes' hypothesis (Stokes, 1845), hence the viscous stress sensor is deviatoric. The energy flux, q_i, can be expressed as a combination of conduction as described using Fourier's law and an inter-diffusive heat flux brought about by the diffusion of species with different enthalpy. As shown below, where λ is the thermal conductivity, T the temperature and h_k the enthalpy for species k.

$$q_i = -\lambda\frac{\partial T}{\partial x_i} + \rho\sum_{k=1}^{N} h_k Y_k V_{k,i} \tag{2.11}$$

Strictly speaking, the treatment of diffusive processes should rely on solving a system of equations reliant on binary diffusion coefficients (D_{kj}) for the relevant diffusion velocities. However this can quickly become very cumbersome for multi-species systems, therefore most combustion codes will use a simplification with Fick's law being the most common choice. Fick's law becomes an exact solution to the system based on binary diffusion constants when pressure gradients are small, volume forces are neglected, there are more than two species, and all species have identical diffusion coefficients ($D_k = D$) but otherwise still remains a relatively reasonable approximation. The diffusion velocity is hence given by:

$$\rho V_{k,i} Y_k = -\rho D_k\frac{\partial Y_k}{\partial x_i} = -\rho D\frac{\partial Y_k}{\partial x_i} \tag{2.12}$$

Further neglecting Soret and Dufour effects, as well as external body forces, the equations of momentum, total energy and species reduce to the following while continuity remains unchanged :

$$\frac{\partial \rho u_i}{\partial t} + \frac{\partial \rho u_i u_j}{\partial x_j} = -\frac{\partial p}{\partial x_i} + \frac{\partial \tau_{ij}}{\partial x_i}, \quad i = [i, j, k] \tag{2.13}$$

$$\frac{\partial \rho e_t}{\partial t} + \frac{\partial \rho u_i e_t}{\partial x_i} = -\frac{\partial q_i}{\partial x_i} - \frac{\partial p u_i}{\partial x_i} + \frac{\partial \tau_{ij} u_j}{\partial x_i} \tag{2.14}$$

$$\frac{\partial \rho Y_k}{\partial t} + \frac{\partial \rho u_i Y_k}{\partial x_i} = \frac{\partial}{\partial x_i}\left(\rho D \frac{\partial Y_k}{\partial x_i}\right) + \dot{\omega}, \;\; k = [1,...,N] \tag{2.15}$$

2.1.3 Diffusion and Mass Conservation

There is a notable exception to the previous section where for some of the cases (e.g. hydrogen combustion) considered in this work the assumption of equal diffusivities for all species is dropped. As a result Fick's law as described in Equation 2.12 is no longer exact. As is common for most combustion codes (see Poinsot and Veynante (2005); Williams (2018) for more detailed derivation) the Hirchefelder and Curtiss approximation is adopted instead:

$$V_{k,i} = \frac{-D_k}{X_k}\frac{\partial X_k}{\partial x_i}, \;\; D_k = \frac{1 - Y_k}{\sum_{j \neq k} X_j / D_{jk}} \tag{2.16}$$

Where D_k replaces the system of binary diffusion constants by acting as the equivalent diffusion coefficient of species k into the rest of the mixture. However it can be shown from the continuity equation that a necessary condition for mass conservation is $\sum_{k=1}^{N} Y_k V_{k,i} = 0$ and although this is not a problem when using an exact solution, the condition is not satisfied when approximations such as Hirchfelder's Law or Fick's law (for the case of non-equal diffusivities) are used.

One solution is to only solve Equation 2.15 for $N-1$ species and treat the last species as a dilutent which effectively "absorbs" the approximation errors to conserve mass by being forced to conform to $Y_N = 1 - \sum_{k=1}^{N-1} Y_k$.

A more accurate method is used here where a correction velocity (V^c) is introduced into the expression for diffusion velocities and is set to :

$$V_i^c = \sum_{k=1}^{N} D_k \frac{W_k}{W}\frac{\partial X_k}{\partial x_i} \tag{2.17}$$

When this expression is substituted back into the species transport equation the modified result is :

$$\frac{\partial \rho Y_k}{\partial t} + \frac{\partial \rho (u_i + V_i^c) Y_k}{\partial x_i} = \frac{\partial}{\partial x_i}\left(\rho D_k \frac{\partial Y_k}{\partial x_i}\right) + \dot{\omega}, \;\; k = [1,...,N] \tag{2.18}$$

The above can be shown to reduce to Equation 2.15 in the case of equal diffusivities. As for the majority of the cases being considered here the latter assumption is upheld the original Equation 2.15 will be used in the theoretical derivation that follows for simplicity.

2.2 Large Eddy Simulation

Equations 2.6 and 2.13 - 2.15 coupled with an equation of state are sufficient to describe a general, multi-component, reactive system. Analytical solutions however remain elusive except for very simplified cases, with DNS being very computationally expensive hence often limited to low Reynolds numbers. A reduction in scales that need to be resolved can be achieved via temporal average giving rise to RANS, however all turbulent scales are then required to be modelled and naturally any transient dynamics are lost. A viable alternative is Large Eddy Simulation (LES), which relies on a separation of scales. Large scales hold the majority of a system's energy content and are resolved by the mesh directly, meanwhile the smaller scales resulting from a turbulent cascade are usually dissipative in nature, thus removed and replaced with appropriate models. This removal is usually achieved by applying a filtering operation to the governing equations (Sagaut, 2006).

2.2.1 Filtering Operation

The spatial filter of a function $f = f(\mathbf{x},t)$ is defined as its convolution integral with a filter function G, according to:

$$\overline{f}(\mathbf{x},t) = \int G(\mathbf{x}-\mathbf{x}';\Delta) f(\mathbf{x}',t)\mathrm{d}\mathbf{x}' \tag{2.19}$$

Where $\mathbf{x}'$ is the position vector, t is the time coordinate,Δ is the characteristic filter width in each respective direction and $\overline{f}$ is the filtered quantity. The usual choices for a filter function are a cut-off filter in spectral space, a box filter in physical space or a Gaussian filter in physical space. All filter functions are subject to the normalisation (Pope and Pope, 2000) :

$$\int_{-\infty}^{\infty}\int_{-\infty}^{\infty}\int_{-\infty}^{\infty} G(x_1,x_2,x_3)dx_1dx_2dx_3 = 1 \tag{2.20}$$

This work employs a box/top-hat filter of the form below where the cut-off scale/filter width is usually taken to be the cubic root of the volume of the cell, $\Delta = (\Delta_{x_1}\Delta_{x_2}\Delta_{x_3})^{\frac{1}{3}}$:

$$G(\mathbf{x}-\mathbf{x}';\Delta) = \begin{cases} \frac{1}{\Delta}, & \text{if } |\mathbf{x}-\mathbf{x}'| \leq \frac{\Delta}{2}. \\ 0, & \text{otherwise.} \end{cases} \tag{2.21}$$

For variable density flows it is convenient to introduce the mass-weighted Favre filtering operation :

$$\overline{\rho}\widetilde{f}(\mathbf{x},t) = \int G(\mathbf{x}-\mathbf{x}';\Delta(\mathbf{x}))\rho f(\mathbf{x}',t)\mathrm{d}\mathbf{x}' \tag{2.22}$$

where $\widetilde{f}$ is the Favre filtered variable. The choice of this filter function has the added benefit of introducing no Sub Filter/Grid Scale (SFS/SGS) terms that require modelling in the continuity equation as shown below.

2.2.2 Filtered Balance Equations

Applying the filtering operation to Equations 2.6 along with 2.13-2.15 results in:

$$\frac{\partial\overline{\rho}}{\partial t} + \frac{\partial\overline{\rho}\widetilde{u_i}}{\partial x_i} = 0 \tag{2.23}$$

$$\frac{\partial\overline{\rho}\widetilde{u_i}}{\partial t} + \frac{\partial\overline{\rho}\widetilde{u_i}\widetilde{u_j}}{\partial x_j} = -\frac{\partial\overline{p}}{\partial x_i} + \frac{\partial\overline{\tau}_{ij}}{\partial x_j} - \frac{\partial\tau_{ij}^{sgs}}{\partial x_j} \tag{2.24}$$

$$\frac{\partial\overline{\rho}\widetilde{u_i}\widetilde{e_t}}{\partial t} + \frac{\partial\overline{\rho}\widetilde{u_i}\widetilde{e_t}}{\partial x_j} = -\frac{\partial\overline{q}_i}{\partial x_i} - \frac{\partial\overline{p}\widetilde{u_i}}{\partial x_i} + \frac{\partial\widetilde{\tau}_{ij}\widetilde{u_j}}{\partial x_i} + \frac{\partial}{\partial x_i}\left(H_i^{sgs} + \sigma^{sgs}\right) \tag{2.25}$$

$$\frac{\partial\overline{\rho}\widetilde{Y_k}}{\partial t} + \frac{\partial\overline{\rho}\widetilde{u_i}\widetilde{Y_k}}{\partial x_j} = \frac{\partial}{\partial x_i}\left(\overline{\rho}D\frac{\partial\widetilde{Y_k}}{\partial x_i}\right) - \frac{\partial J_i^{sgs}}{\partial x_i} + \overline{\rho}\widetilde{\dot{\omega}(p,Y_k,T)} \tag{2.26}$$

Where the sub-filter terms are defined as:

$$\tau_{ij}^{sgs} = \overline{\rho}\widetilde{u_iu_j} - \overline{\rho}\widetilde{u}_j\widetilde{u}_i \tag{2.27}$$

$$H_i^{sgs} = \overline{\rho}\widetilde{u_ie_t} - \overline{\rho}\widetilde{u}_i\widetilde{e}_t + \overline{p}\widetilde{u}_i - \overline{pu_i} \tag{2.28}$$

$$\sigma_{ij}^{sgs} = \overline{\tau_{ij}u_j} - \widetilde{\tau}_{ij}\widetilde{u}_j \tag{2.29}$$

$$J_i^{sgs} = \overline{\rho}\widetilde{u_i Y_k} - \overline{\rho}\widetilde{u}_i\widetilde{Y}_k \tag{2.30}$$

The above set of equations represents the standard set of filtered conservation equations broadly used in many LES configurations (Gong et al., 2017), prior to the introduction of modelling for SGS terms. Implicit in their derivation is the assumption of commutability of the filtering and derivative operators, that is to say:

$$\overline{\frac{\partial \phi}{\partial x_i}} = \frac{\partial \overline{\phi}}{\partial x_i} \tag{2.31}$$

This relation is only true under several assumptions, including the very restrictive condition of constant filter width throughout the domain. This has been investigated in detail by Ghosal and Moin (1995) who developed a nonlinear mapping technique to derive an alternative filtering operation that commutes with differentiation up to an error of second order in filter width. This essentially leads to an additional closure problem not just for the nonlinear terms above but for the convective terms as well. In general (Poinsot and Veynante, 2005), most combustion codes neglect this error and assume the effects are well incorporated into the SGS models. This assumption is upheld without testing in this work for the case where changes in filter width are smooth so the terms SGS and SFS are used interchangeably for now. While multiple alternatives are proposed and evaluated for simulations with sharp changes of mesh resolution in Chapter 5.

2.2.3 SGS Modelling

The filtered momentum equation requires modelling for the SGS stress tensor. A common strategy found in many LES studies is the use of an eddy viscosity-like assumption founded on Boussinesq's hypthothesis. These methods are founded on the premise that the small scales are dissipative in nature, that is to say that their role is essentially the removal of energy from larger scales as per the well known energy cascade (Piomelli, 1999). The Smagorinsky model (Smagorinsky, 1963) is a common choice due to its simple implementation which assumes isotropy of the small scales of turbulence and models the deviatoric part of the stress tensor as:

$$\tau_{ij}^{sgs} - \frac{\delta_{ij}}{2}\tau_{kk}^{sgs} = -2\nu_t\left[\frac{1}{2}\left(\frac{\partial \widetilde{u}_i}{\partial x_j} + \frac{\partial \widetilde{u}_j}{\partial x_a}\right) - \frac{1}{3}\frac{\partial \widetilde{u}_k}{\partial x_k}\delta_{ij}\right] \tag{2.32}$$

Where ν_t has been introduced as a SGS kinematic viscosity that is defined using dimensional arguments as :

$$\nu_t = (C_\mu \Delta)^2 \left|\left|\widetilde{S}_{ij}\right|\right|; \quad \widetilde{S}_{ij} = \frac{1}{2}\left(\frac{\partial \widetilde{u}_i}{\partial x_j} + \frac{\partial \widetilde{u}_j}{\partial x_i}\right) \tag{2.33}$$

with $||.||$ being the Frobenius norm, $\widetilde{S}_{ij}$ representing the filtered deformation tensor and C_μ is the Smagorinsky constant. An improvement to eddy-viscosity models can be attained by allowing the the coefficient to vary in space and time. A method first suggested by Germano et al. (1991) in an incompressible context before being being extended to compressible flows by Moin et al. (1991) allows for just that and is often referred to as as the Dynamic Smagorinsky Model (DSM). However DSM essentially relies on an algebraic identity between the SGS terms at two different levels of filtering, hence increases computational burden by requiring a second "test" filter larger than the LES filter.

Therefore the simplified approach of Equation 2.33 will be retained here. Although it should be noted that the model is known to perform poorly near walls for which damping functions have been proposed in literature (Moin and Kim, 1982; Piomelli et al., 1990) to compensate. These are not needed in this work and instead where relevant mesh refinement will be used in such regions to limit the importance of SGS terms.

There is no unique value for the Smagorinsky constant that is applicable to all possible configurations, with values being found in literature commonly ranging between 0.1 to 0.25 (Lilly, 1967; Moin and Kim, 1982; Piomelli, 1999; Speziale et al., 1988). An intermediate value of 0.15 will be used here unless otherwise stated (Almeida and Navarro-Martinez, 2019; De and Acharya, 2009).

The isotropic contribution in Equation 2.32 (τ_{kk}^{sgs}) corresponds to twice the SGS turbulent kinetic energy, defined as :

$$k_{sgs} = \frac{1}{2}(\widetilde{u_i u_i} - \widetilde{u}_i^2) \tag{2.34}$$

This term has been shown to be small (Erlebacher et al., 1992) compared to the thermodynamic pressure and as a result is often neglected. It is also possible to use a one-equation model to solve a transport equation for the SGS kinetic energy as done by Gong et al. (2017) or Génin and Menon (2010). A common alternative that will be used here is the model derived by Yoshizawa and Horiuti (1985):

$$k_{sgs} = C_Y \left(||\widetilde{S}_{ij}||\Delta\right)^2 \tag{2.35}$$

where the constant C_Y is taken to be 0.0066 (Garnier et al., 2009). Inclusion into the unclosed filtered momentum transport equation leads to the closed form of :

$$\frac{\partial \overline{\rho}\widetilde{u}_i}{\partial t}+\frac{\partial \overline{\rho}\widetilde{u}_i\widetilde{u}_j}{\partial x_j}=-\frac{\partial \overline{p}}{\partial x_i}+\frac{\partial}{\partial x_j}\left[\overline{\rho}(\nu+\nu_t)\left(\frac{\partial \widetilde{u}_i}{\partial x_j}+\frac{\partial \widetilde{u}_j}{\partial x_i}-\frac{2}{3}\frac{\partial \widetilde{u}_k}{\partial x_k}\delta_{ij}\right)\right]+\frac{\partial}{\partial x_j}\left(\frac{2}{3}\overline{\rho}k_{sgs}\delta_{ij}\right) \tag{2.36}$$

The filtered total energy equation requires closure for the SGS convective, pressure-velocity correlation and viscous dissipation terms in Equation 2.47 which can be modelled as (Gong et al., 2017):

$$-H_i^{sgs}+\sigma_{ij}^{sgs}=\overline{\rho}\frac{\nu_t}{Pr_t}\left(\frac{\widetilde{h}}{\partial x_i}+\widetilde{u}_j\frac{\partial \widetilde{u}_j}{\partial x_i}+\frac{\partial k_{sgs}}{\partial x_i}\right) \tag{2.37}$$

where Pr_t is the subgrid Prandtl number and $\widetilde{h}$ is the resolved enthalpy of the mixture. The heat flux of Equation 2.11 is rewritten in terms of enthalpy and molecular Prandtl number, which under assumptions of equal diffusivities (i.e. unity Lewis/Schmidt numbers) can be shown to reduce to:

$$\overline{q}_i=-\overline{\rho}\frac{\nu}{Pr}\frac{\partial \widetilde{h}}{\partial x_i} \tag{2.38}$$

Substitution of the above results in the closed form of the filtered total energy equation :

$$\begin{aligned}\frac{\partial \overline{\rho}\widetilde{u}_i\widetilde{e}_t}{\partial t}+\frac{\partial \overline{\rho}\widetilde{u}_i\widetilde{e}_t}{\partial x_j}=\frac{\partial}{\partial x_i}\left[\overline{\rho}\left(\frac{\nu}{Pr}+\frac{\nu_t}{Pr_t}\right)\frac{\partial \widetilde{h}}{\partial x_i}\right]-\frac{\partial \overline{p}\widetilde{u}_i}{\partial x_i}+\frac{\partial \widetilde{\tau}_{ij}\widetilde{u}_j}{\partial x_i}\\ +\frac{\partial}{\partial x_i}\left[\overline{\rho}\frac{\nu_t}{Pr_t}\left(\widetilde{u}_j\frac{\partial \widetilde{u}_j}{\partial x_i}+\frac{\partial k_{sgs}}{\partial x_i}\right)\right]\end{aligned} \tag{2.39}$$

Closures reliant on eddy viscosity models are typical of many nonreactive flow simulations. Their direct carry over and use in a reactive context relies on the argument of there being a distinct separation of scales between turbulence and combustion (Peters, 2001). In other words, the SGS combustion only affects turbulence at the resolved scale, which is why it does not need to be explicitly accounted for in terms such as τ_{ij}^{sgs}. However strictly speaking this approximation only holds true provided the mesh is fine enough and determining whether there is a need to account for effects on the SGS turbulence field remaining an open question (Gonzalez-Juez et al., 2017).

Note that the array of SGS closures described earlier are by no means perfect. Even though they are still common in literature and despite their early success, they are often only included as a baseline to compare more sophisticated methods in recent studies. A notable weakness of purely dissipative, eddy-viscosity models is the inability to capture "backscatter" , that is to say the local transfer of energy from small to large scales. Backscatter is well

established as common even in nonreactive flows with (Piomelli et al., 1991) identifying its occurrence at about half the total points at any given time instant in their studies of channel flow and compressible isotropic turbulence. Furthermore this proportion is expected to be larger for non-equilibirum flows, perhaps even more so for combustion (Sankaran and Merkle, 2014) where the energy deposit may well be happening at the smallest of scales at times. O'Brien et al. (2017) show that for certain combustion regimes the transfer of energy from SGS to resolved scales can even occur on average rather than just sporadically. With the root cause being identified as SGS thermal expansion that eventually brings about the transformation of a small proportion of enthalpy of combustion into SGS kinetic energy.

It has been suggested (Germano et al., 1991; Sankaran and Merkle, 2014) that DSM may to a certain degree account for back scatter as the coefficients can locally undergo a sign change. However since DSM essentially relies on the Prandtl mixing length ideology, it is ill suited (not to mention non-physical) if applied with the hopes of capturing a flux of energy from small to large scales. Despite this and its other shortcomings, a simplified approach to closure models is retained here with more focus being placed on the aspect of combustion. This is for primarily two reasons, firstly the nature of ATF includes turning off SGS modelling within the actual flame front. Therefore the region of interest considered here is only indirectly affected by SGS models used for fluid transport. Not to mention the combustion regimes tested here are less prone to backscatter based on the preliminary scaling suggested by O'Brien et al. (2017). Secondly the modified ATF formulation proposed is by design very general and if need be can easily be extended to include more complex transport models in the future. With the focus being on its validation and subsequent application rather than optimisation for now.

The filtered mass fraction equation requires closures for the convective and reactive terms. The former can be done with a subgrid viscosity type formulation as done before:

$$-J_i^{sgs} = \overline{\rho}\frac{\nu_t}{Sc_t}\frac{\partial \widetilde{Y}_k}{\partial x_i} \tag{2.40}$$

where Sc_t is the subgrid Schmidt number, usually taken to be unity (Hawkes and Cant, 2001; Sankaran and Menon, 2005). The resulting transport equation is closed with the exception of the source term:

$$\frac{\partial \overline{\rho}\widetilde{Y}_k}{\partial t} + \frac{\partial \overline{\rho}\widetilde{u}_i\widetilde{Y}_k}{\partial x_i} = \frac{\partial}{\partial x_i}\left[\overline{\rho}\left(\frac{\nu}{Sc} + \frac{\nu_t}{Sc_t}\right)\frac{\partial \widetilde{Y}_k}{\partial x_i}\right] + \overline{\rho}\,\widetilde{\dot{\omega}_k(p, Y_k, T)} \tag{2.41}$$

Note that similar to before it has been shown (Boger et al., 1998; Boughanem and Trouvé, 1998) that both gradient or counter-gradient unresolved fluxes can be observed in RANS as

well as LES. Pfadler et al. (2009) confirm in conjunction with experimental investigation that a simple gradient model was not suitable for the premixed flames they considered. Nevertheless this counter-gradient transport is known to involve almost all characteristic length scales (Poinsot and Veynante, 2005), and since LES resolves at least a portion of them the net consequences are expected to be much less severe than for RANS.

Use of the Arrhenius law (Kuo and Acharya, 2012) in determining the reaction rate introduces exponential functions in the source term. Hence the source term is a strong source of non-linearity and is often the most demanding avenue for modelling efforts since:

$$\widetilde{\dot{\omega}_k(p, Y_k, T)} \neq \dot{\omega}_k(\overline{p}, \widetilde{Y}_k, \widetilde{T}) \tag{2.42}$$

Numerous solutions have been proposed to this effect, such as the flamelet model (Weller et al., 1998) which has been widely validated however requires the use of tabulated chemistry lookup databases and is only valid in the regime of thin, locally laminar flames (Van Oijen and De Goey, 2000; Van Oijen et al., 2016). The Eddy Dissipation Concept is a straightforward method in principle that relies on the factored weighting between a fine structure and its surroundings in the same filtered volume (Moule et al., 2014), however may need tuning on a case by case basis. PDF methods can theoretically provide a "perfect closure" via an exact treatment for the convective and source terms (Pope, 1985). Yet the joint PDF transport equation for the scalars/scalars-velocity remains unclosed. For a more detailed account the reader is referred to the reviews of Pitsch (2006) or Fureby (2009). The discussion here will be restricted to the family of methods relying on an Artificially Thickened Flame (ATF) which has been shown to outperform many of the alternatives (Kuhlmann et al., 2022), with details provided in Section 2.3.

Filtering of the ideal gas law results in:

$$\overline{p} = \overline{\rho} R_u \left(\sum_{k=1}^{N} \frac{\widetilde{Y}_k}{M_k} \right) \widetilde{T} + \left(\overline{\rho} R_u \left(\widetilde{\sum_{k=1}^{N} \frac{Y_k}{M_k}} \right) T - \overline{\rho} R_u \left(\sum_{k=1}^{N} \frac{\widetilde{Y}_k}{M_k} \widetilde{T} \right) \right) \tag{2.43}$$

Evidently even when using the ideal gas law the filtered pressure is not exactly closed. However it is common to neglect the SGS mass fraction and temperature correlations while calculating the pressure from the filtered values at the node cell (i.e. $\widetilde{f(x)} \approx f(\widetilde{x})$) to give:

$$\overline{p} = \overline{\rho} R_u \left(\sum_{k=1}^{N} \frac{\widetilde{Y}_k}{M_k} \right) \widetilde{T} \tag{2.44}$$

An evaluation (Ribert et al., 2017) of this approximation found that although the associated errors can be large in high pressure methane/oxygen flames, it is reasonably accurate

for the methane/air mixtures which constitute the majority of cases studied here. Lastly, all diffusion coefficients are treated as having no SGS fluctuations. While mass and thermal diffusion coefficients are obtained from the Prandtl and Schmidt numbers (assumed to be unity), and the role of preferential diffusion is not investigated for any of the hydrocarbon flames. Moreover in any case the latter is expected to only be relevant for either non-premixed combustion or hydrogen chemistry.

2.2.4 Closed Filtered Transport Equations

The final set of filtered transport equations after incorporating SGS closures (with the exception of the reactive source term) discussed above is as follows:

$$\frac{\partial \overline{\rho}}{\partial t} + \frac{\partial \overline{\rho}\widetilde{u}_i}{\partial x_i} = 0 \tag{2.45}$$

$$\frac{\partial \overline{\rho}\widetilde{u}_i}{\partial t} + \frac{\partial \overline{\rho}\widetilde{u}_i\widetilde{u}_j}{\partial x_j} = -\frac{\partial \overline{p}}{\partial x_i} + \frac{\partial}{\partial x_j}\left[\overline{\rho}(\nu+\nu_t)\left(\frac{\partial \widetilde{u}_i}{\partial x_j} + \frac{\partial \widetilde{u}_j}{\partial x_i} - \frac{2}{3}\frac{\partial \widetilde{u}_k}{\partial x_k}\delta_{ij}\right)\right] + \frac{\partial}{\partial x_j}\left(\frac{2}{3}\overline{\rho}k_{sgs}\delta_{ij}\right) \tag{2.46}$$

$$\begin{aligned}\frac{\partial \overline{\rho}\widetilde{u}_i\widetilde{e}_t}{\partial t} + \frac{\partial \overline{\rho}\widetilde{u}_i\widetilde{e}_t}{\partial x_j} = \frac{\partial}{\partial x_i}\left[\overline{\rho}\left(\frac{\nu}{Pr} + \frac{\nu_t}{Pr_t}\right)\frac{\partial \widetilde{h}}{\partial x_i}\right] - \frac{\partial \overline{p}\widetilde{u}_i}{\partial x_i} + \frac{\partial \widetilde{\tau}_{ij}\widetilde{u}_j}{\partial x_i} \\ + \frac{\partial}{\partial x_i}\left[\overline{\rho}\frac{\nu_t}{Pr_t}\left(\widetilde{u}_j\frac{\partial \widetilde{u}_j}{\partial x_i} + \frac{\partial k_{sgs}}{\partial x_i}\right)\right]\end{aligned} \tag{2.47}$$

$$\frac{\partial \overline{\rho}\widetilde{Y}_k}{\partial t} + \frac{\partial \overline{\rho}\widetilde{u}_i\widetilde{Y}_k}{\partial x_i} = \frac{\partial}{\partial x_i}\left[\overline{\rho}\left(\frac{\nu}{Sc} + \frac{\nu_t}{Sc_t}\right)\frac{\partial \widetilde{Y}_k}{\partial x_i}\right] + \overline{\rho}\widetilde{\dot{\omega}_k(p, Y_k, T)} \tag{2.48}$$

$$\overline{p} = \overline{\rho}R_u\left(\sum_{k=1}^{N}\frac{\widetilde{Y}_k}{M_k}\right)\widetilde{T} \tag{2.49}$$

2.2.5 Implicit and Explicit Filtering

The use of explicit filters in general allows for greater control of errors by allowing ease of separation between grid and model dependency. However a common approach adopted in *traditional* LES (Bose et al., 2010) is the use of a box filter with a cut-off scale equivalent to the local mesh size (usually the cube root of cell volume). The filtering process is therefore no longer explicit but implicitly achieved via the discretisation scheme and grid resolution (Lesieur et al., 2005; Sagaut, 2006). This is done by approximating the innate attenuation of

high wavenumbers present in most discretisation schemes as an "implicit" low-pass filter and remains the most widely used approach in LES (Denaro, 2011) .

Indeed this equivalence is somewhat genuine as can be seen in:

$$\frac{\delta u}{\delta x}\Big|_i = \frac{u(x+h)-u(x-h)}{2h} = \frac{d}{dx}\left[\frac{1}{2h}\int_{x-h}^{x+h} u(\beta)d\beta\right] = \frac{d\overline{u}}{dx}\Big|_i \tag{2.50}$$

where a second order central difference approximation for a continuous variable is equivalent to the exact derivative of its filtered counterpart (Rogallo and Moin, 1984). Similarly in a finite volume approach (Zhiyin, 2015), the integration over a control volume is equivalent to convolution with a top-hat filter.

While the prospect of solving for the filtered Navier-Stokes without any use of explicit filtering is alluring, it should be kept in mind that the above suggestion is not without any imperfections. For starters this equivalence essentially applies filtering only in the direction that the derivative is being taken rather than a three-dimensional operation. Therefore with each term undergoing a different (1D) filter that changes depending on coordinate direction, it is no longer possible to rigorously derive the actual set of conventional LES equations being solved from the Navier-Stokes (Lund, 2003).

A further more practical consideration is the inability to separate model and grid resolution effects as making the mesh finer will reduce the filter width which essentially adds more scales into the resolved fields. In extreme cases grid refinement has even been found to cause a deterioration of agreement with DNS/experiments (Kravchenko and Moin, 2000; Meyers and Sagaut, 2007). More generally speaking however in the realm of implicit filtering, increasing grid refinement should tend to convergence with DNS as the filter width continues to decrease and all scales are resolved, as opposed to the true LES equations. This can make it difficult to compare with filtered experimental/DNS data as well as thoroughly understand the implications of grid resolution effects.

Despite all of this, an implicit approach to filtering is maintained here, as in the context of ATF models all SGS models are turned off in the vicinity of the flame. Therefore the solution will inherently devolve into one that depends on implicit filtering here in any case. The aforementioned errors are also expected to be small, as evidenced by how implicit LES (ILES) is a large family of methods (Aspden et al., 2009) which rely on implicit grid based filtering. In conjunction with using numerical dissipation to replace an explicit SGS dissipative model, they have been shown to work remarkably well (Hickel et al., 2006).

2.3 Combustion Modelling

The use of Artificially Thickened Flame models is widespread in literature and has been applied in a variety of configurations, including Deflagration to Detonation Transition (Emami et al., 2015), stratified combustion (Kazmouz et al., 2022), gas turbine combustors (Gicquel et al., 2012) and even non-premixed flames (Cuenot et al., 2021) among others. This section first introduces the "classical" approach to ATF before reviewing subsequent improvements made over the years, most notable of which is the introduction of an efficiency function. Finally a modified approach is derived from the governing equations and proposed as a viable alternative to traditional methods before being validated in the remaining chapters.

2.3.1 Thickened Flame Model

The ATF model was first suggested in Butler and O'rourke (1977) and subsequently applied to the LES of combustion instabilities in Thibaut and Candel (1998). Motivation for the approach stems from the fact that the flame front is often too thin to be resolved on a typical LES mesh, and instead simply perceived as a region of sharp discontinuity. The method is essentially a spatial and temporal transformation of the flame from a coarse mesh (x_i, t) to a finer mesh (ξ_i, τ). The aim is to provide adequate resolution within the flame front (i.e. region of sharpest gradients) on the transformed mesh despite having insufficient resolution on the coarse LES mesh. The geometry transformation ratio, $\mathcal{F}$, is called the thickening factor. In the original work the thickening factor was independent of spatial coordinate, leading to $\xi_i = \mathcal{F} x_i$ and $\tau = \mathcal{F} t$. Conventionally (Colin et al., 2000; De and Acharya, 2009) the transformation is applied to the species transport equation only:

$$\frac{\partial \rho Y_k}{\partial \tau} + \frac{\partial \rho u_i Y_k}{\partial \xi_i} = \frac{\partial}{\partial \xi_i}\left(\rho D \mathcal{F} \frac{\partial Y_k}{\partial \xi_i}\right) + \frac{\dot{\omega}}{\mathcal{F}} \tag{2.51}$$

The flame speed and thickness following basic laminar premixed flame theory (Kuo, 1986; Williams, 2018), are respectively :

$$s_l^0 \propto \sqrt{D\dot{\omega}} \quad \text{and} \quad \delta^0 \propto D/s_l^0 \tag{2.52}$$

and their respective transformed quantities, denoted by $\hat{\cdot}$, are

$$\hat{s}_l^0 \propto \sqrt{D\mathcal{F}(\dot{\omega}/\mathcal{F})} \quad \text{and} \quad \hat{\delta}^0 \propto \mathcal{F} D/s_l^0 \tag{2.53}$$

The transformation "thickens" the flame but maintains the correct flame speed by increasing diffusion accordingly. If the grid is able to capture the flame zone accurately with the

appropriate $\mathcal{F}$ then inside the thickened region the flame is equivalent to the unfiltered, fully resolved flame. Which is why the ˜ indicating filtered quantities has been temporarily dropped here as within the flame $\widetilde{Y}_k \rightarrow Y_k$. This is naturally tempting as it suggests there is no need for SGS modelling of the filtered source term. However DNS of flame/vortex interaction (Poinsot et al., 1991) has shown that the thickened flame responds differently to turbulence. Even if the transformation preserves laminar flame speed the same is not true for the Damköhler number which represents the ratio between characteristic turbulent and chemical time scales:

$$\mathrm{Da} = \frac{\tau_t}{\tau_c} = \frac{l_t}{u'}\frac{s_l^0}{\delta^0} \tag{2.54}$$

For the thickened flame the characteristic size of turbulent motions (l_t) remains unchanged while the flame thickness is $\mathcal{F}$ times bigger, leading to a reduction of Damköhler number by the same thickening factor. As a result the flame becomes increasingly insensitive to turbulence where vortices smaller than $\mathcal{F}\delta^0$ are no longer able to interact with the flame (Colin et al., 2000; Poinsot et al., 1991). This can be graphically interpreted as removing the SGS flame wrinkling as seen in Figure 2.1 below.

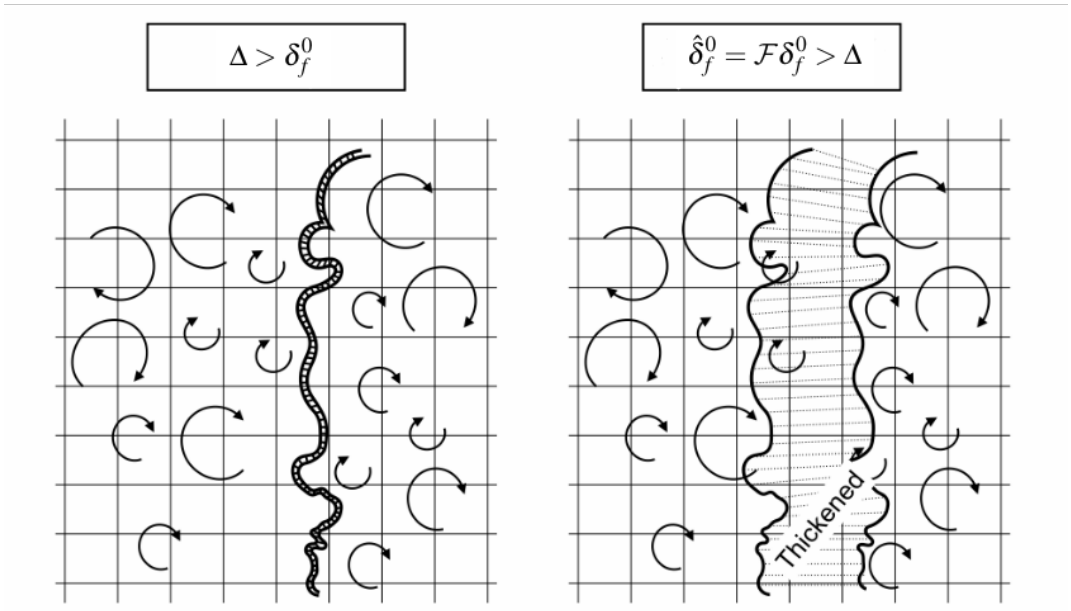

Fig. 2.1 Classical ATF. Only the flame is thickened while turbulence is unaffected by the transformation.

The sub-grid wrinkling requires modelling and this is usually done in ATF context by the inclusion of the so called *efficiency function* Charlette et al. (2002); Colin et al. (2000).

The efficiency function, E, is defined by a dimensionless wrinkling factor $\mathcal{E}$, and its ratio between a laminar flame compared with its thickened counterpart. Inclusion into the ATF model results in a modification to the reactive scalar transport equation:

$$\frac{\partial \rho Y_k}{\partial \tau} + \frac{\partial \rho u_i Y_k}{\partial \xi_i} = \frac{\partial}{\partial \xi_i}\left(\rho D E \mathcal{F} \frac{\partial Y_k}{\partial \xi_i}\right) + \frac{E\dot{\omega}}{\mathcal{F}} \tag{2.55}$$

$$E = \frac{\mathcal{E}|_{\delta_f=\delta_f^0}}{\mathcal{E}|_{\delta_f=\hat{\delta}_f^0}} \geq 1 \tag{2.56}$$

The factor $\mathcal{E}$ essentially relates the the total flame front wrinkling with its resolved component. It can be approximated as:

$$\mathcal{E} \approx 1 + \beta\Delta| < \nabla.\vec{n} >_{sgs} | \tag{2.57}$$

where β is a modal constant and $| < \nabla.\vec{n} >_{sgs} |$ is the SGS surface curvature. Colin et al. (2000) proposed a model (assuming equilibrium between SGS flame surface and turbulence) that relates the SGS curvature to the straining rate which is then approximated by a fitting function (Γ) to agree with DNS data of flame-vortex interaction. The resulting expression is:

$$\mathcal{E} = 1 + \beta \frac{u'_\Delta}{s_l^0} \Gamma\left(\frac{\Delta}{\delta_f^0}, \frac{u'_\Delta}{s_l^0}\right) \tag{2.58}$$

where the fitting function depends on the filter width to flame thickness and turbulent SGS velocity (u'_Δ) to flame speed ratios. This formulation has been revisited over the years, for example by Charlette et al. (2002) who suggested a power law model which relates flame surface area to a characteristic cut-off scale, or by De and Acharya (2009) who suggest modifications to the fitting parameter to allow for better agreement with DNS.

Despite these improvements the model remains reliant on several assumptions, most notably perhaps on approximations used to find SGS quantities needed as inputs. Evaluation of the SGS turbulent velocity fluctuation (u'_Δ) is not trivial, although it may be tempting to approximate it using the LES turbulent viscosity model for example where:

$$u'_\Delta \approx \frac{\nu_t}{C_s \Delta} = C_s ||\widetilde{S}_{ij}|| \tag{2.59}$$

This approach is not suitable as the Smagorinsky constant is designed to optimise kinetic energy dissipation and not to provide the correct velocity fluctuation at a given filter width. Furthermore (u'_Δ) should be independent of thermal expansion which will not be the case for

$\sqrt{2\widetilde{S}_{ij}\widetilde{S}_{ij}}$ above. With these restrictions in mind Colin et al. (2000) proposed the expression which was used in many subsequent models (including Charlette et al. (2002)):

$$u'_{\Delta} = C_2\Delta^3|\nabla^2(\nabla\times\vec{\widetilde{u}})| \tag{2.60}$$

and argued that this expression is independent of heat release. However strictly speaking, vorticity transport is known to be affected by heat release (Louch and Bray, 2001; McMurtry et al., 1989, 1986) it is likely there will be some effect passed onto the expression via changes in the resolved vorticity field i.e. $(\nabla\times\vec{\widetilde{u}})$.

Moreover the larger obstacle remains in determining the many empirical constants used in finding the efficiency function as well as their application outside of already validated regimes. Although work has been done is attempting to automate this process with dynamic evaluation on the fly (Rochette et al., 2018) or eliminating the dependency on a SGS velocity fluctuation (Wang et al., 2011) , most implementations rely on user defined parameters. The effects of choice of constants and method of parameter evaluation remains unclear and often necessitates *a posteriori* assessment in realistic engineering configurations (De and Acharya, 2009).

Since its original conception, the ATF model has been extended to included the use of a sensor to apply the transformation in the local region of the flame only (Légier et al., 2002). For perfectly premixed flames the differences are expected to be small since the model only has significant effects in regions where there are gradients in the scalar field i.e. inside the reaction zone. However the use of flame sensors (Durand and Polifke, 2007) has allowed application to more general cases such as non-perfectly premixed flames, while preserving mixing processes outside of the flame.

Despite theoretical shortcomings, the ATF model and its variants have been applied successfully in various LES configurations Kraus et al. (2018); Kuenne et al. (2011); Vermorel et al. (2017). Good practice is to maintain $\hat{\delta}^0/\Delta \geq 7$ (Rochette et al., 2018), and use moderate thickening factors $\mathcal{F} \leq 10$ (Kuenne et al., 2011; Popp et al., 2019).

Note ATF models can respond differently in time since the equations are solved with respect to thickened time, τ, instead of t, so care needs to be taken for configurations that involve large transients (Charlette et al., 2002). Despite its success, applications of the ATF model to systems where the flame has large dynamics are rare. Auzillon et al. (2011) showed that in acoustically forced quasi-laminar flames, the thickening approach strongly affects the flame dynamics. Similarly, strained flames using the ATF model predict lower consumption speeds (Popp et al., 2019).

2.3.2 Modified Thickened Flame Model

The proposed model applies the geometric transformation to all of the governing transport equations instead of just the reactive scalars. The idea is that by "thickening" *all scales*, including the turbulent integral scale, flame/turbulence interaction is better preserved as reflected by the Damköhler number:

$$\widehat{Da} = \frac{\hat{l}_t}{u'}\frac{s_l^0}{\hat{\delta}_f^0} = \frac{\mathcal{F}l_t}{u'}\frac{s_l^0}{\mathcal{F}\delta_f^0} = Da \tag{2.61}$$

where the thickened Damköhler number remains unchanged even without the inclusion of an efficiency function. Theoretically with a large enough thickening factor it would be possible to preserve Karlovitz numbers as well since Kolmogorov scales would also "thicken". However in large-scale simulations this may be impractical if the filter width is much larger than Kolmogorov scales, with the significance of this investigated in later chapters.

The transformation is kept local in the region of the flame via the use of a flame sensor, Ω. The sensor helps to limit effects on transient response of the system since as compared with before all the equations are now with respect to thickened time and not just the species transport equation. There is a stark contrast when comparing the modified and classical ATF in that the absence of a sensor with the proposed methodology is meaningless as it equates to scaling the entire domain. That is to say everything just becomes bigger and longer- a trivially meaningless outcome. The real challenge and objective is to blend the two sub-domains into the same simulation, one thickened and one not. To this end the sensor is critical and behaves in the same manner as shock-detectors in shock/turbulent simulations (Ducros et al., 1999; Pirozzoli, 2011), where the shock is numerically thickened by an artificial viscosity, either explicitly or implicitly by the numerical scheme. Figure 2.2 illustrates this new approach which simultaneously transforms both flame and turbulent scales.

To derive the corresponding set of equations consider a generic thickening factor that now depends on position, the coordinate transformation in 2D (from $(x,y) \rightarrow (\zeta,\eta)$ is represented by :

$$d\zeta = \frac{\partial \zeta}{\partial x}dx + \frac{\partial \zeta}{\partial y}dy \tag{2.62}$$

$$d\eta = \frac{\partial \eta}{\partial x}dx + \frac{\partial \eta}{\partial y}dy \tag{2.63}$$

$$\frac{\partial \zeta}{\partial x} = \frac{\partial \eta}{\partial y} = \mathcal{F} \tag{2.64}$$

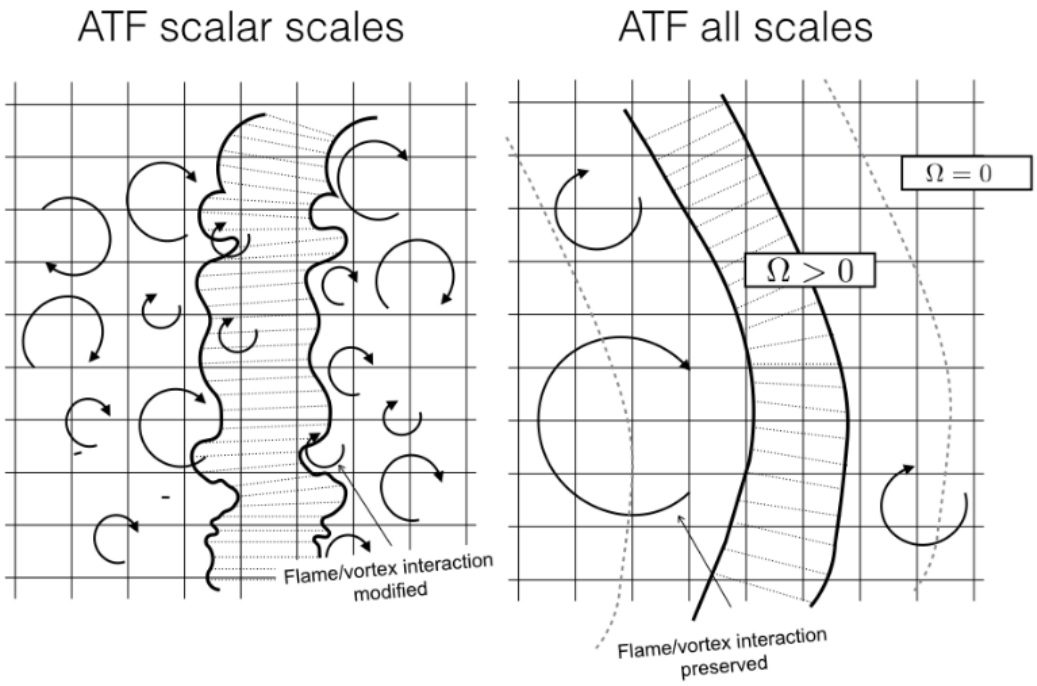

Fig. 2.2 Modified ATF model. By thickening turbulent scales as well it preserves flame/turbulence interaction within the reaction zone ($\Omega > 0$)

and

$$\frac{\partial \eta}{\partial x} = \frac{\partial \zeta}{\partial y} = 0 \tag{2.65}$$

where $\mathcal{F} = \mathcal{F}(x,y)$. Using chain rule, the derivative of an arbitrary scalar ,ϕ, is

$$\frac{\partial \phi}{\partial x} = \frac{\partial \phi}{\partial \zeta}\frac{\partial \zeta}{\partial x} = \frac{\partial \phi}{\partial \zeta}\mathcal{F} \tag{2.66}$$

similarly

$$\frac{\partial \phi}{\partial y} = \frac{\partial \phi}{\partial \eta}\mathcal{F} \tag{2.67}$$

The **convective** term:

$$\frac{\partial \rho u \phi}{\partial x} = \frac{\partial \rho u \phi}{\partial \zeta}\mathcal{F} \tag{2.68}$$

The **diffusive** term:

$$\frac{\partial}{\partial x}\left[D\frac{\partial \phi}{\partial x}\right] = \frac{\partial}{\partial \zeta}\left[D\frac{\partial \phi}{\partial x}\right]\mathcal{F} = \frac{\partial}{\partial \zeta}\left[D\mathcal{F}\frac{\partial \phi}{\partial \zeta}\right]\mathcal{F} = \mathcal{F}\frac{\partial}{\partial \zeta}\left[\underbrace{D\mathcal{F}}_{D^*}\frac{\partial \phi}{\partial \zeta}\right] \tag{2.69}$$

Replacing in a convection-diffusion equation, with $\xi_i = (\zeta, \eta)$:

$$\frac{\partial \rho\phi}{\partial t} + \mathcal{F}\frac{\partial \rho u_i \phi}{\partial \xi_i} = \mathcal{F}\frac{\partial}{\partial \xi_i}\left[D\mathcal{F}\frac{\partial \phi}{\partial \xi_i}\right] + \dot{\omega} \tag{2.70}$$

Note at this point that length scales have been transformed from $x_i \rightarrow \xi_i$ however this is not enough. In order to preserve velocities and eventually Reynolds number it is necessary to transform in time as well.

The **temporal term**:

$$\frac{\partial \phi}{\partial t} = \frac{\partial \phi}{\partial \tau}\frac{\partial \tau}{\partial t} = \frac{\partial \phi}{\partial \tau}\mathcal{F} \tag{2.71}$$

Replacing into the convection-diffusion equation:

$$\frac{\partial \rho\phi}{\partial \tau}\mathcal{F} + \mathcal{F}\frac{\partial \rho u_i \phi}{\partial \xi_i} = \mathcal{F}\frac{\partial}{\partial \xi_i}\left[D\mathcal{F}\frac{\partial \phi}{\partial \xi_i}\right] + \dot{\omega} \tag{2.72}$$

Dividing through by $\mathcal{F}$:

$$\frac{\partial \rho\phi}{\partial \tau} + \frac{\partial \rho u_i \phi}{\partial \xi_i} = \frac{\partial}{\partial \xi_i}\left[D\mathcal{F}\frac{\partial \phi}{\partial \xi_i}\right] + \frac{\dot{\omega}}{\mathcal{F}} \tag{2.73}$$

$$\frac{\partial \xi_i}{\partial x_i} = \frac{\partial \tau}{\partial t} = \mathcal{F}(x_i) \tag{2.74}$$

The above transformation is now applied to the full set of conservation equations to give:

$$\frac{\partial \overline{\rho}}{\partial \tau} + \frac{\partial \overline{\rho}\widetilde{u}_i}{\partial \xi_i} = 0 \tag{2.75}$$

$$\frac{\partial \overline{\rho}\widetilde{u}_i}{\partial \tau} + \frac{\partial \overline{\rho}\widetilde{u}_i\widetilde{u}_j}{\partial \xi_i} + \frac{\partial \overline{p}}{\partial \xi_i} = \frac{\partial 2\mathcal{F}\mu\widetilde{S}^*_{ij}}{\partial \xi_i} - (1-\Omega)\frac{\partial \tau^{sgs}_{ij}}{\partial \xi_j} \tag{2.76}$$

$$\frac{\partial \overline{\rho}\widetilde{e}}{\partial \tau} + \frac{\partial (\overline{\rho}\widetilde{e} + \overline{p})\widetilde{u}_i}{\partial \xi_i} = \frac{\partial \overline{q_i}}{\partial \xi_i} + \frac{\partial 2\mathcal{F}\mu\widetilde{S}^*_{ij}\widetilde{u}_j}{\partial \xi_i} + (1-\Omega)\frac{\partial}{\partial \xi_j}(H^{sgs}_i + \sigma^{sgs}) \tag{2.77}$$

$$\frac{\partial \overline{\rho}\widetilde{Y}_k}{\partial \tau} + \frac{\partial \overline{\rho}\widetilde{u}_i\widetilde{Y}_k}{\partial \xi_i} = \frac{\partial}{\partial \xi_i}\left(\overline{\rho}\mathcal{F}D\frac{\partial \widetilde{Y}_k}{\partial \xi_i}\right) + \frac{\overline{\rho}\dot{\omega}}{\mathcal{F}} - (1-\Omega)\frac{\partial J^{sgs}_i}{\partial \xi_j} \tag{2.78}$$

where $S^*_{ij} = S_{ij} - \delta_{ij}S_{kk}/3$ and SGS turbulent transport models have been turned off in the vicinity of the flame by the $(1-\Omega)$ term which is approximately zero in this neighbourhood.

This avoids an artificial increase to diffusivity and subsequently flame speed (De and Acharya, 2009) while maintaining $\widetilde{\phi} \rightarrow \phi$ in the reactive zone as before.

Previous research endeavours have also experimented with thickening alternative equations in addition to those describing reactive scalar transport. Notable examples include Picciani et al. (2018a,b) who apply a thickening transformation to the stochastic fields equations or Yu and Navarro-Martinez (2015) who employ a more generalised thickening but only in the context of DDT where turbulence-flame interaction is of little relevance . To the author's knowledge this work forms the first thorough validation, evaluation and subsequent application to a variety of subsonic premixed flames with the modified ATF model described above. This is in conjunction with the novel dynamic formulation described next.

2.3.3 Dynamic Formulation

The thickening factor used above in Equations 2.75-2.78 is expanded to give its dynamic form as

$$\mathcal{F} = 1 + (\mathcal{F}_0 - 1)\Omega \tag{2.79}$$

where $\mathcal{F}_0$ is a user defined function of mesh spacing that determines the desired number of points within the flame. Meanwhile the spatial dependence is incorporated into the flame sensor , Ω, usually by conditioning on progress variable. Several options are available in literature that range in complexity from static definitions (Proch and Kempf, 2014) to self adapting methods (Rochette et al., 2020) as well as various optimisations dependant on equivalence ratio regime (Zhang et al., 2021). For the cases considered here which are limited to premixed flames close to stoichiometric conditions, static sensors are shown to be sufficient and simple to implement. The commonly used implementation of Durand and Polifke (2007) is given by Equation 2.80, note that here the progress variable is normalised on fuel mass fraction to be zero in the fresh region and unity in the burnt.

$$\Omega = 16[\mathcal{Y}(1-\mathcal{Y}]^2 \tag{2.80}$$

Modest improvement was observed when using a new flame sensor correlated on a regression of the heat release distribution from a 1D flame onto progress variable. This was done by conduction DNS of a 1D stable flame before extracting the heat release rate conditioned on progress variable and fitting a polynomial to the data. The resulting expression for methane flames used here is given by the fifth order polynomial :

$$\Omega = -0.006 + 0.488\mathcal{Y} - 7.729\mathcal{Y}^2 + 46.365\mathcal{Y}^3 - 67.638\mathcal{Y}^4 + 28.473\mathcal{Y}^5 \tag{2.81}$$

The specific value of coefficients in the above expression are naturally subject to change when using a different chemistry scheme as the profile of heat release in progress variable space will be somewhat different. However the overhead for this is insignificant since it relies on a single one dimensional flame simulation that only needs to be run once and can be done a priori. Moreover the key takeaway from the proposed methodology is the generation of sensors that are asymmetric in nature as seen in Figure 2.3.

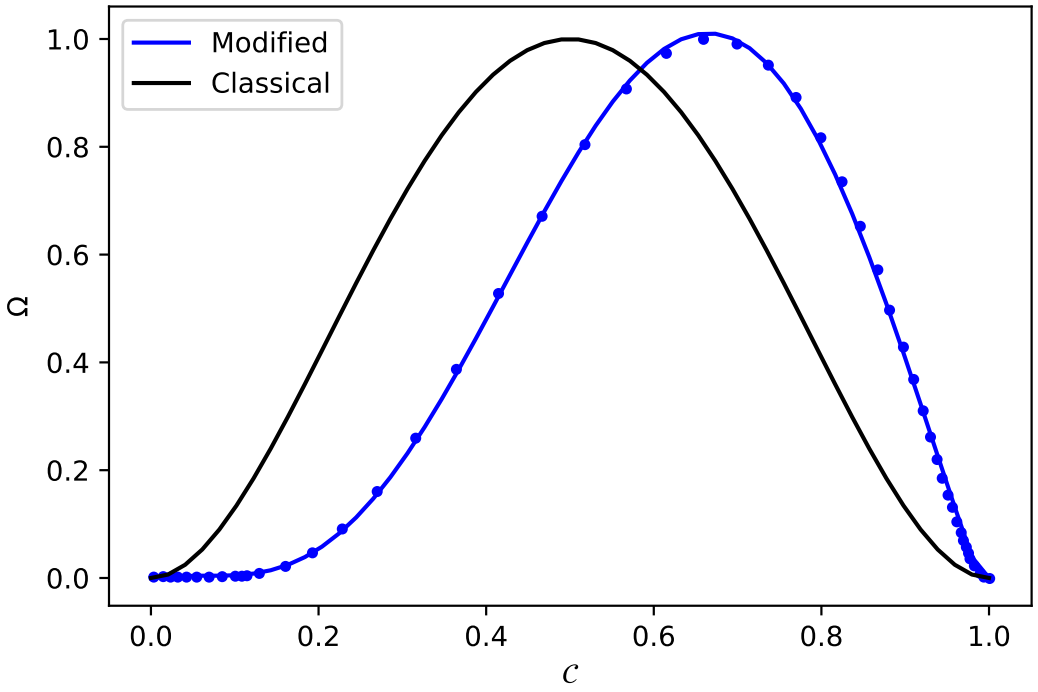

Fig. 2.3 Structure of the "classical" flame sensor of Durand and Polifke (2007) and the proposed asymmetric modification for which both regression data points and polynomial fit are displayed.

Since the reactions occurring at higher progress variable (i.e. closer to the burnt side) are at higher temperature and release more energy, it is argued this is the region that requires the most thickening in order to resolve nonlinear flame dynamics. Indeed the notion of a flame sensor peaking at progress variable of 0.5 originates more from numerical motivations than any particular physical justification.

Furthermore from a more practical standpoint, many modern combustion codes include a cutoff temperature for calculating chemical kinetics. This is a purely empirical "minimum activation temperature" designed to increase computational efficiency by restricting the number of points that enter chemical subroutines. The asymmetric sensor inherently accommodates this by limiting thickening close to zero on the lower temperature, fresh side thus avoiding an artificial increase in diffusivity in regions where the chemistry is numerically turned off.

2.4 Small-Scale Scalar Structures

The classification of small scale scalar structures into coherent categories has long been an active field of research. Small-scale structures have a strong influence on turbulent mixing and in turn the thermal fields or chemical kinetics. However their identification across the turbulent flame brush remains challenging due to a need to resolve the internal flame structure, hence previous studies have mostly been restricted to DNS.

Gibson (1968) conducted an analysis into the smallest scale features of a steady-state turbulent passive scalar distribution, and used physical as well as geometric considerations to explain their occurrence in terms of points where the scalar gradient vector is zero (i.e. critical points). The driving mechanism was found to be the local strain rate which agreed well with and extended the earlier findings of Batchelor (1952). Moffat (2003) classified these critical points in terms of the scalar Hessian tensor, with a separation into either elliptic or saddle points based on the index of the critical points. Wang and Peters (2006) further extended the analysis by determining local minimum and maximum points of the scalar field by computing gradient trajectories starting from every grid point resulting in their definition of "dissipation elements".

For premixed combustion, curvature has been one of the most crucial factors in determining the local structure of the scalar field with the early works of Clavin and Williams (1982) demonstrating it's relevance for thermal-diffusive instability. Flame stretch is often used to define the structure and extinction mechanisms of turbulent flames and was decomposed into components dependant on tangential strain rate and mean curvature in the work of Candel and Poinsot (1990). They proved that mean curvature and tangential strain correlates well with extinction mechanisms of turbulent flames and laid much of the groundwork for future combustion models. With the experimental work of Renou et al. (1998) finding a negative correlation between local flame curvature and tangential strain rate for a variety of fuels.

Echekki and Chen (1996) investigated the effects of scalar geometry on the displacement speed of an unsteady stoichiometric flame embedded within a two dimensional vortical flow field. Demonstrating that the displacement speed is primarily dependant on a balance

between reaction, diffusion and local flame curvature. Poinsot et al. (1991) studied the vortex induced quenching of 2D flames and observed that interaction of small vortices with the flame are dominated by viscous and curvature effects. Indeed Gran et al. (1996) also found that chemical effects on flame displacement speed are negligible compared to molecular diffusion in regions with large flame curvature.

Rutland et al. (1991) conducted a study of premixed flames in homogenous, isotropic turbulence under the simplifying assumptions of low heat release and single step chemistry, finding both positive and negative curvatures to be equally likely. Moreover Baum et al. (1994) suggests that away from rich combustion configurations, simplified chemistry can usually discover the same correlation of flame structure on curvature as more detailed models. They also agreed with earlier findings that the curvature PDF tends to be centered near zero and is close to symmetric.

A rigorous description of the relation between local curvature and coherent scalar structure was carried out for constant density turbulent flows by Dopazo et al. (2006, 2007). The type of local geometry was identified based on either principal curvatures or equivalently the Gauss and mean curvatures. The approach has also been successfully applied to variable density flame configurations (Cifuentes et al., 2014) and the mathematical background is briefly described below.

The collection of points over which the value of a scalar is constant is defined as an iso-scalar surface (Pope, 1988). In the context of the reactive fields present in combustion, the choice of scalar is the reduced fuel mass fraction (normalised to be zero in burnt and unity in fresh). With a unit normal to an iso-surface defined as :

$$\mathbf{n} = \frac{\nabla \mathcal{Y}}{|\nabla \mathcal{Y}|} \tag{2.82}$$

In the convention employed here the unit normal is pointing towards the fresh mixture. The local geometry can be characterised by the curvature tensor, which expressed in terms of scalar field derivatives and closely following the notation of Dopazo et al. (2006) is :

$$n_{i,j} = \frac{\partial n_i}{\partial x_j} = \frac{1}{|\nabla \mathcal{Y}|}(\delta_{ik} - n_i n_k)\frac{\partial^2 \mathcal{Y}}{\partial x_j x_k} \tag{2.83}$$

The relationship between $n_{i,j}$ and the intrinsic curvatures of iso-scalar surfaces can be obtained using Weingarten's theorem (Aris, 2012), where the intrinsic curvatures form the eigenvalues (k) along with eigenvectors ($\mathbf{N}$) that satisfy :

$$N_i(k\delta_{ij} - n_{i,j}) = 0 \tag{2.84}$$

and non-trivial solutions only exist if :

$$det||k\delta_{ij} - n_{i,j}|| = 0 \tag{2.85}$$

Equation 2.85 is equivalent to the characteristic polynomial:

$$k^3 + I_1 k^2 + I_2 k + I_3 = 0 \tag{2.86}$$

where the invariants of the curvature tensor are defined as

$$I_1 = -\nabla.\mathbf{n} \tag{2.87}$$

$$I_2 = \frac{1}{2}(n_{i,i}n_{j,j} - n_{i,j}n_{j,i}) \tag{2.88}$$

$$I_3 = -det||n_{i,j}|| \tag{2.89}$$

$\mathbf{N} = \mathbf{n}$ along with $k = 0$ is a solution to the system of equations (as $n_i n_{i,j} = 0$), which coupled with the definition in Equation 2.89 implies that $I_3 = 0$. The cubic characteristic polynomial is therefore reduced to the quadratic below.

$$k^2 + I_1 K + I_2 = 0 \tag{2.90}$$

which gives solutions for the principal curvatures :

$$k_1, k_2 = \frac{-I_1 \pm \sqrt{I_1^2 - 4I_2}}{2} \tag{2.91}$$

These are related to the Gauss and mean curvatures by:

$$k_g = k_1 k_2 \tag{2.92}$$

$$k_m = \frac{k_1 + k_2}{2} = \frac{1}{2}\frac{\partial n_i}{\partial x_i} \tag{2.93}$$

The different local geometries are mapped out in $k_m - k_g$ phase space and presented in Figure 2.4. For a positive mean curvature the surface is convex towards the fresh reactants and concave for a negative mean curvature. The region $k_g > k_m^2$ implies complex principal curvatures which is non-physical and hence excluded.

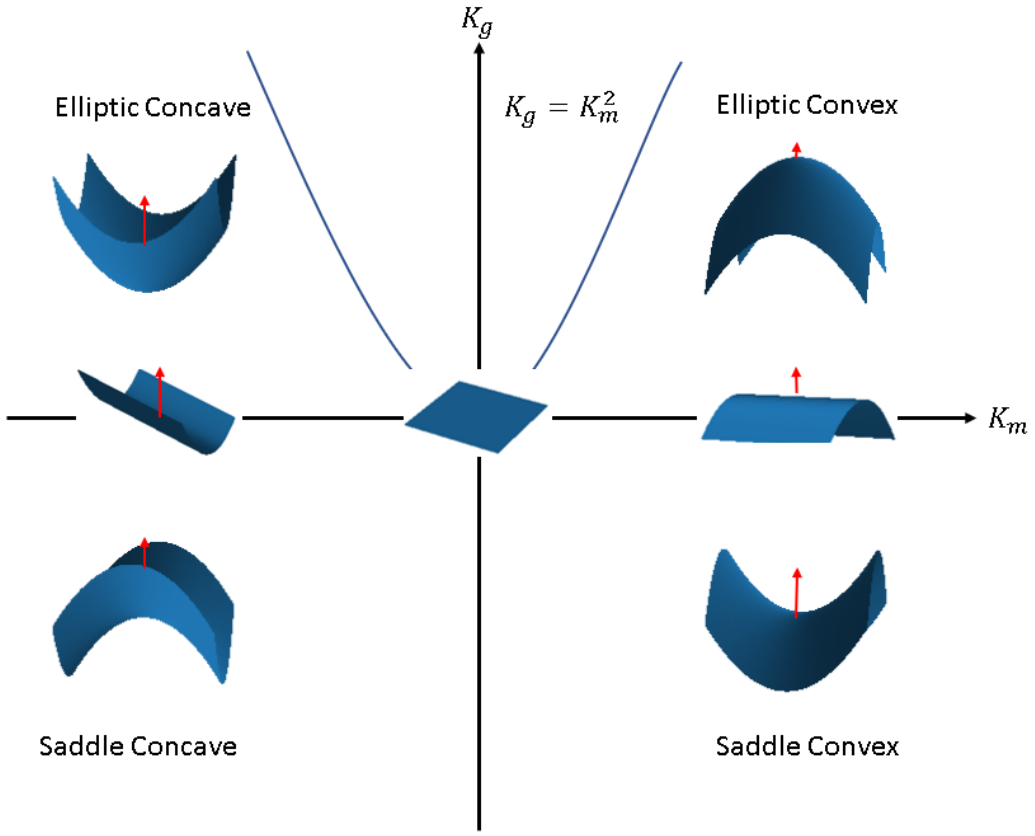

Fig. 2.4 Classification of small scale structures in terms of their mean and Gaussian curvatures. Red arrows indicate surface normal and point towards the fresh mixture.

2.5 Local Flow Topology

A topology refers to regions over which some properties of the flow exhibit significant correlation in space and time. The topic has been the focus of many discussions over the years since the early attempts of Kuo and Corrsin (1972) to characterise the geometric structure of the random small-scale, fine-structure regions dispersed in turbulent fields. Using highly idealised paradigms, the latter attempted to categorise fine structures as either spheres, cylinders or plane slabs and found that the most common small-scale vortical structures are cylindrical in nature.

However Schwarz (1990) conducted a visualisation experiment on a tank of water undergoing oscillating grid-turbulence and found the common vortical structure to be sheet-like rather than cylindrical. A finding suggested to be the most plausible in the earlier work of Betchov (1956) as well. The direct spectral simulation for a stationary, homogeneous

and isotropic turbulence field by Siggia (1981) also revealed the presence of coherent and persistent "tubes, sheets and blobs" in vorticity dominated regions.

The existence of organised coherent structures at the small scale in a turbulent field was further confirmed in the works of Kerr (1985); She et al. (1990); Vincent and Meneguzzi (1991). Kerr (1985) showed that the assumption of small scale structures being distributed with random orientation in fully developed turbulence is not always applicable and noted a preference towards formation of extended cylindrical vorticity tubes in their cases. Despite having studied idealised turbulent flows they suggest that since small scales of turbulence are believed to be decoupled from the large scales the findings of local flow topology are applicable to more general cases as well. The DNS of Vincent and Meneguzzi (1991) corroborated well with these findings and also attempted to characterise the scale of the cylindrical vorticity tubes, suggesting a width of a few dissipation scales and a length potentially reaching the integral scale of the flow.

Ruetsch and Maxey (1991) attempted to reconcile the earlier differences found between a bias towards either sheet like or cylindrical structures as a result concluding that the most intense regions exist as cylindrical structures while lower regions of vorticity prefer sheet-like structures. However a precise cutoff region was difficult to identify with a transition region aptly identified where both are equally likely. Jiménez et al. (1993) further studied these "worm like" cylindrical vorticity structures and found them to have an extensional strain rate in the direction of the vorticity vector i.e. along the axis of the tube. The structures were postulated to be intense realisations of the background vorticity and confirmed to not be an artificial manifestation of forced turbulence, as if they were removed from the flow they would naturally reappear on their own.

A generalised classification of small-scale flow patterns was put forth by Chong et al. (1990); Perry and Chong (1987) based on invariants $(\mathcal{P}, \mathcal{Q}, \mathcal{R})$ of the velocity gradient tensor. As will be seen shortly by definition the first invariant is zero for constant density flows, allowing for a simpler description of topology statistics solely in the $\mathcal{Q}-\mathcal{R}$ plane. This lead to a large host of both numerical and experimental investigation such as the work of Soria et al. (1994) on finding the large positive values of $\mathcal{Q}$ to be the most likely in incompressible mixing layers with a prevalence of stable focus/stretching topologies. A brief review of the mathematical framework is presented first, with the 8 principal topologies commonly observed in the context of flames out of the 27 possible generalised cases of Chong et al. (1990) listed in Table 2.1 with their corresponding acronyms.

The velocity gradient tensor (A_{ij}) can be split into its symmetric, strain rate tensor (S_{ij}) and corresponding skew-symmetric, rotation rate tensor (W_{ij}) components:

$$S_{ij} = \frac{1}{2}(A_{ij} + A_{ji}) \tag{2.94}$$

$$W_{ij} = \frac{1}{2}(A_{ij} - A_{ji}) \tag{2.95}$$

The rotation rate tensor has an associated axial vorticity vector ($\mathbf{w} = \nabla \times \mathbf{u}$) thus can be expressed as :

$$W_{ij} = -\frac{1}{2}\varepsilon_{ijk} w_k \tag{2.96}$$

where ε_{ijk} is the Levi-Civitá tensor. The eigenvalues (Λ_i) of the velocity gradient tensor satisfy the following characteristic equation :

$$\Lambda^3 + \mathcal{P} + \mathcal{Q}\Lambda + \mathcal{R} = 0 \tag{2.97}$$

With the following expressions for the three invariants:

$$\mathcal{P} = -tr[\mathbf{A}] = -S_{ii} \tag{2.98}$$

$$\mathcal{Q} = \frac{1}{2}(\mathcal{P}^2 - tr[\mathbf{A}]^2) = \frac{1}{2}(\mathcal{P}^2 - S_{ij}S_{ji} - W_{ij}W_{ji}) \tag{2.99}$$

$$R = \frac{1}{3}(-\mathcal{P}^3 + 3\mathcal{P}\mathcal{Q} - tr[\mathbf{A}^3]) = \frac{1}{3}(-\mathcal{P}^3 + 3\mathcal{P}\mathcal{Q} - S_{ij}S_{jk}S_{ki} - 3W_{ij}W_{jk}S_{ki}) \tag{2.100}$$

The nature of the local flow topology can be classified on the basis of roots to the characteristic Equation 2.97. With 4 different possibilities clearly identifiable as (i) all real and distinct roots (ii) all real and two equal roots (iii) all real and equal roots (iv) one real and

Table 2.1 Indices and Acronyms for the different flow topologies being considered.

Index	Acronym	Description
S1	UFC	Unstable focus/compressing
S2	UN/S/S	Unstable node/saddle/saddle
S3	SN/S/S	Stable node/saddle/saddle
S4	SFS	Stable focus/stretching
S5	SFC	Stable focus/compressing
S6	SN/SN/SN	Stable node/stable node/stable node
S7	UFC	Unstable focus/stretching
S8	UN/UN/UN	Unstable node/unstable node/ unstable node

two complex conjugate roots. However rather than having to solve the characteristic equation, the type of solution can be directly inferred based on the local values of the invariants in conjunction with properties of their phase space.

Chong et al. (1990) show that the $\mathcal{P}-\mathcal{Q}-\mathcal{R}$ space can be partitioned into distinct spatial regions that each represent a particular type of solution and hence corresponding topology. The surface dividing regions of real and complex roots is described by setting the discriminant to zero:

$$27\mathcal{R}^2+(4\mathcal{P}^3-18\mathcal{P}\mathcal{Q})\mathcal{R}+(4\mathcal{Q}^3-\mathcal{P}^2\mathcal{Q}^2)=0 \tag{2.101}$$

Furthermore this surface can be divided into two constituents (S_{1a}, S_{1b}) which osculate each other, forming a cusp. While S_2 further divides the complex plane and contains points associated with purely imaginary roots.

$$S_{1a}: \quad \frac{1}{3}\mathcal{P}\left(\mathcal{Q}-\frac{2}{9}\mathcal{P}^2\right)-\frac{2}{27}(-3\mathcal{Q}+\mathcal{P}^2)^{\frac{1}{2}}-\mathcal{R}=0 \tag{2.102}$$

$$S_{1b}: \quad \frac{1}{3}\mathcal{P}\left(\mathcal{Q}-\frac{2}{9}\mathcal{P}^2\right)+\frac{2}{27}(-3\mathcal{Q}+\mathcal{P}^2)^{\frac{1}{2}}-\mathcal{R}=0 \tag{2.103}$$

$$S_2: \quad \mathcal{P}\mathcal{Q}-\mathcal{R}=0 \tag{2.104}$$

$-\mathcal{P}=\nabla.\mathbf{u}$ is essentially the local volumetric dilatation rate, hence is zero for incompressible flows. While $-\mathcal{P}<0$ indicates regions of local fluid element compression and $-\mathcal{P}>0$ entails local element expansion. It is convenient to dissect the generalised $\mathcal{P}-\mathcal{Q}-\mathcal{R}$ space at discrete values of $\mathcal{P}$ as this allows a reduction of the surfaces S_1 and S_2 into curves that separate the regions of different topology type.

Three representative such slices conditioned for different signs of $\mathcal{P}$ are presented in Figure 2.5. On the $\mathcal{P}=0$ plane, S_2 coincides with the the $\mathcal{Q}$ axis, which combined with the symmetric S_{1a} and S_{1b} curves divides the space into 4 regions, each with it's own distinctive flow topology. Of these structures UN/S/S and SN/S/S are non-focal structures with all real eigenvalues while UFC and SFS have one real and two complex conjugate eigenvalues, leading to structures with a focus and out-of-plane strain. As the dilatation moves away from zero, the S_2 surface is no longer coincident with the $\mathcal{Q}$ axis and the symmetry of the S_1 lines is lost, leading to the possibility of additional topologies. The plane in $\mathcal{Q}-\mathcal{R}$ is now divided into 6 regions for both cases, representing three focal and three non-focal potential topologies.

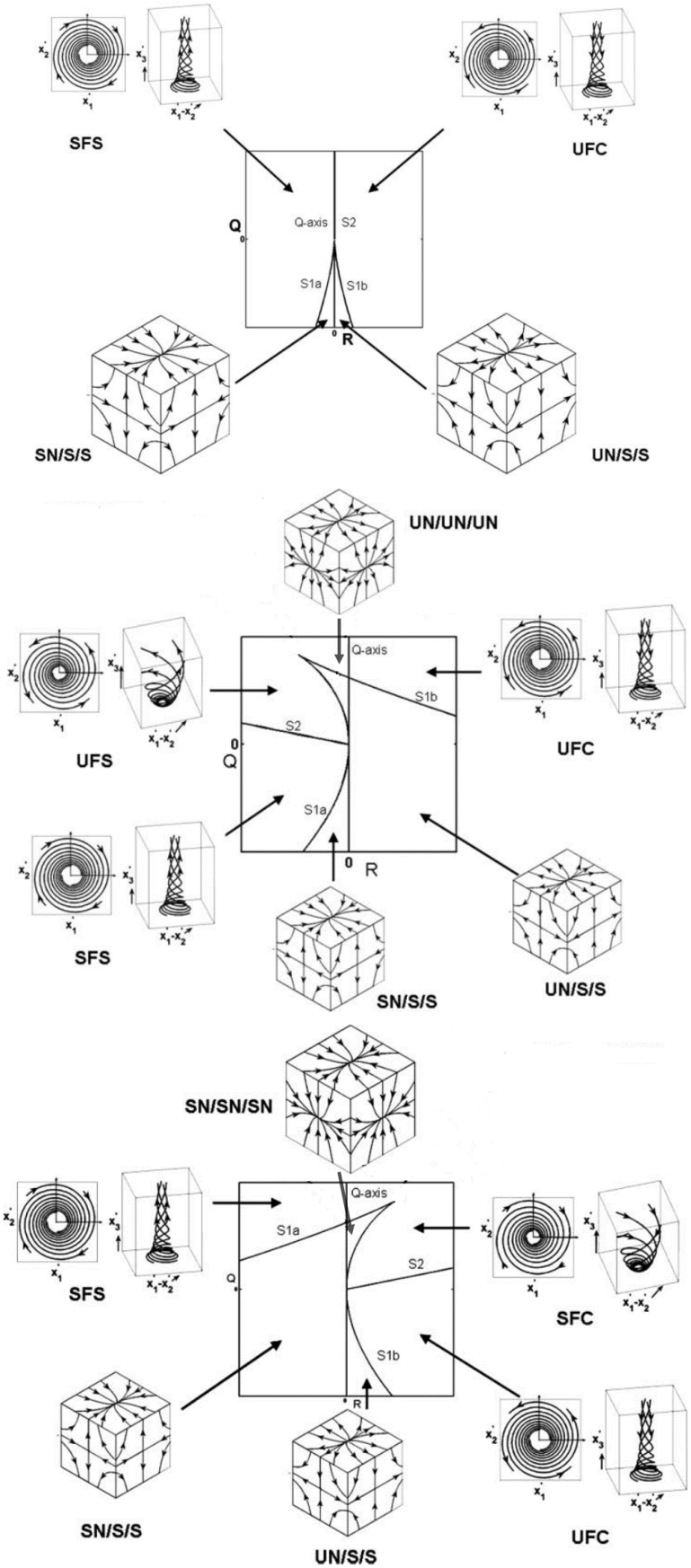

$\mathcal{P} = 0.$

$\mathcal{P} < 0$

$\mathcal{P} > 0$

Fig. 2.5 Flow patterns on the $\mathcal{Q} - \mathcal{R}$ plane for different signs of $\mathcal{P}$. Adapted from Suman and Girimaji (2010).

Blackburn et al. (1996) investigated turbulent channel flow and identified discrete tube like structures connecting the buffer layer to the outer flow regions and discussed the influence of the boundary. Away from the wall the $\mathcal{Q}-\mathcal{R}$ phase space was explored finding the topologies of stable focus/stretching and unstable node/saddle/saddle to be the preferred outcomes and were suggested to be typical of more general transitional flows. Chacin and Cantwell (2000); Chong et al. (1998) discovered a tear-drop shape in the $\mathcal{Q}-\mathcal{R}$ joint PDF in their studies of the wall bounded shear flows, a finding also observed experimentally (Andreopoulos and Honkan, 2001)under wall bounded turbulence, suggesting perhaps some degree of universality in small scale structures. With Elsinga and Marusic (2010a) following the evolutionary orbits of flow particles in time and identifying a transition on average cyclically from unstable/focus, unstable/node, stable/node to stable/focus topologies. Elsinga and Marusic (2010b) went on to provide a justification for the observed teardrop joint PDF by creating a spatial organization of coherent structures, based on the average flow pattern in the local coordinate system defined by the eigenvectors of the strain rate tensor.

Dopazo et al. (2007) conducted a combined investigation into the correlations between local flow topology and scalar structure for a passive scalar. Finding saddle point structures are related with intense strain ($\mathcal{Q}<0$) while elliptic surfaces related well with topologies dominated by vorticity ($\mathcal{Q}>0$). da Silva and Pereira (2008) carried out DNS of turbulent plane jets and characterised the evolution of invariant statistics across the turbulent/non-turbulent (T/NT) interface for both the velocity gradient and rate of rotation tensors. Reporting no discernible sign of the coherent flow topology distributions discussed earlier right at the T/NT interface, however a noticeable jump in all invariants while crossing over to the turbulent region. At a distance of only 1.7 times the Kolmogorov microscale from the interface, large scale coherent vortices were identified and the "universal" teardrop joint PDF of $\mathcal{Q}-\mathcal{R}$ was recovered. Moreover with similar findings being observed experimentally (Khashehchi et al., 2010).

The study of local flow topologies in compressible turbulent flows is comparatively limited when compared with its constant density counterpart. However, significant progress has been made since Chen et al. (1989) first applied a three dimension invariant analysis in terms of $\mathcal{P}-\mathcal{Q}-\mathcal{R}$ space for a variable density plane wake. Sondergaard et al. (1991) conducted a combined study for invariants of both the velocity gradient and symmetric strain-rate tensor for a turbulent shear flow, revealing a correlation between the latter that depends on Reynolds number and flow type. Maekawa et al. (1999) studied the geometry of flow patters in isotropic turbulence, finding that a significant portion of the turbulent kinetic energy dissipation was characterised by unstable node/saddle/saddle and stable focal/stretching topologies across a range of Mach Numbers.

Tanahashi et al. (2000) used the second invariant of the velocity gradient tensor to separate strain dominant regions ($\mathcal{Q} < 0$) from coherent fine scale eddies ($\mathcal{Q} > 0$). They showed that these fine scale eddies can have a significant axial flow which impinges on the flame and can locally enhance burning by increasing the speed at which fresh mixture is provided to the flame when the eddy axes is perpendicular to the flame front. While in regions where the eddy axis is parallel, the azimuthal flow component transported fresh mixture into the flame front, leading to a similarly tube shaped like structure in the heat release distribution. The resulting PDF of flame curvature was far from Gaussian with evident exponential tails for large curvatures, where the regions that were convex towards the burned side seem to have the higher heat release.

(Suman and Girimaji, 2010) attempted to isolate compressiblity effects by categorising topology behaviour as a function of local dilatation. Building on the earlier work of Maekawa et al. (1999) which only distinguished by sign of the dilatation and not intensity. As expected the statistics at low dilatation approximated similar results to that of incompressible turbulence, however significant changes were observed for other regions. At higher positive values of dilatation, topologies with stable solution trajectories (e,g, SFS AND SN/S/S) are replaced with the more favoured unstable solution trajectories (UFC, UN/S/S, UFS, UN/UN/UN). Intuitively this might not be too surprising as the diverging streamlines of such topologies are consistent with the tendency of a fluid element to have an increase in volume and subsequent decrease in density under positive dilatation. In particular the Un/UN/UN and UFS topologies dominate in this regime. Meanwhile as expected the opposite is observed for regions with negative dilation where stable trajectories are preferred over unstable ones in line with the notion of fluid element having decreasing volume/increasing density under negative dilatation. At higher (i.e. more negative values) the dominant topologies are SN/SN/SN and SFC. With Wang and Lu (2012) reporting a similar dependency on dilatation of stability of local topologies. Furthermore for the range studied, Suman and Girimaji (2010) described little dependency on Mach or turbulent Reynolds numbers.

Grout et al. (2011) carried out a DNS investigation into flame stabilisation mechanisms for a transverse fuel jet in cross flow. Finding the highest heat release in the farfiel to occur in regions of the node/node/node (unstable) topology which is also where the flame was thickest. Strong jet vortices were observed to have "arms" of focus/stretching (stable) sperated from the core by node/saddle/saddle (unstable) regions. While the length scale of vortical regions was described to be comparable or slightly smaller than the flame thickness. Wang and Lu (2012) investigated the variation across a boundary layer at Mach 2, identifying a preference for UFC and UN/S/S topologies in the inner and outer layer respectively.

2.6 Summary

Starting from a general description of basic conservation equations relevant to compressible reactive systems, a review of current state in the art for ATF models was provided. ATF methods rely on a transformation from a coarse grid to a *thickened* grid that provides sufficient resolution within a flame front. This is usually done to transport equations for the reactive scalars only. However by only transforming flame scales the relations between flame and turbulence are altered whereby small vortices can no longer wrinkle the thickened flame front. Efficiency functions have been proposed in literature to account for the unresolved flame wrinkling at the subgrid level. However they have a dependency on tuning parameters, limited ranges of applicability, are complex to determine and often their accuracy is difficult to know *a priori* for practical configurations.

A modified ATF model is proposed that applies the thickening transformation to all scales, both spatial and temporal. This is coupled with a novel flame sensor to produce a dynamic formulation that does not require an efficiency function, is easy to implement and is suggested to better preserve flame-turbulence interaction. The method does not depend on tuning parameters other than the thickening factor which is readily determined beforehand. As such it has a wide range of applicability and can easily be coupled with other LES methods for a hybrid approach. The primary expected limitation is a restriction to relatively moderate Karlovitz numbers as flow scales cannot be transformed if they are too small to even be seen by the coarse mesh. Relevant implications of this are discussed in the following chapters through a range of relevant validation cases.

Finally the characterisation of coherence at the small scale for scalar and flow topologies is reviewed. These structures can have a profound effect on local flame behavior, including aspects such as heat release, chemical kinetics and reaction regime. Curvature is shown to be an important parameter for a range of motivations, such as distinguishing between convex and concave geometrical structures. As the proposed approach equally transforms all scales, it should theoretically be able to provide meaningful insight on the above by preserving the intrinsic flame structure and associated curvatures. This is a potential advantage over alternative LES methods and investigated further in Chapter 5.

Chapter 3

Numerical Implementation

This chapter provides a review of the numerical methods used during the course of this investigation. All results presented were obtained through the use of an in-house finite difference, fully compressible reactive flow solver named CompReal. Considerable work was undertaken in implementing and subsequently validating several facets of code functionality with a particular focus on discretisation schemes, Adaptive Mesh Refinement (AMR), coupling with reduced chemical schemes and boundary conditions. The discretisation of convective terms evolved over the course of this work from a Riemann formulation, to a hybrid Dispersion Relation Preserving (DRP) scheme and finally into a skew-symmetric conservative form . Each of these methods provide a unique blend of advantages and disadvantages, thereby creating the need for an informed balance between between accuracy, computational cost and stability. After several iterations of a development cycle, final results presented here were produced using the skew-symmetric formulation so details on alternative schemes will be brief.

Methods such as grid stretching and AMR were relied on heavily in order to optimise domain discretisation and are reviewed. The latter was developed as one of research outcomes from the project, which is why as it was not available from the start some of the results presented retain a reliance on the former. Discussion of boundary conditions and their validation campaign are left for the subsequent chapter.

3.1 Inviscid Flux

In the framework of CompReal all variables are collocated and cell centered, with a finite difference formulation where the indices i, j, k describe the local nodal value. The index $i+1/2$ refers to the cell boundary surface between nodes i and $i+1$. The Euler contribution to the governing equations is considered first under the premise of DNS i.e. without the

demarcation of filtered variables to simplify the elucidation of discretisation techniques. The conservation of Euler convective fluxes is therefore described as :

$$\frac{\partial W}{\partial t} + div(F^n) = 0 \tag{3.1}$$

with

$$W = (\rho, \rho u_1, \rho u_2, \rho u_3, \rho e, \rho Y_k)^T, \quad F^n = \begin{pmatrix} \rho u_n \\ \rho u_n u_1 + p\delta_{n1} \\ \rho u_n u_2 + p\delta_{n2} \\ \rho u_n u_3 + p\delta_{n3} \\ u_n(\rho e + p) \\ \rho u_n Y_k \end{pmatrix}, div(F^n) = \sum_{n=1}^{3} \frac{\partial F^n}{\partial x_n} \tag{3.2}$$

3.1.1 Riemann Formulation

Modern Riemann solvers are essentially higher order extensions to the first order method of Godunov and Bohachevsky (1959), although exact solvers can be expensive which has led to development of more efficient but approximate methods. By preserving monotonicity this class of methods is well suited to dealing with shocks without introducing oscillations into the system and offer superb numerical stability, as by definition they accept discontinuous solutions.

Riemann methods usually recast the governing equations into their integral form, which for one dimension is given as :

$$\oint (\mathbf{W}dx - \mathbf{F}dt) = 0 \tag{3.3}$$

When coupled with a suitable marching in time from state $n \rightarrow n+1$ across a control volume of size Δx this results in

$$W_i^{n+1} = W_i^n - \frac{\Delta t}{\Delta x}(F_{i+1/2} - F_{i-1/2}) \tag{3.4}$$

The algorithm is complete when combined with a method to obtain the boundary fluxes ($F_{i+1/2}/F_{i-1/2}$) at each node, which are determined by considering a simplified Riemann problem. The latter is defined as an initial value problem for Equation 3.1 with two initial states separated by a discontinuity, which is to say $F_{i+1/2}(U_L, U_R)$ where $U_L = U^-_{i+1/2}$ and $U_R = U^+_{i+1/2}$. Solution to the Riemann problem are similarity solutions that only depend on x/t. An example is the HLL solver of Harten et al. (1983) which ignores the intermediate

degenerate zone by only considering two waves separating the states. CompReal uses the Harten-Lax-van Leer contact solver (HLLC) of Toro et al. (1994) which improves on the latter by also including the intermediate contact wave which is critically important in combustion applications. This is coupled with a Total Variation Diminishing (TVD) limiter second order scheme to compute the fluxes and hence allow the solution to advance in time.

3.1.2 Hybrid Formulation

An alternative discretisation is derived from the family of Dispersion Relation Preserving (DRP) schemes (Tam and Webb, 1993), which can be deployed by CompReal for a wide range of user defined orders of accuracy. The preferred choice was fourth order accuracy based on a 13-point stencil. DRP schemes are high order, explicit methods that are inherently designed to minimise dispersion and dissipation. Consider a classical finite difference approximation for a derivative at the node l, based on M values of f to the right and N values to the left:

$$\left(\frac{\partial f}{\partial x}\right)_l \approx \frac{1}{\Delta x}\sum_{j=-N}^{M} a_j f_{l+j} \tag{3.5}$$

In general the coefficients a_j can be determined from a Taylor expansion of the derivative. However the underlying objective of DRP schemes is to create a finite difference approximation that preserves the physical behaviour of wave solutions to the governing equations. In the context of Euler equations the system admits three different wave solutions, namely isotropic,nondispersive,nondissipative acoustic waves propagating at the speed of sound, as well as directional, nondispersive, nondissipative entropy and vorticity waves that are convected by the mean flow. Although CFD codes must obviously guarantee stability, they do not *a priori* guarantee the aforementioned wave behaviour (Tam and Webb, 1993). DRP schemes aim to tackle this issue by optimising the choice of coefficients in order to minimise the error between analytical derivatives and their numerical counterparts in frequency and wavenumber space. The Fourier transform of Equation 3.5 is given by :

$$\int_{-\infty}^{+\infty}\left(\frac{\partial f}{\partial x}\right)_l e^{-i\lambda x}dx \approx \int_{-\infty}^{+\infty}\frac{1}{\Delta x}\sum_{j=-N}^{M} a_j f_{l+j}e^{-i\lambda x}dx \tag{3.6}$$

With $f(\lambda)$ signifying the Fourier transform of f this can be simplified as :

$$i\lambda f(\lambda) \approx \left(\frac{1}{\Delta x}\sum_{j=-N}^{M} a_j f_{l+j}e^{-i\lambda x}\right) f(\lambda) = i\mathcal{K}f(\lambda) \tag{3.7}$$

where $\mathcal{K}$ is the effective wawe number of the Fourier transform of the finite difference scheme and is defined as :

$$\mathcal{K} = \frac{-i}{\Delta x} \sum_{j=-N}^{M} a_j e^{-ij\lambda\Delta x} \tag{3.8}$$

$\mathcal{K}\Delta x$ is a periodic function of $\lambda\Delta x$ of period 2π, therefore the integrated error of the discretisation scheme for wave numbers of interest (i.e. wavelengths longer than $4\Delta x$) is defined as

$$E = \int_{-\pi/2}^{\pi/2} |\lambda\Delta x - \mathcal{K}\Delta x|^2 d(\lambda\Delta x) \tag{3.9}$$

Minimisation of this error leads to a series of linear algebraic equations that can be used to determine the coefficients a_j. The resultant scheme is low dispersive, low dissipative and optimised to preserve wave behaviour and thus especially suitable for thermoacoustic applications where capturing the acoustic or entropy waves is essential (Berland et al., 2007) .

A pure DRP scheme can be quite challenging to implement in practice due to instability in regions of sharp discontinuities. To alleviate this drawback a hybrid scheme is used in CompReal that couples the traditional method with a HLLC solver through the use of a sensor similar to that of Ferrer (2013). Consider a function of a variable, Q, centered on node i (in one particular coordinate direction), with the user set coefficient C_1 the sensor returns one of two possible values:

$$\mathcal{Z} = \begin{cases} 1, & if \ \ |Q_{i+1} - Q_{i-1}| > C_1 Q_i \\ 0, & otherwise \end{cases} \tag{3.10}$$

Inclusion of the above creates a hybrid scheme which switches to the HLLC-TVD solver in regions of sharp gradients (second order accurate) and a DRP discretisation in regions further away (at least fourth order accurate) :

$$\left(\frac{\partial f}{\partial x}\right)_i \approx \mathcal{Z}\frac{1}{\Delta x}(f(Q)_{i+1/2} - f(Q)_{i-1/2}) + (1-\mathcal{Z})\frac{1}{\Delta x}\sum_{j=-N}^{M} a_j f_{l+j} \tag{3.11}$$

Unfortunately centred schemes alone often have trouble avoiding spurious oscillations (Sjögreen and Yee, 2017; Yee and Sjögreen, 2018), therefore the DRP aspect is supplemented with a filtering operation to remove excess build up of energy at the small scales. Following a similar methodology to the finite difference scheme this filter is somewhat optimised to preserve wave behaviour.

3.1.3 Skew-symmetric Formulation

Numerical errors associated with discretisation can be decomposed into a sum of truncation or aliasing errors (Kravchenko and Moin, 1997; Lilly, 1965). Hence the notion of order alone is not enough to describe performance. The properties mentioned earlier such as dissipation,dispersion, and conservation have a strong dependence on the form used for the discretisation of the convective term. Consider a one-dimensional scalar equation and three prospective descriptions of the nonlinear, hyperbolic term:

$$\frac{\partial U}{\partial t} + H = \frac{\partial U}{\partial t} + \frac{\partial UV}{\partial x} = 0 \tag{3.12}$$

$$H_{div} = \frac{\partial UV}{\partial x} \tag{3.13}$$

$$H_{conv} = U\frac{\partial V}{\partial x} + V\frac{\partial U}{\partial x} \tag{3.14}$$

$$H_{skew} = \frac{1}{2}\left(\frac{\partial UV}{\partial x}\right) + \frac{1}{2}\left(U\frac{\partial V}{\partial x} + V\frac{\partial U}{\partial x}\right) \tag{3.15}$$

Although all three forms above are equivalent at the continuous level, their respective discretisations differ in terms of intrinsic properties and performance. The skew-symmetric form in the context of centered schemes has been shown to guarantee conservation of quadratic quantities of interest such as the kinetic energy in the incompressible limit (Morinishi, 1995). The conservation of these quadratics has been shown to be a result of reduced aliasing errors (Kravchenko and Moin, 1997; Lilly, 1965) and indeed a Fourier transform of the three forms shows that H_{skew} has better built-in de-aliasing characteristics (Blaisdell et al., 1996).

In contrast to Finite Volume (FV) formulations that naturally ensure local conservation, Finite Difference (FD) schemes tend to be only approximately conserving. Of course FD schemes have their own strengths, such as a much weaker reliance on the typical upwinding and resultant artificial damping employed in FV schemes (Brouwer et al., 2014). Even optimised FV schemes in general have trouble reaching the quality of FD alternatives, particularly in acoustic applications (Reiss and Sesterhenn, 2014). Although the property of local conservation might be inconsequential for FD incompressible applications, they form the basis for the Rankine-Hugonoit conditions which describe shocks and becomes a prerequisite for correctly capturing shock behaviour.

The skew symmetric operator of Equation 3.15 splits the equation into a mixture of conservative and quasi-linear terms. Although managing to preserve a stable energy norm estimate (Jameson, 2008), it is not in conservative form. This has motivated many attempts at rewriting the skew symmetric operator into a term with the telescoping sum property of

Lax (1959) , typically in a discrete form of the divergence. Examples include the work of Morinishi (1995) who derived conservative schemes for LES of incompressible flows or the methods of Verstappen and Veldman (1997) for staggered meshes, which required definition of an additional secondary control volume.

The method implemented here is the approach of Ducros et al. (2000), which capitalises on the built in de-aliasing property of the skew-symmetric operator of centred schemes, while ensuring local conservation by employing the flux-based formulation:

$$\frac{\partial \int_\Omega U d\Omega}{\partial t} + F_{i+1/2}S_{i+1/2} - F_{i-1/2}S_{i-1/2} = 0 \tag{3.16}$$

where $F_{i+1/2}S_{i+1/2}$ is the flux through the interface at $i+1/2$. Returning to the original system of Equation 3.1, the spatially discretised counterpart is given as

$$\frac{\partial W_i}{\partial t} + \frac{F_{i+1/2} - F_{i-1/2}}{\Delta_i} - \mathcal{E}_i = 0 \tag{3.17}$$

where $\mathcal{E}$ denotes the truncation error. Note that U_i and W_i are both the same vector of conserved variables in the subsequent descriptions, however their conservation equations differ in terms of treatment of the flux term. The equation for U_i only incorporates the nonlinear flux term, although this is easily extended to an equation for W_i by adding the linear pressure term to the momentum equations. The pressure term is discretised independently of the skew-symmetric treatment with a classic centred derivative scheme of corresponding order, therefore the following discussion will be restricted to purely the convective flux.

It is easily verified that the choice of flux that is substituted into the divergence conservative form of Equation 3.17 can lead to either the discretised divergence or discretised skew-symmetric forms of Equation 3.13 and 3.15 respectively. For example plugging in the second order formulation for the flux

$$F_{i+1/2} = (U_i V_i + U_{i+1} V_{i+1})/2 = F^{div}_{i+1/2} \tag{3.18}$$

into Equation 3.17 leads to

$$\frac{\partial U_i}{\partial t} + \frac{U_{i+1}V_{i+1} - U_{i-1}V_{i-1}}{2\Delta x} = \mathcal{E}^{div}_i \tag{3.19}$$

which is essentially the second order divergence form. Meanwhile the second order skew-symmetric form is obtained by substituting

$$F_{i+1/2} = \frac{(U_i + U_{i+1})}{2}\frac{(V_i + V_{i+1})}{2} = F^{skew}_{i+1/2} \tag{3.20}$$

into Equation 3.17 to give:

$$\frac{\partial U_i}{\partial t} + \frac{1}{2}\left(\frac{U_{i+1}V_{i+1} - U_{i-1}V_{i-1}}{2\Delta x}\right) + \frac{1}{2}U_i\left(\frac{V_{i+1} - V_{i-1}}{2\Delta x}\right) + \frac{1}{2}V_i\left(\frac{U_{i+1} - U_{i-1}}{2\Delta x}\right) = \mathcal{E}_i^{skew} \tag{3.21}$$

This is equivalent to the second order finite volume scheme of Jameson et al. (1981) since up to second order accuracy the difference between FV and FD schemes is purely conceptual - a caveat that does not hold true for higher orders. The works of Ducros et al. (2000); Morinishi (1995) discussed next extends the idea to higher order implementations.

A general formulation for the non-linear flux is first defined as :

$$F_{i+1/2} = \sum_{k,p\in[i-n/2+1,i+n/2]} \beta_{k.p} U_{i+p} V_{i+k} \tag{3.22}$$

where the coefficients $\beta_{k,p}$ depend only on on the order of scheme and local metrics while for the search of skew-symmetric schemes $k \neq p$. Correspondingly the discretised scalar derivative is approximated as

$$\left(\frac{\partial U}{\partial x}\right)_i = \frac{1}{\Delta} \sum_{l\in[i-n/2,i+n/2]} \gamma_l U_{i+l} \tag{3.23}$$

where γ_l is obtained from Taylor expansions. For the sake of consistency , the following constraints exist on the coefficients

$$\sum_l \gamma_l = 0, \quad \sum_{k,p} \beta_{k,p} = 1 \tag{3.24}$$

while naturally the search for centred schemes necessitates $\gamma_l = \gamma_{-l}$ and $\gamma_0 = 0$. Now substituting these discrete approximations into Equation 3.15 :

$$\begin{aligned} H_{skew} &= \frac{1}{2} \sum_{l\in[i-n/2,i+n/2]} \frac{\gamma_l U_{i+l} V_{i+l} + U_i(\gamma_l V_{i+l}) + V_i(\gamma_l U_{i+1})}{\Delta} \\ &= \sum_{k,p\in[i-n/2+1,i+n/2]} \beta_{k,p} \frac{U_{i+p}V_{i+k} - U_{i-1+p}V_{i-1+k}}{\Delta} \end{aligned} \tag{3.25}$$

Solutions to Equation 3.25 can be sought to find the constants $\beta_{k,p}$ hence finding the sought conservative, skew-symmetric scheme for a chosen order n. Although Ducros et al. (2000) present solutions for fourth and sixth order accuracy, the latter was very rarely employed in the cases considered during this work so only the former is repeated here :

$$F^{skew}_{o4,i+1/2} = \frac{1}{3}(U_i + U_{i+1})(V_i + V_{i+1}) - \frac{1}{24}(U_{i-1}V_{i-1} + U_{i-1}V_{i+1} + U_iV_i + U_iV_{i+2} + U_{i+1}V_{i+1}U_{i+1}V_{i-1} + U_{i+2}V_i + U_{i+2}V_{i+2}) \tag{3.26}$$

The skew-symmetric splitting method has been widely adopted by the research community and subsequently modified over the years. Recently Sjögreen and Yee (2017) proposed a hybrid DRP-skew symmetric scheme highlighting flexibility of the procedure. At it's core the skew-symmetric scheme despite having built in de-aliasing is still a derivative from the family of centred schemes and as such can encounter stability challenges. Additional treatments to prevent oscillations and resolve shock waves are discussed next.

3.2 Artificial Flux

In order to suppress spurious oscillations, the skew-symmetric discretisation method is augmented by the High-Resolution Switched Scheme (Tatsumi et al., 1995) first put forward by Jameson et al. (1981). The scheme introduces a blend of artificial dissipation terms in order to damp high frequency, spurious modes and to accommodate shock capturing. The latter is done by designing the corresponding dissipation term to facilitate a local switching of the scheme to upwinding. The switch is based on the improved pressure sensor of Tatsumi et al. (1995), but is also extended to include density variation for stability during combustion applications.

With artificial dissipation active, the Euler flux term from the previous section is rewritten as

$$F_{i+1/2} = F(W_{i+1/2}) - d_{i+1/2} \tag{3.27}$$

$$d_{i+1/2} = d^{sc}_{i+1/2} + d^{hf}_{i+1/2} \tag{3.28}$$

$$d^{sc}_{i+1/2} = \varepsilon^{sc}_{i+1/2}(W_{i+1} - W_i) \tag{3.29}$$

$$d^{hf}_{i+1/2} = -\varepsilon^{hf}_{i+1/2}(W_{i+2} - 3W_{i+1} + 3W_i - W_{i-1}) \tag{3.30}$$

to include a blend of second and fourth order dissipation terms that allow shock capturing (d^{sc}) and enforce high frequency damping (d^{hf}) respectively. With

$$\varepsilon^{sc}_{i+1/2} = k^{sc}\ \mathcal{R}_{i+1/2}\Phi_{i+1/2} \tag{3.31}$$

$$\varepsilon^{hf}_{i+1/2} = max(0.0, k^{hf}\ \mathcal{R}_{i+1/2} - \varepsilon^{sc}_{i+1/2}) \tag{3.32}$$

where k^{sc}/k^{hf} are user defined parameters used to fix the amount of diffusion introduced into the solution by their corresponding operators. Meanwhile $\mathcal{R}_{i+1/2}$ is the spectral radius of the jacobian matrix $(\partial F/\partial W)$ at the cell face. The switch Φ, is computed as the maximum between the sensor value at the node just before and after the interface :

$$\Phi_{i+1/2} = max(\Phi_i, \Phi_{i+1}) \tag{3.33}$$

with the sensor based on a variable ϕ given as :

$$\Phi_i = \frac{|\phi_{i+1} - 2\phi + \phi_{i-1}|}{(1-C_1)\mathcal{P}_{TVD} + C_1\mathcal{P}_{JST} + \varepsilon_0} \tag{3.34}$$

coupled with

$$\mathcal{P}_{TVD} = |\phi_{i+1} - \phi_i| + |\phi_i - \phi_{i-1}| \tag{3.35}$$

$$\mathcal{P}_{JST} = \phi_{i+1} + 2\phi + \phi_{i-1} \tag{3.36}$$

ε_o is simply a small offset to ensure the denominator is never zero, while the constant C_1 is a user defined parameter that controls the nature of the switch. A value of unity recovers the original switch of Jameson et al. (1981), while $C_1 = 0$ results in the TVD replacement of Swanson and Turkel (1992). In CompReal a default value of 0.5 is used resulting in a blend of the two as suggested by Lodato (2008). The aforementioned works rely on pressure based sensors i.e. where $\phi = P$. CompReal implements the improved approach of Bouheraoua (2014) by including an additional density sensor and coupling the two as :

$$\Phi_i = \frac{(\Phi_i^P)^2 + (\Phi_i^\rho)^2}{\Phi_i^P + \Phi_i^\rho} \tag{3.37}$$

The default values for k^{sc} and k^{hf} were set to be 0.5 and 0.016 (Bouheraoua, 2014; Lodato, 2008) respectively, with the former being increased to 1.5 (Ducros et al., 1999) for supersonic cases. However large values of k^{sc} were found to significantly affect flame behaviour, therefore the goal was to always use as small a possible a value that still ensured numerical stability.

Note that the artificial flux term designed for shock capturing in Equation 3.29 is only second order. Realistically this is still a decent approximation, however theoretically it does not result in proper up winding when used in conjunction with higher order schemes. Which is why as suggested by Ducros et al. (2000) an additional term is added depending on the flux discretisation order to ensure correct switching up to fourth order:

$$d^{sc}_{i+1/2} = \begin{cases} \varepsilon^{sc}_{i+1/2}(W_{1+1} - W_i), & with\ Equation\ 3.20 \\ \varepsilon^{sc}_{i+1/2}\frac{1}{6}(-W_{i+2} + 7W_{i+1} - 5W_i - W_{i-1}), & with\ Equation\ 3.26 \end{cases} \tag{3.38}$$

3.2.1 Additional Considerations

Computing viscous flux contributions is done by first evaluating fourth order derivatives using a classical finite difference approach to give:

$$\left(\frac{\partial f}{\partial x}\right)_i = \frac{\frac{1}{12}f_{i-2} - \frac{2}{3}f_{i-1} + \frac{2}{3}f_{i+1} - \frac{1}{12}f_{i+2}}{\Delta x} \tag{3.39}$$

This derivative is then multiplied by the appropriate diffusion coefficient to give the viscous flux before finding the numerical divergence. The latter is done once again by fourth order classical central difference methods as the benefit of skew-symmetric or other de-aliasing methods on the viscous contribution is expected to be small.

The final choice of discretisation scheme was motivated by leveraging concerns of versatility, accuracy, speed and stability to obtain a suitable compromise. A brief comparative study of the three discretisations schemes used during the course of this work, namely Riemann-HLLC-TVD, Hybrid DRP and Skew-symmetric schemes was conducted. Although the Riemann solver was found to be the most stable, this came with the caveat of the most numerical diffusion. Hybrid DRP schemes perhaps best countered this downside but came at an increased computational cost from large stencils resulting in more communication. Meanwhile the skew symmetric formulation provided a significant boost to computational speed and operates on a relatively compact stencil. Fourth order accuracy was deemed sufficiently accurate for intended purposes while the stability provided by artificial flux terms was verified across a range of canonical configurations.

Without going into excessive details a brief sample of some of the tests used to inform this choice are presented below. Figure 3.1 displays the density spatial distribution a short time after initiating a discontinuity in the domain in line with the well known Sod's shock tube. While the DRP simulation directly fails to deal with such sharp gradients, the Riemann Solver is seen to be able to resolve the system well without any additional shock capturing treatments. The skew symmetric treatment with the help of artificial flux terms also exhibits good stability. Some small, localised wiggles ($7 < x < 8$m) are observed but these quickly disappear upon including the fourth order diffusive flux term. With overall accuracy even being slightly better than the Riemann solver.

Figure 3.2 relates to the classic bench-marching case (Wang et al., 2013) of vortex convection through a simple domain with periodic boundary conditions under inviscid conditions. The transverse velocity profile after ten periods is sampled along the centerline and compared with the initial distribution. The DRP coupled with an optimised filter solution captures the state almost perfectly, highlighting the technique's excellent preservation qualities. Meanwhile the Riemann solver despite its greater stability suffers from excessive damping with the vortex being only barely noticeable. A pure implementation of the skew-symmetric form does reasonably well in maintaining the peaks but results in small fluctuations throughout the domain. Including the artificial flux term geared towards high frequency damping helps eliminate the latter, but this comes at the cost of additional diffusion influencing the vortex structure slightly. The degree of diffusion can be reduced since it depends on a user controlled parameter, however this highlights the importance of trying to use as small a value as possible.

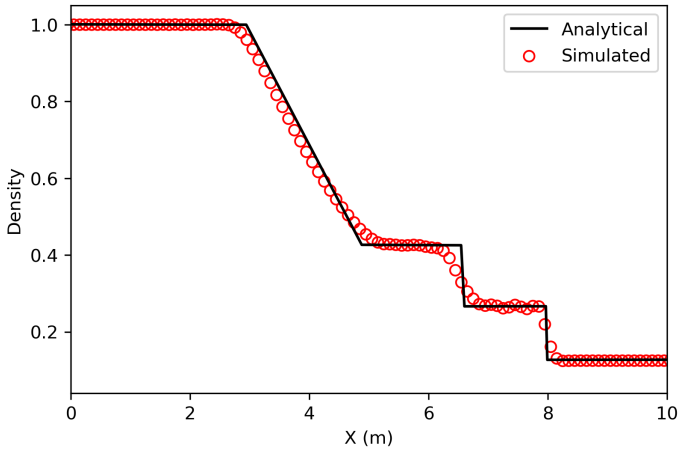

Riemann solver + Second order TVD

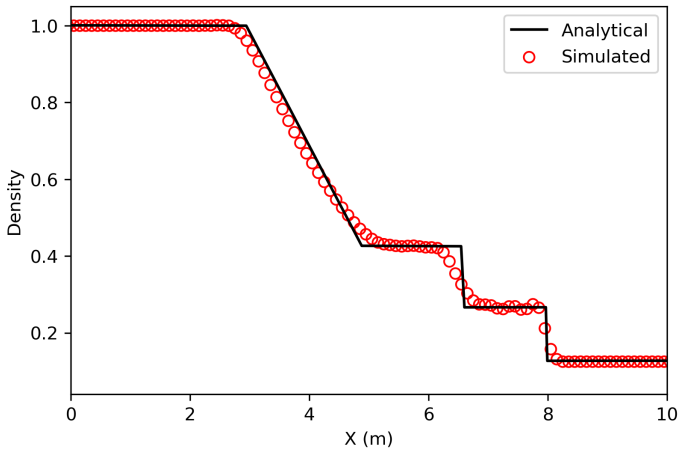

Skew-symmetric with second order shock capturing.

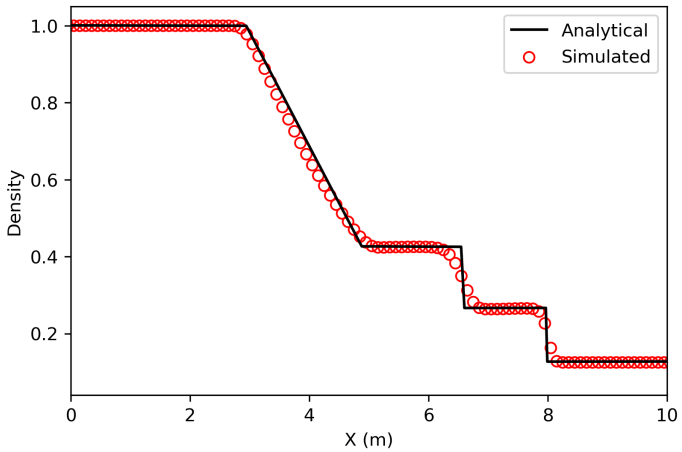

Skew-symmetric with fourth order shock capturing.

Fig. 3.1 Illustration of numerical techniques for dealing with discontinuities using canonical Sod's shock tube configuration.

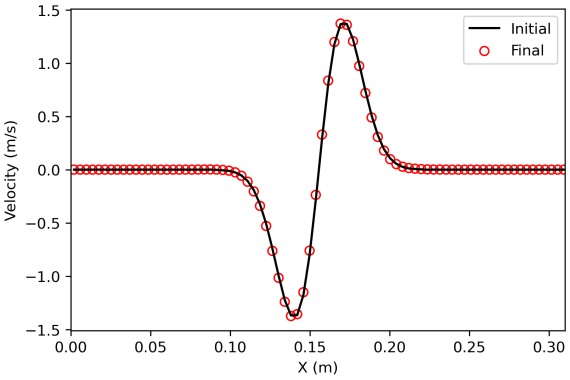

Fourth order DRP

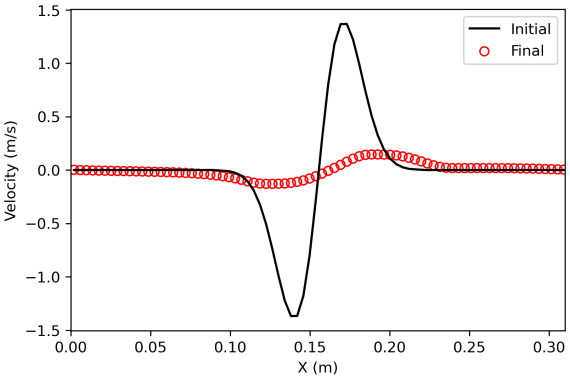

Riemann solver + second order TVD

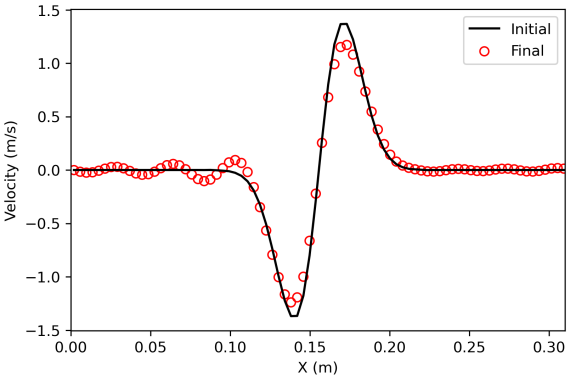

Fourth order skew-symmetric

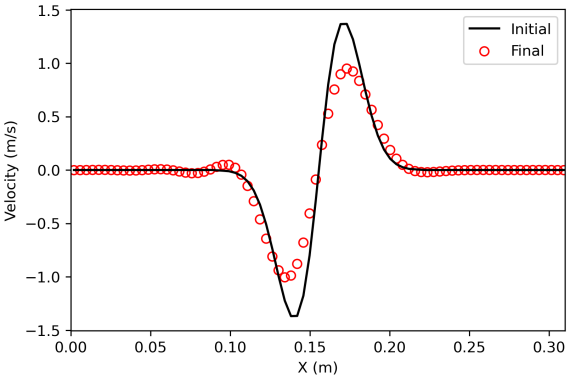

Fourth order skew-symmetric with high frequency damping.

Fig. 3.2 Effects of numerical damping illustrated on vortex convection.

3.3 Chemical Source Term

A detailed discussion of chemical reaction modelling in CFD is nontrivial and well beyond the scope of topics considered here. Therefore the reader is referred to some of the abundant literature (Turns et al., 1996; Warnatz et al., 2006) focused on the topic for further details, while the discussion here is restricted to fundamentals and their implementation in CompReal. This initially relied on an interface with the CHEMKIN (Kee et al., 1989) external package which was later replaced with explicitly written chemical reaction files to increase computational efficiency.

3.3.1 Reaction Kinetics

Combustion can be described as a sum of elementary reactions involving K species :

$$\sum_{k=1}^{K} \nu_{ki}^{f} A_k \Longleftrightarrow \sum_{k=1}^{K} \nu_{ki}^{r} A_k \tag{3.40}$$

where $\nu_{ki}^{f}/\nu_{ki}^{r}$ are the stoichiometric coefficients for the forward and reverse directions respectively and A_k is the corresponding chemical symbol for the k-th species. Since an arbitrary species may take part in more than one reaction, its production rate is found by a summation of the rate-of-progress variable across all relevant reactions :

$$\dot{\omega}_k = \sum_{i=1}^{L} \nu_{ki} q_i \tag{3.41}$$

subject to the following sign convention

$$\nu_{ki} = \nu_{ki}^{f} - \nu_{ki}^{r} \tag{3.42}$$

and the rate-of-progress variable determined by the difference between forward and reverse reaction rates for the i-th reaction as :

$$q_i = k_{fi} \prod_{k=1}^{K} [X_k]^{\nu_{ki}^{f}} - k_{ri} \prod_{k=1}^{K} [X_k]^{\nu_{ki}^{r}} \tag{3.43}$$

where [] is used to indicate concentration and k_{fi}/k_{ri} indicate forward/backward rate constants for a particular reaction. The forward rate constants are determined by the widely used Arrhenius law (Wright, 2005) :

$$k_{fi} = A_i T^{\beta_i} exp\left(\frac{-E_i}{R_c T}\right) \tag{3.44}$$

where the pre-exponential factor (A_i), temperature exponent (β_i) and activation energy (E_i) are specified a priori. Generally the reverse reaction rate is determined following equilibrium arguments

$$k_{ri} = \frac{k_{fi}}{K_{ei}} \tag{3.45}$$

where the equilibrium constant (K_{ei}) is used to relate the forward/reverse reaction rates. The equilibrium constant is readily evaluated from the Gibbs free energy which can be further broken down into variations of thermodynamic properties such as entropy and enthalpy, in conjunction with a pressure term :

$$K_{ei} = exp\left(\frac{\Delta S_i^0}{R} - \frac{\Delta H_i^0}{RT}\right)\left(\frac{P_{atm}}{RT}\right)^{\Sigma_{k=1}^{K}\nu_{ki}} \tag{3.46}$$

With the Δ here representing the change in going from the reactants to the products, for example for a general variable ϕ :

$$\Delta\phi = \sum_{k=1}^{K} \nu_{ki}\phi \tag{3.47}$$

Equation 3.46 is thus used to first find the equilibrium constant before substituting into 3.45 to find the reverse rate constant which then completes the calculations of rate-of-progress variable via Equation 3.43. Although this approach follows directly from thermodynamic arguments there are some notable exceptions in practice, namely not all elementary reactions may be known or incorporated into a reduced scheme. Such schemes have varying levels of accuracy, but often tend to rely heavily on curve fitting to match a desired criteria, such as flame speed. A consequence is often the use of user defined reaction rate orders in Equation 3.43 that better approximate target data than the use of stoichiometric coefficients when only using a limited number of elementary reactions. Another common tactic is the independent description of a reverse rate constant based on data matching/stability rather than purely equilibrium arguments (Equation 3.45) Naturally these adjustments optimised to ensure flame speed may not necessarily maintain microscopic reversibility, which is a limitation of reduced schemes.

3.3.2 Reduced Reaction Schemes

Detailed reaction schemes can easily surpass several hundreds of constituent reactions and species, increasing computational requirements immensely. Moreover rendering their use infeasible for realistic LES applications to combustion systems. A derivative from these

complex descriptions are the large family of reduced schemes which aim to balance the trade-off between cost and accuracy. Their use is commonplace in combustion studies (Griffiths, 1995; Law, 2007; Qian et al., 2017) and consist of a wide range of possible formulations.

The schemes employed during this work are geared towards either hydrogen or methane fuel systems. The former involved a 19 step chemical pathway consisting of 9 species as described in Table 3.1 in order to facilitate detailed resolution of flame structure for fundamental test cases carried out. As configurations involving methane were significantly more complex, the corresponding chemical schemes employed were restricted to either four or two steps as indicated in Tables 3.2 and 3.3 respectively. A common weakness of two step schemes is over-prediction of burning rates, however this is mostly for rich mixtures (Franzelli, 2011; Garby et al., 2013) and not envisioned to be of much detriment for the works considered here.

3.3.3 Time Integration

Inclusion of a chemical source term constitutes a notably stiff system of equations. CompReal depends on explicit time integration to advance the solution however with such strong nonlinearities this would require an impractically small time step to ensure stability. Therefore the reaction subroutines are advanced by an implicit Newton-Raphson method which is then coupled with the overall solver to allow for greater speed and flexibility in global time step. The source term is related to the species temporal derivative as

$$\frac{\partial \mathbf{Y}}{\partial t} = \dot{\omega}(\mathbf{Y}), \quad \mathbf{Y} = [Y_1, Y_2, ..., Y_K]^T \tag{3.48}$$

Searching for an implicit solution leads to the following, where n is the time step index :

$$\mathbf{Y}^{n+1} = \mathbf{Y}^n + \dot{\omega}(\mathbf{Y}^{n+1})\Delta t \tag{3.49}$$

which requires knowledge of species mass fraction at step $n+1$ in order to evaluate $\dot{\omega}_k$. The mass fraction distribution is found by first defining the function $f : \mathbf{Y} \rightarrow \mathbf{Y}$:

$$f(\mathbf{Y}^{n+1}) = \dot{\omega}(\mathbf{Y}^{n+1}) - \left(\frac{\mathbf{Y}^{n+1} - \mathbf{Y}^n}{\Delta t} \right) = 0 \tag{3.50}$$

The Newton-Raphson method looks for the $\mathbf{Y}^{n+1}$ that gives the root of $f(\mathbf{Y}^{n+1})$ by searching through the former state space using Taylor approximations on the latter :

$$f(\mathbf{Y}^{n+1} + \delta\mathbf{Y}^{n+1}) = f(\mathbf{Y}^{n+1}) + \mathbf{J}\delta\mathbf{Y}^{n+1} \tag{3.51}$$

Table 3.1 Comprehensive mechanism for Hydrogen oxidation. Sourced from Yetter et al. (1991). M refers to a third body.

Reaction	Step
$O_2 + H = OH + O$	1
$H_2 + O = OH + H$	2
$H_2 + OH = H_2O + H$	3
$OH + OH = H_2O + O$	4
$H_2 + M = H + H + M$	5
$O + O + M = O_2 + M$	6
$O + H + M = OH + M$	7
$H + OH + M = H_20 + M$	8
$H + O_2 + M = HO_2 + M$	9
$HO_2 + H = H_2 + O_2$	10
$HO_2 + H = OH + OH$	11
$HO_2 + O = OH + O_2$	12
$HO_2 + OH + H_2O + O_2$	13
$HO_2 + HO_2 = H_2O_2 + O_2$	14
$H_2O_2 + M = OH + OH + M$	15
$H_2O_2 + H = H_2O + OH$	16
$H_2O_2 + H = H_2 + HO_2$	17
$H_2O_2 + O = OH + HO_2$	18
$H_2O_2 + OH = H_2O + HO_2$	19

Table 3.2 Jones-Lindstedt mechanism for methane oxidation. Sourced from Jones and Lindstedt (1988)

Reaction	Step
$CH_4 + 0.5O_2 = CO + 2H_2$	1
$CH_4 + H_2O = CO + 3H_2$	2
$H_2 + 0.5O_2 = H_2O$	3
$CO + H_2O = CO_2 + H_2$	4

Table 3.3 BFER mechanism for methane oxidation. Sourced from Franzelli et al. (2010)

Reaction	Step
$CH_4 + 1.5O_2 = CO + 2H_2O$	1
$CO + 0.5O_2 = CO2$	2

where the Jacobian is defined as

$$\mathbf{J} = \frac{\partial f(\mathbf{Y}^{n+1})}{\partial \mathbf{Y}^{n+1}} = \frac{\partial \dot{\omega}(\mathbf{Y}^{n+1})}{\partial \mathbf{Y}^{n+1}} - \frac{1}{\Delta t}\mathbf{I} \tag{3.52}$$

The differential increment is broken down as $\delta\mathbf{Y}^{n+1} = \mathbf{Y}_{j+1}^{n+1} - \mathbf{Y}_{\mathbf{j}}^{\mathbf{n+1}}$, where the j index indicates the Newton-Raphson step. Now setting Equation 3.51 to zero and inverting the Jacobian using linear algebra algorithms, the next step value can be obtained:

$$\mathbf{Y}_{j+1}^{n+1} = \mathbf{Y}_{j}^{n+1} - \mathbf{J}_{j}^{-1} f(\mathbf{Y}_{j}^{n+1}) \tag{3.53}$$

Once $\mathbf{Y}^{n+1}$ is found this way, it can be used to advance the reactive source term to step $n+1$ using Equation 3.49. This process can be iterated over more than one smaller, local time step to match a larger global time step used in the explicit time advancement. An exception to this algorithm was implemented for some specific cases where the global time step was already so small that the reactive source term could be temporally advanced explicitly. This was in cases with very fine (DNS) meshes that required a very small time step in order to maintain the suitable CFL number. This bypasses the partially implicit time integration component and costly iterative Jacobian inversion, resulting in significant computational speedup. Finally the global time marching is done by a standard fourth order Runge-Kutta explicit integration.

3.4 Mesh Generation

There is a large scale disparity between a flame front and acoustic waves, thus it is desirable to adapt grid resolution in the domain accordingly. A method to achieve this is the concept of grid stretching which relies on a transformation between the original Cartesian mesh and its stretched counterpart. Although straightforward the method is essentially static and does not update during run time. Significant effort was dedicated towards AMR functionality in CompReal to allow for real time optimisation of the mesh and both methods are reviewed next. Note that solid geometries were read into the domain using Immersed Boundary Methods. However due to its limited relevance for the majority of cases shown later the interested reader is referred to suitable literature for background material (Mittal and Iaccarino, 2005; Peskin, 2002).

3.4.1 Grid Stretching

Grid stretching relies on the transformation between a computational (x) and physical domain(ξ). Analytical relations between the two frames of reference can usually be expressed with some manipulation of a hyperbolic tangent function or alternatively a polynomial dependency. The computational grid is uniformly spaced and subject to the finite differencing during discretisation. Derivatives in the physical space are then obtained a posteriori by multiplying with the transformation metric ($\partial x/\partial \xi$) as shown in Equation 3.54.

$$\frac{\partial f}{\partial \xi} = \frac{\partial f}{\partial x}\frac{dx}{\partial \xi} \tag{3.54}$$

A simple example is the case of clustering points near certain regions of interest (such as walls at both boundaries) for improved local resolution where the analytical relation is given by

$$\xi = \frac{1}{2\Gamma}\frac{tanh\beta}{\Gamma} tan\beta\Gamma \tag{3.55}$$

where $\Gamma = \tanh\beta/2$ and β is the clustering parameter with a higher value resulting in more pronounced grouping of points near the zone of interest. From this the derivative is readily found and the required metric evaluated as

$$\frac{\partial x}{\partial \xi} = 2\frac{\Gamma}{\beta}\cosh^2\beta x \tag{3.56}$$

This is equivalent to computationally solving on the regular,computational grid of Figure 3.3 but obtaining solutions for a corresponding physical grid which has reallocated the points for a more dense clustering close to boundaries.

The transformation is a uni-directional, 1D mapping between $x \rightarrow \xi$ (or $y \rightarrow \eta$), therefore there is no Jacobian required to map $(x,y) \rightarrow (\xi,\eta)$. However note the resultant higher cell aspect ratios in Figure 3.3 due to no corresponding stretching in the vertical direction. The latter coupled with drastic changes in neighbouring cell size for cases of steep stretching can lead to numerical errors (Diskin and Thomas, 2008; Katz and Sankaran, 2012). Therefore grids used here employ hybrid stretching functions to conform to uniform spacing in regions of interest and a very gradual exponential increase in spacing towards the far field.

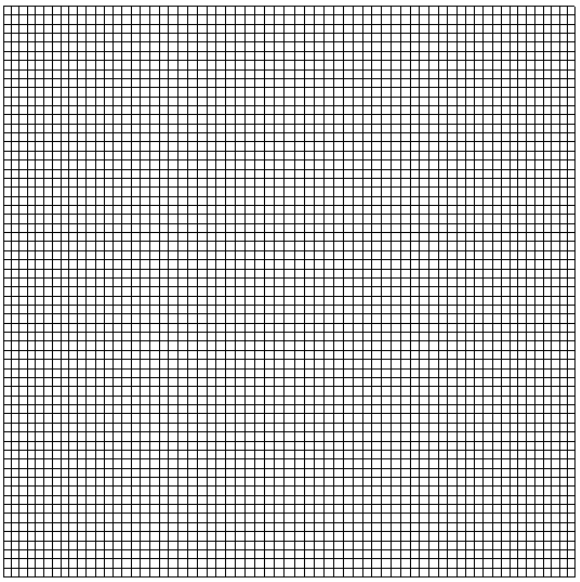

Computational Grid (x, y)

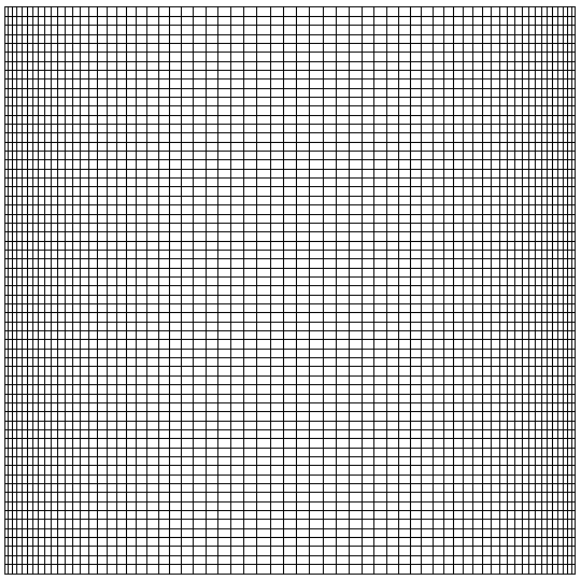

Physical Grid (ξ, y)

Fig. 3.3 Illustration of the effects of stretching metrics applied in the axial direction.

3.4.2 Adaptive Mesh Refinement

Structured Adaptive Mesh Refinement (SAMR) methods organise grids into hierarchical data structures with specialised connectivity functions between levels. These algorithms are intrinsically more complex than simple grid stretching but offer the advantage of adaptability in real simulation time. A notable portion of literature has been dedicated to optimising the various facets of AMR frameworks and its continued innovation (Cant et al., 2022; Pal et al., 2021; Potgieter et al., 2021; Sezen and Atlar, 2022) ever since they first appeared in literature (Berger and Oliger, 1984) close to 40 years ago. The goal here is not to contribute to the development of these algorithms but rather their effective implementation into CompReal and subsequent coupling with relevant turbulence or combustion models. Therefore discussion is limited to a high level overview with more detailed references provided.

AMR methods are broadly classified into either patch or tree based and both aim to facilitate an automated solution-based update of the grid structure based on physics based refinement criteria. For tree based approaches in regions requiring refinement a 'parent' block is divided into a fixed number of 'children'. Children and parents tend to have the same number of cells and the former can be recombined to return the latter when needed. Connectivity between blocks is retained by explicitly storing parent-child lineages into quadtree/octree structures. Examples of tree based AMR implementations include the works of Badia et al. (2020); Holke (2018); Popinet (2003).

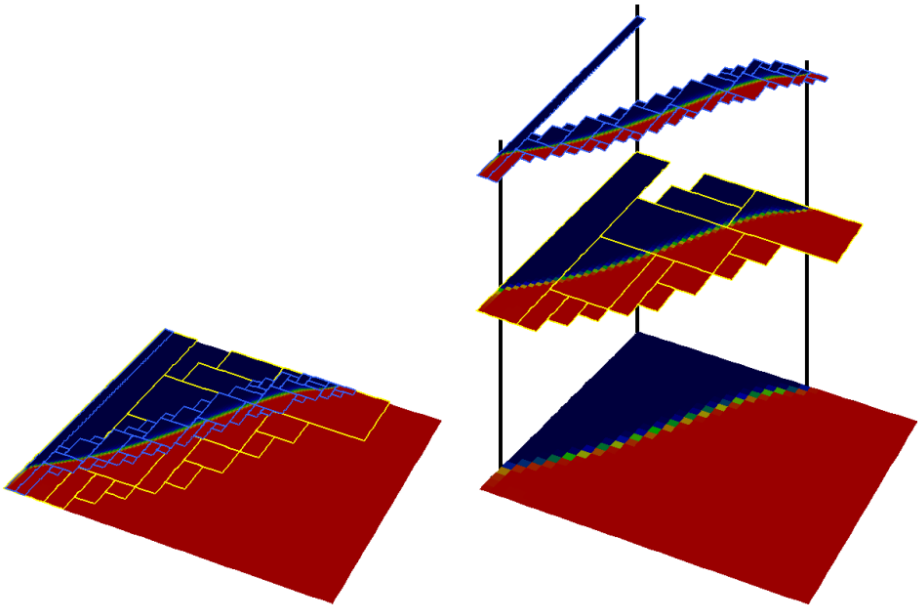

Fig. 3.4 Patch structure: sample grid with two levels of refinement. Base grid covers the entire domain and higher levels are properly nested. Source Bell et al. (2012).

Alternatively patch based methods organise the data into a series of sub-grids called patches containing cells of the same size. There is no explicit parent-child relation and at each level of refinement the domain consists of a series of patches whose locations are determined by the refinement criteria. Therefore the structural hierarchy is described by a union of all patches at each level and this is the method class incorporated into CompReal. This was done using Boxlib (Rendleman et al., 2000), an open source patch/block based library that provides generalised AMR functionality, been used for a large range of applications (Chan et al., 2016; Jost et al., 2016; Weber et al., 2012) and demonstrated good scalability (Dubey et al., 2014).

Figure 3.4 illustrates a simple representation of refinement about an interface where within the hierarchy it is important to ensure levels are properly nested. Meaning that the coarsest level covers the entire domain but each successively finer level only conforms to a portion of the interior of the previous level. Therefore the mesh at each level is a series of discontinuous gridded regions, termed patches, each of which are skirted by a collection of halo/ghost cells. "Ghost cells" are a region around the grid on which the solution operator does not act but is needed to evaluate the operator itself and so are used to ensure connectivity. This is done via interpolation methods (Hornung et al., 2006) applied recursively across levels which can be a significant numerical challenge.

There is a need to exchange communication between irregularly spaced patches at the same level but also between levels. The fundamental paraellilsation manifestation for Boxlib is the "multi-fab" defined as the collection of all "fabs" at a particular level with each fab being a collection of data points on a single patch. During an operating on a multifab each of the constituent fabs are distributed among the nodes and multifabs at different levels are also assigned independently. Each node has access to a set of meta-data required to dynamically rebuild system connectivity in order to maximally isolate direct inter-processor communication. Furthermore as the simulations evolves the entire mesh structure must be reevaluated and redistributed across nodes, effienct implementation of which is paramount to arguing for the scalability of any AMR based framework.

The appropriate choice of refinement criteria is one of the keys in determining overall optimatility of the system. Each level scales by a factor of two in CompReal, which can quicly accrue into a large computational burden for too vague a refinement target. The criteria to tag a certain cell for refinement can be evaluated based on Richardson's error approximation or even combined with adjoint optimisation methods (Müller and Giles, 2001; Rendleman et al., 2000). Despite several proposals for self-adapting refinement such as (Haldenwang and Pignol, 2002), a survey of combustion literature (Drennan et al., 2017; Echekki and Chen, 1996; Sitaraman et al., 2021; Yuan and Tang, 2007) quickly reveals a

heavy dependence on user specified heuristic criteria. Common choices include thresholds based on gradients of temperature or density, vorticity and progress variable. The latter was used here in conjunction with enough relaxation to ensure the flame front is always resolved on the finest level.

Employing AMR in combustion applications introduces two characteristic resolution levels, namely one for the flow and a second finer one for the flame. Most combustion models do not account for a difference in mesh resolution despite having an intrinsic dependency on its local value. By having different grid sizes both the local scale of resolved structures and the subsequent cascade will be influenced and can have an important impact on subgrid modelling terms. Recently Mehl et al. (2018) studied implications of this for the conventional ATF model which has a dependency on an approximation for filter width and showed it significantly under-performed when coupled with AMR.

Mehl et al. (2021) propose a solution based on the assumption that the scales not resolvable on the coarse mesh are somewhat recoverable on the finer flame mesh if the cascade is given enough time to redevelop. This assumption has a very strong dependency on the relative magnitude of turbulent and flame time scales. If the former is much smaller than the latter it can be approximated that the cascade is fully established within a time frame that was too short for the flame to move enough for the mesh to regrid. For this limiting case out of the three shown in Figure 3.5, Mehl et al. (2021) suggest a blended functional approximation for the effective local filter width to be used for SGS terms in the coupled ATF model. This solution although elegant and effective clearly increases computational complexity and is also an upper bound that does not account for situations where there is only a partial cascade. Simpler alternatives are explored in Chapter 5 for the ATF-AMR coupling incorporated into CompReal in a LES context.

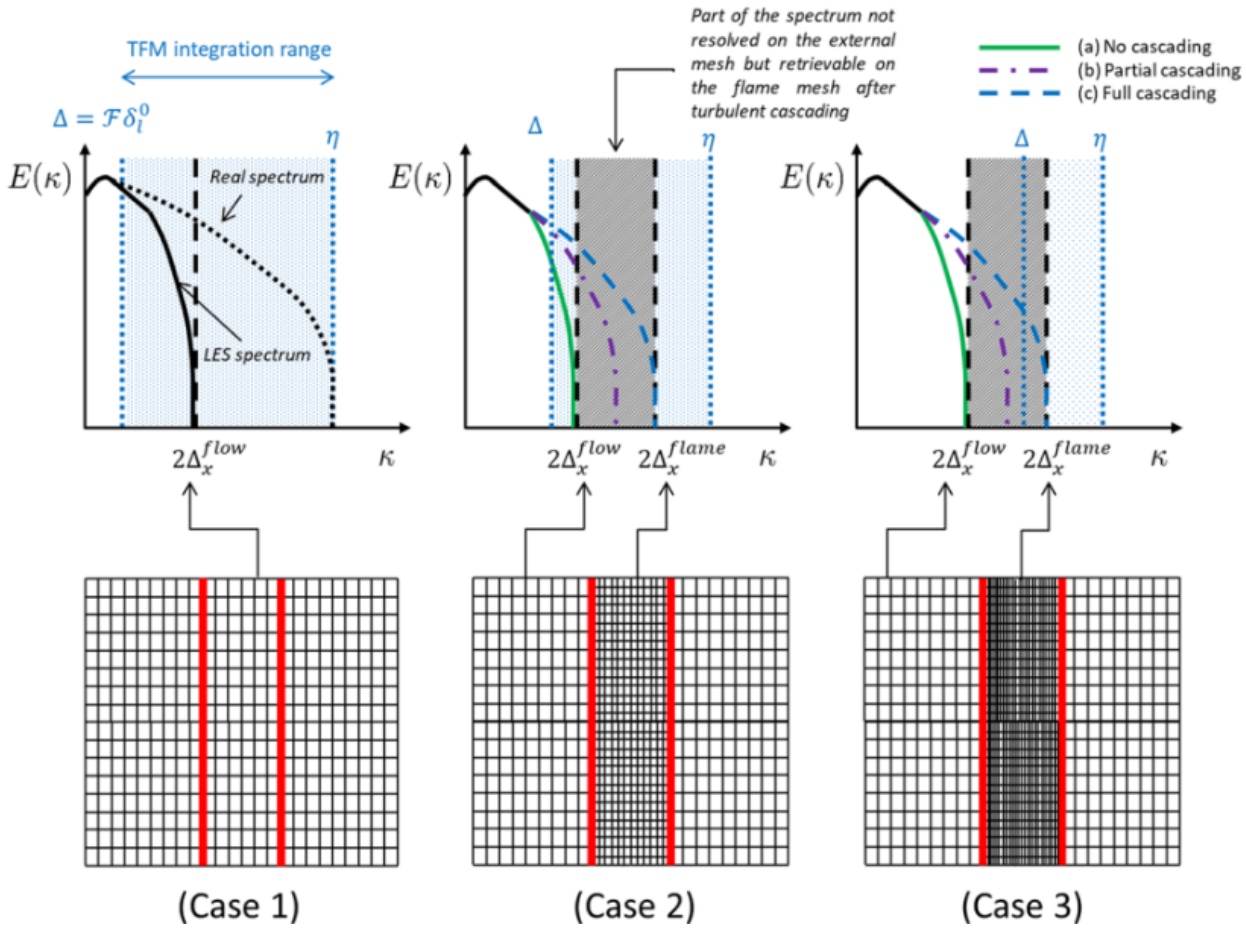

Fig. 3.5 Impact of AMR on the relevant integration range for ATF with no level interface (Case 1) and a level interface but larger filter width (case 2) or intermediate filter width (Case 3) . Source Mehl et al. (2018).

3.5 Summary

The discretisation scheme employed by CompReal has evolved over the course of this work through three different iterations. Riemann solvers exhibit unparalleled stability due to their built-in acceptance of discontinuous solutions however are limited in accuracy and susceptible to excessive damping. DRP schemes are optimised specifically to preserve wave behaviour and as such display the least numerical dispersion and dissipation. However on their own, like most centred schemes, they are unable to maintain stability in regions with sharp gradients. A hybrid Riemann-DRP scheme was used to try and best leverage the strengths of these two formulations by limiting the lower order Riemann solver to discontinuous regions only. This solution exhibited good stability and high accuracy but the larger DRP stencils come with increased computational cost, especially in AMR.

Finally, a skew-symmetric approach was employed due to its inherent resistance to aliasing errors coupled with significant speed. This required inclusion of artificial flux terms to limit high frequency oscillations and also accommodate shock capturing by numerically thickening discontinuities. The latter provided a considerable increase in stability but can adversely affect the flow solution and as such is recommended to be minimised as much as possible.

Chemical pathways for reactive systems are modelled with reduced schemes in order to keep the simulation tractable. Several were tested and evaluated in terms of cost and preserving flame speed for the particular configurations of relevance to this study, with the final selections outlined. In addition to having limited ranges of validity these schemes introduce significant stiffness into the system and as such were locally coupled with an additional implicit temporal integrator while the global time advancement is explicit in nature.

Custom grid stretching metrics were created prior to run time in order to best allocate grid points. The general paradigm was to always ensure a uniform mesh in the neighbourhood of a flame front with a gradual and progressive coarsening towards boundaries. Adaptive mesh refinement functionality was incorporated into the code and evaluated in the context of a unified AMR-LES-ATF framework. The matter of incorporating AMR into LES simulations is not trivial as introducing two (or more) levels of resolution has important implications for the local turbulent cascade.

State of the art conventional ATF methods have been shown to perform poorly in conjunction with AMR, with solutions proposed only very recently. In principle the modified ATF model proposed here is uniquely placed to best take advantage of AMR due to only an implicit dependence on local filter width. As the latter is not an explicit combustion model parameter, the effects of perturbed local energy cascades are secondary in nature.

Chapter 4

Navier-Stokes Characteristic Boundary Conditions

The treatment of boundaries is a recurring challenge faced in compressible flow simulations. Boundary conditions inherently attempt to anticipate the flow behaviour at the very limit of the computational domain, thus must infer information about how features just inside relate to those just outside. This depends on knowledge of flow behaviour just beyond the region where the governing transport equations are being solved, which requires approximation of outside flow features. Disparity between the two states on either side of a boundary can lead to numerical noise generation which propagates upstream (Giles, 1990; Givoli, 1991). As high order and particularly DRP optimised schemes do not damp these spurious waves (Kim and Lee, 1997; Tam and Webb, 1993) they can be very detrimental to the overall flow solution and must be mitigated. Several approaches have been proposed to tackle this issue and the interested reader to referred to several review papers detailing recent and continued research in the field (Du, 2019; Odier et al., 2019; Shehadi and van der Weide, 2021; Sierra et al., 2019).

This chapter focuses on the description and evaluation of a particular class of methods stemming from characteristic wave analysis that was implemented into CompReal. Initially developed for a system of Euler equations (Thompson, 1987, 1990), these approaches decompose the solution at a boundary into corresponding incoming and outgoing waves. Knowledge from inside the domain can be used to determine outgoing waves while waves coming in can be specified from physics based expectations on the nature of the boundary. In theory this should allow a direct control over reflection characteristics since the incoming waves can be fixed accordingly.

Poinsot and Lele (1992) expanded on this approach to account for viscous term resulting in the Navier-Stokes Characteristic Boundary Conditions (NSCBCs), which have since been

improved by many authors. This includes extension to multi-component flow simulations (Baum et al., 1995), different equations of state (Okong'o and Bellan, 2002), inclusion of reactive source terms (Sutherland and Kennedy, 2003) and coupling with a plane masking approach for normal-incident waves (Polifke et al., 2006). Prosser (2005) also suggest a method to decouple acoustic and convective scales in order to apply the boundary condition on acoustic scales directly.

The above methods mostly relied on a locally one dimensional flow with normal incidence on the boundary and an associated uni-dimensional characteristic decomposition. Although sufficient for simple flows the role of in-plane, so called *transverse* terms, was shown to be significant for a range of flows of interest and NSCBCs were subsequently extended to include their effects in two (Yoo et al., 2005) and three dimensions(Lodato et al., 2008). This however gave rise to a problem about how best to treat the flow at a corner with Lodato et al. (2008) presenting a methodical and unified framework.

4.1 Mathematical Background

A brief overview of the method is provided to orient the reader with general principles of characteristic boundary conditions. Implementation founds in literature can differ drastically in terms of treatment of source terms, corners, relaxation techniques or indeed even choice of variables used. The subsequent description follows very closely the approach put forward in Coussement et al. (2012), which employs temperature as a primitive variable instead of pressure. This greatly simplifies the characteristic equations in terms of complexity but in principle both systems should be equally valid, although a poignant difference for reactive flow simulations will be shown shortly.

4.1.1 Characteristic Equations

Prior to characteristic decomposition it is is convenient to convert the governing equations into primitive instead of governing form, details of which and relevant matrices are provided in Appendix A. As viscous and reactive conditions are added *a posteriori* the transport equations in primitive form thus read:

$$\frac{\partial W^p}{\partial t} + \mathbf{A}_i \frac{\partial W^p}{\partial x_i} = 0 \tag{4.1}$$

These are next recast at the boundary into a form consisting of characteristic waves, by applying Eigen-decomposition to matrix $\mathbf{A}_i$ and rewriting it in terms of corresponding

eigenvalues and eigenvectors. For a boundary normal to the x_1 coordinate axis the system of equations now becomes

$$\frac{\partial W^p}{\partial t} + \boldsymbol{S}\boldsymbol{\Lambda}\boldsymbol{S}^{-1}\frac{\partial W^p}{\partial x_1} + \mathbf{A}_2\frac{\partial W^p}{\partial x_2} + \mathbf{A}_3\frac{\partial W^p}{\partial x_3} = 0 \tag{4.2}$$

Premultiplying by the right eigenvector and grouping together in plane components into a collection of transverse terms $\mathcal{T}$:

$$\boldsymbol{S}^{-1}\frac{\partial W^p}{\partial t} + \boldsymbol{\Lambda}\boldsymbol{S}^{-1}\frac{\partial W^p}{\partial x_1} + \boldsymbol{S}^{-1}\mathcal{T} = 0 \tag{4.3}$$

A characteristic variable now be defined as W^c, along with $\mathcal{L} = \Lambda S^{-1}\partial W^p \partial x_1$ and $\mathbb{T} = S^{-1}\mathcal{T}$ to give

$$\frac{\partial W^c}{\partial t} + \boldsymbol{\mathcal{L}} + \mathbb{T} = 0 \tag{4.4}$$

where

$$\boldsymbol{\mathcal{L}} = \begin{pmatrix} \lambda_1(\frac{1}{2\gamma}\frac{\partial \rho}{\partial x_1} - \frac{\rho}{2c}\frac{\partial u_1}{x_1} + \frac{\rho}{2T\gamma}\frac{\partial T}{\partial x_1} + \sum_{k=1}^{N}\frac{\rho\overline{W}}{2W_k\gamma}\frac{\partial Y_k}{\partial x_1}) \\ \lambda_2(-\frac{RT}{\overline{W}\rho c_p}\frac{\partial \rho}{\partial x_1} + \frac{1}{\gamma}\frac{\partial T}{\partial x_1} - \sum_{k=1}^{N}\frac{RT}{W_k c_p}\frac{\partial Y_k}{\partial x_1} \\ \lambda_3(u_1\frac{\partial u_2}{\partial x_1}) \\ \lambda_4(u_1\frac{\partial u_3}{\partial x_1} \\ \lambda_5(\frac{1}{2\gamma}\frac{\partial \rho}{\partial x_1} + \frac{\rho}{2c}\frac{\partial u_1}{x_1} + \frac{\rho}{2T\gamma}\frac{\partial T}{\partial x_1} + \sum_{k=1}^{N}\frac{\rho\overline{W}}{2W_k\gamma}\frac{\partial Y_k}{\partial x_1}) \\ u_1\frac{\partial Y_1}{\partial x_1} \\ \vdots \\ u_1\frac{\partial Y_n}{\partial x_1} \end{pmatrix} \quad \lambda_i = \boldsymbol{\Lambda}^1 = \begin{pmatrix} u_1 - c \\ u_1 \\ u_1 \\ u_1 \\ u_1 + c \\ u_1 \\ \vdots \\ u_1 \end{pmatrix} \tag{4.5}$$

Equation 4.4 is readily identified as the wave equation when rewritten (in one dimension for now) as

$$\frac{\partial W^c}{\partial t} + \mathcal{L}_{=}0 \quad \text{or} \quad \frac{\partial W_i^c}{\partial t} + \lambda_i\frac{\partial W_i^c}{\partial x} = 0 \tag{4.6}$$

Moreover this shows that the characteristic variables, W^c, are in essence wave amplitudes and constant along characteristic lines in the x-t plane as defined by $dx/dt = \lambda_i$. λ_i is the

collection of speeds at which each corresponding characteristic wave travels in a direction normal to the x_1-coordinate aligned boundary. While the parameters $\mathcal{L}_i$ are the corresponding rate of change in time of characteristic amplitudes.

This formulation is convenient as it allows a simple segregation of incoming and outgoing waves dependant on their characteristic speeds, λ_i. Furthermore waves of interest can be directly modulated by controlling $\mathcal{L}$. Outgoing waves can have all their parameters evaluated from information inside the domain but incoming waves are obviously dependant on derivatives outside of the simulation domain which are not known and thus require approximation. This is usually done by choosing a desired physical boundary condition and setting the wave amplitudes accordingly. The common options discussed next are non-reflecting outflows and inflows.

4.1.2 Non-reflective Outflow

Consider a subsonic outflow located at the downstream axial boundary, $x_{max}(u_1 > 0)$. From Equation 4.5 it is clear that there is only one wave entering the domain and that is $\mathcal{L}_1$ at a speed of $u_1 - c$ where c refers to the local sonic velocity. A simple solution is to simply set this wave amplitude to zero (i.e. $\mathcal{L}_1 = 0$) to achieve a perfectly non-reflecting outflow. However by completely severing system-boundary feedback like this, simulations have been shown to exhibit a drift in mean pressure (Poinsot and Lele, 1992). Therefore its is more practical to allow for a partially reflecting boundary that traces a target far field pressure P_t :

$$\mathcal{L}_1 = \sigma \frac{1 - \mathbb{M}^2}{2cL_x}(P - P_t) \tag{4.7}$$

where σ is a relaxation coefficient with Lodato et al. (2008) suggesting an optimal value of 0.28 based on the simplified linear stability analysis of Rudy and Strikwerda (1980), $\mathcal{M}$ is the maximum Mach number in the boundary and L_x is a characteristic axial length usually taken to be the domain size. The original locally one dimensional treatments stop here however inclusion of transverse corrections leads to

$$\mathcal{L}_1 = \sigma \frac{1 - \mathbb{M}^2}{2cL_x}(P - P_t) - \mathbb{T}(1) + \beta(\mathbb{T}(1) - \mathbb{T}(1)_t) \tag{4.8}$$

β is a relaxation coefficient for the transverse terms with differing views on its optimal value. While some authors prefer to fix it in accordance with a farfield Mach number (Lodato et al., 2008) others suggest having it adapt dynamically to the local Mach number (Yoo and Im, 2007). Furthermore it is difficult to determine a target for the transverse terms to relax towards so $\mathbb{T}_t$ is usually set to zero for most free shear flows. A similar procedure would be

applied if the outflow was located at $x_1 = 0 (u_1 < 0)$ with the exception of the incoming wave being $\mathcal{L}_5$ instead of $\mathcal{L}_1$ at a velocity of $u_1 + c$.

4.1.3 Non-reflective Inflow

Consider an inflow located at x_{min} $(u_1 > 0)$, with the exception of $\mathcal{L}_1$ which travels upstream with a velocity of $u_1 - c$, all other waves are entering the domain. Soft boundary conditions that relax to target temperature (T_t), velocities (u_{1t}, u_{2t}, u_{3t}) and species mass fractions (Y_{kt}) are specified with a set of corresponding relaxation parameters (η) as

$$\begin{aligned}
\mathcal{L}_2 &= \eta_2 (T - T_t) - \mathbb{T}(2) \\
\mathcal{L}_3 &= \eta_3 (u_2 - u_{2t}) - \mathbb{T}(3) \\
\mathcal{L}_4 &= \eta_4 (u_3 - u_{3t}) - \mathbb{T}(4) \\
\mathcal{L}_5 &= \eta_5 (u_1 - u_{1t}) - \mathbb{T}(5) \\
\mathcal{L}_{5+k} &= \eta_{5+k} (Y_k - Y_{kt}) - \mathbb{T}(5+k)
\end{aligned} \tag{4.9}$$

There is no consensus in the literature on a unique value for η. While larger values provide better control over the inlet state they also drive the formulation closer to the classical hard/reflecting inlet. Smaller values result in better wave transmission however come at the cost of poorer control and greater transient fluctuations. Since the majority of characteristic waves are specified and there are less degrees of remaining freedom, Sutherland and Kennedy (2003) suggest there is no need for a relaxation parameter on the transverse terms.

4.1.4 Rebuilding Governing Equations

In summary, outgoing waves are calculated from knowledge of the solution inside the domain, and physical boundary conditions are applied to any incoming waves based on an intuitive understanding of expected farfield behaviour. However this is all done at the characteristic level and in order to be compatible with the global time integration schemes of a conventional flow solver there is a need to recast the boundary conditions back into either primitive or conservative form.

This is done by simply doing the opposite of when going from primitive to characteristic and pre-multiplying by S_1 instead of its inverse to give Equations 4.10-4.15. This can then be further regressed back to conservative form by pre-multiplying with the appropriate Jacobian specified in Appendix A. Furthermore if source terms are being retained then they are added here a posteriori to the species transport equations.

Viscous conditions are also applied ad-hoc in line with the required number of equations required to maintain the mathematical problem as well posed (Lodato et al., 2008; Poinsot and Lele, 1992). However these effectively amount to setting certain diffusion coefficients as locally zero depending on the configuration which are omitted here and shown to have had little impact.

$$\frac{\partial \rho}{\partial t} = -\mathcal{L}_1 + \frac{\rho}{T}\mathcal{L}_2 - \mathcal{L}_5 + \sum_{k=1}^{N} \frac{\rho \overline{W}}{W_k}\mathcal{L}_{5+k} - \mathcal{T}_1 \tag{4.10}$$

$$\frac{\partial u_1}{\partial t} = -\frac{c}{\rho}(\mathcal{L}_5 - \mathcal{L}_1) - \mathcal{T}_2 \tag{4.11}$$

$$\frac{\partial u_2}{\partial t} = -\mathcal{L}_3 - \mathcal{T}_3 \tag{4.12}$$

$$\frac{\partial u_3}{\partial t} = -\mathcal{L}_4 - \mathcal{T}_4 \tag{4.13}$$

$$\frac{\partial T}{\partial t} = -\frac{RT}{\rho \overline{W} c_v}(\mathcal{L}_1 + \mathcal{L}_5) - \mathcal{L}_2 - \mathcal{T}_5 \tag{4.14}$$

$$\frac{\partial Y_k}{\partial t} = -\mathcal{L}_{5+k} - \mathcal{T}_{5+k} \tag{4.15}$$

At corners, characteristic waves from all three directions can enter or leave the domain. Therefore instead of grouping the in-plane derivatives as transverse terms, all three flux matrices in Equation 4.2 are diagonalised to give :

$$\frac{\partial \boldsymbol{U}^p}{\partial t} + \boldsymbol{S_1 \Lambda S_1^{-1}} \frac{\partial \boldsymbol{U}^p}{\partial x_1} + \boldsymbol{S_2 M S_2^{-1}} \frac{\partial \boldsymbol{U}^p}{\partial x_2} + \boldsymbol{S_3 N S_3^{-1}} \frac{\partial \boldsymbol{U}^p}{\partial x_3} = 0 \tag{4.16}$$

where addition to $\mathcal{L}$, wave amplitude time variations in the other two directions are defined as

$$\boldsymbol{\mathcal{M}} = \boldsymbol{M S_2^{-1}} \frac{\partial \boldsymbol{U}^p}{\partial x_2} \quad , \quad \boldsymbol{\mathcal{N}} = \boldsymbol{N S_3^{-1}} \frac{\partial \boldsymbol{U}^p}{\partial x_3} \tag{4.17}$$

Following the same algorithm as before, characteristic boundary conditions are applied to incoming waves and the corresponding primitive system rebuilt to give Equations 4.18- 4.23. However the system of equations now becomes coupled as in order to apply a condition to $\mathcal{L}$ knowledge of the corresponding transverse terms is required but these depend on knowledge of $\mathcal{M}$ and $\mathcal{N}$. This requires special considerations to ensure system connectivity between multi-dimensional effects and is discussed next.

$$\frac{\partial \rho}{\partial t} = -(\mathcal{L}_1+\mathcal{L}_5)-(\mathcal{M}_1+\mathcal{M}_5)-(\mathcal{N}_1+\mathcal{N}_5)+\frac{\rho}{T}(\mathcal{L}_2+\mathcal{M}_3+\mathcal{N}_4)+ \sum_{k=1}^{N}\frac{\rho\overline{W}}{W_k}(\mathcal{L}_{5+k}+\mathcal{M}_{5+k}+\mathcal{N}_{5+k}) \tag{4.18}$$

$$\frac{\partial u_1}{\partial t} = -\frac{c}{\rho}(\mathcal{L}_5-\mathcal{L}_1)-\mathcal{M}_2-\mathcal{N}_2 \tag{4.19}$$

$$\frac{\partial u_2}{\partial t} = -\mathcal{L}_3-\frac{c}{\rho}(\mathcal{M}_5-\mathcal{M}_1)-\mathcal{N}_3 \tag{4.20}$$

$$\frac{\partial u_3}{\partial t} = -\mathcal{L}_4-\mathcal{M}_4-\frac{c}{\rho}(\mathcal{N}_5-\mathcal{N}_1) \tag{4.21}$$

$$\frac{\partial T}{\partial t} = -\frac{RT}{\rho\overline{W}c_v}(\mathcal{L}_1+\mathcal{L}_5+\mathcal{M}_1+\mathcal{M}_5+\mathcal{N}_1+\mathcal{N}_5)-\mathcal{L}_2-\mathcal{M}_3-\mathcal{N}_4 \tag{4.22}$$

$$\frac{\partial Y_k}{\partial t} = -\mathcal{L}_{5+k}-\mathcal{M}_{5+k}-\mathcal{N}_{5+k} \quad ,k=1,\ldots,N \tag{4.23}$$

4.1.5 Corner Treatments

Two common cases of particular relevance are discussed here with the interested reader referred to Coussement et al. (2012); Lodato et al. (2008) for more general formulations. The meeting of three outflows at a corner equates to one incoming wave in each direction and applying a partially non-reflective boundary condition to each results in a coupled system of equations. For a corner located at $x_{max}, y_{max}, z_{max}(u_1 > 0, u_2 > 0, u_3 > 0)$ this system reads as

$$\mathcal{L}_1 = \sigma\frac{1-\mathbb{M}^2}{2cL_{x1}}(P-P_t)-(\beta-1)\mathbb{T}^x(1) \tag{4.24}$$

$$\mathcal{M}_1 = \sigma\frac{1-\mathbb{M}^2}{2cL_{x1}}(P-P_t)-(\beta-1)\mathbb{T}^y(1) \tag{4.25}$$

$$\mathcal{N}_1 = \sigma\frac{1-\mathbb{M}^2}{2cL_{x1}}(P-P_t)-(\beta-1)\mathbb{T}^z(1) \tag{4.26}$$

$$\tag{4.27}$$

where the transverse terms are all computed in terms of wave amplitudes with

$$\mathbb{T}^x(1) = \frac{1}{2}(\mathcal{M}_1 + \mathcal{M}_5 + \mathcal{N}_1 + \mathcal{N}_5) - \frac{\rho}{2c}(\mathcal{M}_2 + \mathcal{N}_2) \tag{4.28}$$

$$\mathbb{T}^y(1) = \frac{1}{2}(\mathcal{L}_1 + \mathcal{L}_5 + \mathcal{N}_1 + \mathcal{N}_5) - \frac{\rho}{2c}(\mathcal{L}_2 + \mathcal{N}_2) \tag{4.29}$$

$$\mathbb{T}^z(1) = \frac{1}{2}(\mathcal{L}_1 + \mathcal{L}_5 + \mathcal{M}_1 + \mathcal{M}_5) - \frac{\rho}{2c}(\mathcal{L}_2 + \mathcal{M}_2) \tag{4.30}$$

Using a different target pressure or transverse relaxation coefficient for the various directions has been found to be detrimental and is not recommended (Coussement et al., 2012). While Lodato et al. (2008) suggest solving these equations as a coupled linear system, Coussement et al. (2012) noted a negligible impact in stability when prescribing them independently, at least for weak mean flow configurations.

Alternatively for a corner located at $x_{min}, y_{min}, z_{min}$, with an inflow in the x direction ($u_1 > 0$) but outflows on the remaining two faces ($u_2 < 0, u_3 < 0$). With the exception of $\mathcal{L}_1$, all the remaining characteristic waves normal to x are entering the domain and require physical boundary conditions. In addition to this $\mathcal{M}_5$ and $\mathcal{N}_5$ are also entering the domain.

Once again the transverse terms for $\mathcal{L}$ are a function of characteristic waves in the other directions. Giving rise to to the following system of equations:

$$\mathcal{L}_2 = \eta_2(T - T_t) - \mathcal{M}_3 - \mathcal{N}_4 \tag{4.31}$$

$$\mathcal{L}_3 = \eta_3(u_2 - u_{2t}) - \frac{c}{\rho}(\mathcal{M}_5 - \mathcal{M}_1) - \mathcal{N}_3 \tag{4.32}$$

$$\mathcal{L}_4 = \eta_4(u_3 - u_{3t}) - \mathcal{M}_4 - \frac{c}{\rho}(\mathcal{N}_5 - \mathcal{N}_1) \tag{4.33}$$

$$\mathcal{L}_5 = \eta_5(u_1 - u_{1t}) - \frac{1}{2}(\mathcal{M}_1 + \mathcal{M}_5 + \mathcal{N}_1 + \mathcal{N}_5) - \frac{\rho}{2c}(\mathcal{M}_2 + \mathcal{N}_2) \tag{4.34}$$

$$\mathcal{L}_{5+k} = \eta_{5+k}(Y_k - Y_{kt}) - \mathcal{M}_{5+k} - \mathcal{N}_{5+k} \tag{4.35}$$

With regards to the incoming waves normal to y and z, applying a partially non-reflective boundary condition that traces a target pressure is equivalent to specifying pressure, temperature and velocity at a point which leads to an over-determined system. Therefore to allow enough freedom for the system to relax towards a physical state a purely non-reflective condition such as Equation 4.36 is applied to allow the pressure to locally adapt to the neighbouring flow field as recommended by Lodato et al. (2008).

$$\mathcal{M}_5 = 0 \quad , \quad \mathcal{N}_5 = 0 \tag{4.36}$$

4.2 Results

Following implementation of NSCBCs into CompReal a two pronged, extensive validation campaign was conducted. The first goal of which was obviously to assess whether the method was working as intended and provided a significant advantage over previous CompReal functionality. This was done using a range of canonical configurations such as vortex convection and multi-dimensional pressure waves. In addition to this a second aim was motivated by some of the open questions lingering in the field of boundary treatments. These in essence stem from the question of how *far really is farfield*. By placing the boundary at a very distant location from regions of interest, of course most of the prevalent problems disappear albeit at the cost of increased computational cost. However having a boundary really close to the flame front or a region of reversed flow, even with characteristic treatments poses difficult challenges which are subsequently discussed.

4.2.1 Vortex Convection

A typical case study commonly found in literature (Coussement et al., 2012; Lodato et al., 2008; Poinsot et al., 1991) for testing boundary conditions is the convection of a vortex through the interface. The initial flow field for a two dimensional vortex superposed on a mean flow, U_0 is given by the stream function :

$$\Psi = S_v \exp\left(\frac{-r^2}{2R_v^2}\right) + U_0 x_2 \tag{4.37}$$

$$u_1 = \frac{\partial \Psi}{\partial x_2} \tag{4.38}$$

$$u_2 = -\frac{\partial \Psi}{\partial x_1} \tag{4.39}$$

where $r = \sqrt{x_1^2 + x_2^2}$, while S_v controls the vortex strength and R_v determines its radius. The corresponding pressure is readily found from an analytical solution (Colonius et al., 1991) and determined by

$$P = P_\infty \exp[-\frac{\gamma}{2}(\frac{S_v}{cR_v})^2] \tag{4.40}$$

which in conjunction with a specified inlet temperature can be used to evaluate density using an equation of state. Problem parameters were specified in accordance with the configuration found in Lodato et al. (2008) and correspond to a vortex strength of $0.005 m^2/s$,a radius of 10% of the domain size at 1atm and 300K. The computational domain is a square

of size 0.013m with periodic conditions in the y-coordinate and the test outflow located at the downstream axial boundary. In reality these simulations were run for a variety of flow speeds however in the interests of brevity only the intermediate case of Mach = 0.575, corresponding to a Reynolds number close to 17000 is described below.

A quantitative measure of performance is the pressure field normalised relative to farfield conditions as given by

$$P^*(\boldsymbol{x},t) = \frac{P(\boldsymbol{x},t) - P_\infty}{P(\mathbf{0},0) - P_\infty} \tag{4.41}$$

where $P(\mathbf{0},0)$ refers to the initial drop in pressure at the vortex center. This parameter has the convenient intuitive interpretation in that it is expected to be unity at the vortex center but should be zero if the vortex has cleanly and completely vacated the domain. Figure 4.1 shows these distributions for the cases of a locally one dimensional (LODI) and transverse corrected non-reflective outflows. The values are in excellent agreement with literature (Lodato et al., 2008) demonstrating the method's correct implementation. The LODI approach even with pressure relaxation is also to fail in vacating complex, multi-dimensional flow structures without reflection. In fact an acoustic wave of significant strength is seen reentering the domain, complete with alternative minima-maxima regions.

Distortion is not just limited to the acoustic field and subsequent hydrodynamic anomalies are observed in the flow as shown in Figure 4.2. While the transverse corrections preserve vortex structure upon contact with the boundary, LODI assumptions result in numerical noise and even some localised back flow into the domain.

The previous study considers the simple case of orthogonal mean flow even if the structure itself is locally two dimensional. For non-normal impact of flow features the NSCBCs perform much poorer, however Coussement et al. (2012) propose a viable correction. The authors built upon a low Mach perturbation analysis conducted earlier by Yoo and Im (2007) that investigated the ideal relaxation parameter for transverse terms at a non-reflecting outflow. By extending the previous analysis to include non-zero mean flows in non-normal coordinate direction, (Coussement et al., 2012) show that the system relaxes much smoother if a corrected velocity is used for evaluating transverse terms and is given by

$$\tilde{u_1} = u_1 - \overline{u_1} \tag{4.42}$$

$$\tilde{u_2} = u_2 - \overline{u_2} \tag{4.43}$$

$$\tilde{u_3} = u_3 - \overline{u_3} \tag{4.44}$$

Fig. 4.1 Evolution of normalised pressure (P^*) during vortex-boundary interaction for LODI-NSCBCs (left) and NSCBCs with transverse terms (right). Increasing time from top to bottom.

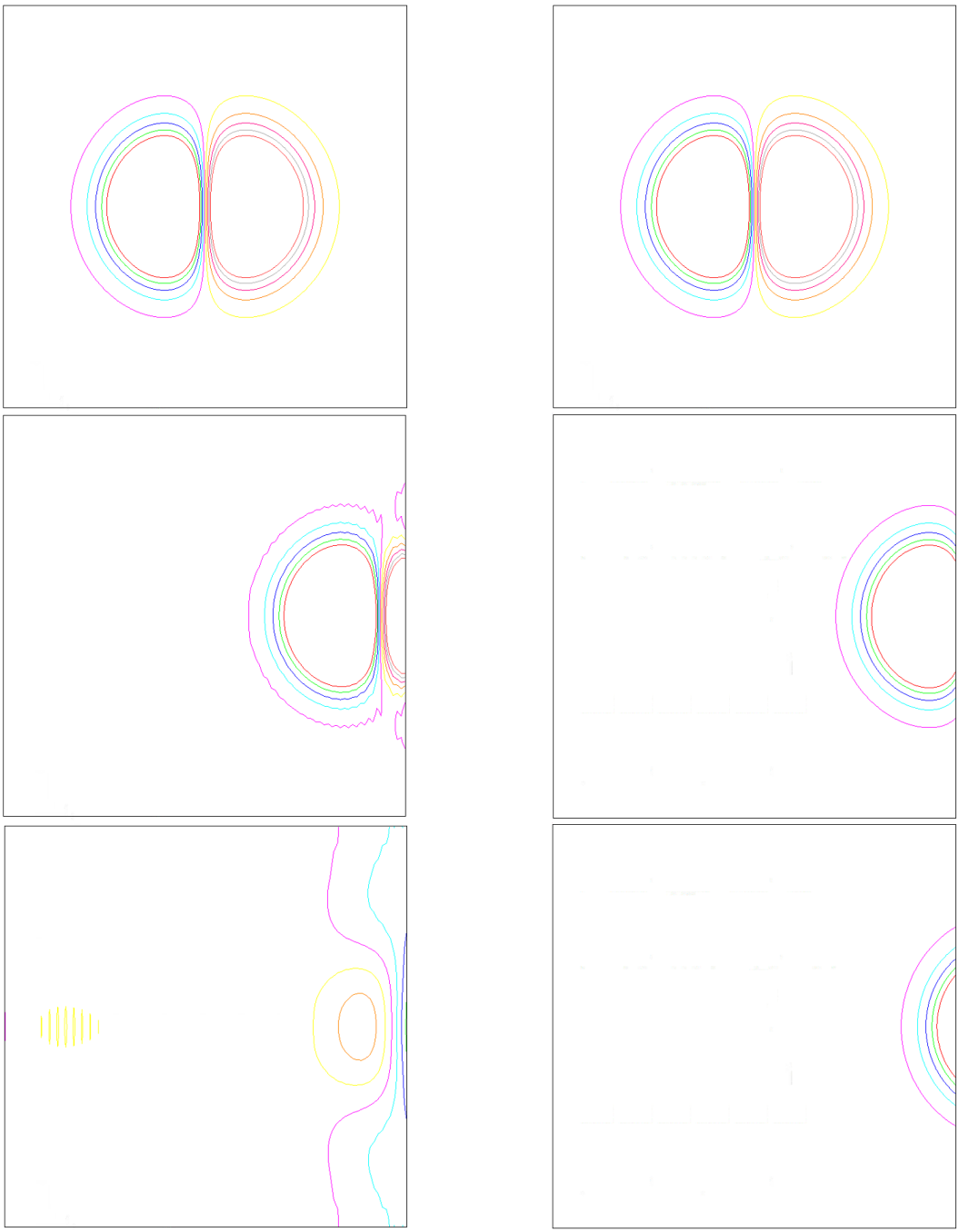

Fig. 4.2 Evolution of transverse velocity contours during vortex-boundary interaction for LODI-NSCBCs (left) and NSCBCs with transverse terms (right). Increasing time from top to bottom.

Since the correction simply involves subtracting the corresponding mean, any gradients are unchanged and do not need to be recomputed. The only difference is any multiplication terms in evaluation of transverse terms is done using this corrected instead of instantaneous velocity. This suggestion was incorporated into CompReal and subsequently tested by repeating the previous case but with a mean velocity of $100m/s$ in the x_2 coordinate axis with the resulting time evolution of normalised pressure shown in Figure 4.3. The standard NSCBC formulation with transverse term evidently still performs reasonable well given a long enough time horizon as P^* does eventually approach zero. However this is preceded by a strong spike and almost quadrupling of normalised pressure due to spurious noise generation even for the same vortex but at an oblique impact angle. Using the corrected velocities shows much better transient response for the same set of relaxation parameters and is a promising step forwards.

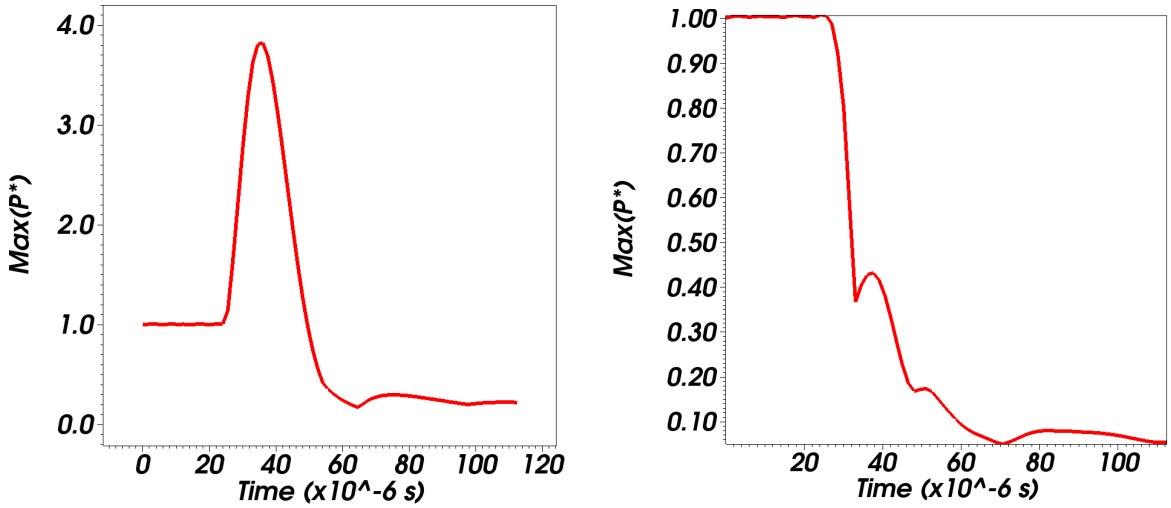

Original velocity

Corrected velocity

Fig. 4.3 Implications of choice of velocity used to evaluate transverse terms for the case of non-orthogonal mean flows. Illustrated using the time evolution of maximums in the normalised pressure field.

However direct extension of this approach to practical flows is unlikely, as it is can be difficult to compute the non-normal mean flows *a priori*. Even in the presence of a zero transverse mean velocity component, turbulent flows exhibit strong multi-dimensional perturbations and can bring flow structures into contact with a boundary at a *locally* oblique angle. Therefore mitigation of these transient events cannot be done beforehand and poses an interesting challenge.

4.2.2 Corner Collisions

Originally proposed in (Lodato et al., 2008) the case of an outward expanding pressure pulse has since become a staple of testing regimes for boundary conditions. A domain with non-reflecting outflows for each face is initialised with a quiescent medium at room temperature and pressure. A spike in pressure was initialised using Equation 4.45 before being allowed to expand and impact on all corners simultaneously.

$$P = P_t(1 + \delta \exp(\frac{-x_1^2 - x_2^2}{2R_p^2})) \tag{4.45}$$

where δ was taken as 0.01 and R_p as 0.02 for a square domain of side 0.16m. The pressure wave was observed to vacate the domain relatively cleanly however the case highlights impact of uncertainty in the many relaxation parameters involved in NSCBC. Despite (Yoo and Im, 2007) suggesting through their perturbation analysis that the local Mach number should be used for optimal transverse relaxation this is not always true. As shown in Figure 4.4 a higher relaxation parameters maintains the intrinsic nature of a spherical pressure wave upon boundary impact with higher accuracy. This raises questions about how best to proceed for semi-quiescent flows or indeed even those at just low exit Mach numbers. Furthermore in practical applications due to differences in local flow structure, adjacent points at a boundary will be experiencing a different Mach number and it is unclear what the long term impact of relaxing adjacent points differently may be.

Mitigating this very low speed dependency on transverse relaxation, a secondary evaluation for corner stability was conducted at higher Mach number. This was done by impacting a vortex travelling at $100m/s$ in both the x_1 and x_2 coordinate directions directly onto a corner as shown in Figure 4.5. The corner formulations of (Lodato et al., 2008; Yoo and Im, 2007) which do not employ corrected velocities into the transverse terms exhibit excessive distortion and noise generation. The case further highlights potential benefits of using corrected velocities despite the difficulty in always knowing them beforehand.

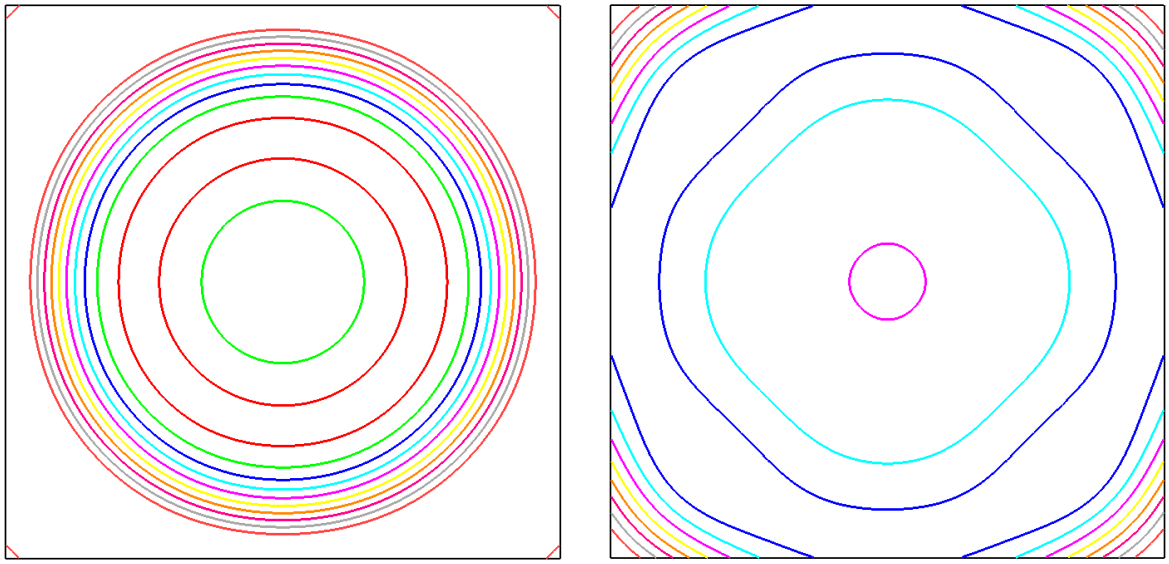

Pressure contours from 101200 Pa to 101400Pa at increasing times from left to right. Transverse relaxation parameter using local Mach

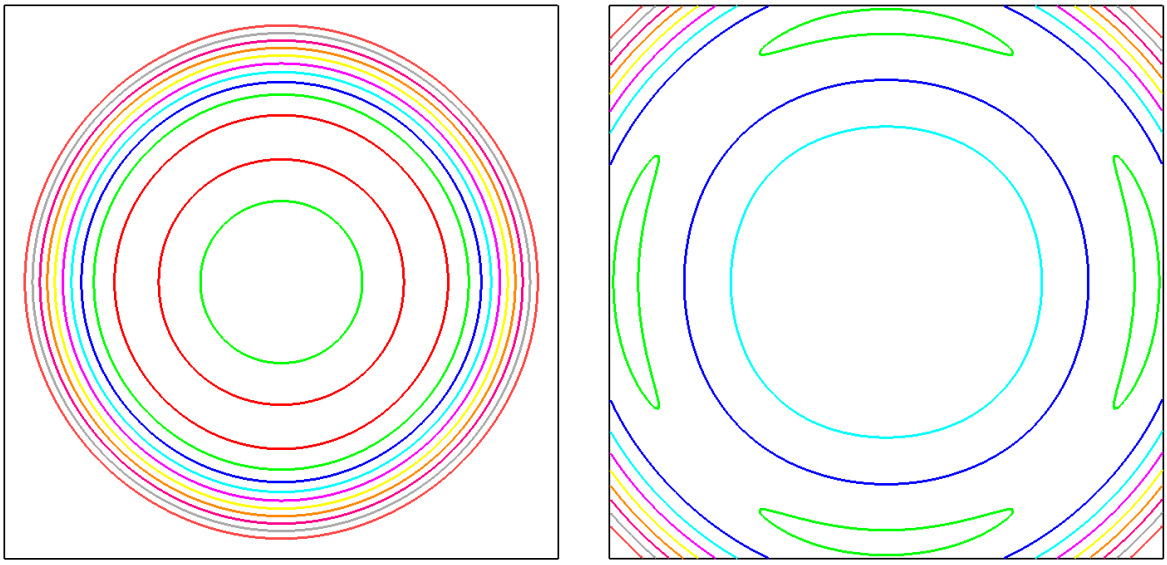

Pressure contours from 101200 Pa to 101400Pa at increasing times from left to right. Transverse relaxation parameter 0.5

Fig. 4.4 Impact of choice of relaxation parameter on an outward expanding 2D pressure wave.

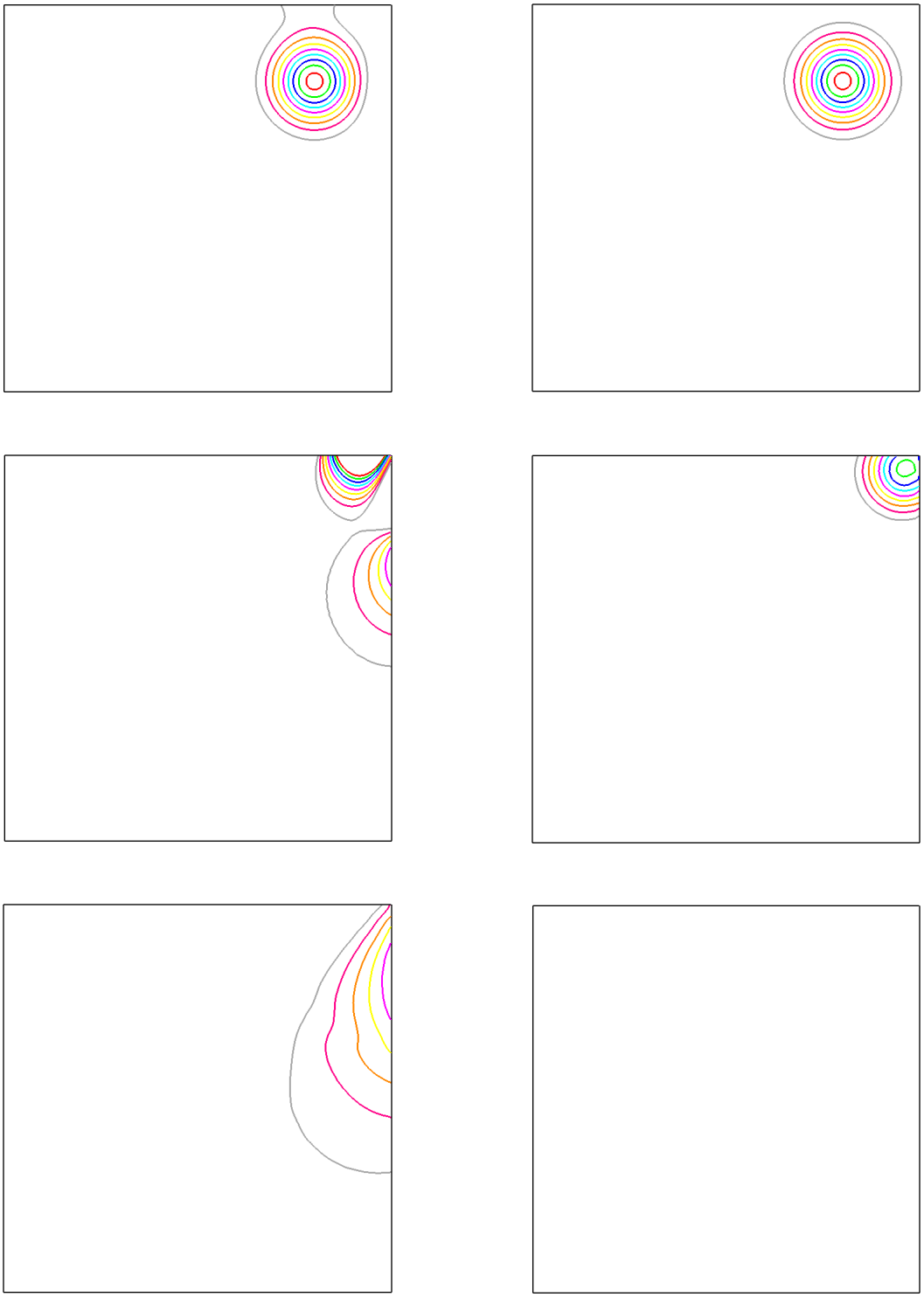

Fig. 4.5 Pressure isolines from 100500 to 101325Pa at increasing times from top to bottom for transverse terms evaluated using original (left) and corrected (right) velocities.

4.2.3 Reactive Systems

Extension of the NSCBC approach to an inert scalar is relatively straightforward since it mirrors very closely the procedure applied to the momentum transport equations. However when the scalar is reactive there is the matter of deciding what to do with the chemical source term. Sutherland and Kennedy (2003) suggest that inclusion of the chemical source term in the boundary ghost cells is essential in preserving natural flow behaviour.

They justify this statement using a simple 1D flame-boundary interaction simulation shown in Figure 4.6. Where a quiescent mixture of stoichiometric hydrogen and air at 300K and 1atm is subject to a a Gaussian temperature spike located at $x = 1.4$mm to ignite the mixture. This leads to an associated velocity field induced by thermal expansion and due to the off-centered spark the flame encounters the rightmost boundary first as visualised by the mass fraction of HO_2. Figure 4.6 isolates the moment of impact for two different cases, namely when the chemical source term is either retained or omitted in the boundary cells. The latter is seen to result in simulation failure where the local flow has reversed to the extent that the flame is propagating back into the domain instead of out. Meanwhile the former exhibits a stable flow solution as the flame impacts and subsequently vacates the domain.

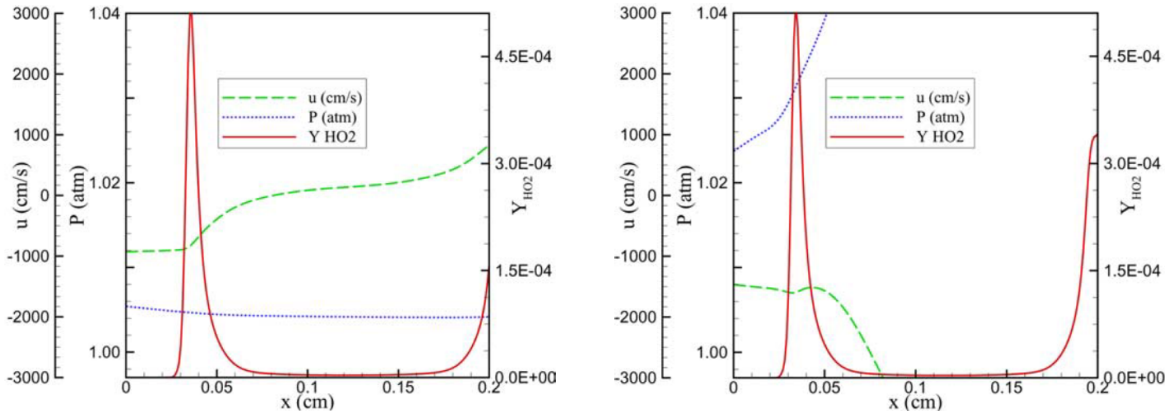

Source terms retained. Source term omitted.

Fig. 4.6 Impact of treating the chemical source term on the solution during flame-boundary interaction. Source Sutherland and Kennedy (2003).

This configuration was replicated using CompReal for both potential treatments of the source term as shown in Figure 4.7 The 19 step Yetter chemistry scheme was used for hydrogen combustion and flame surface is visualised once again using HO_2 mass fraction distributions. These are seen to rise rapidly and move away from point of ignition as the flame front propagates into fresh mixture before boundary impact. Moreover there is no significant observable difference between the different source term treatments contrary to the

findings of (Sutherland and Kennedy, 2003). If the chemical subroutines can be bypassed in boundary cells this has the potential to offer notable computations savings due to their expensive and often iterative nature.

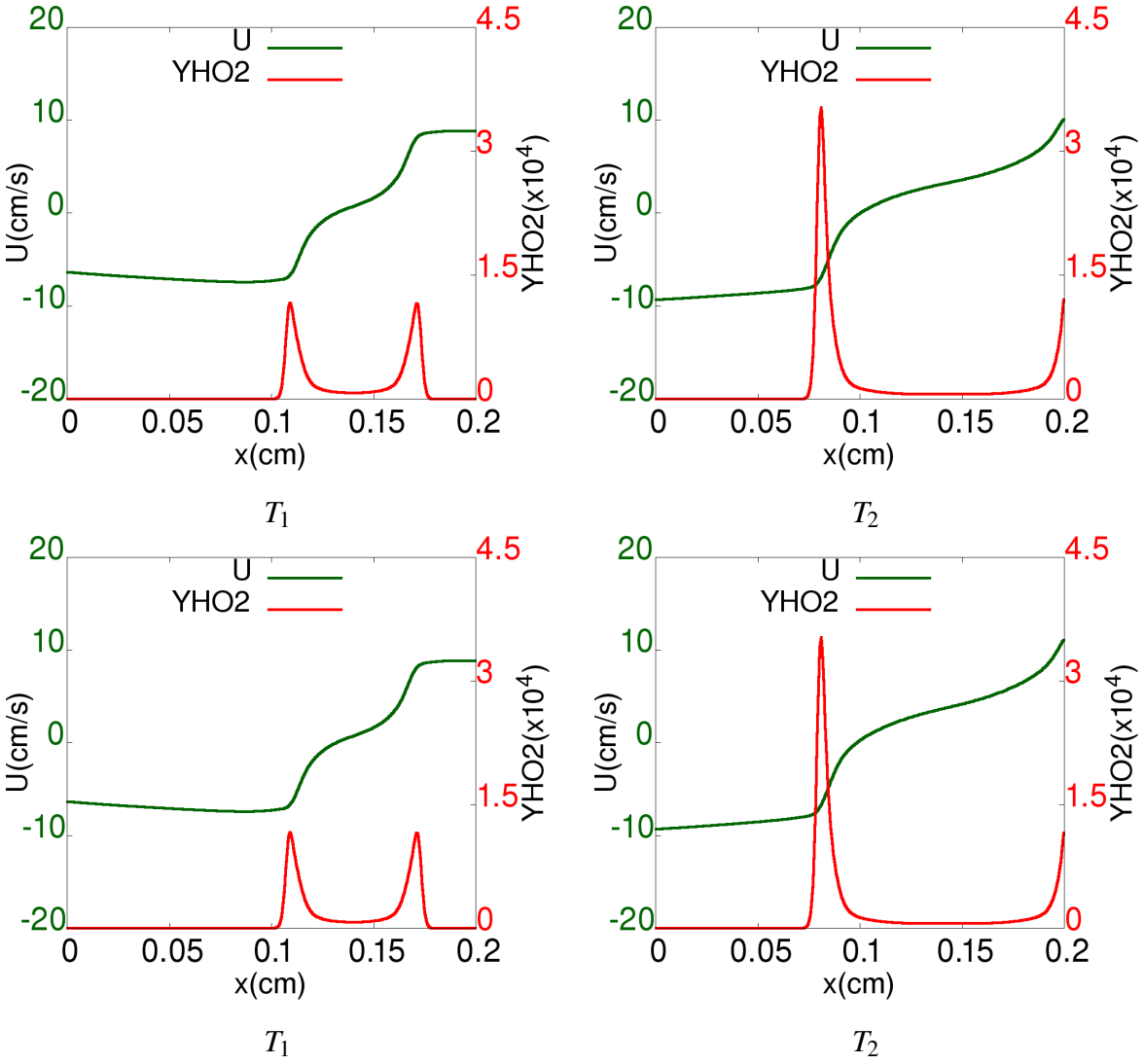

Fig. 4.7 Time evolution of 1D flame simulation for source terms omitted (top) and retained (bottom) in the boundary cells.

To further validate this suggestion a more complex case that incorporates multi-dimensional flow features into the flame-boundary action as shown in Figure 4.8 was also simulated. The case involves a two dimensional domain of size $2.10^{-3}m$, with an initially quasi-1D flame front initialised downstream of a pair of counter-rotating vortices as done in Coussement et al. (2012). The vortices are stronger than in previous sections, with relevant parameters of

$R_v = 2.10^{-4}$ and $S_v = 2.10^{-2}$. This is a very challenging case for any boundary and often such simulations are stopped before the flame actually impacts.

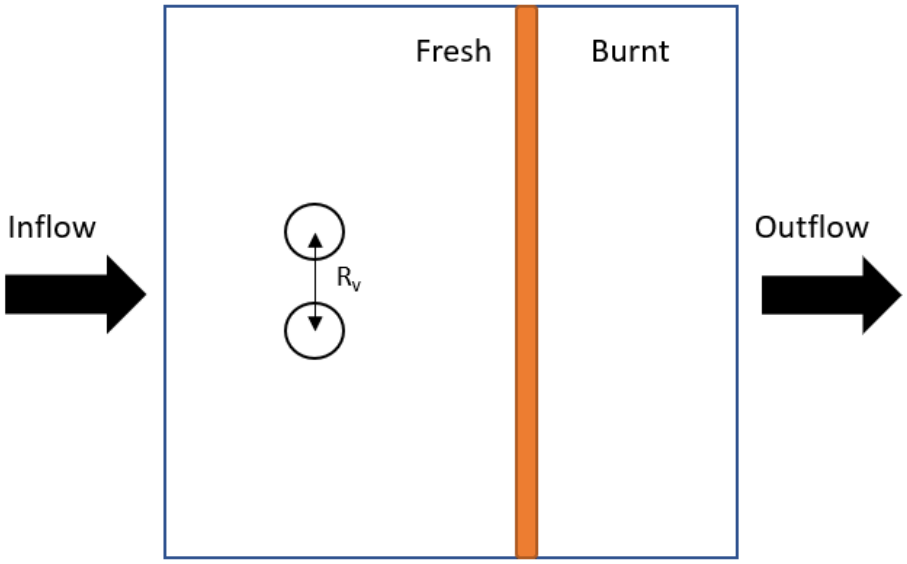

Fig. 4.8 Domain configuration for flame-vortex-boundary interaction. Initial one dimensional flame thickness illustrated in orange, downstream of a pair of counter-rotating vortices.

A reference solution was created by simulating the same configuration with an axial dimension twice as long and sampling results at the same location and time as the original boundary. Statistics of H mass fraction along the x_2 coordinate axis at an axial location very close to the boundary are presented in Figure 4.9 at progressive time instants during the interaction. In general the results shows excellent agreement with the reference solution. Suggesting that using a non-reflective outlet did not result in artificial behavior near the boundary. The full range of physical behavior expected is clearly visible, with a sudden drop in concentration along the center as the counter-rotating vortices propel fresh mixture down the center line, almost like a jet. The width of this fresh region exiting the boundary then slowly decreases as the flame re-establishes and burns away at the sides as can be seen in the final frame.

Figure 4.9 did show that the absence of source terms in the boundary does cause some minor detriment in the solution as can be seen in the second frame. Yet the magnitude seems to be small and an isolated, momentary occurrence with good agreement in other frames. The remaining small discrepancies may well be explained by the fact that these simulations did not incorporate any viscous conditions at the halos as part of the NSCBC

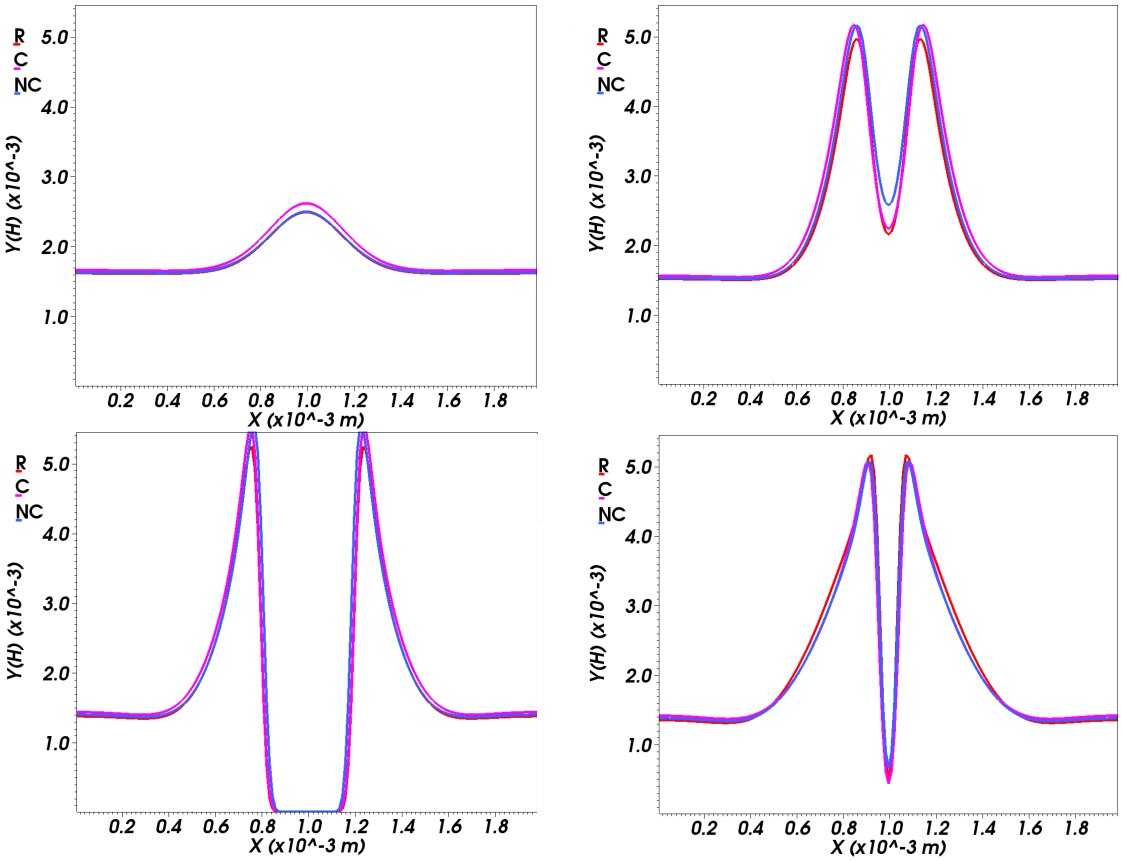

Fig. 4.9 Mass fraction of H at increasing times from left to right. R= reference, C=chemical source terms retained, NC= no chemical source terms

treatment. Generally speaking diffusion process can be important in premixed flame such as this. However the effect of having inviscid halos once again seems negligible.

Therefore it appears that CompReal exhibits greater stability in reactive configurations than was perhaps expected. One potential reason for this could be that Sutherland and Kennedy (2003) employ a pressure based formulation of NSCBC. In principle choice of primitive variable should not make a difference and constitute a physically arbitrary and irrelevant decision. However if one was to choose pressure as the primitive variable then the soft boundary conditions for waves entering the domain are a function of chemical source terms. The latter boundary condition is given below to be compared with Equation 4.8.

$$\mathcal{L}_1 = \sigma c \frac{1-\mathbb{M}^2}{2L_x}(P-P_t) + \frac{1}{2}(1-\gamma)\sum_{i-1}^{N}(h_i - c_p TW/W_i)\dot{\omega}_i \tag{4.46}$$

Therefore choosing temperature might aid stability by eliminating a prominent source of non-linearity from the characteristic boundary condition at a non-reflecting outflow. Figure 4.10-4.11 compares a pressure based formulation of NSCBCs which was also implemented into CompReal to a temperature one for the simple case of a 1D pressure wave in a quiescent multi-component mixture. The pressure based formulation is seen to perform poorer and results in a reflection back into the domain albeit of smaller magnitude and transient in nature. The same phenomena is not reproduced for a single component medium even with the choice of pressure as a primitive variable. Therefore suggesting that temperature is better suited to configurations involving reactive scalar transport equations.

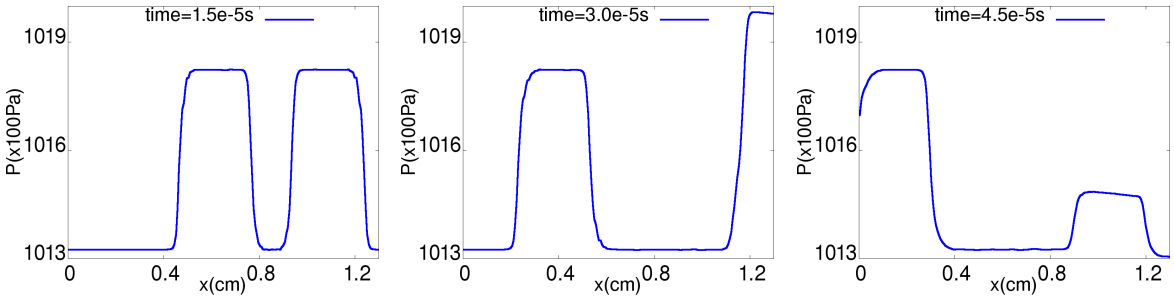

Fig. 4.10 Off-centered pressure pulse: using pressure as primitive variable

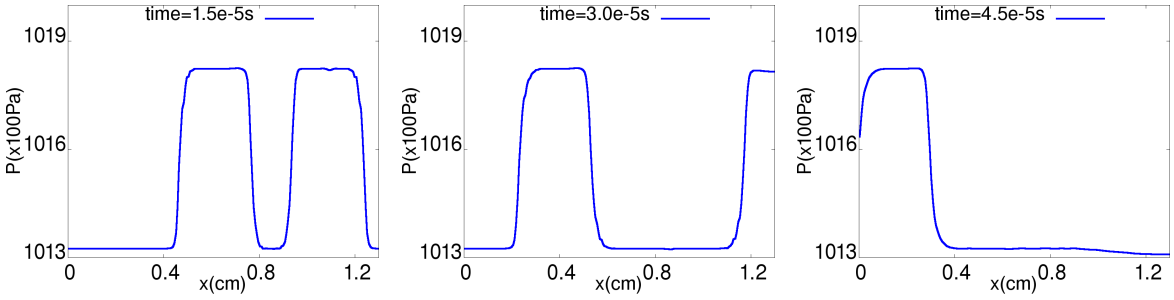

Fig. 4.11 Off-centered pressure pulse: using temperature as primitive variable

4.2.4 Extension to Axisymmetric Flows

The assumption of axisymmetric significantly reduces computational complexity of a system by allowing simulation of quasi-3D phenomena on a two dimensional mesh. Therefore the approximation holds practical relevance for a wide range of applications, but has received relatively little attention towards its coupling with Cartesian boundary methods. Relevant changes to the governing equation are briefly reviewed before a modification to classic NSCBCs proposed and evaluated using a pulsating vortex ring.

The divergence of a vector is defined in cylindrical coordinates as

$$\nabla \cdot \boldsymbol{F} = \left(\frac{\partial F_x}{\partial x} + \frac{\partial F_r}{\partial r} + \frac{F_r}{r} + \frac{1}{r}\frac{\partial a_\theta}{\partial \theta} \right) \tag{4.47}$$

which simplifies for axisymmetric configurations to

$$\nabla \cdot \boldsymbol{F} = \left(\frac{\partial F_x}{\partial x} + \frac{\partial F_r}{\partial r} + \frac{F_r}{r} \right) \tag{4.48}$$

Many computational codes generate regular, Cartesian meshes by default therefore it is convenient to realise that the above can be directly related to the Cartesian divergence with an additional source term by defining a mapping between $r \rightarrow y$:

$$\nabla \cdot \boldsymbol{F}|_{x,r} = \nabla \cdot \boldsymbol{F}|_{x,y} + \frac{F_r}{r} \tag{4.49}$$

As the right hand side of the Euler equations is the divergence of a flux vector, one can solve for axisymmetric conditions by simply adding the last term in Equation 4.49 as an additional source term to a Cartesian solver. Of course this needs to be coupled with the appropriate mirror boundary condition at the line of axisymmetry. There seems to be little work in literature extending these ideas to the application of NSCBCs and it is proposed that this term should be added as an extra source in the boundary halos, even if this is done *a posteriori* to the characteristic decomposition.

To test verify this suggestion, an axisymmetric channel is simulated and the inflow dynamically adjusted to facilitate entry of a pulsating vortex ring (using method of Danaila et al. (2015)) into the domain. This is a much more challenging case then simply initialising the structure inside the domain as its entry and convection release acoustic waves at non-normal angles which impact the outflow downstream.

Figure 4.12 illustrates evolution of the case with a standard NSCBC non-reflective outflow, including transverse corrections and pressure relaxation. As the structure enters the domain a large pressure wave is set off and shortly followed by continuous pulsations which impact the boundary ahead of the vortex itself. This impact is not at normal incidence yet the boundary manages to cope reasonably well and strong oscillations are not observed yet. However when the doughnut shaped vortex ring interacts with the boundaries a strong distortion across the entire length of the face is observed. Not only does this disfigure the outgoing structure but very strong reflections ($P^* \approx 0.45$) are observed returning into the domain. Therefore it seems that in its original form the boundary conditions are not well poised to deal with such quasi-3D phenomena.

Figure 4.13 displays the result of including the proposed axisymmetric correction. As before pressure waves ahead of the flow features are handled very well, suggesting the modification does not have detrimental effect on acoustic transmission. Furthermore when the vortex ring makes contact there is significantly less distortion this time, with the spreading of noise across the entire face seen earlier now absent. The vortex also manages to vacate the domain with minimal warping and the magnitude of pressure waves is much lower ($P^* \approx 15$ compared with 45). Moreover demonstrating that not only does the modification handle acoustic waves equally well even at odd angles, but the real benefit is observed when complex multi-dimension flow structures interact with the boundary.

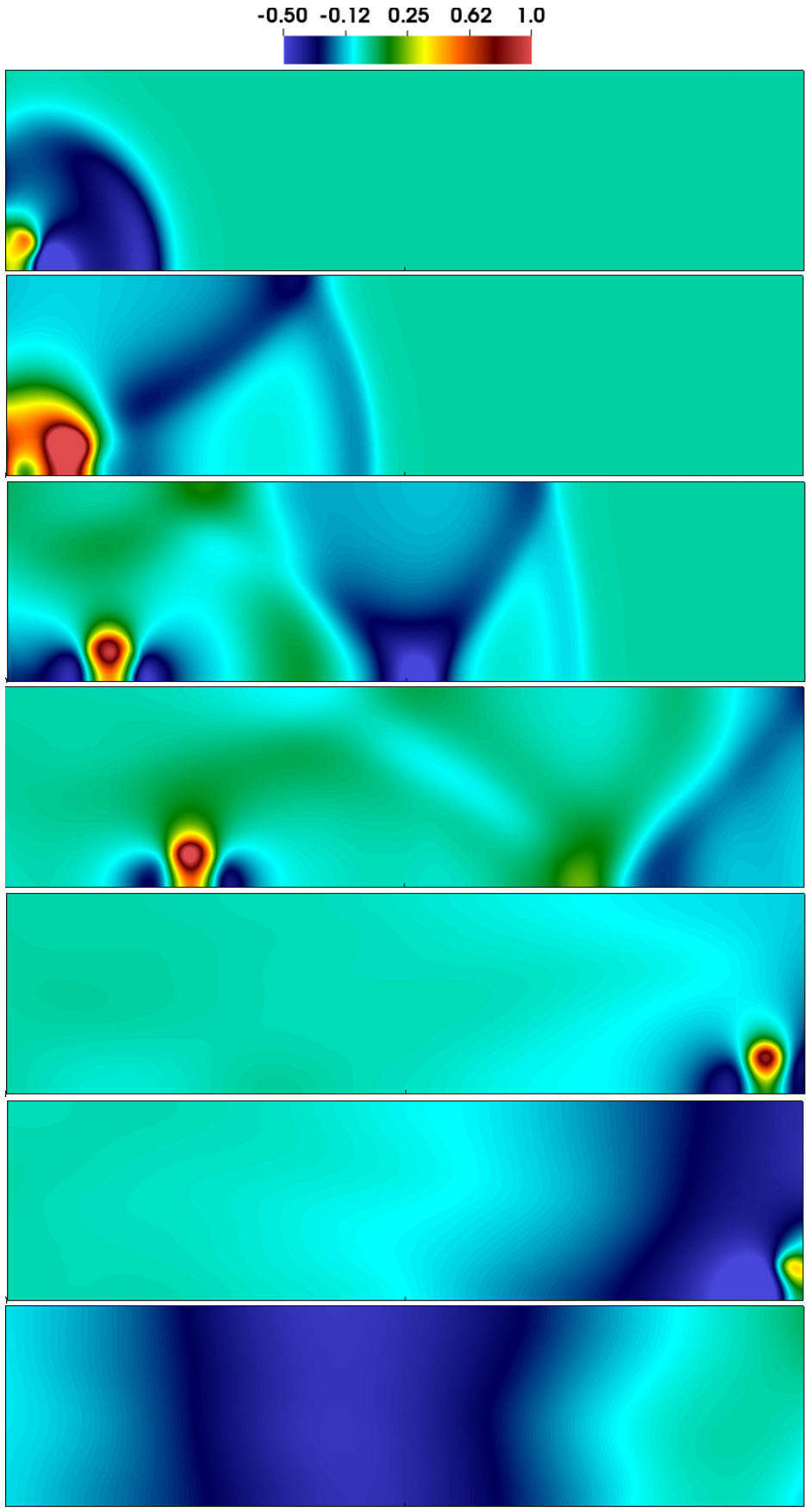

Fig. 4.12 Pulsating vortex ring with standard NSCBCs.

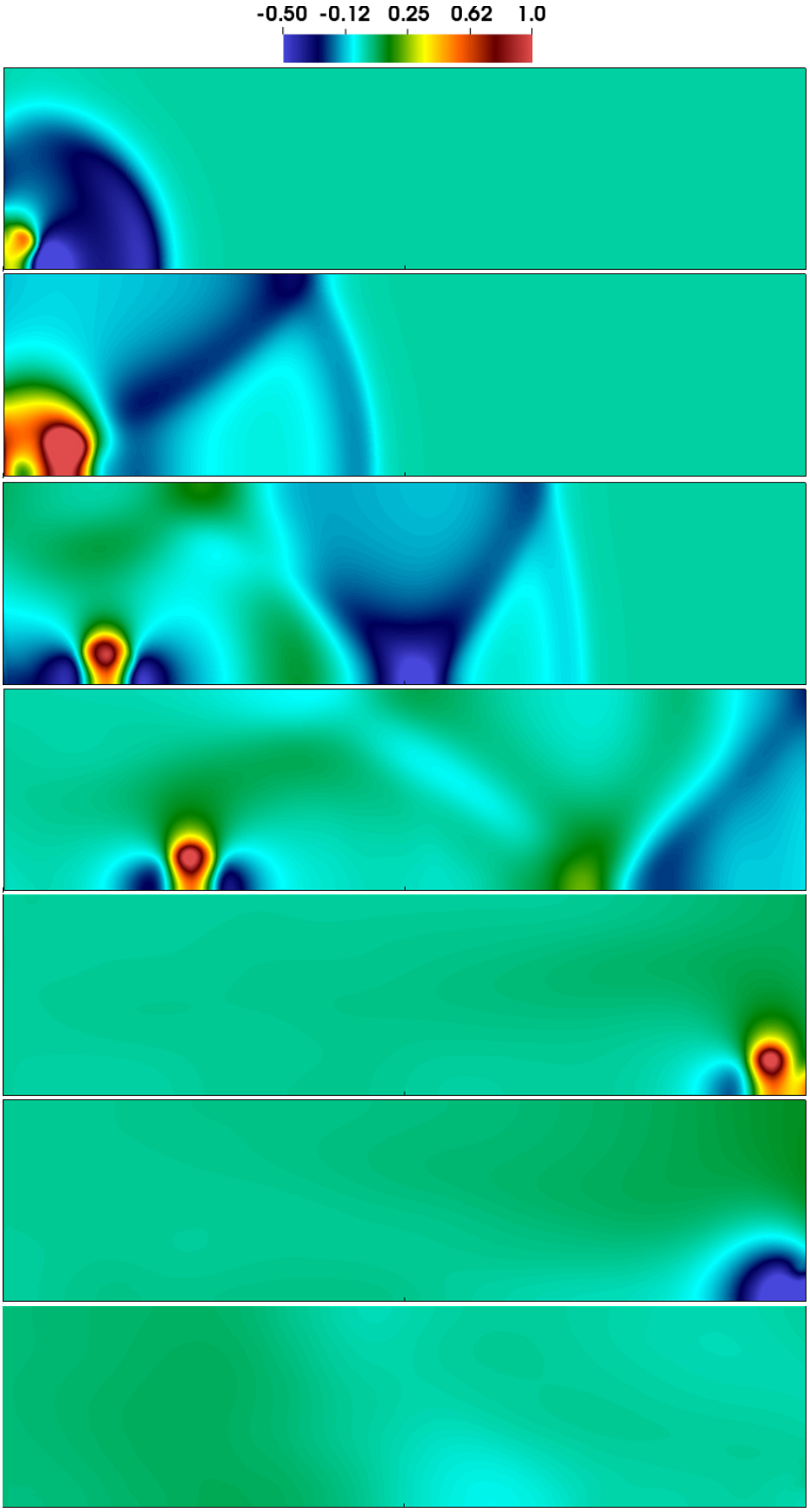

Fig. 4.13 Pulsating vortex ring with standard NSCBCs and proposed axisymmetric correction.

4.2.5 Remaining Challenges

This section aims to highlight some of the lingering weaknesses that persist in characteristic boundary methods. The configuration takes heavy inspiration from studies of indirect noise generation due to acceleration of compositional inhomogeneities through a nozzle (Kings and Bake, 2010; Lourier et al., 2014; Tam and Parrish, 2018). The problem is a simplification of the much more complicated but still very relevant problems faced in operating turbine blades downstream of a combustor in gas turbines (Bake et al., 2016).

Figure 4.14 displays a slice of the general configuration of interest where a cylindrical pipe contracts through a converging nozzle. Upstream of the pipe there may be an injection point whereby perturbations of composition can be forced by injecting an additional gas as has been done in experiments (Bake et al., 2009; Moreau and Duran, 2011; Rolland et al., 2018). Studies have tried to isolate the noise generated by convection of these entropy hot spots through the nozzle by enforcing a non-reflective boundary at the inlet. Experimentally this can be achieved by simply having a long enough section of pipe upstream that the reflection time is sufficient to approximate anechoic conditions.

However numerically simulating many dozens of meters of upstream pipe is clearly not feasible. Which is why an appropriate non-reflecting inflow condition is crucial for early domain truncation. The characteristic boundary conditions discussed earlier were employed to such a configuration assuming axi-symmetry of both the injection and flow so that it could be done in 2D. The goal here is not to present findings on indirect noise generation or its associated mechanisms but simply to use a realistic configuration to highlight two remaining challenges of interest.

Firstly even for subsonic inflows the nozzle can quickly become choked and decouple upstream and downstream sections. The conventional non-reflecting inflow can struggle to cope with such a challenging case as shown in Figure 4.15 which shows pressure evolution sampled on each side of the nozzle. The outflow still performs reasonably well, despite being noisy the downstream pressure continues to oscillate roughly about the initial pressure.

The upstream section however experiences a significant overshoot in pressure compared to the prescribed value. This is a result of reverberation despite the inlet being supposedly non-reflecting. As NSCBCs in their practical form are only *partially* non-reflective, the inflow continuously produces small reflections. However unlike in most cases these reflections now have no where to go other than down to the nozzle before being reflected back towards the inlet. The process gradually repeats as pressure builds up. A potential solution is to use lower relaxation parameters at the inflow for increased wave transmission. However this decreases control significantly and although it did manage to prevent reverberation it also resulted in larger variability of inflow quantities such as velocity and subsequently mass flow.

Therefore striking an optimal balance is not always trivial and the case highlights a more stringent examination of non-reflecting inflows than usually seen in literature.

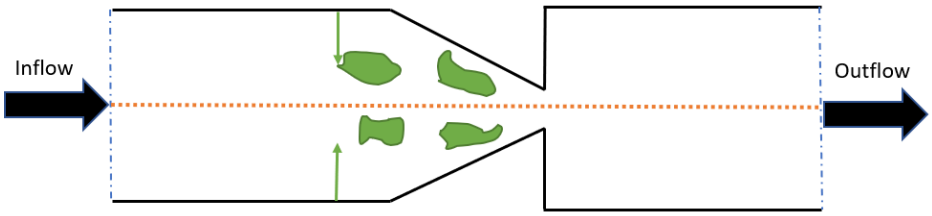

Fig. 4.14 General configuration for indirect noise generation by convection of compositional inhomgeneities (green) injected upstream of a nozzle.

The second challenge is dealing with reversed flow at the exit as a result of strong vortices generated at the throat. Coupled with a re-circulation zone post-nozzle this can result in outflows locally becoming inflows due to negative velocities, warranting an adjustment of characteristic boundary conditions. There is however no general consensus on how this should be done. As the exit locally becomes an inflow there are now four incoming waves instead of just one. (Lodato et al., 2008) suggest setting them all to zero while Coussement et al. (2012) suggest using the usual non-reflecting inflow condition with target relaxation. Although this has been shown to work reasonably well in simple configurations that is not the case here when coupled with fluctuations in composition. As the appropriate target quantity to relax species mass fraction towards cannot be known, and simply setting all incoming waves leads to stagnation zones near the outflow where the complex flow in unable to exit cleanly. As a result of the latter, in order to make the configuration work compensatory techniques such as buffer zones with increased viscosity that damp out strong flow motions were needed here as standard NSCBCs on their own were not enough.

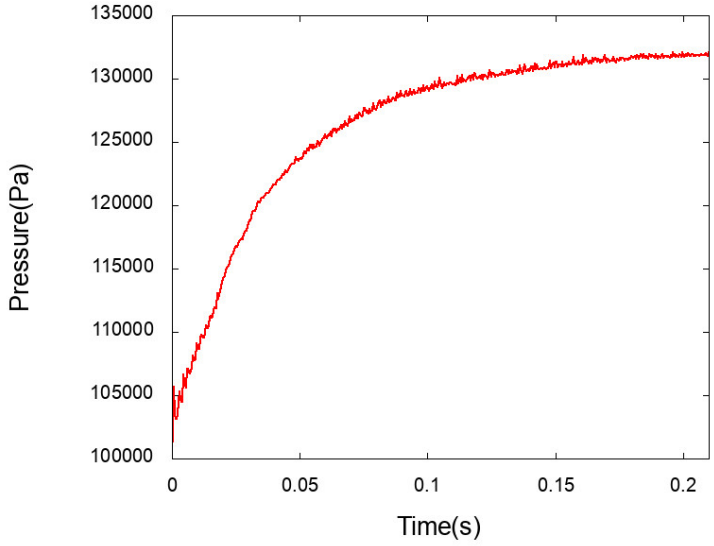

Upstream

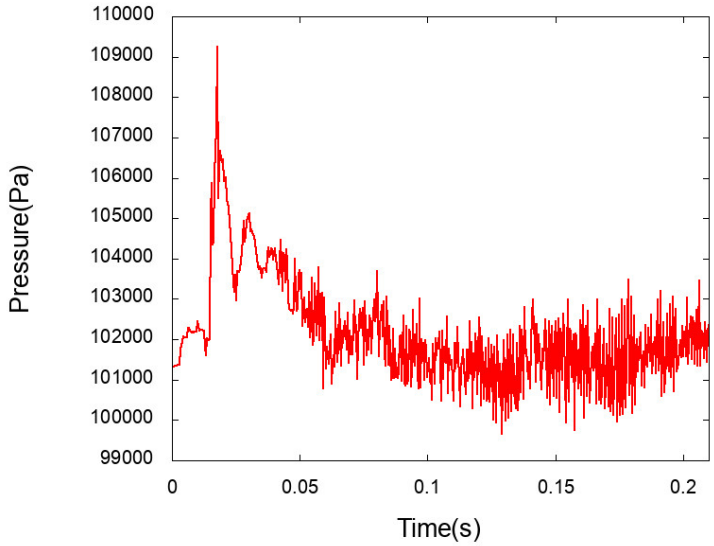

Downstream

Fig. 4.15 Pressure evolution for either side of the nozzle prior to injection.

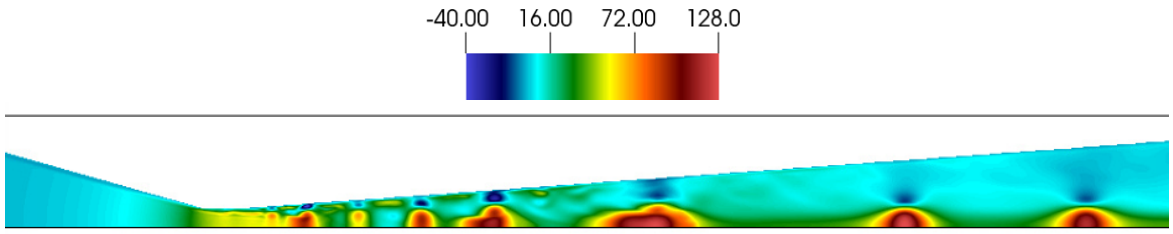

Fig. 4.16 Generation of strong vortices at the nozzle (shaded white) illustrated using axial velocity distribution

4.3 Summary

Fully 3D Navier-Stokes Characteristic Boundary Conditions were implemented into an in-house flow solver and subsequently validated. Thest cases ranged from pressure pulses to vortex convection and also highlighted limitations of the classical method for non-normal flows. A solution to the latter was found from literature and involves using corrected velocities for evaluation of transverse terms.

The role of chemical source terms in boundary cells was investigated using a 1D flame and contrary to literature found to be negligible. This was further corroborated by the more complex case of a burning pair of counter-rotating vortices impacting on an outflow. Where the net detriment in solution quality form using nonreactive halos was barely noticeable. Even if in practice simulations are truncated before the flame can impact a boundary this is still an important finding that can save computational resources by bypassing costly chemical subroutines for halo points. The precise cause of differences with a previous study are not clear, however the difference in choice of primitive variables has been proposed as one factor of relevance. By choosing temperature the reactive source term does not appear in the characteristic outflow boundary condition but it does for pressure. Suggesting a stronger correlation of the latter with retention of chemical reactions at the boundary.

A novel extension for axisymmetric flows is also proposed and tested using the challenging case of a pulsating vortex ring. The modification was shown to reduce reflected noise by upwards of 50% when dealing with such multi-dimensional flow features. The vortex ring itself also underwent much less warping while exiting the domain and pressure waves incident across a range of angles were handled equally well.

Lastly a model problem inspired from recent investigations into indirect or so called *entropy* noise was simulated with the intention of highlighting shortcomings and open questions that still remain in the field. Non-reflecting inflows have received much less attention than their outflow counterparts. Indeed even if tighter control is retained at the inlet using higher relaxation parameters, usually the increased oscillations do not affect the system as they are transient in nature and vacated from the outflow downstream. However if there is a choked nozzle downstream these fluctuation will be reflected back towards the inlet, and depending on the distance may not dissipate significantly. This can lead to build up of acoustic waves via reverberation even with theoretically anechoic inlets the optimal choice of relaxation coefficients for which remains an open area of uncertainty.

Furthermore treatments for locally reversed flow where an outflow momentarily become an inlet are not robust. Common solutions which may work in simple configurations are ill posed in dealing with compositional inhomogeneities on top of a reversed base flow and warrant further investigation.

Chapter 5

Model Validation and Evaluation

This chapter presents results from a validation campaign designed to assess the performance of the proposed ATF methodology. Each test case was specifically selected to evaluate the performance of a particular modelling aspect. Starting with the flame-vortex interaction to assess the effect of thickening on flame-turbulence interaction in a controlled environment. Despite its apparent simplicity this configuration laid much of the framework for the original efficiency function based methods of Charlette et al. (2002); Colin et al. (2000).

Next an axisymmetric flame undergoing acoustic excitation is examined in order to determine the effect of the thickening transformation on not just the reactive scalar but also momentum equations. This is a challenging case for ATF models due to the fact that transients can be difficult to capture as the solution is also thickened in *time*. By studying the formation and subsequent convection through a shear layer of an instability in the flame surface from root to tip, promising groundwork has been laid that suggests the approach can be readily applied to advection dominated flows.

The remainder of this chapter is dedicated to reconciling the LES-ATF methodology with AMR. This is first done by considering a nonreactive jet to isolate the effects of LES-AMR coupling for which defining the filter width across a change in levels of refinement remains a somewhat open question. To this end several solutions are suggested and subsequently evaluated while trying to leverage complexity of implementation with both theoretical rigour and solution accuracy. In doing so creating a more justified basis for the complete LES-ATF-AMR framework that was developed as part of this work. Finally the overall unified method is evaluated against a realistic 3D turbulent Bunsen flame, showing good agreement.

5.1 Flame-Vortex Interaction

The most common criticism of ATF models is its difficulty in capturing turbulence induced flame wrinkling, hence the need for SGS efficiency functions. Simulating flame response to a single pair of counter-rotating vortices is an attempt to address the latter in a controlled environment for the proposed methodology. Naturally the size and intensity of the vortex pair are parameters of critical importance and as such based on earlier findings (Colin et al., 2000), only the most challenging cases are evaluated here. Following on from the Damköhler number arguments presented in Section 2.3, general trends regarding vortex interaction with thickened flames reported in Colin et al. (2000) can be summarised as:

- Eddies smaller than $\mathcal{F}\delta_f^0$ are no longer able to interact with the flame
- Eddies larger than $\mathcal{F}\delta_f^0$ interact with the flame but may be substantially impaired in efficiency and subsequently induced wrinkling. This implies that even eddies which are resolved on the mesh may require a SGS correction.
- In agreement with the earlier work of Poinsot et al. (1991), the degree of impairment depends mostly on the length scale ratio between vortex size and thickened flame thickness. Interestingly enough this ratio is relatively independent of the actual value of the thickening factor.

Complementary to the last point, Colin et al. (2000) expands on the work of Poinsot et al. (1991) that only addressed effects of the length scale ratio to include the influence of the vortex velocity scale. Essentially larger vortex induced strain rates create more flame stretch and subsequently flame wrinkling which needs to be accounted for in an efficiency function approach. With this in mind three different vortex configurations were chosen and paired with a variety of thickening factors. Note that these configurations are already very challenging since the chosen vortex size is roughly of the order of laminar flame thickness *i.e.* smaller than the vortex considered in Colin et al. (2000). Which means that in a thickened context the vortex will always see the flame as *thick*, hence placing the interaction somewhere between the cut-off (where vortices can no longer interact with the flame) and intermediate (where flame-vortex interaction is impaired) scales for which classical ATF fails.

5.1.1 Computational Setup

The following simulations were run with a 19 step, 9 species reduced chemical scheme for hydrogen combustion, at equivalence ratio of unity, pressure of 1atm and fresh gas temperature of 300K. The burnt state was initialised downstream separated from fresh

Table 5.1 Vortex characteristic size (estimated from separation distance) and velocities considered during flame-vortex interaction.

Vortex	R_v/δ_f^0	v'/S_l
A	≈ 1	4
B	≈ 1	2
C	≈ 1	1

mixture by an initially 1D flame. Upstream of the reaction zone a pair of counter-rotating vortices were superposed onto the mean flow and are characterised by the separation distance between their cores as done earlier in Section 4.2.3. Of the vortex parameters presented in Table 5.1, Vortex A was the primary target of investigation with Vortices B and C having the intended purpose of trying to find limits of the model. Hence for the following results it should be assumed any plots correspond to Vortex A unless otherwise stated.

The same mesh is used for all cases with sufficient resolution to place around ten points within the original laminar flame thickness. So that all relevant scales are resolved *a priori* in order to isolate only the effects of the thickening transformation itself. A secondary implication of using fine grids is having enough resolution in regions of sharp gradients that the artificial dissipation term of Equation 3.29 can be switched off. Note that this term was originally designed for shock capturing and essentially adds an additional diffusive flux into regions exhibiting discontinuities. However a flame can exhibit sharp gradients and cause the shock sensor to trigger locally.

Furthermore as gradients are naturally different between ATF and DNS flames, the contribution of an artificial flux will not be the same for both and would make direct comparisons difficult. It is always desirable to eliminate this term in order if possible, with the broader consequences of situations where stability considerations might not allow this briefly commented on in Section 5.4.

5.1.2 Small to Moderate Thickening

The primary goal is to evaluate the proposed methodology in terms of induced flame wrinkling in the context of small to moderate thickening factors. A qualitative representation of the flame-vortex interaction and its evolution in time is displayed in Figure 5.1. Wherein generally speaking the model captures the nature of the interaction very well across a wide

range of phenomena ranging from initial wrinkling (Row 1) to neck formation (Row 2) and subsequent pinch-off/pocket formation (Row 3) even without an efficiency function.

There are some small differences with respect to the transient response, however this is not surprising as ATF models solve respect to *thickened time*. Despite this the use of an appropriate sensor to limit the transformation to the reaction zone does seem to have mitigated most of these inherent shortcomings, albeit not perfectly.

To better understand temporal discrepancies, note that the thickened flame initial response (Row 1) is slightly ahead of its DNS counterpart. This is a result of all simulations having the flame initialised in the same location, which in the context of thickening results in a flame front slightly closer to the upstream vortex pair once the system stabilises. This initial "head start" for thickened flames is quickly over taken in the second row of Figure 5.1 where the DNS solution can be seen to advance through the domain faster. The lag for ATF flames in this phase is likely due to the inherent limitation of *thickened time*.

However an additional contribution is observed in Row 3 where thickening essentially displaces the reaction zone across a wider area. For the purposes of pinch-off this means that the "neck" region is slightly wider, and as the ATF model preserves flame speed the time taken for opposing flame elements to traverse this distance before mutual annihilation is slightly longer. Moreover considering that these phenomena are characterised by incredibly small and fast scales and even then the transient differences are negligible, the net detriment is likely inconsequential for a wide range of flames. Furthermore the remainder of the base flame can be seen to recover for all cases following pinch-off with good agreement.

Figure 5.2 changed perspective now to focus on any discrepancy at the most challenging scales. Row 1 highlights the phenomena described earlier where the wider neck region brought about by thickening can lead to a delay in pinch off. For thickened necks, flame elements must cross a slightly larger distance to meet which is why the DNS solution is the first to produce pinch-off. However despite this the actual shape of the pocket is preserved very well as can be seen in Row 2. Not only has the mechanism of pinch off been accurately reproduced by the proposed methodology but the shape of the pocket is still relatively consistent as it subsequently burns off. It is only near its end of life where the local curvature is defined by even smaller scales that some of the finer details are lost as seen in Row 3. Structures of the order of δ_f^0 may indeed be distorted or lost as two flame elements separated by a distance of about δ_f^0 may no longer be separated when transformed into thickened space. Despite this, overall flame dynamics in vorticity controlled regions across challenging phenomena such as quenching and pocket formation are replicated reasonably well with the proposed methodology even for unsteady flames.

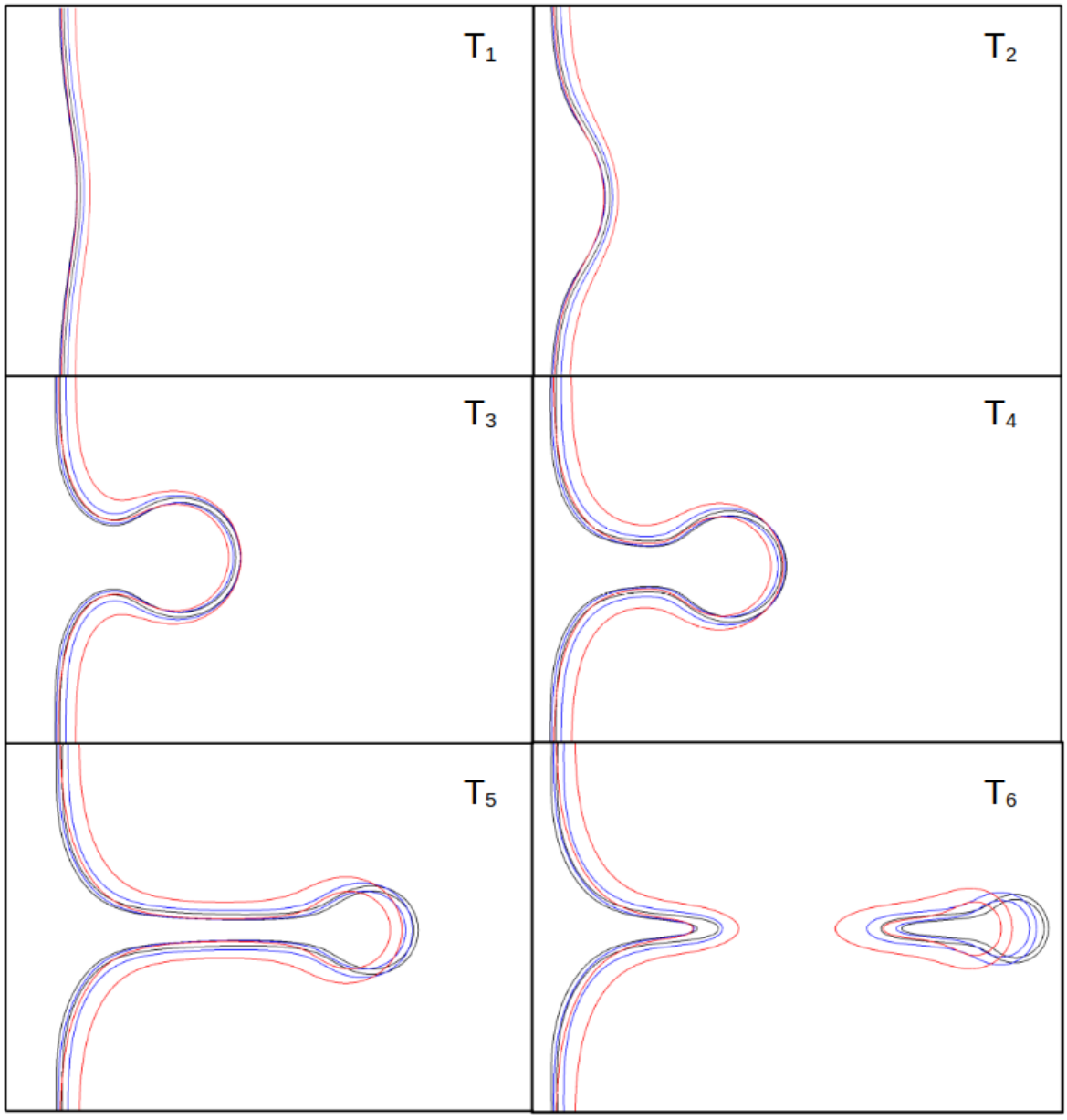

Fig. 5.1 Evolution of the progress variable iso-contours (0.1 and 0.9) in time during flame-vortex interaction for DNS (black), $\mathcal{F} = 2$ (blue) and $\mathcal{F} = 4$ (red).

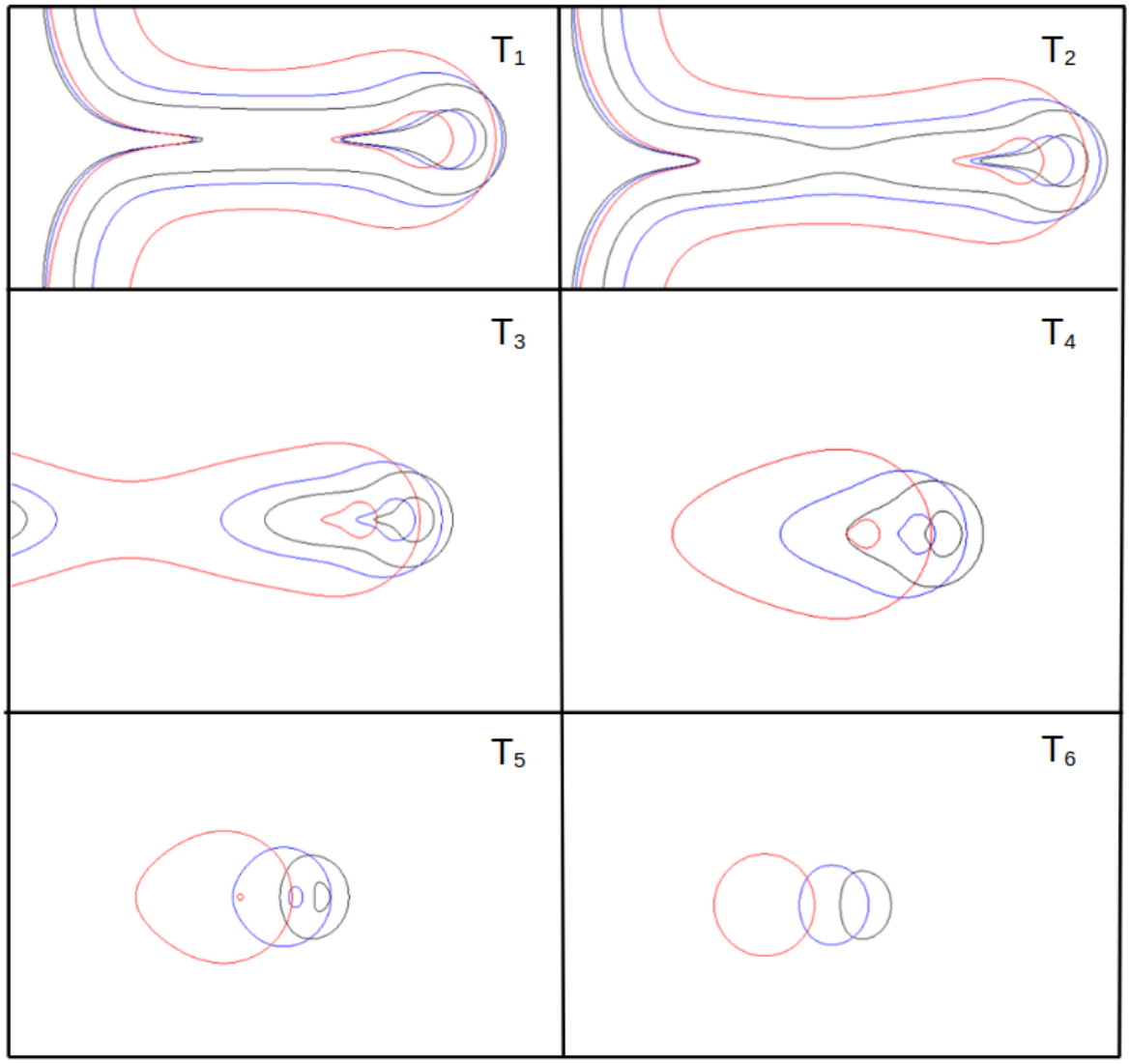

Fig. 5.2 Evolution of the progress variable iso-contours (0.1 and 0.9) in time during pocket formation and burnout for DNS (black), $\mathcal{F} = 2$ (blue) and $\mathcal{F} = 4$ (red).

Furthermore the aforementioned localised distortion has little effect on global system dynamics. Figure 5.3 displays the evolution of total heat release in time. For simple configurations like this the neat heat release rate can be considered as indicative of net flame surface area, hence consequentially representative of the effectiveness of a vortex at inducing flame wrinkling (Colin et al., 2000). Which is why the very close agreement in peak heat release rate of Figure 5.3 implies that the proposed methodology manages to capture the overall effect of vortex induced flame wrinkling and it's associated creation of flame surface. At this stage the latter claim is accompanied by two caveats, firstly that the mesh is fine enough and secondly thickening factors kept moderate.

Note that as expected there are some differences in the transients of flame response identified in Figure 5.3, such as heat release increasing sooner for thickened flames due to earlier contact with the vortex. Furthermore the annihilation of surface area (as indicated by the fall in heat release) following the peak seems to lag behind and is attributed to the temporal considerations discussed earlier. Namely an inherent delay for solving thickened time and the fact that time-dependant dynamics at the very smallest scales can be slightly skewed by the spreading out of flame elements in thickened space.

From tracking the heat release response, the moment of maximum wrinkling is identified for each case and the PDF of mean curvature at this time was extracted as shown in Figure 5.4. Note that curvatures in thickened space need to be re-scaled back to physical space via the thickening factor. In summary since the proposed thickening transforms all scales, the radius of curvature is also thickened, hence the reciprocal (i.e. the mean curvature) shrinks by the same amount. Therefore the thickened mean curvature is rescaled back into physical space by multiplying with the thickening factor. Note that this is not possible with conventional ATF due to the use of an efficiency function, with more details provided in Appendix B. Returning to Figure 5.4, all curves peak at zero, where very small radii are essentially seen as flat. The peaks for thickened flames are slightly higher in this vicinity, implying that the cutoff requirement for a radii to not be inferred as flat is slightly higher. Alternatively this can be interpreted as an inability to resolve wrinkling at the very finest of scales.

However there is very good agreement across the remainder of the range of possible curvatures. In addition to this the relative preference between positive and negative values is preserved across the vast majority of interaction time horizon. This can be better seen in Figure 5.5 which shows the curvature distribution demarcated by sign between bounding flame progress variable iso-contours (of 0.1 and 0.9). The weakly curved base flame can be seen to be responsible for the longer positive tails in Figure 5.4 earlier. Moreover the relative distribution patterns of positive/negative regions induced by the vortex are well represented across the many stages of interaction. The first notable discrepancies only start

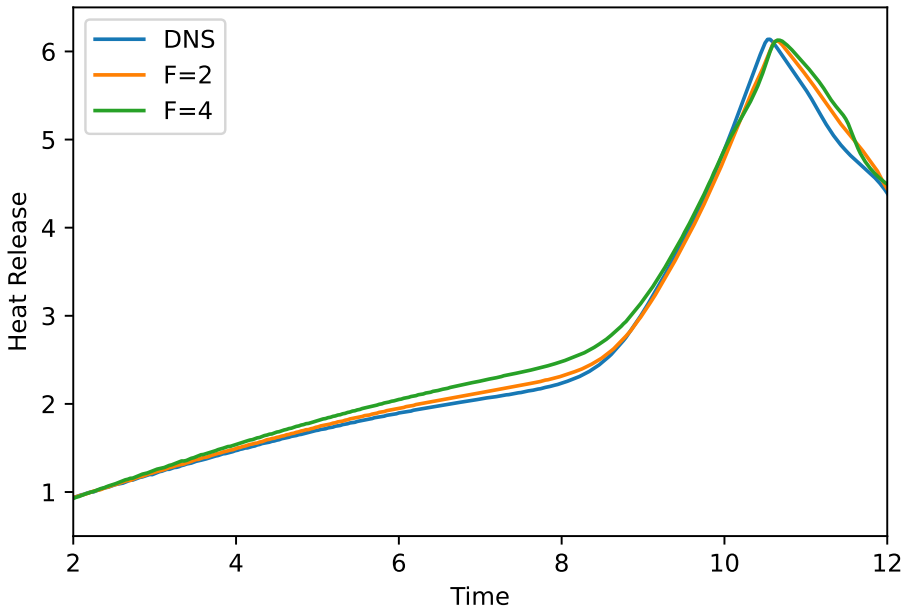

Fig. 5.3 Total non-dimensional heat release plotted against non-dimensional flame time.

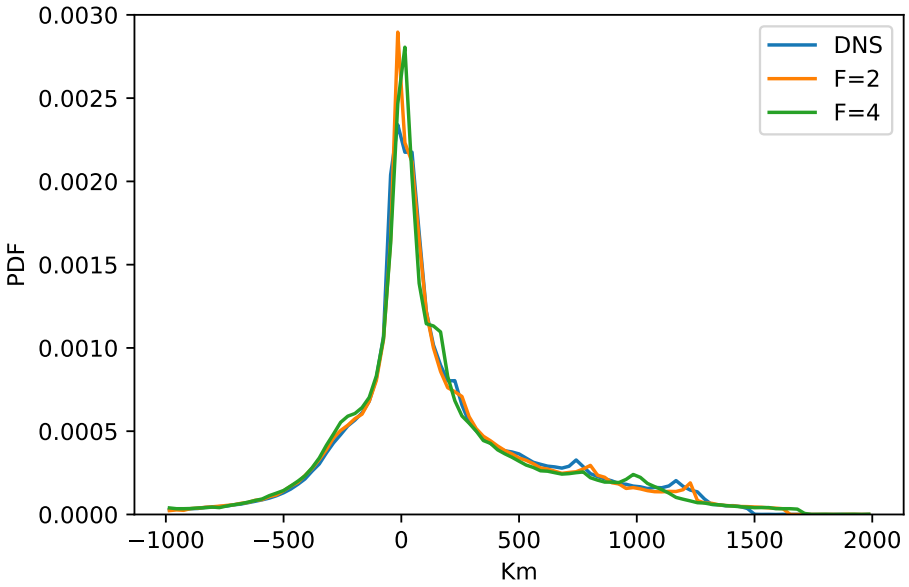

Fig. 5.4 Curvature distributions at moment of max flame wrinkling.

to be observed in Rows 3-4 just prior to and after pinch-off, where the thickened case takes longer to form a pocket and this naturally leads to differences in curvature in the local necking region. Meanwhile the now displaced and delayed (in time) pocket right after formation loses some of the finer details present in DNS. However following the (very short) lifetime of the pocket it is observed that differences in feature recognition quickly disappear with the distributions converging as seen in Row 5. Note that each of the rows in Figure 5.5 are temporal increments of only 0.02ms, which is to say the discrepancies in Row 4 were short lived and momentary. Furthermore the good agreement in curvature implies it is possible to extract meaningful scalar topologies from the gradients directly provided by the proposed method which is one of its main advantages.

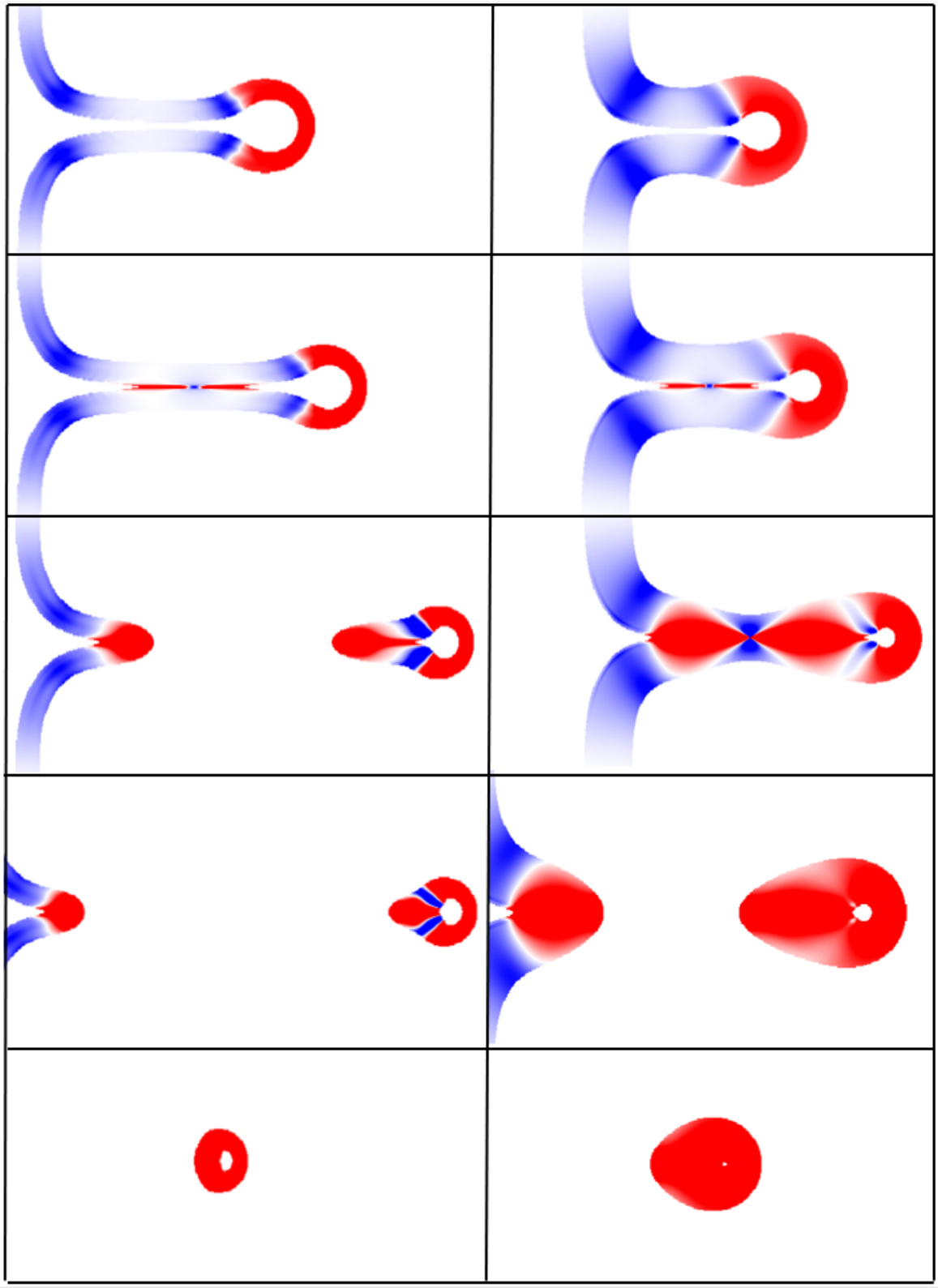

Fig. 5.5 Temporal evolution of curvature distribution across the flame front (i.e. progress variables $0.1 - 0.9$) for DNS (left) and $\mathcal{F} = 4$ (right) demarcated by sign. Blue represents positive and red is negative.

5.1.3 Large Thickening

The proposed approach is now tested across a larger range of thickening factors. Even if some of these values go beyond what is recommended for practical applications in order to identify potential weaknesses of the model.

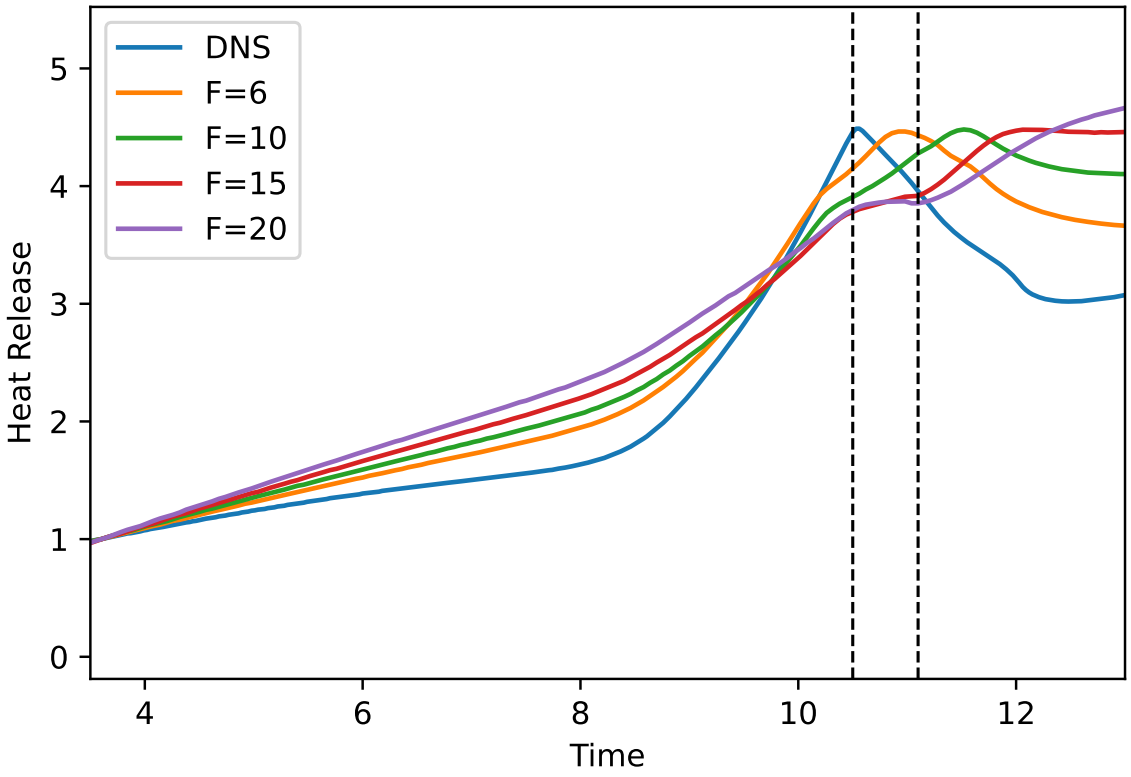

Fig. 5.6 Non-dimensional heat release against non-dimensional flame time. Dotted black lines encompass the region of time 10.5-11.1

Figure 5.6 illustrates the heat release evolution where the responses can be divided into two categories. Up to $\mathcal{F} = 10$ the peak heat release is captured well even if there are increasing difference in the transient buildup and subsequent annihilation of flame surface. This suggests good overall behaviour of the model in preserving the nature of flame response even under strain dominated behaviour. For values of the thickening factor greater than 15 there is a qualitative change in flame response, starting with the formation of a region resembling a plateau between times $10.5 - 11.1$, directly after which the heat release continues to increase instead of falling.

To investigate this further Figure 5.7 displays a side by side comparison of progress variable distribution for DNS and $\mathcal{F} = 20$ in time increments of 0.3 from 10.5 to 11.1. For

the DNS solution this sampling window starts at the instant of peak heat release which can be seen by the first snapshot is the moment just after necking. Essentially right after pinch-off as the pocket of entrained fresh mixture breaks away it brings about the creation of additional flame surface. Following this the overall heat release drops as the remaining neck recovers and merges into the base flame while the tail trailing the pocket similarly assimilates into itself and the pocket burns out.

In comparison the thickened solution lags behind and only just begins to exhibit necking, which correlates well with how the extent of ascent in heat release is lower in Figure 5.6 at the same time. After which there is pinch off where a pocket of fresh gas tries to break away from the neck, however it does not manage to escape the reaction zone or completely break away before being burned off. Hence the drastic increase in flame surface previously observed during pinch off is lost in the plateau region.

It is difficult to narrow down the exact cause for why the pocket of fresh mixture fails to break away completely. Flame stretch can be perceived as a measure of flame surface generation and is essentially a balance between tangential strain and curvature effects. In *principle* by transforming all scales this relationship should be maintained: a caveat which is not true for classical ATF. Even if in reality there will be some error as the dilatation contribution will be different due to distribution of heat release over a wider area affecting thermal expansion of the fluid and its associated flow field.

Furthermore there is the interplay between multiple transients to consider, such as how the temporal lag coupled with a larger reaction thickness results in any entrained fresh mixture spending a longer duration in the flame zone before breaking away. Evidently the pocket burns out during this extended stay in the flame region. These phenomena are clearly influenced by scales very much smaller than the flame thickness and it was shown earlier than the localised transformation to thickened space can displace opposing iso-contours further apart in the neck region.

The second deviation from expected behaviour at large thickening is the continued increase of total heat release post-plateau. It is postulated that this is due to the growing importance of a secondary reaction zone that continues to generate heat outside of the primary reaction area. Such effects are unique to cases with detailed multi-step chemistry and were not observed in the simplified chemical approximations of (Colin et al., 2000). Figure 5.8 provides credence to this suggestion by mapping out the distribution of heat release per unit volume in progress variable space right after the plateau for $\mathcal{F} = 20$. At the lower end of progress variable space (i.e. < 0.2) the distributions are fairly similar since the asymmetric sensor being employed is close to null in the vicinity so thickening has little effect. For increasing values of progress variable the ATF sensor value grows and larger degrees of

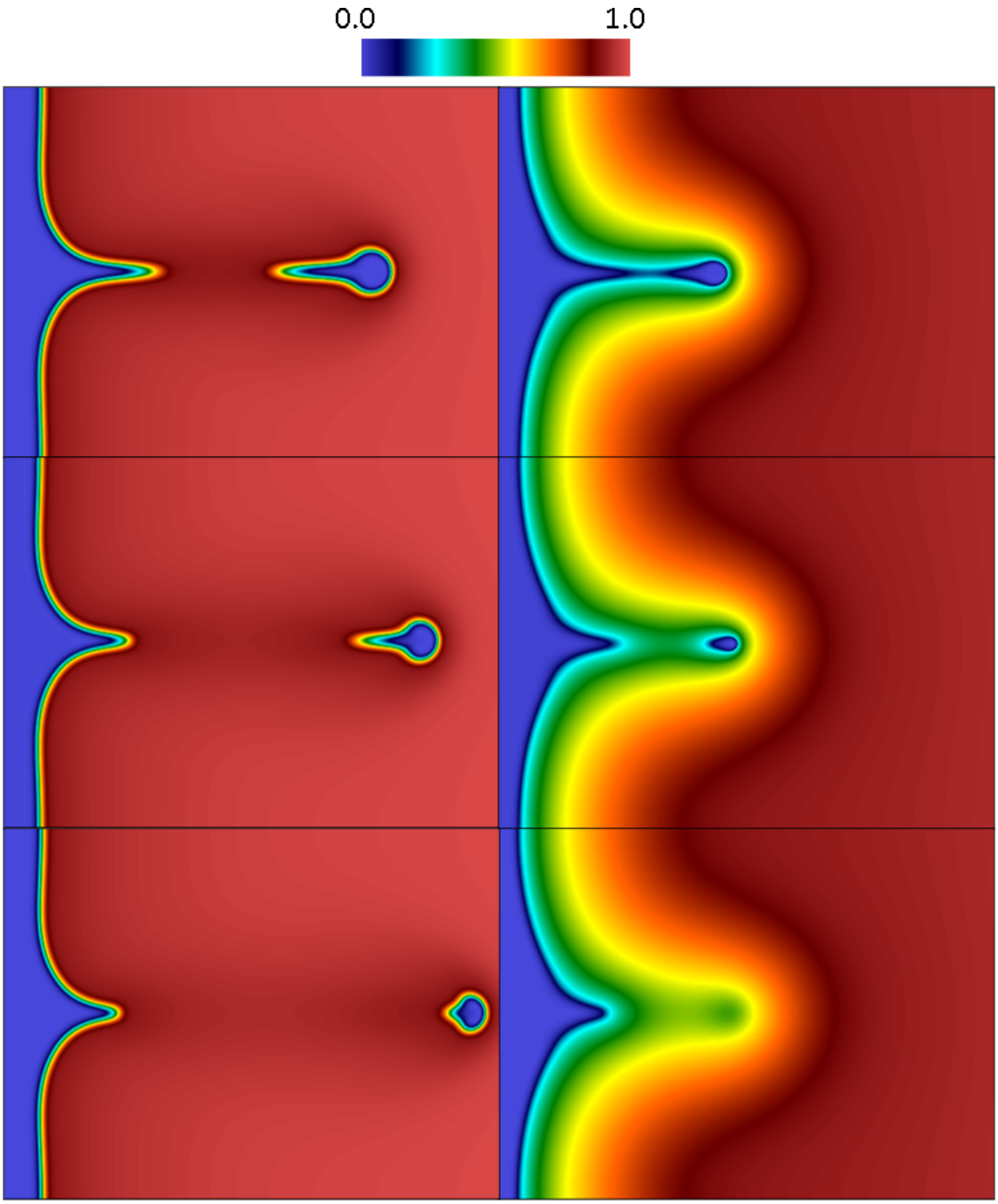

Fig. 5.7 Evolution of progress variable distribution through times $10.5 - 11.1$ (as marked on Figure 5.6 earlier) for DNS (left) and $\mathcal{F} = 20$ (right).

thickening are applied, the flame is spread over a larger area therefore the heat release *per unit volume* falls at each point. Of particular note is the conglomeration of points very close to the burnt state (i.e. > 0.9) that produce a significant amount of heat and also have a high frequency of occurrence. Such a large bias towards significant heat release from a close to burnt state is not found when compared to the structure of a corresponding DNS flame.

This is likely due to the continued accumulation of a secondary reaction zone (i.e. a region outside of the main flame zone defined in terms of progress variable, where the mixture is very close to the burnt state so reactions occur at a slower rate) from the start of the simulation which struggled to burn to completion earlier due to the large reduction of reaction rates here via thickening. In comparison the contribution to total heat release in a DNS context from this zone is much smaller, firstly due to the fact that the chemistry is not slowed as for ATF. Therefore areas close to the burnt state are faster in completely burning off, not only does this keep the size of the total secondary reaction zone smaller but the heat release is also spread out more evenly in time rather than taking time to manifest as is the case for $\mathcal{F} = 20$.

Figure 5.9 compares total heat release profiles for the original solution of $\mathcal{F} = 20$ to the same data-set but clipped in progress variable space for values greater than 0.9. Of course the peak is now lower since the clipping was done throughout the entire time horizon and is hence equivalent to removing part of the flame. More importantly however a qualitative difference is observed soon after the plateau where the heat release now falls much like the DNS solution rather than continuing to increase. Hence highlighting the importance of sustained and prolonged burn-off in secondary reaction zones when using multi-step chemistry at large values of thickening.

Despite a priori *theoretical* arguments for how ATF should be able to naturally accommodate the latter, most of the groundwork was laid using one step chemistry (Charlette et al., 2002; Colin et al., 2000; Légier et al., 2002) with many practical implementations also adopting similarly simplified chemical kinetics (De and Acharya, 2009; Hernández-Pérez et al., 2011; Strakey and Eggenspieler, 2010). Few studies (Emami et al., 2015; Straub et al., 2018) go beyond just one or two steps and incorporate detailed chemical schemes. With some recent works (Bénard et al., 2019; Maio et al., 2019) beginning to attribute over predictions in intermediate species to the thickening transformation.

The challenge arises from recognising that in the very non-linear region of a flame reaction thickness, curves for different reactions peak at different values in progress variable space and are usually inter-dependant. Therefore applying a broadband thickening at large values does not necessarily conserve the nature of this inter-dependence, and as a result could influence global system parameters such as net reaction rate/heat release.

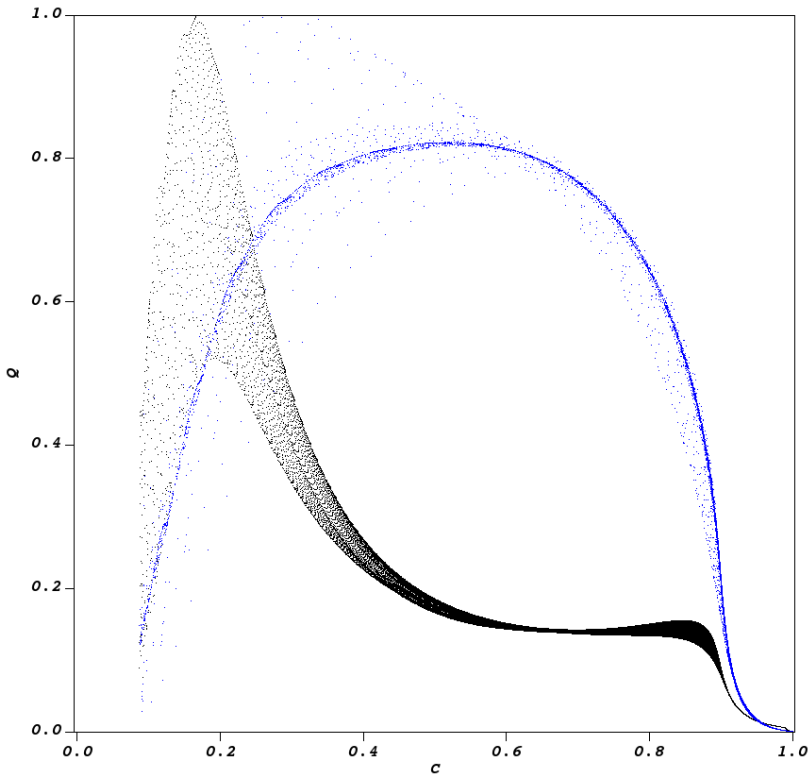

Fig. 5.8 Non-dimensional heat release rate conditioned on progress variable just after plateau region i.e. at time 10.8 shown on Figure 5.6 earlier.

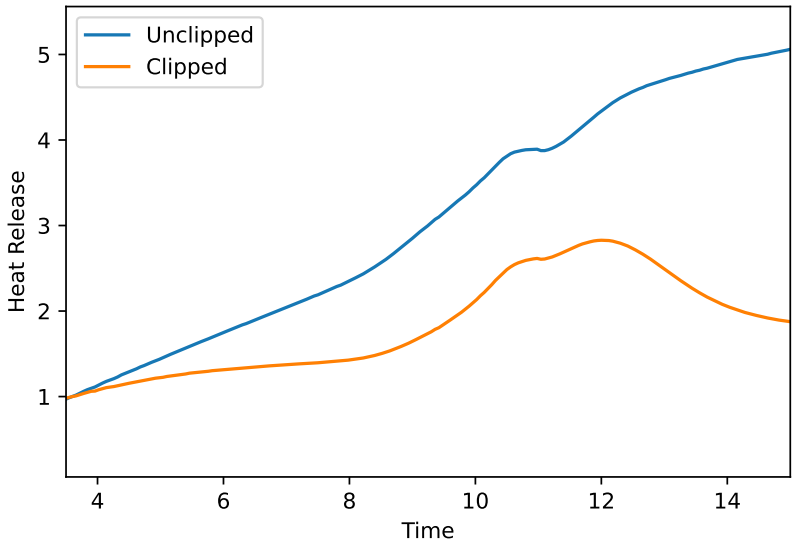

Fig. 5.9 Non-dimensional heat release rate against non-dimensional flame time. For original and clipped at progress variable < 0.9 solutions.

This is illustrated in Figure 5.10 where the net reaction rate for each species (excluding nitrogen which is effectively inert) in the system is compared between DNS and $\mathcal{F} = 15$. The peak consumption of H_2/O_2 can be seen to be lower for the thickened solution and this corroborates with the result in Figure 5.7 where due to the displacement brought about by the transformation a large degree of the entrained "fresh" mixture in the pocket is already partly reacted instead of pure premixed H_2/O_2. Despite this some of the trajectories for other short lived radicals overshoot while others undershoot when compared with DNS. Essentially the global balance which is highly inter-dependant is not preserved as thickening does not affect all reactions equally. For practical systems where the complex balance between endo/exo-thermic reactions can determine the nature of local heat release and possible even system stability this warrants caution. However that these effects seem to be significant only at very large thickening factors and the approach has already shown to be reasonably accurate across a significant range of practical interest.

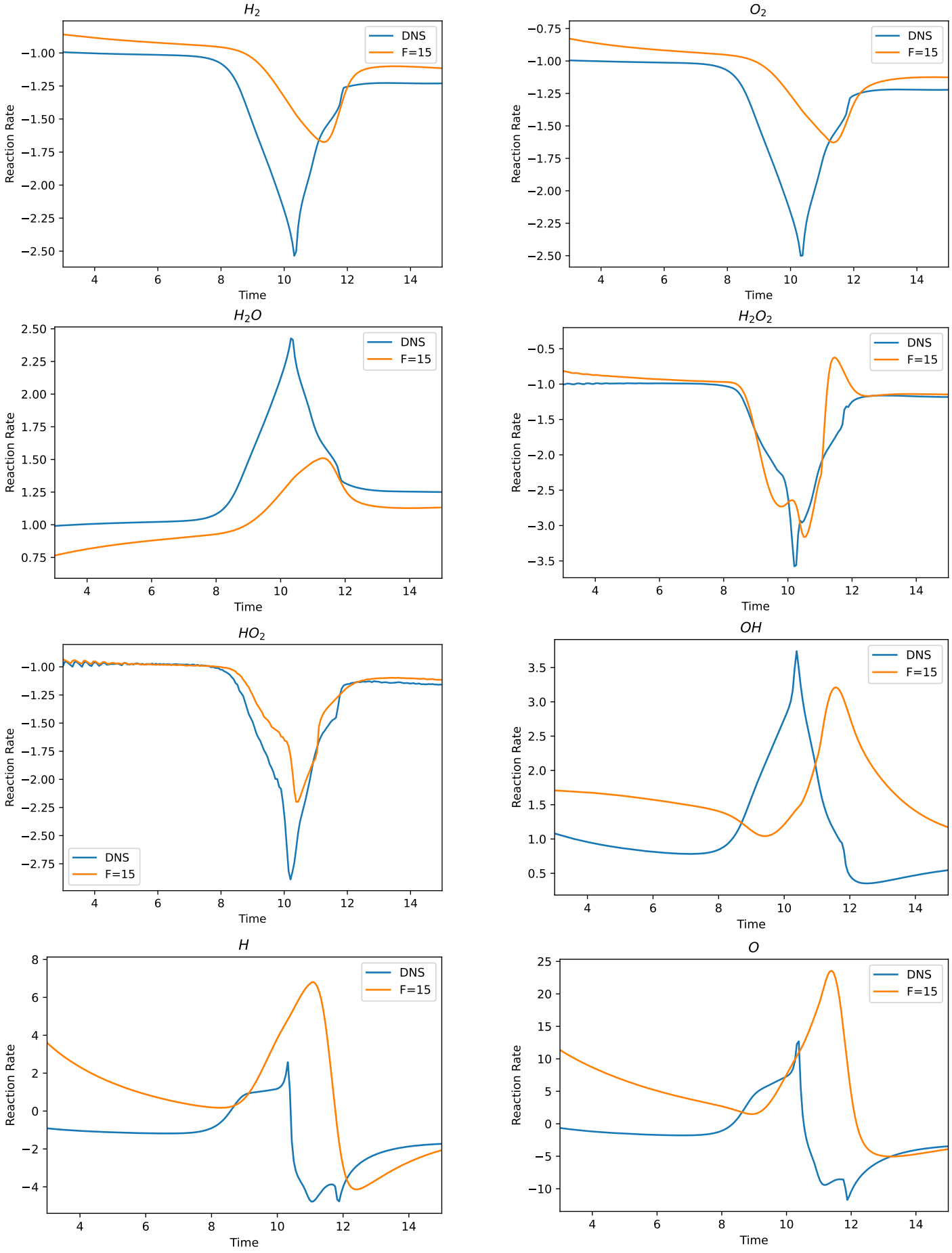

Fig. 5.10 Non-dimensional reaction rates for $\mathcal{F} = 15$ compared with DNS.

Figure 5.11 highlights the benefits of the novel sensor that was proposed as part of this work when compared to the implementation of Durand and Polifke (2007), hitherto referred to as the "classical" sensor. The peak heat release is captured well, suggestive of improved resolution of flame surface as well as potentially better conservation of complex chemistry effects. Meanwhile the classical sensor exhibits a small loss in peak heat release indicative of some detriment in capturing the finest scales.

This suggestion is further supported by Figure 5.13 which is a side by side comparison just before and after the moments of peak heat release for the two different sensor implementations. By dynamically limiting the transformation to the vicinity of significant heat release, the novel sensor exhibits better behaviour even in strain dominated regions such as the neck. While a modest improvement in the amount of entrained fresh mixture is also observed during pocket formation, coupled with a slightly better preservation of its shape particularly in the tail region post pinch-off.

The complimentary DNS snapshots are shown in Figure 5.14 which also includes the corresponding solution for CATF. Recall that classically, ATF transforms the species transport equations only, and as such for perfectly premixed flames does not require a sensor. The approach clearly under-performs when compared to the proposed modifications shown earlier in Figure 5.13. Not only does the neck form sooner, suggesting a potential sensitivity of the model in resolving strain dominated behaviour in regions of high stretch. The amount of entrained fresh mixture is also somewhat compromised while the finest structures (usually located in the trailing edge right after pocket formation) are seen to be lost. As a result the pocket exhibits burnout sooner while the proposed modifications help increase agreement with DNS.

Despite the reduced resolved wrinkling with CATF the net heat release is grossly over predicted as illustrated in Figure 5.12. Some contribution towards this is likely from the deformed pocket shape leading to faster albeit nonphysical in nature heat release. Moreover this is compounded with the consequences of broadband thickening unevenly affecting the reaction zone. Figure 5.15 illustrates how even if the global consumption of fuel and oxidiser are in relatively good agreement with DNS, the same cannot be said for all of the intermediate species. This shift in chemical dynamics is seen to occur at much lower values of the thickening factors for CATF than when compared with the proposed framework.

Coupling CATF with the novel sensor developed as part of this work to give CATF_s in Figure 5.11 shows a significant improvement albeit still resulting in slight overshoot. Meanwhile the novel sensor coupled with proposed modifications to ATF leads to an improvement prediction that not only is closer to the peak but also subsequently recovers faster afterwards too. Admittedly the benefits are not very large for this particular case as all scales

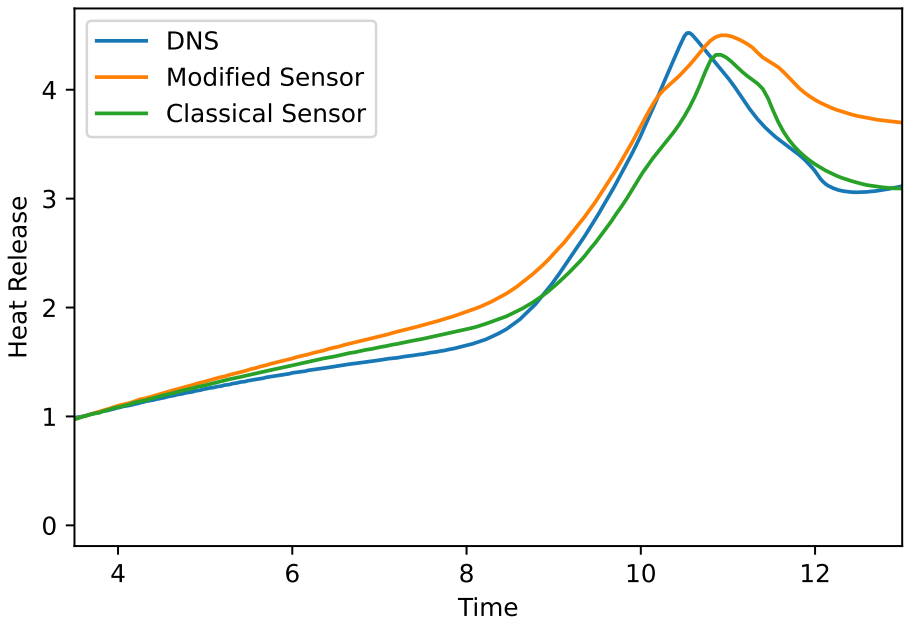

Fig. 5.11 Evolution of heat release for DNS and two sensor implementations coupled with $\mathcal{F} = 6$.

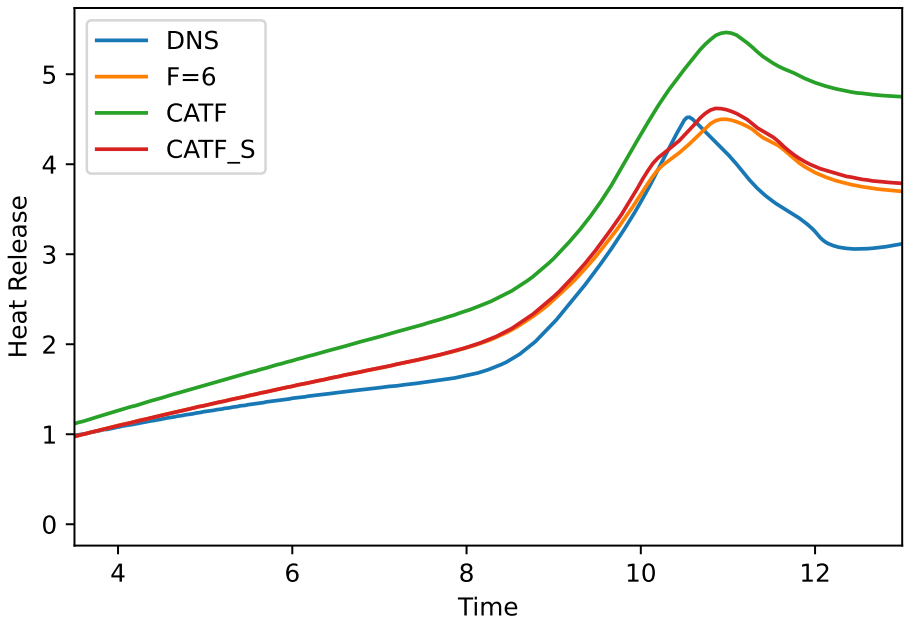

Fig. 5.12 Non-dimensional heat release against non-dimensional flame time for classical ATF (CATF), proposed modifications and DNS.

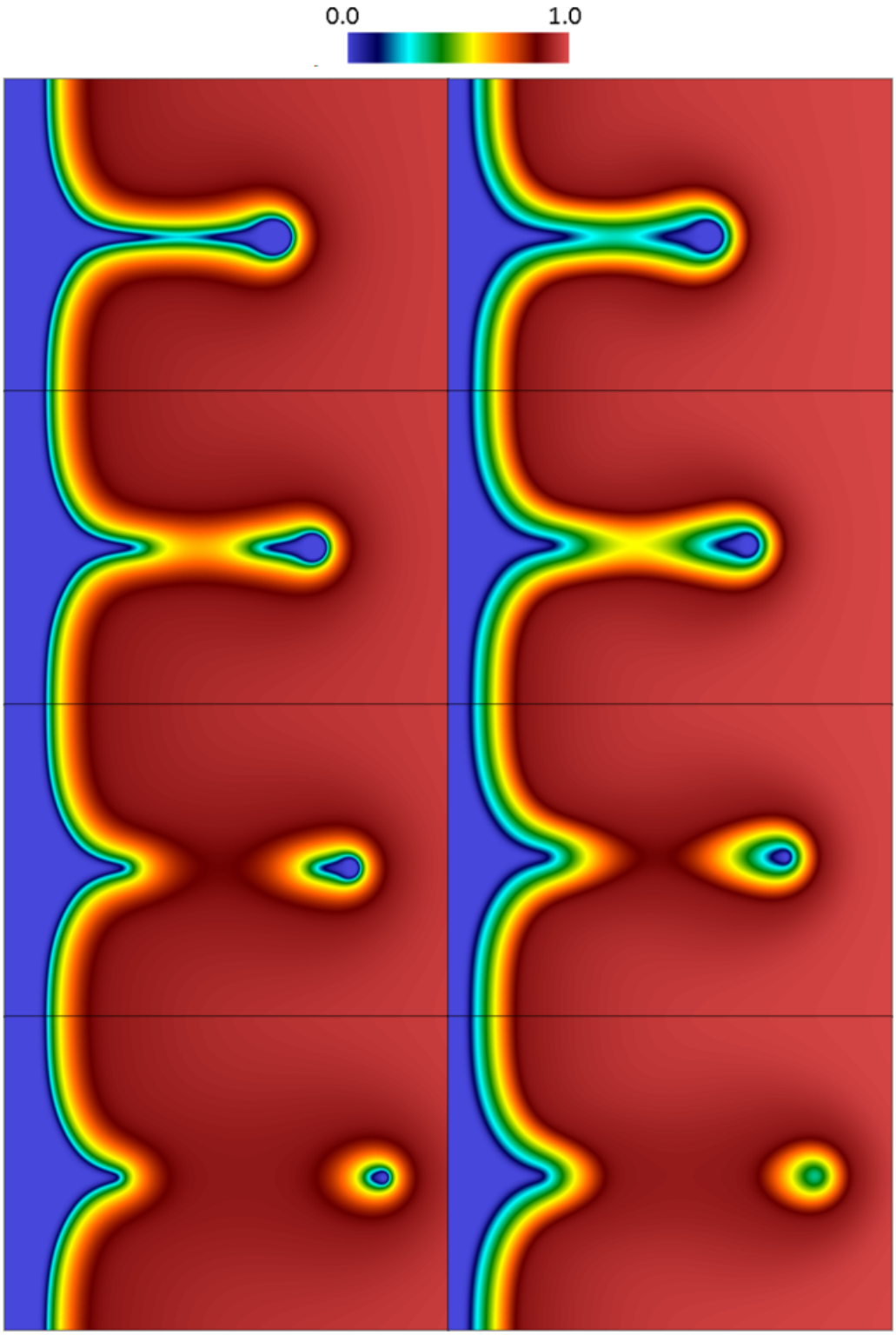

Fig. 5.13 Temporal evolution of flame structure displayed using progress variable, during pinch off for asymmetric (left) and symmetric (right) sensors in the modified ATF model with $\mathcal{F} = 6$.

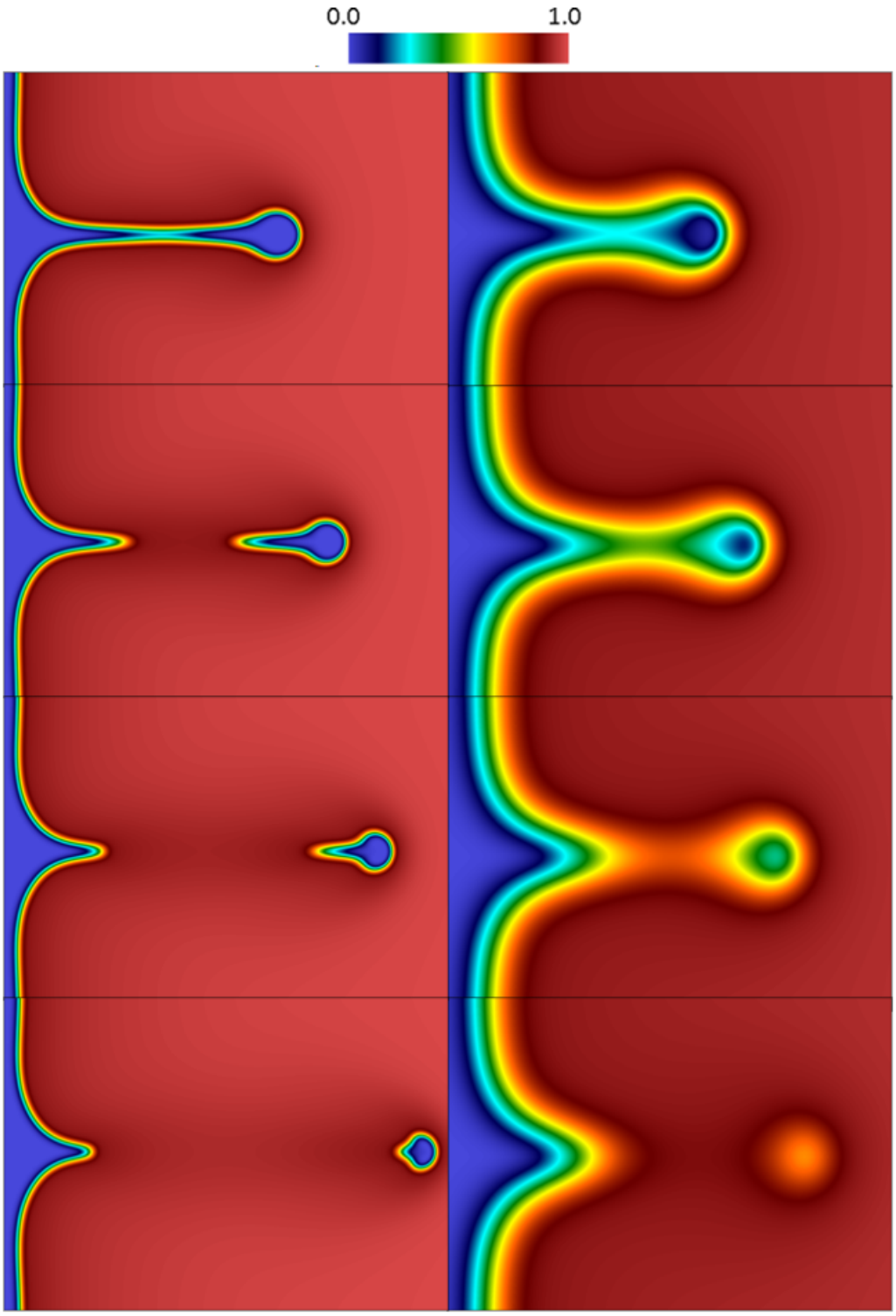

Fig. 5.14 Temporal evolution of flame structure displayed using progress variable, during pinch off for DNS (left) and CATF with $\mathcal{F} = 6$ (right).

were resolved on the mesh. Regardless a direct comparison is not entirely relevant since the main advantage of the modifications is to achieve reasonable accuracy *without* the use of an efficiency function.

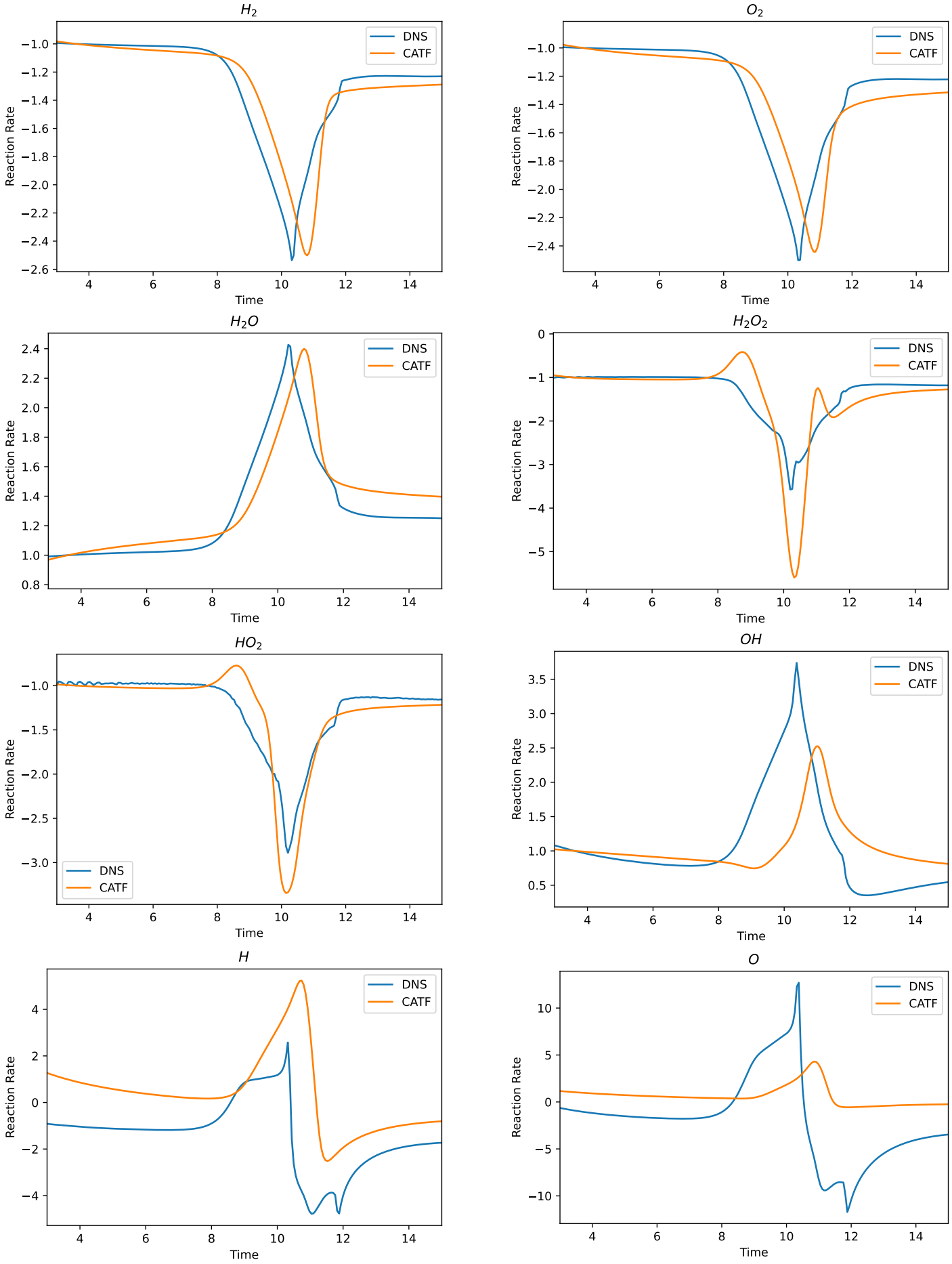

Fig. 5.15 Non-dimensional reaction rates for classical ATF with $\mathcal{F} = 6$ compared with DNS

5.1.4 Varying Vortex Induced Strain

Classically flamelet models assume that flame stretch can be evaluated from strain alone (Candel and Poinsot, 1990; Cant and Bray, 1989). Yet the theoretical strain rate for a particular eddy size does not necessarily correlate directly to the degree of induced flame stretch. For example Kolmogorov scales do not have the expected effect on flame surface despite having the highest strain rate. This is mainly due to their shorter lifetimes as implied by the equivalence between Kolmogorov and flame scales in their relation to viscosity by $\eta u'_k/\mu \approx \delta^0_f s^0_l/\mu \approx 1$ as detailed in Poinsot et al. (1991) for example. Which is to say that viscous dissipation is of similar importance at scales close to the flame or Kolmogorov scales and thus prevents the sustained interaction between a flame and very small eddies necessary for behaviour such as quenching.

Moreover even if large structures and their interaction with a flame front can be approximated as strain dominant, the same is not true for smaller scales where the incomplete conversion of strain into flame stretch provided much of the motivation for early efficiency functions. Aside from viscous dissipation, small vortexes can create very large curvatures locally which can resist the influences of strain by invoking thermodiffusive effects (Meneveau and Poinsot, 1991). Moreover this is compounded by geometric considerations where a small vortex can struggle to stretch a thick flame surface (Peters, 1988).

In summary there is a complex interplay between competing mechanisms, resulting in stretch being a function of both strain and curvature with a clear hierarchy of importance not always evident for small scales. The initial vortex size being considered is already geometrically challenging as the flame is *thick* in comparison. This is now complemented with progressively decreasing the vortex intensity in accordance with Table 5.1.

Note that *a priori*, from a theoretical perspective the nature of interaction should be preserved in the proposed framework as illustrated by the three representative dimensionless numbers (Poinsot et al., 1991) corresponding to a particular length scale (r) :

- $Vr(r) = u'(r)/s^0_l$ is the ratio of turbulent velocity fluctuation to laminar flame speed and must be greater than unity as a necessary condition for strong interaction (e.g. pocket formation). As velocities are unchanged this ratio is preserved for both classical and the proposed ATF formulations.

- $Ka(r) = (u'(r)/r)/(s^0_l/\delta^0_f)$ is the scale specific Karlovitz number. Revisiting classical combustion diagrams it can be observed that a necessary condition of $Ka(r) > 1$ is required for localised quenching, essentially separating flamelet and distributed reaction zones. Classical ATF does not preserve this as only the characteristic flame length scale is enlarged. However the proposed modification transforms all scales by

the thickening factor, in theory preserving the structure specific Karlovitz and better reproducing quenching. This will be illustrated shortly.

- $P(r) = (r^2 s_l^0)/(\nu \delta_f^0) \approx (r/\delta_f^0)$ is a measure of the so called "power" of the vortex. As the ratio between lifetime of the vortex (r^2/ν) to chemical time (δ_f^0/s_l^0)) this can be intuitively interpreted as a measure of penetration length into the flame front with respect to its thickness. In absolute terms the vortex lifetime is not exactly the same as everything is solved in *thickened* time, however the critical ratio defining $P(r)$ is conserved by scaling both characteristic times equally by the thickening factor.

Note that under these simplified approximations the "power" of the vortex is not a function of its turbulent velocity and only depends on a ratio of length scales. However there is strong reason to investigate Vortex B and C (i.e. vortices of weaker strength but same size) as the significance of vortex induced hydrodynamic effects in the flow field is evident by the Karlovitz and velocity ratio numbers.

Figure 5.16 displays net heat release transient profiles for the proposed methodology ($\mathcal{F} = 6$) and the corresponding solution with a thickening factor of 6 in the context of classical ATF (CATF) for Vortex B. The latter is also coupled with the novel sensor to give CATF_s and an unthickened DNS solution is included for comparison.

Trends are largely similar to before with CATF over-predicting heat release and significant improvement observed upon coupling with the modified flame sensor. The proposed modifications once again leads to the best agreement, while the relative improvement when compared to CATF_s is also greater than the improvement observed for Vortex A.

Figure 5.17 shows the heat release rate for Vortex C for the same implementations of ATF as above. It can be seen that using net heat release rate as a marker for performance is becoming increasingly questionable, likely due to the effects of multiple step chemistry. The latter is more significant now due to the weaker vortex requiring much longer to convect downstream and impact on the flame. The longer time horizon allows for secondary reactions zones to interfere with expected behaviour, yet some meaningful conclusions can still be extracted. The slope post-peak for CATF fails to decrease at the rate that would be indicative of flame recovery following vortex induced wrinkling, suggesting a much larger portion of the increase is due to other sources. Meanwhile the modified approach once again has the best alignment with DNS in terms of peak heat release rate and still shows reasonable recovery afterwards. However these inferences warrant further supporting evidence at this stage and will be supplemented by flame surface contours next.

Figure 5.18 displays the progress variable iso-contours during interaction for Vortex B. CATF is observed to skew chemistry to the extent that the mean flame position is slightly

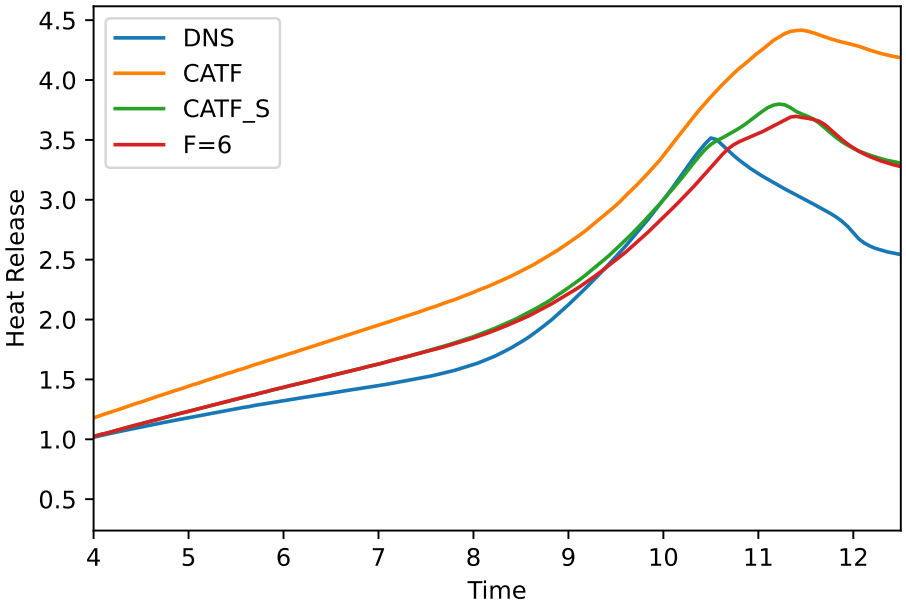

Fig. 5.16 Non-dimensional heat release and flame time for Vortex B.

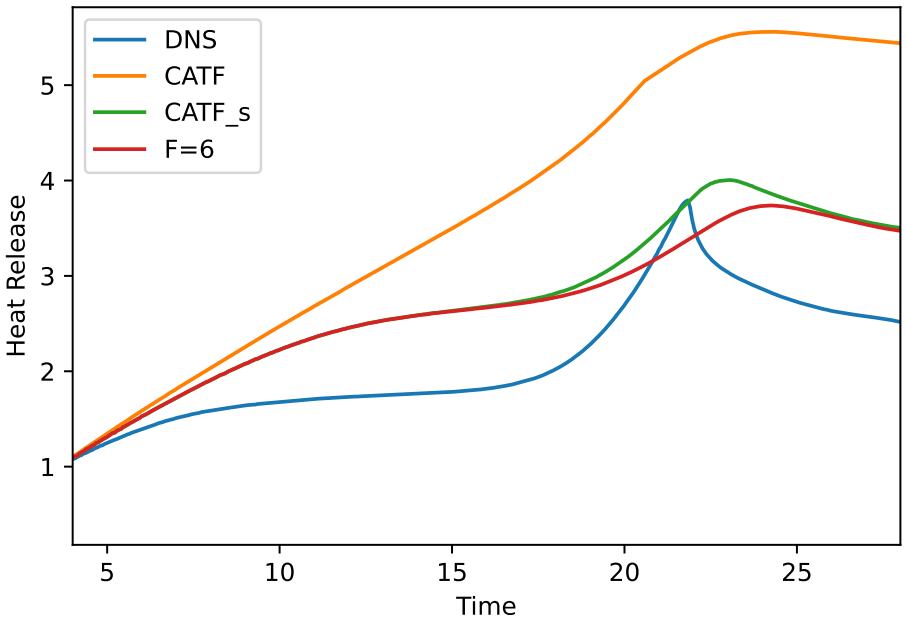

Fig. 5.17 Non-dimensional heat release and flame time for Vortex C.

offset near the start of the interaction. However both ATF solutions follow DNS with relatively decent agreement throughout the necking phase despite considerable thickening. A qualitative difference manifests itself in the final stages, where the DNS and proposed ATF model both result in localised quenching leading to pocket formation but CATF fails to do so. Although there is a pocket of fresh gases thrust into the product mixture side, its boundaries are not under enough stretch to locally extinguish burning. Hence it remains attached to the remainder of the base flame while burning out and the vortex fails to penetrate as deeply into the reactive zone. Meanwhile the modified model continues to resolve complex phenomena such as quenching with reasonable accuracy even for weaker structures.

A further reduction in strength leads to the solution of Vortex C as shown in Figure 5.19, where the structure is now too weak to induce quenching. A pocket is no longer formed with localised wrinkling leading to entertainment of fresh mixture in the vortex trail instead. The proposed model follows DNS relatively well in the early stages however does not quite manage to capture the finer details of the entrained profile. Note that the flame elements on either side of the entertainment zone are separated by a distance very close to the laminar flame thickness in the case of DNS (see Row 3). Features at this scale have already been described as difficult to preserve via a thickening transformation so some discrepancy is expected. Moreover a thickening factor of 6 induces a noticeable time lag as observed by how in the final row the DNS solution is already receding as the vortex wake disappears while the thickened solutions are still advancing. The flame response is inherently unsteady and depends on the transient variations of stretch coinciding with the vortex state at that particular times. As such some differences between specific instantaneous states identified during very fast and non-steady processes are not surprising. More importantly, behaviour of the flame front is seen to be significantly better when compared with CATF. Thus showing potential advantages of the approach even for very weak structures that traditionally would require efficiency corrections.

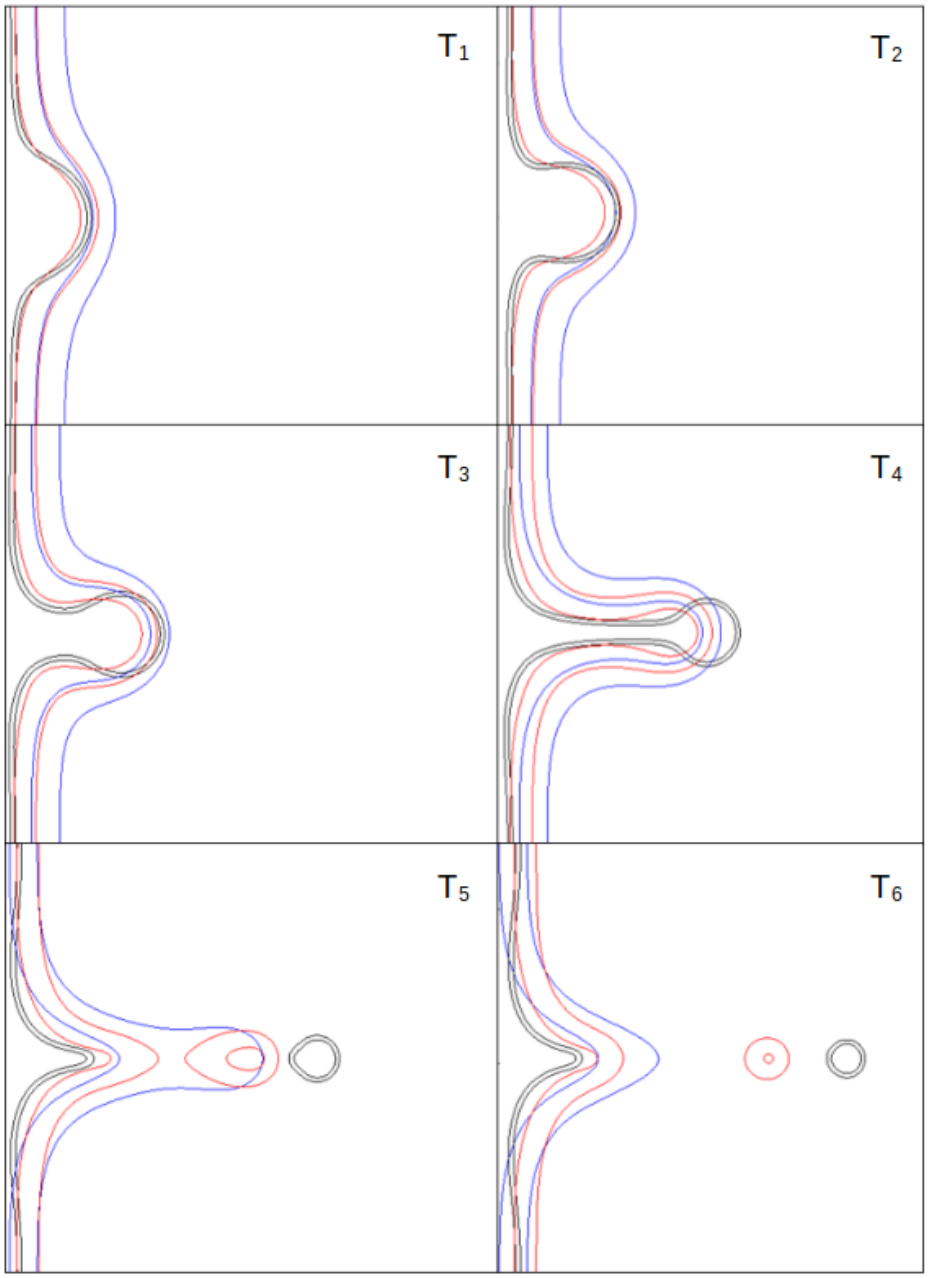

Fig. 5.18 Progress variable iso-contours ($0.1 - 0.9$) for Vortex B, shown for DNS (black) and CATF (blue)/MATF(red) with a thickening factor of 6.

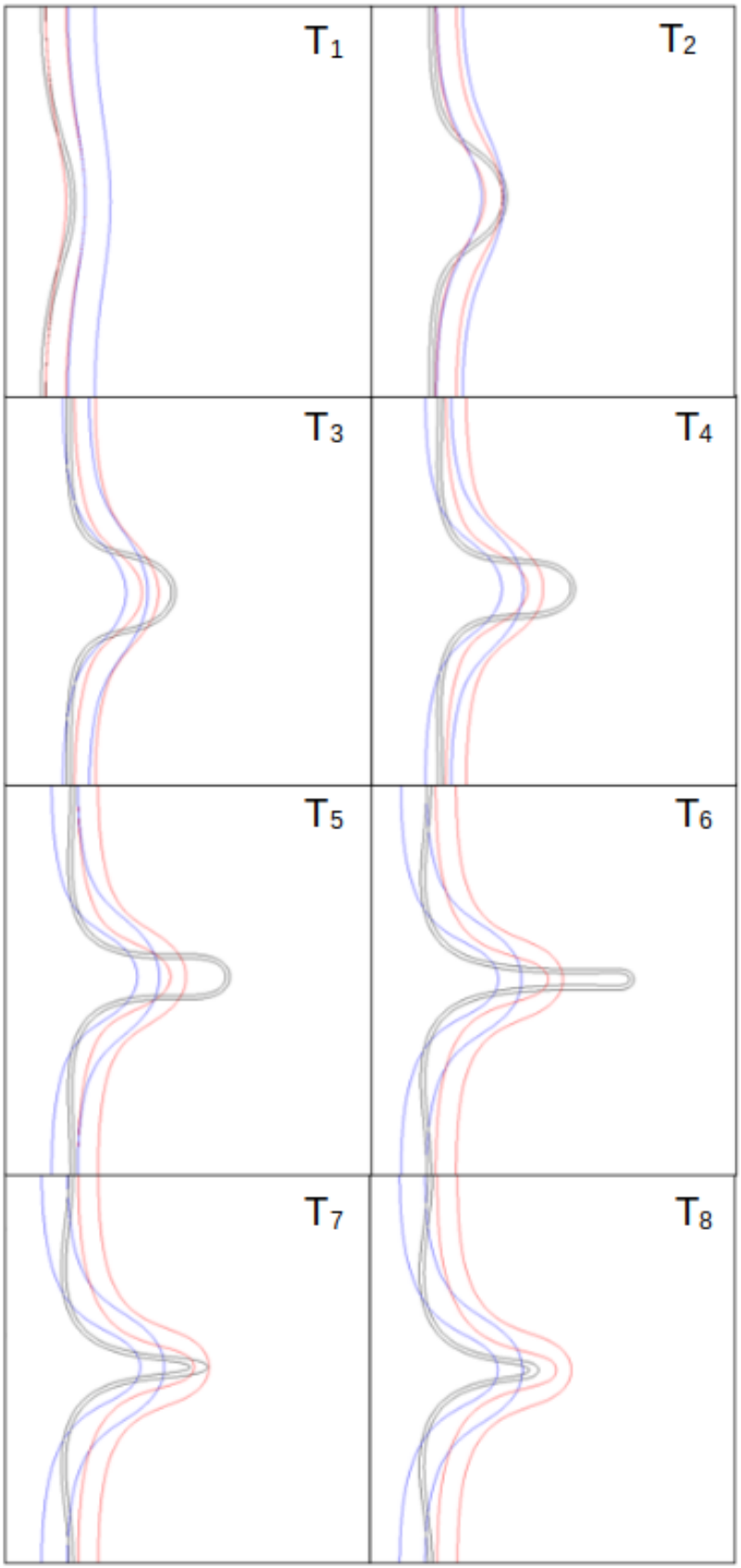

Fig. 5.19 Progress variable iso-contours ($0.1 - 0.9$) for Vortex C, shown for DNS (black) and CATF (blue)/MATF(red) with a thickening factor of 6.

5.2 Acoustically Forced Flames

Flame response to acoustic waves is one of the most prevalent fields of uncertainty in premixed combustors (Candel et al., 2009). With much of the difficulty stemming from lacking a comprehensive understanding of either flame dynamics (Driscoll, 2008) or the underlying physics for thermoacoustic instabilities themselves(Candel et al., 2009; Zhao et al., 2014). The latter is complicated mostly by the interaction between sound and flame(Karimi et al., 2008, 2010) but also system boundaries (Hield and Brear, 2008; Hield et al., 2009).

Laminar flames have been studied extensively in an endeavour to uncover fundamental physics of importance, using a wide variety of methods ranging from numerical (Talei et al., 2011, 2013) to theoretical (Talei et al., 2012) and experimental (Karimi et al., 2009). Despite their apparent simplicity, much of the resultant physical insight has significant carry over and applicability to more complex turbulent flames (Karimi, 2014; Shin and Lieuwen, 2013).

In this large and varied body of work, significant effort has been dedicated to the classical, conical Bunsen flame (Birbaud et al., 2006; Bourehla and Baillot, 1998; Kartheekeyan and Chakravarthy, 2006; Schlimpert et al., 2016), even in the context of acoustic modulation as a means to improve heat transfer (Zhen et al., 2022). General system dynamics in such simplified configurations are relatively well understood.

In summary there is a threshold frequency which may vary slightly for a particular burner, but above which the acoustic wavelength is too small to induce perturbations in the flame front (Bourehla and Baillot, 1998). Below this the flame response to acoustic perturbations is dominated by a convective wave. Acoustic excitation of the convectively unstable shear layer leads to velocity perturbations that distort the flame surface as they travel downstream (Kashinath et al., 2013). This causes flame area fluctuations and associated heat release rate oscillations as well.

There is a strong coupling between the flame response and nature of acoustic perturbation. Flame wrinkling for example can be either symmetric or asymmetric about the center-line, yet the latter is usually reserved for higher frequencies (Bourehla and Baillot, 1998; Zhen et al., 2022). Furthermore despite a wealth of studies (Wee et al., 2002; Wu et al., 1991) on receptivity of shear layers to acoustic forcing, formally parameterizing the perturbation convection speed remains a matter of contention. It is often assumed to be equal to the mean flow (Cuquel et al., 2011, 2013) but can vary depending on parameters such as the excitation frequency (Baillot et al., 1992; Kashinath et al., 2013) and be a driving source of non-linearity in the system (Preetham et al., 2008).

In a real system undergoing combustion instability multiple frequencies are expected to coexist simultaneously. Whether it be the different acoustic modes of the system (Morgans and Dowling, 2007), hydrodynamic instabilities (Balusamy et al., 2015; Li and Juniper, 2013)

or turbulence fluctuations there can be significant transfer of energy and interaction between frequencies making the overall system very nonlinear (Balusamy et al., 2015; Bellows et al., 2008), leading to some authors looking into forcing at multiple frequencies Balachandran et al. (2005); Ćosić et al. (2012); Han et al. (2016). Yet much of the work to date operates within the linear limit , where the flame response to multiple different frequencies is assumed to be equivalent to the sum of the response at each of those frequencies. Correspondingly most studies on flame dynamics only consider the response to a single forcing frequency and this paradigm is retained here.

Despite these simplifications, an acoustically forced conical Bunsen flame retains significant value both in literature and for the validation purposes used here. Firstly, the periodic nature of the system paves the way for a better understanding of time delays discussed earlier for the proposed ATF model. Where good performance can extend the potential range of applicability to a much wider class of quasi-steady problem configurations. Furthermore Durox et al. (2005, 2009) from their studies spanning various laminar premixed flame configurations, point out the crucial importance of accurately capturing the oscillating flow field (including motion in the shear layer) in order to reproduce reasonable flame response. Therefore testing the model across a much wider blend of facets which include disturbance formation but also convection through an active shear layer in order to potentially extend application to advection dominated flows.

5.2.1 Computational Setup

Figure 5.20 illustrates the employed configuration where a 22mm exit diameter burner issues perfectly premixed methane-air mixture at an equivalence ratio of 1.05, corresponding to a laminar burning velocity of 0.39ms^{-1}. The inlet flow velocity is harmonically modulated in accordance with Equation 5.1. Where the mean inflow velocity ($\overline{v}$) is taken to be 0.97ms^{-1}, the inflow RMS (v') set to 0.19ms^{-1} at a frequency (f) of 62.5Hz.

$$v = \overline{v} + 2^{1/2} v' sin(2\pi f t) \tag{5.1}$$

This collection of parameters is essentially a 2D simplification of the experiments by Ducruix et al. (2000); Schuller et al. (2002a). From the latter it has been established that the flame response remains symmetric at this frequency, allowing for only half the domain to be resolved in conjunction with symmetry boundary conditions along the center-line as shown in Figure 5.21. Furthermore this case was also chosen as the objective for a recent numerical study (Auzillon et al., 2011) that compared the effectiveness of different LES models in

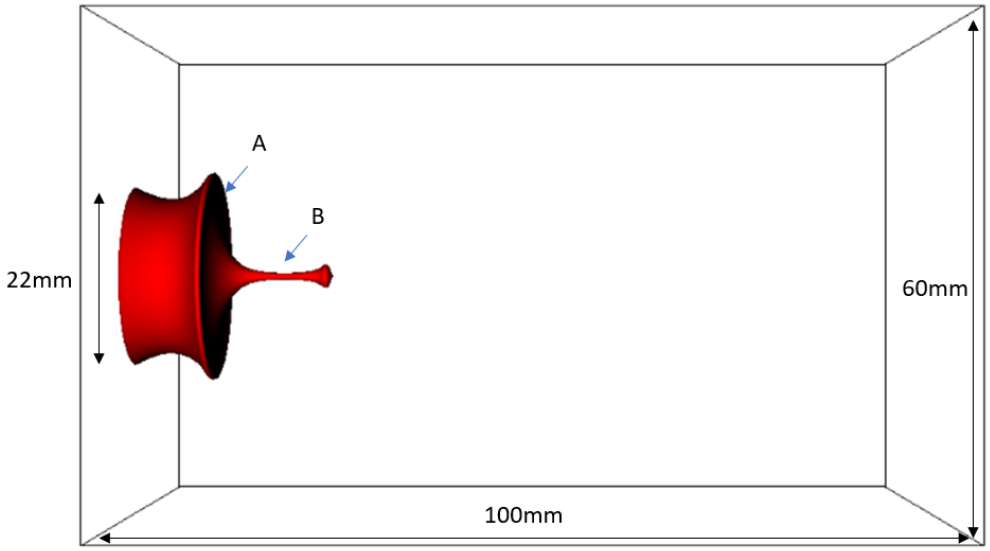

Fig. 5.20 General domain configuration with revolved flame solution showing cusping (A) and necking prior to pocket pinch off (B) during acoustic cycle.

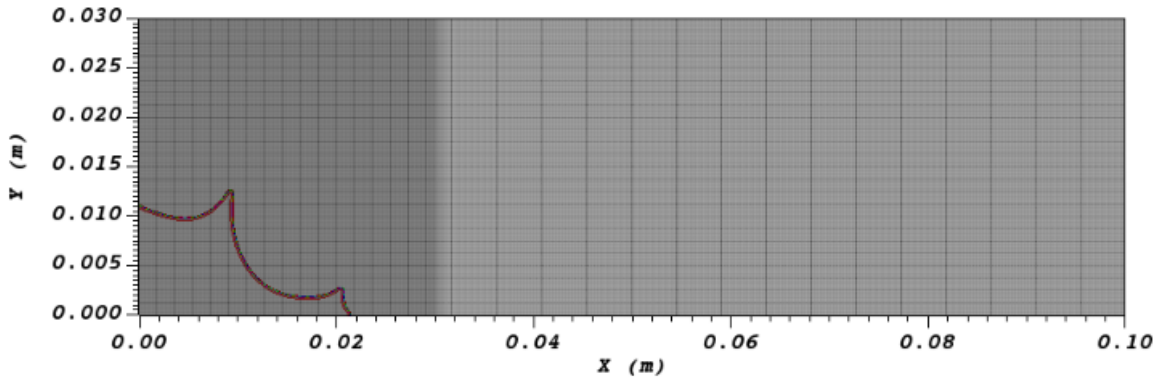

Fig. 5.21 Computational domain for simulated flame. Grid remains uniform in the near field prior to progressive stretching downstream towards the outlet

Table 5.2 Mesh resolution in near field of acoustically modulated flame simulations.

Description	$\approx \delta_f^0/\Delta$	$\approx \hat{\delta}_f^0/\Delta$	Total Points ($\times 10^6$)
Fine	8	30	4.3
Coarse	3	10	1.8

capturing flame response. Among which was the classic ATF model which was shown to perform poorly even at relatively low thickening factors, making it ideal for comparison.

The objective of this case is to evaluate the effects of thickening on flame front dynamics and structure under the influence of acoustic loading. So in order to limit undue uncertainties arising from SGS closures this is carried out in an environment where the flame is not wrinkled at the subgrid level i.e. all flow motions are fully resolved but the internal flame structure is not. Auzillon et al. (2011) similarly assume all SGS flow motions are resolved by the mesh in a bid to isolate effects of the thickening transformation itself.

Simulations were run for at least five forcing cycles after initial transients had passed, before data was sampled. This was done on two separate meshes, a finer mesh that was considered equivalent to DNS in order to isolate the effects of thickening only, and a coarser one to highlight the potential benefits of the proposed model. Relevant parameters in terms of points within the flame thickness for a thickening factor of 4 are presented in Table 5.2 where grid stretching was used to obtain the desired resolution. Note that validation studies with equivalent resolution and no stretching were also done to ensure that the customised stretching did not compromise the order of the numerical scheme or introduce any undue errors into the domain by being too sharp.

5.2.2 Results

Figure 5.22 contrasts instantaneous flame shapes assumed throughout a single acoustic cycle for four different simulations. Namely DNS, the modified ATF approach (MATF) on two different meshes in accordance with Table 5.2 and no-model (NM) run on the course mesh which is representative of poorly resolved DNS. Most notable perhaps is the observation that MATF simulations exhibit strikingly similar behaviour at all times despite the differing mesh resolutions. This suggests a significant advantage in obtaining grid independent solutions much earlier than DNS, as evident by the discrepancies in NM.

All cases are seen to feature disturbance formation at the base which then moves downstream along the flame front in the form of a convected wave, prior to tip instability. NM is seen to exhibit significant deviation from DNS even at the very start, as a consequence of delayed recovery from pinch off during the previous acoustic cycle. Meanwhile MATF shows relatively good agreement at the beginning, suggesting that even if there are some instantaneous differences due to temporal thickening, the overall periodic state of the system is preserved. This demonstrating that the approach can be applied to a wide range of quasi-steady systems with reasonable temporal accuracy. Of course there is likely a situation-dependant cutoff frequency beyond which the thickened flame cannot keep up with

high speed transients. However investigating the latter is not the goal here and left for future endeavours.

Row 2 of Figure 5.22 displays moments just before neck formation as the disturbance rolls up the flame sheet near the tip, causing breakaway pockets of fresh mixture. Note how the next disturbance which has only convected about a third of the way up the flame still remains relatively in phase for all simulations. The fact that this upstream conical roll up of the flame is still in phase even for Case NM but the downstream state is not, suggests the main driving force behind this disparity is failure to capture non-linearity of tip dynamics due to poor grid resolution. Meanwhile MATF closely follows the DNS solution even if some of the tiniest scales are slightly distorted.

Row 3 shows recovery from pinch off for DNS and MATF and demonstrates how the more dominant kinematic restoration effects negate small transient delays that arise during necking, as both solutions come close to realigning. NM however exhibits impaired tip behaviour both in terms of time but also in the size of pocket formation which is significantly smaller.

Moreover MATF has been shown to provide large gains in accuracy when run on meshes too coarse to resolve internal flame structure even for the case of time dependant dynamics. The method reliably reproduced not just formation but also convection of a disturbed flame front through an active shear layer, suggesting good preservation of not just flame dynamics but also the interplay with local hydrodynamics. Thus extending the potential application of the approach to a wider class of advection dominated flows.

A brief comparison with CATF at the same thickening factor of 4 is also included in Figure 5.23. Where it is observed that much of the finer details of the unsteady flame dynamics are lost, particularly near the tip region. The overall response is relatively close to switching from a well defined convective mode where a disturbance progressively rolls up the entire length of the flame front to the more global, bulk oscillation mode as described in Auzillon et al. (2011). Flame shape in vicinity of the tip is not only flatter but also exhibits significant displacement, likely due to an inability of the classically thickened flame to fold in on itself or wrinkle in response to the same hydrodynamic driving force.

The breakout frame zooms in on a region upstream of the tip zone to highlight that even prior to the tip, CATF based flame wrinkling is impaired with the sharp folds observed in DNS - and even MATF - smoothed out in breadth and reduced in depth. Further deteriorating upon convection up the shear layer, the folds are unable to influence the flame tip in the same way resulting in the obvious displacement but also wider and flatter flame pattern. Thus discrepancies are likely not a result of just localised non-linearity, but of the aggregate sum between the latter, impaired disturbance formation and associated wrinkling as well

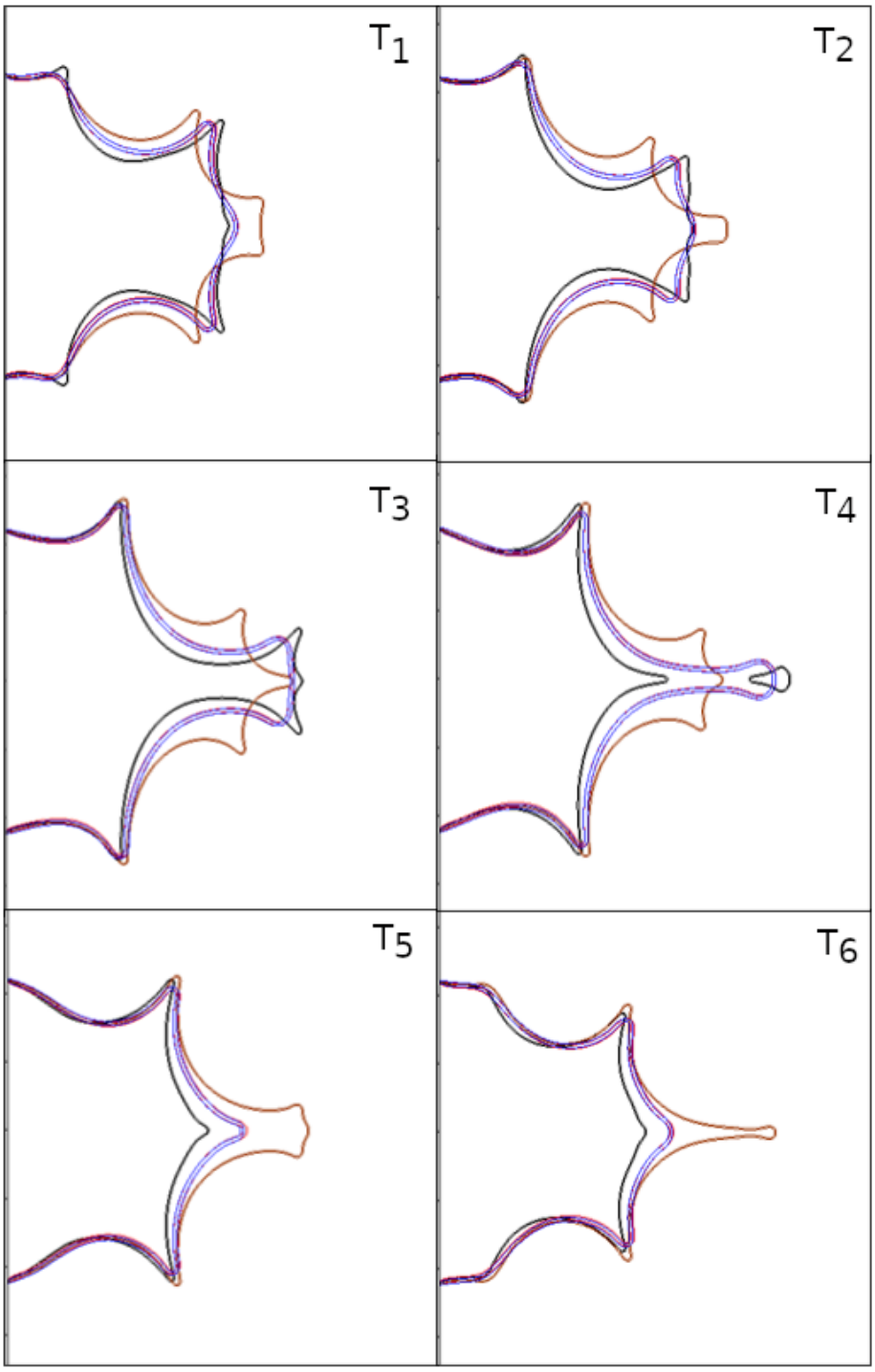

Fig. 5.22 Instantaneous flame positions during one entire acoustic forcing cycle. DNS (black), MATF on a fine mesh (blue), MATF on a course mesh (red) and NM on a course mesh (brown) are superposed.

convection downstream. Overall the DNS and CATF results show very similar behaviour to Auzillon et al. (2011) as expected, with significant improvement in flame patters observed upon the use of the proposed modifications.

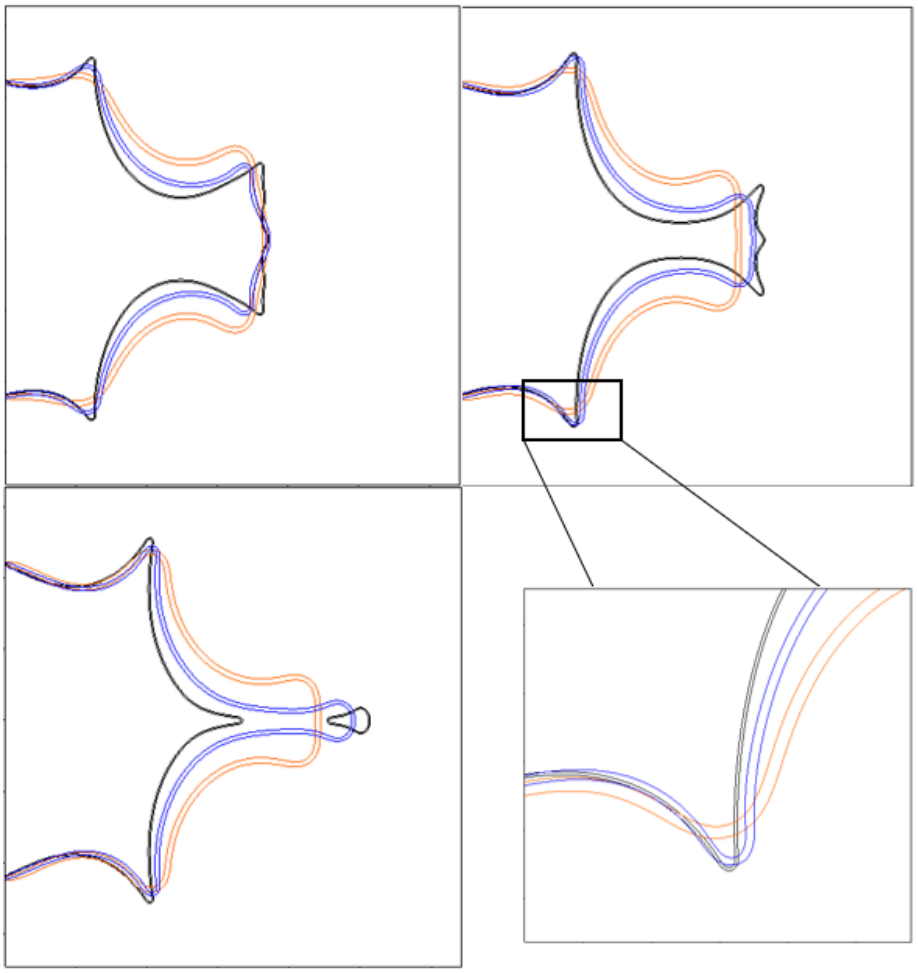

Fig. 5.23 Flame shapes during acoustic cycle. Comparison between DNS (black), MATF (blue) and CATF (Orange).

Note that for the following selection of results, other than DNS only simulations run on the coarse mesh are shown for each modelling approach. With this in mind Figure 5.24 plots the total heat release normalised by the mean, against time normalised by the acoustic period after initial transients have already faded. MATF shows excellent agreement with the peaks across most of the cycles and temporal thickening does not seem to have influenced period structure noticeably. This is a promising and also vital point for application towards thermoacoustic instabilities where arbitrary phase shifts can impact global system

behaviour. There is are still some cycle-to-cycle variation observed even in the DNS but the net differences are small and expected to mostly die out over time.

Meanwhile the no model approach clearly fails to reproduce expected behaviour and undershoots peak heat release. The latter in a context with no subgrid wrinkling and simplified chemistry scheme is indicative of a reduction in resolved flame surface. Much of this is due to to an inability to resolve the internal flame structure on a coarse grid, particularly as the surface folds in on itself due to the hydrodynamic forces. The shape of the peak is also compromised with a noticeable reduction in slope to the extent of almost approaching a plateau. As this occurs just prior to moments of maximum heat release, in light of the behaviours seen in the previous section, this is likely because of impaired pinch off at the tip which was alluded to in Figure 5.22 earlier as well. The phenomena is seen to persist across acoustic cycles and highlights how using the proposed MATF model on the same grid brings about a qualitative change in improving accuracy. Moreover tip dynamics are compromised in the NM approach to the extent that lag between periods when compared to DNS is seen to increase slightly between cycles as time goes on. Demonstrating how important it is to have a grasp of internal flame structure in order to reliably reproduce the steady periodic state.

Similarly Figure 5.25 illustrates the same evolution for classical ATF instead of the no model approach. Although performing better than the latter, CATF still performs poorer than MATF as evident by over shooting of the troughs, likely due to obstructed surface annihilation as the wrinkled folds coalesce at the tip. In general the peaks for MATF are in better agreement with DNS in terms of magnitude. More noticeable is that CATF exhibits obvious changes in the slope close to the peak. Although not as pronounced as with NM there is a stark reduction in slope observed prior to max heat release, likely stemming from impaired pocket formation while MATF manages to better retain a more pronounced and sharp transition. Furthermore the latter also shows improvements in temporal behaviour by maintaining a reasonably accurate period cycle while classical ATF seems to lag behind and have a slightly longer period duration.

By perturbing the flame front, acoustic excitation will also influence the nearby flow field. Particularly in the vicinity of the flame sheet the flow field will have a strong relation to positioning and depth of flame folds due to the focusing or defocusing of thermal expansion. Figures 5.26-5.28 illustrate velocity vector maps superposed onto contours identifying the flame position across an acoustic cycle for DNS, MATF and CATF respectively. The thickened flames both exhibit slightly lower velocity magnitudes overall. As by *thickening* the heat release across the reaction it is spread over a larger area which reduces dilatation induced by thermal expansion. Unfortunately this is an unavoidable drawback inherent to any thickening method, but the practical impact is marginal and observable here only due to

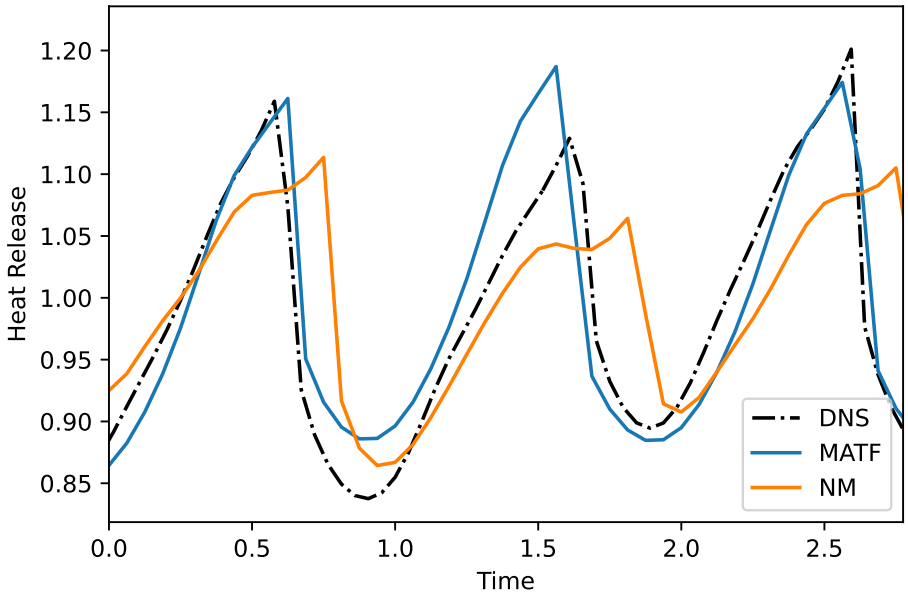

Fig. 5.24 Integrated heat release in the domain during acoustic forcing. Comparison between modified ATF (MATF) and no model (NM).

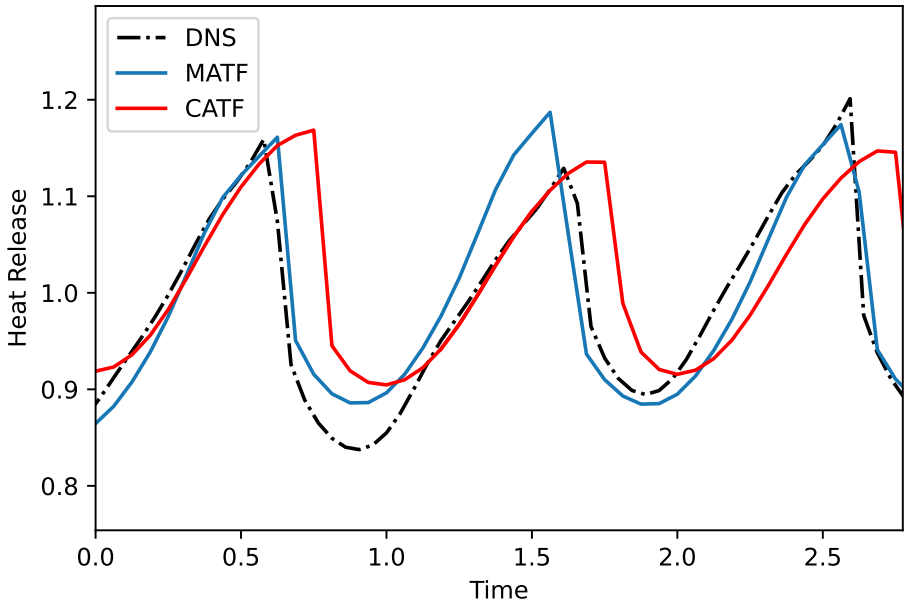

Fig. 5.25 Integrated heat release in the domain during acoustic forcing. Comparison between modified ATF (MATF) and classical ATF (CATF).

the fine scale being applied. In many practical configurations flow behaviour is dominated by other effects such as surrounding turbulence, so the net detriment from slightly impaired thermal flow expansion is likely negligible. The following discussion on Figures 5.26-5.28 considers a decomposition of the domain into three parts; the base where the flame anchors at the inlet, the flame front region where disturbances convect up the shear layer and the tip region.

The anchor points near the base are where hydrodynamic disturbances first take form in the reaction layer and is a region suggested to be dominated by viscous and baroclinic effects (Blanchard et al., 2015). So it is reassuring that the proposed approach preserves these interactions and reproduces relatively accurate disturbances in this zone as suggested by similarities in both flow and flame fields. Although these disturbances are somewhat impaired in CATF it is difficult at this point to separate how much of that is due the formation and convection stages respectively.

In the flame front zone it is observed that radial gradients in particular are strongly tied to the progressive rolling up of the flame sheet and shadow its convection up the shear layer. The sharper and more pronounced wrinkles produced by MATF show an improvement over CATF in approximating the higher velocities seen in DNS by better focusing thermal expansion effects. Yang et al. (2021) used DMD to show dilatation counteracts the convection in the direction normal to flame front, causing confinement of a thin vorticity sheet close to the flame front. Interpreting the movement of disturbances up the flame as convection of localised vorticity which the modified approach seems to do reasonably well.

In the tip region CATF is seen to perform the poorest with differences in the velocity field due to distorted necking clearly noticeable. The wider displaced neck zone causes an artificial increase in the enclosed fresh region where velocity is unaffected by thermal expansion. While the associated local field around a sharp pocket or neck is not seen. Meanwhile qualitatively the distribution for MATF agrees well with DNS, suggesting that any tiny scales that may have been lost are small enough that they have a negligible effect on flow dynamics.

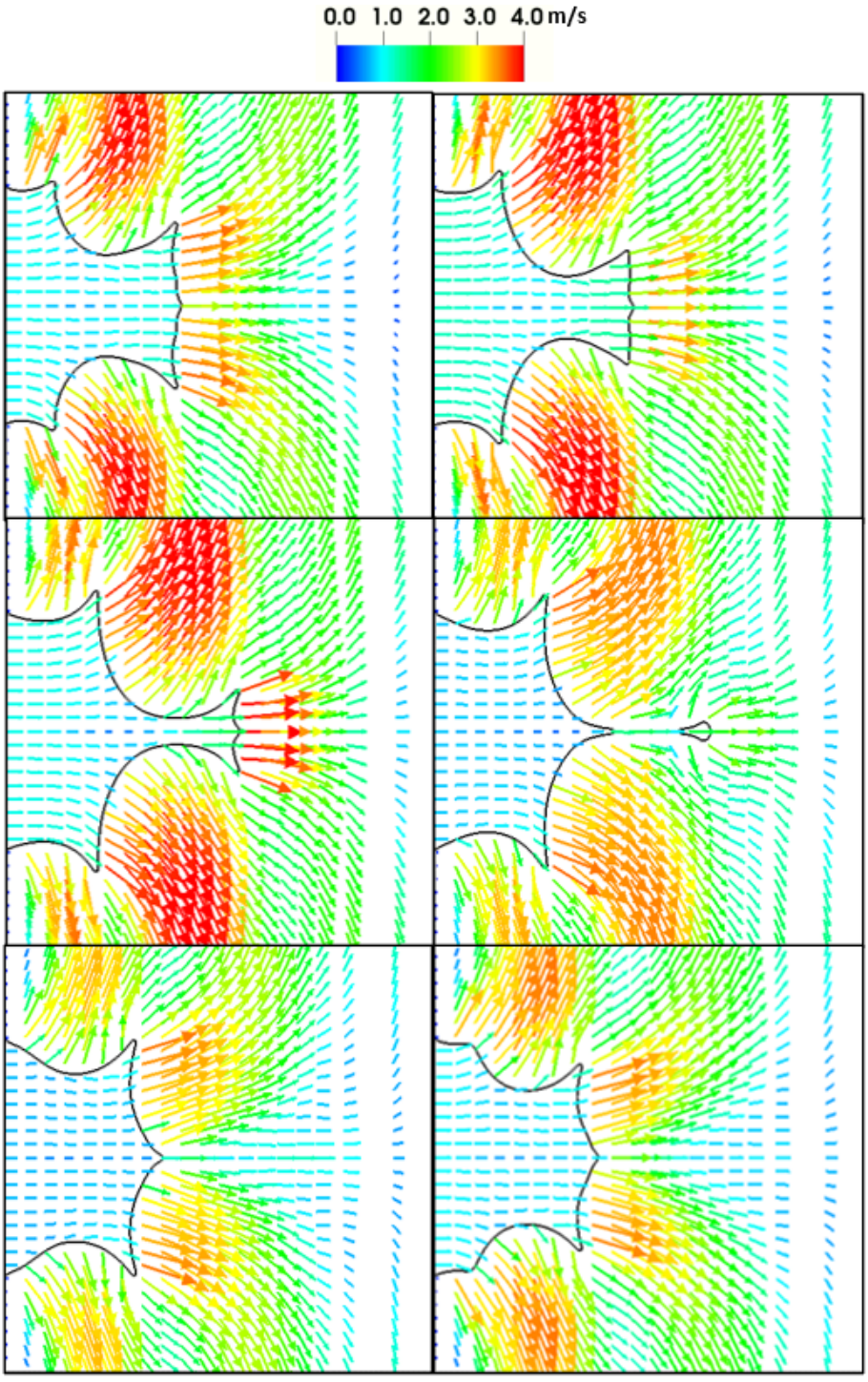

Fig. 5.26 Velocity vector map superimposed onto contours showing flame position for DNS.

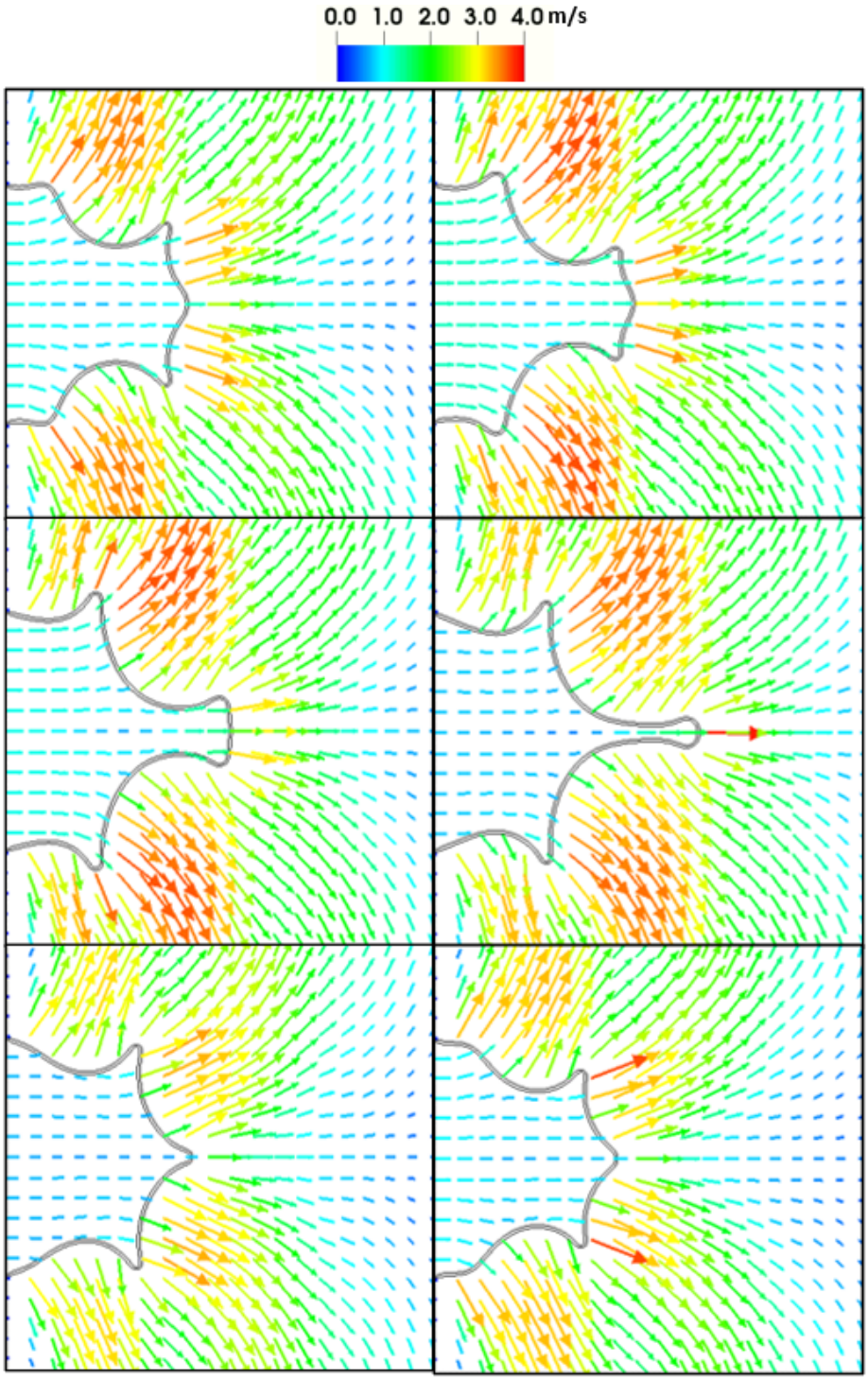

Fig. 5.27 Velocity vector map superimposed onto contours showing flame position for MATF with $\mathcal{F} = 6$.

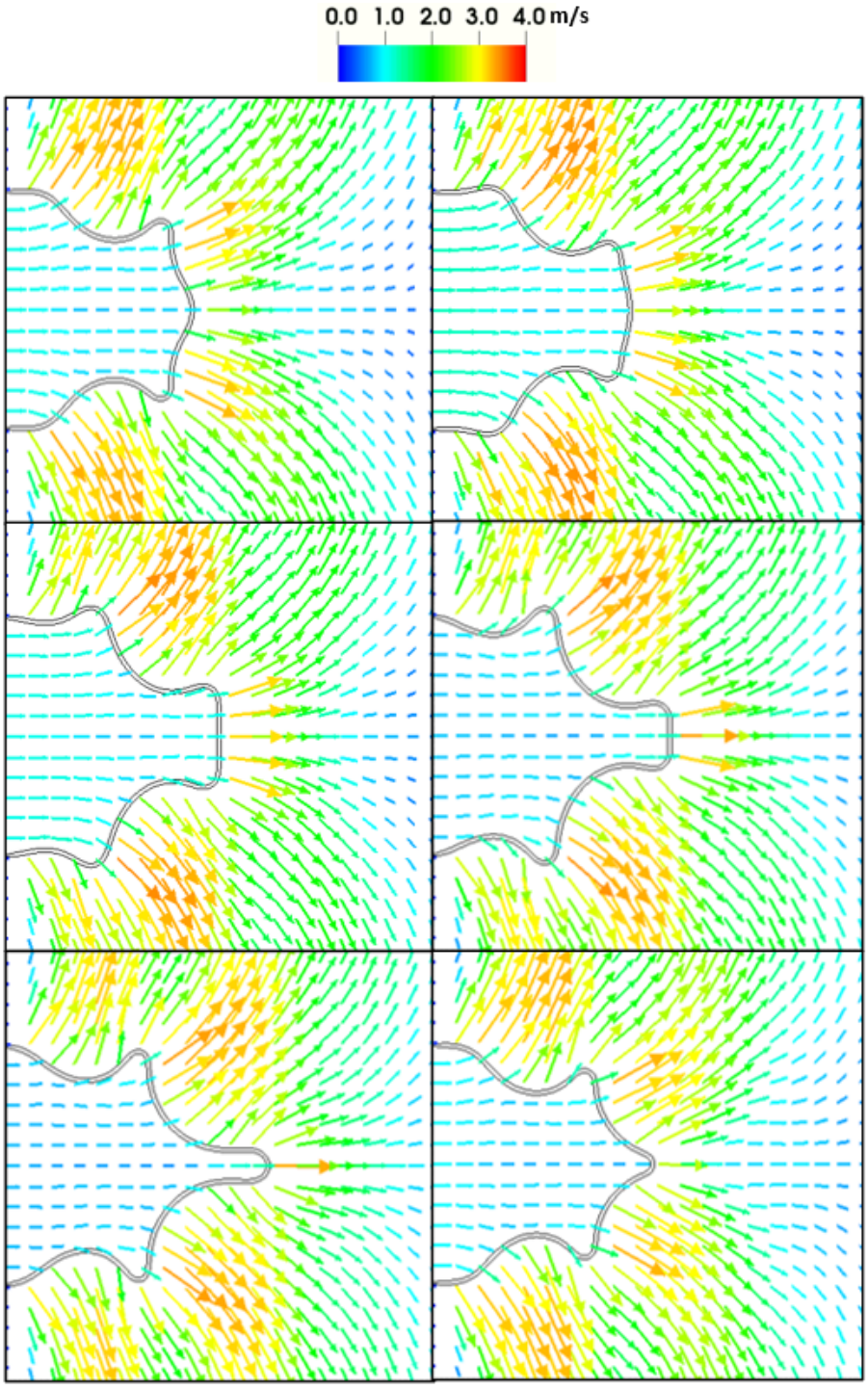

Fig. 5.28 Velocity vector map superimposed onto contours showing flame position for CATF with $\mathcal{F} = 6$.

5.2.3 Reverse Transform

At this point the results in the previous section are used to demonstrate a simple but also very generalised companion technique that has excellent synergy with MATF. The latter is essentially a transformation in space and time for *all* scales, therefore any post-processing imaging or sampling methods will relay the thickened state. Which can result in flame structures that intuitively may at first glance seem strange due to their larger size, or perhaps cause spatial displacement of particular iso-contours which could make direct comparison with experiments somewhat difficult.

As such it would be convenient if an unthickened state could be extracted from a thickened simulation. At the very least this would allow a better intuitive understanding of any illustrative distributions if nothing else. This can be done as a post processing technique by inverting the transform presented in Chapter 2 to go from $\xi \rightarrow x$ instead as follows:

$$dx = \frac{d\xi}{\mathcal{F}(\xi,\eta)} \rightarrow x = x_0 + \int_{\xi_0}^{\xi} \frac{d\xi}{\mathcal{F}(\xi,\eta)} \tag{5.2}$$

$$dy = \frac{d\eta}{\mathcal{F}(\xi,\eta)} \rightarrow y = y_0 + \int_{\eta_0}^{\eta} \frac{d\eta}{\mathcal{F}(\xi,\eta)} \tag{5.3}$$

Recall that in general $\mathcal{F}$ is a function of space when using a sensor and cannot be pulled out of the integral as a constant. Therefore the integral is solved numerically via Equations 5.4-5.5 to obtain an unthickened coordinate system. Where the j-index refers to a sequential loop over all elements in the mesh and $\mathcal{F}_j$ between two points can be approximated by a simple liner interpolation if the variation is smooth enough.

$$x_k = x_0 + \sum_{j=1}^{k} \frac{\xi_j - \xi_{j-1}}{\mathcal{F}(\xi,\eta)} \tag{5.4}$$

$$y_k = y_0 + \sum_{j=1}^{k} \frac{\eta_j - \eta_{j-1}}{\mathcal{F}(\xi,\eta)} \tag{5.5}$$

Strictly speaking this is not a complete reverse transform as the thickening transformation is done to both spatial *and* temporal terms. However the procedure is simple, cheap, can be done *a posteriori* and offers several unique benefits. Figure 5.29 illustrates the process on a slice from the acoustic flame simulation where a thickening factor of 4 was used. Row 1 shows the complete domain profile of progress variable and it can be seen the transform results in a close resemblance to actual flame resolved simulations. The second row contains a solid band representing the core of the flame zone and demonstrates how the procedure essentially shrinks the reactive zone based on the local sensor value which collapses the

spatial solution uniformly to a more compressed state. Similarly this point is further made clear by a close up of the distorted flame surface in the final row where progress variable contours are seen to cluster together post reverse-transform. Note that such a direct reverse transform is only possible because *all* scales are transformed in MATF and an efficiency function formulation would require additional corrections.

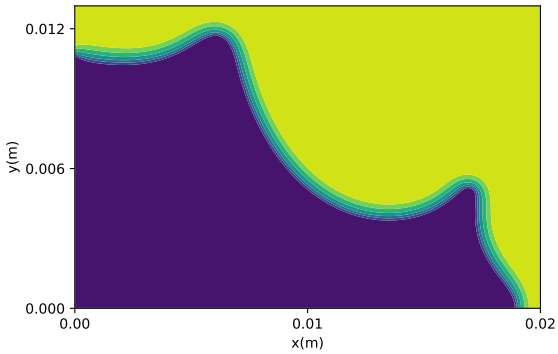

Progress variable distribution (thickened)

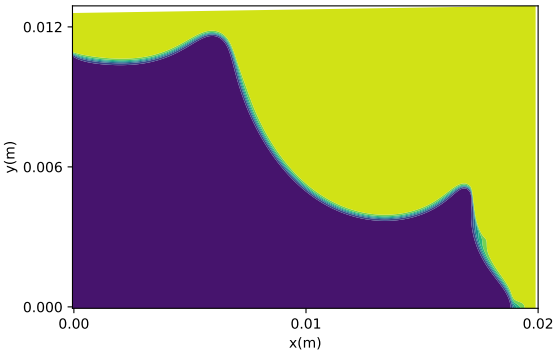

Progress variable distribution (unthickened)

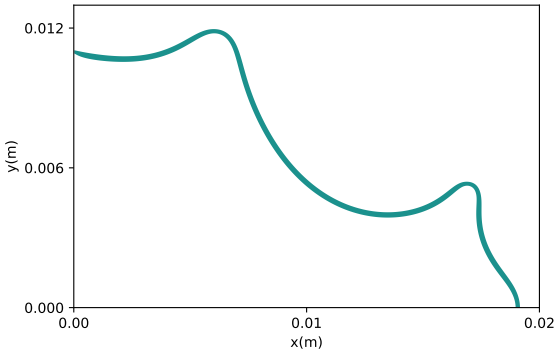

Progress variable 0.3-0.7 only (thickened)

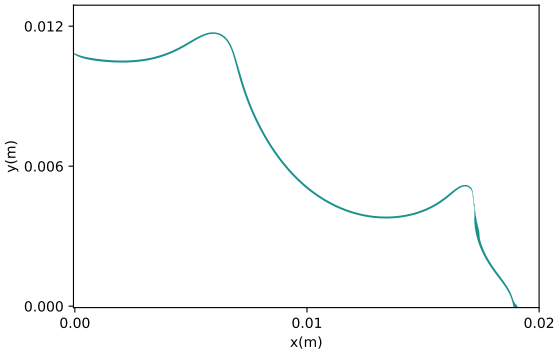

Progress variable 0.3-0.7 only (unthickened)

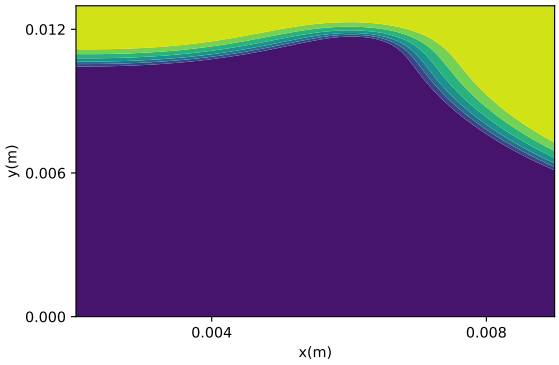

Focus view on first wrinkle (thickened)

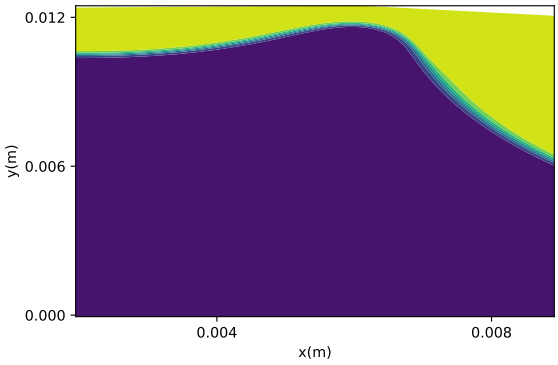

Focus view on first wrinkle (unthickened)

Fig. 5.29 Illustration of the reverse transform technique from a thickened to unthickened solution shown using different views of the progress variable.

5.3 Non-reactive Turbulent Subsonic Jet

The goal of this section is to validate coupling of the LES and AMR functionalities that were implemented into CompReal. A prevailing question in LES-AMR methods is the choice of filter-width, with several common approaches highlighted previously. These methods aim to balance computational simplicity with physical accuracy. A proposition is now made that blending functions can be set aside for the purposes considered here and instead replaced with simplified approximations for the filter width. The validity of this suggestion is evaluated through the study of a nonreactive, subsonic jet test case. With the removal of chemistry allowing a more targeted analysis of the implications choice of filter width has on LES modelling in an AMR context. The findings were then used to facilitate an informed choice for the subsequent setup of a reactive case featuring a 3D turbulent Bunsen flame.

The use of LES for investigating a variety of jet phenomena is prolific and varied in literature, with considerable effort being devoted to noise characterisation and many related fields. While DNS is often restricted to low turbulence configurations, there is significant justification to be made for the use of LES as the larger scales are believed to be the most efficient in noise generation (Mankbadi, 1999). Hybrid approaches (Schoder and Kaltenbacher, 2019) aim to further reduce cost by eliminating the need for an LES mesh throughout the entire domain, instead propagating the acoustic solution to the desired far-field locations via cheaper means such as Kirchoff surface integration (Freund et al., 1996).

However even state of the art approaches tend to rely on LES to capture the unsteady near-field jet hydrodynamic region (Andersson et al., 2005; Bogey et al., 2000, 2001), hence making the use of efficient but also reliable LES jet simulations to be of significant importance. In a different vein there has also been much focus on the study of jets to optimise and understand the impact of nozzle discharge shapes with obvious relevance to many practical applications. A full review of the significance of computation jet studies is not entirely relevant and the interested reader is referred to works such as Bres et al. (2015); Brès and Lele (2019).

Aside from practical applications, jets have been often used as a validation case for evaluating the quality of computation codes or models (Brès et al., 2017; Ingraham and Bridges, 2017; Vuorinen et al., 2011) due to the abundance of data, both numerical and experimental and this is precisely the motivation for the inclusion of such a case here.

The chosen configuration is a spatially developing round jet corresponding to the third set point in the extensive data-set of Tanna (1977), commonly referred to as the *Tanna Matrix*. The complete matrix maps out experimental work across a large range of operating parameters, yet set point 3 was chosen as it also features in the more detailed later works of Bridges and Wernet (2011). Where considerable effort was made to repeat experiments

multiple times as well as compare with existing literature to formulate their so called *consensus* data-set, with the specific intention of laying the ground work for future code validation endeavours. Examples include Bodony and Lele (2005) and Bogey and Bailly (2004) studying the jet acoustics with a sixth order spatial discretisation in conjunction with high order Runge-Kutta time integration. As well as Shur et al. (2005) who only employed a second order finite volume approximation in the context of implicit LES where the SGS model is accounted for via dissipation inherent to the numerical scheme, in conjunction with meshing the actual nozzle geometry to show good agreement with the experiments.

The choice of an implicit LES approach can be useful but care is warranted as suggested by the survey paper of Bodony and Lele (2008) that reviews a large range of previous works for operating points ranging from Mach 0.3 to 2. The authors highlight the uncertainty with regards to SGS model choices on transition within the initial shear layer and stress the lack of a general consensus. Furthermore they identify uncertainty in the inflow conditions, both in terms of initial shear layer thickness and turbulent forcing method to be one of the causes of mismatch in potential core length when comparing simulations and experiments.

5.3.1 Computational Setup

Simulation parameters are summarised in Table 5.3 where D is the jet diameter, Ma is the acoustic Mach number defined based on the jet velocity and ambient speed of sound, T_j/T_a is the ratio of jet and ambient temperatures respectively and Re_D is the Reynolds numbers based on jet diameter and velocity. Recall that the goal of these simulations is to determine whether a simplified approximation for the filter width can be employed throughout the domain in an LES-AMR context. The proposed solutions are either using a varying filter width that depends on the local mesh size at each point, or a constant value everywhere that is based on the mesh resolution at a particular level of refinement. The domain is discretised into four levels, making the total number of options for the filter width to be considered come to five (i.e. four constant and one varying). $\tilde{\Delta}$ in Table 5.3 is the filter width with the corresponding number referring to which level of refinement it is based on *i.e.* 1 is the coarsest and 4 is the finest.

The mixture being considered is air with the almost uniform temperature gradient motivating the use of a constant molecular viscosity model. Furthermore the choice of 0.5 for Mach number is particularly suited for the case of testing filter width modelling approaches by removing (or at least limiting) some of the potential additional influences. Bodony and Lele (2008) also consider the wider Tanna Matrix and find the significance of modelling the nozzle geometry to be most prominent at the lower end of Mach numbers, while Bridges and

Table 5.3 Simulation parameters and filter width choices for subsonic jet.

Case	D(mm)	Ma	T_j/T_a	Re_D	$\tilde{\Delta}$
A	50.8	0.5	0.95	569,020	1
B	50.8	0.5	0.95	569,020	2
C	50.8	0.5	0.95	569,020	3
D	50.8	0.5	0.95	569,020	4
E	50.8	0.5	0.95	569,020	Local

Wernet (2011) report a slightly larger degree of variance at the highest speed cases, making 0.5 a good choice.

Figure 5.30 illustrates the general configuration where the total domain size is $1.627 \times 1.22 \times 1.22$m which corresponds to $32 \times 24 \times 24$D in terms of the jet diameter. The axial dimension is larger to allow for a sponge layer of about $5.5D$ in order to help damp the very strong vortical motions near the outflow. The use of a sponge layer where viscosity is magnified is common practise in jet simulations (Bodony and Lele, 2008; Ingraham and Bridges, 2017; Ranadive et al., 2019) as even non-reflecting boundary conditions are only approximately non-reflecting for waves at arbitrary orientation (Colonius and Lele, 2004). The sponge helps to attenuate any motions just before the boundary and then attenuate again any reflected noise going back in towards the domain. Overall the sizes are very similar to the simulations of Ranadive et al. (2019), which albeit are a bit too small to properly capture the jet self-similar characteristics are sufficient for the purposes of near field statistics. Note that the regions away from the core are at a very course level of refinement so the added computational overhead from having slightly further boundaries is small. Figure 5.31 displays the decomposition of the domain into four nested levels of refinement. Naturally as the name implies, AMR is meant to dynamically adapt mesh resolution on the fly, however this makes it difficult to compare the applicability of the different filter width approaches that are being tested here. Since any variation in flow behaviour can result in a different local grid, making it harder to decouple the effects of model and grid resolution. Therefore the grid is kept fixed for all simulations and Table 5.4 details the mesh quality at each level of refinement, where tag refers to the width of cylindrical region tagged in terms of jet diameter for that particular level.

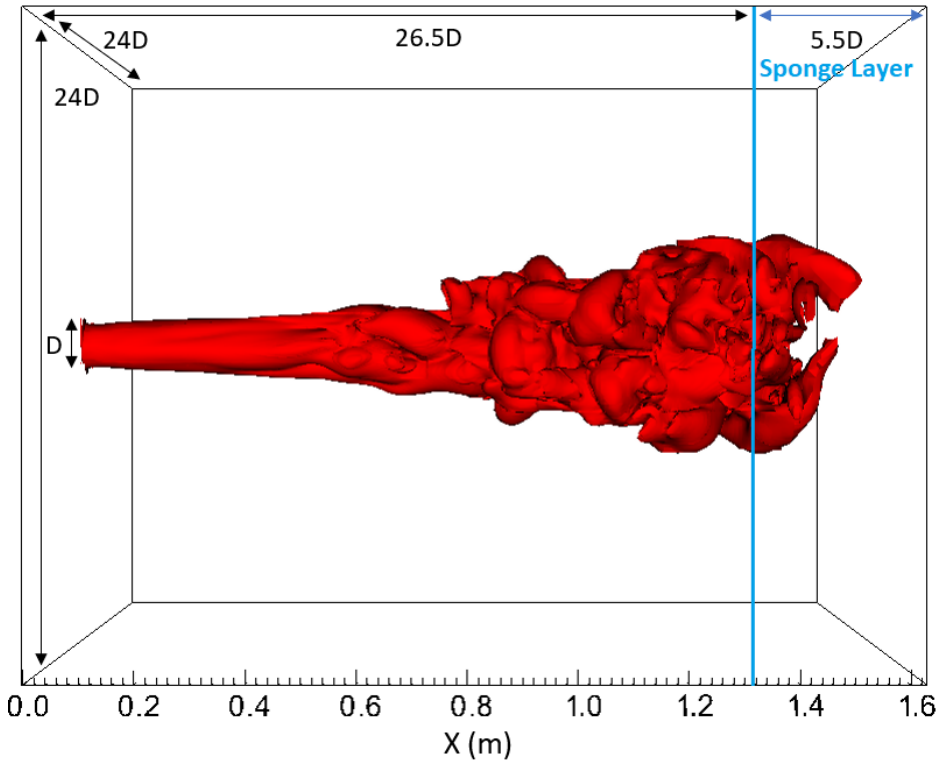

Fig. 5.30 Schematic of jet configuration including iso-contours of density.

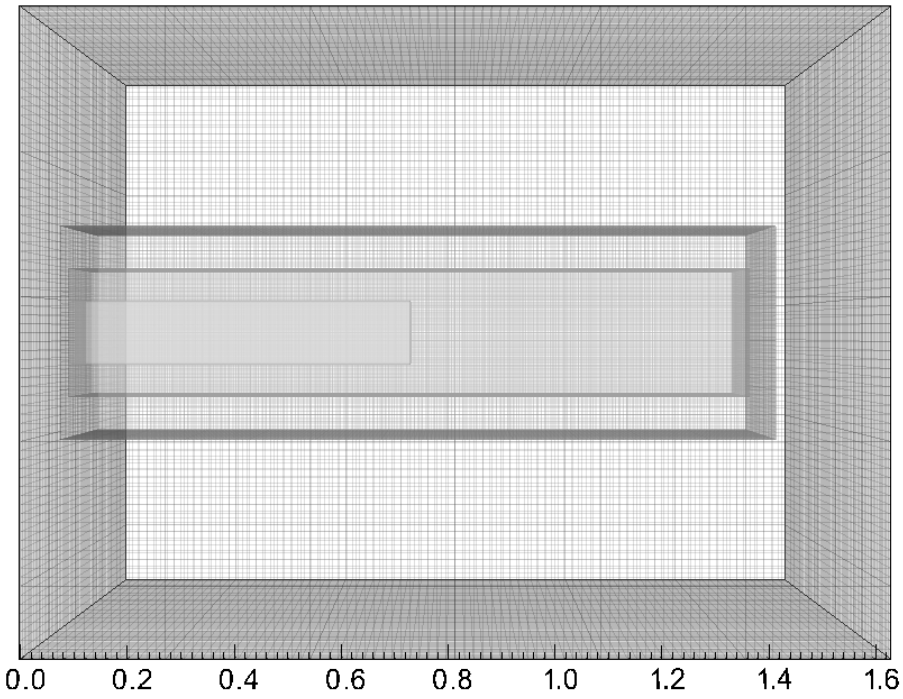

Fig. 5.31 Four level, nested mesh hierarchy with early truncation of finest level at $x \approx 0.7m$.

Table 5.4 Simulation parameters and filter width approaches for non-reactive jet case.

Level	Δ(mm)	D/Δ	Tag Width (D)	Approximate Points
1	16	3.2	-	50000
2	8	6.4	6	49000
3	4	12.7	4	1400000
4	2	25.4	2	1400000

The third level of refinement corresponds to similar resolution as Ranadive et al. (2019) who also investigated the same jet. The authors approximate a cut-off wavenumber of π/Δ and determine an integral length scale via two point velocity correlations before integrating the Kolmogorov model spectrum in the inertial sub-range to arrive at an estimate for unresolved TKE of 23%. Although this can be considered acceptable in the context of LES, the resulting mesh only provides 12 points across the jet diameter, making it difficult to resolve any incoming turbulent eddies. Turbulent fluctuations are imposed at the inlet via a digital filter using a length scale of D/6(i.e. 8.5mm and added to the mean flow. Hence the need for at least a fourth level of refinement in order to somewhat resolve the generated turbulent motions by providing 4 points within an eddy and approximately 24 across the jet diameter. Even so this is considerably courser than other works such as (Ingraham and Bridges, 2017) who employ an unstructured LES solver to place close to 200 points in the jet diameter at the inlet.

Note from Figure 5.31 that the finest level encapsulating the jet core is intentionally terminated early at 0.7m(13.7D) in order to force the flow across an interface between levels. This mimics the situation of flow features passing between refinement levels that may happen in practical simulations as dependent on the particular selection of re-gridding parameters. Moreover by manually controlling the location of this level interface, related phenomena can be readily identified at *a priori* known positions on any center-line statistics.

As the nozzle geometry is not incorporated into the computations there is a need to approximate the inflow. Ball et al. (2012) recommend the use of a hyperbolic tangent profile for the velocity if the jet exits from a nozzle and the well known power law profile otherwise to approximate fully developed pipe flow. Based on the nozzle described in the experiments (Bridges and Wernet, 2011) a hyperbolic tangent is therefore used for the profiles of both velocity and temperature.

Concurrently superposition of turbulent fluctuations was not uniform along the diameter of the jet either. Initially a similar hyperbolic tangent profile to velocity/temperature was used leading to the largest turbulence fluctuations at center line. However this lead to jet breakage vastly different from expected behaviour. Indeed when looking at experimental data (Bridges and Wernet, 2011) it was found that the highest turbulent intensity was not at the center line but in the actual boundary layer. Correspondingly the fluctuations were damped when going from the boundary to center line by a hyperbolic tangent function from an intensity of 14% of the mean flow to 3% respectively.

5.3.2 Results

The time averaged mean axial velocity was extracted along the center line and is presented in Figure 5.32 for each of the modelling choices in Table 5.3 . Note that in subsequent graphs the axial velocity has been normalised by the jet velocity, and the axial position by the jet diameter. Case A, which employed a constant filter width proportional to the mesh resolution at the coarsest level shows the closest alignment with experiments. Both the jet break up location as well as immediate trend afterwards is in relatively excellent agreement and although there is some variation at the furthest downstream locations it is still within acceptable limits when considering mesh resolution in the region. Using any of the other proposed filter models suggested clearly show a detriment both in terms of initial breakup and velocity profile evolution in space. With the largest discrepancies occurring when either a local filter width or one related to the finest level of refinement are used. Meanwhile there is little discernible difference observed in the mean solution as the flow crosses the interface. The large spread in results between modelling approached highlights the potential impact of SGS modelling, and how it can influence jet transition.

Figure 5.33 contains the fluctuating RMS velocity along the center line for the different modelling approaches where Case A shows the best agreement with experiments once again. Some discrepancies are still observed but these will be shown later to be within acceptable limits upon comparison with other implementations sourced from literature. Moreover the disparity between Case A and experiments seem to be on a point by point basis while the larger trends and peaks are in excellent agreement. The same is not true for other cases where not only can the peak be seen to over-predicted, but their axial locations are also significantly earlier, partially explaining the much shorter potential core lengths seen in Figure 5.32.

It seems that having a larger filter width than the local grid size ($\tilde{\Delta} > h$) brings about better jet behaviour, both in terms of mean and turbulence statistics. At this point it is worth making a distinction between Sub-grid Scale (SGS) and Sub-filter Scale (SFS). This was not addressed earlier as under the assumption of a filter width equal to the grid size the two are

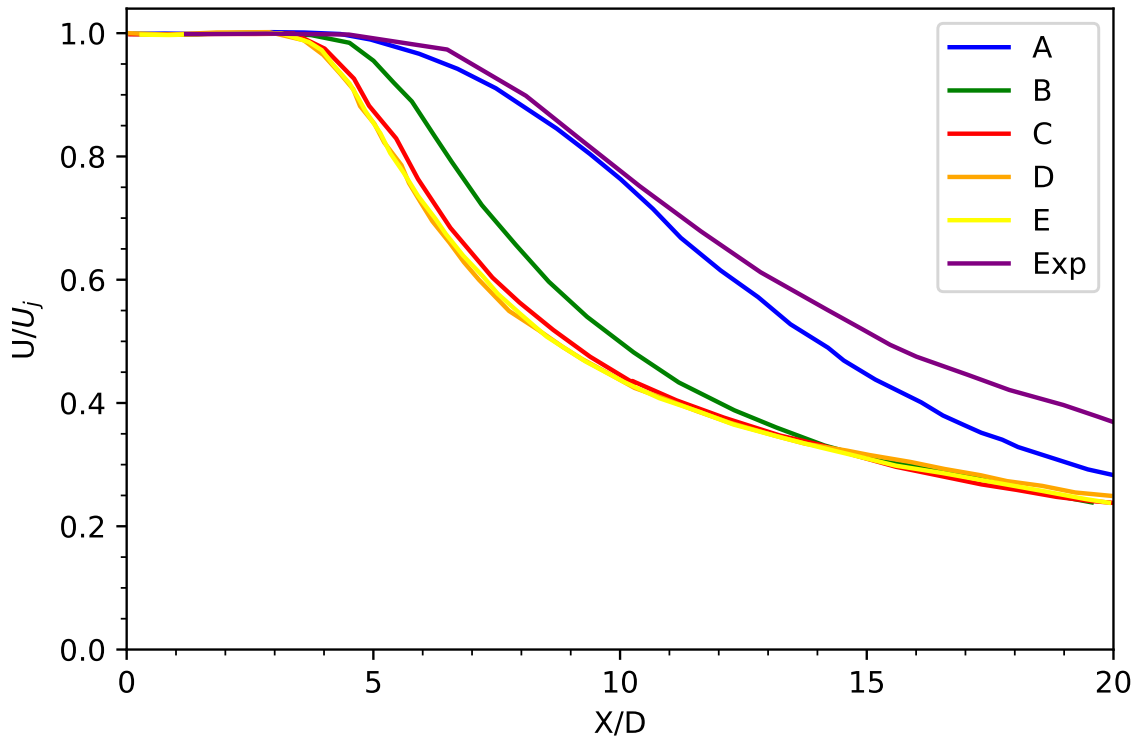

Fig. 5.32 Time averaged mean velocity profile along jet center line.

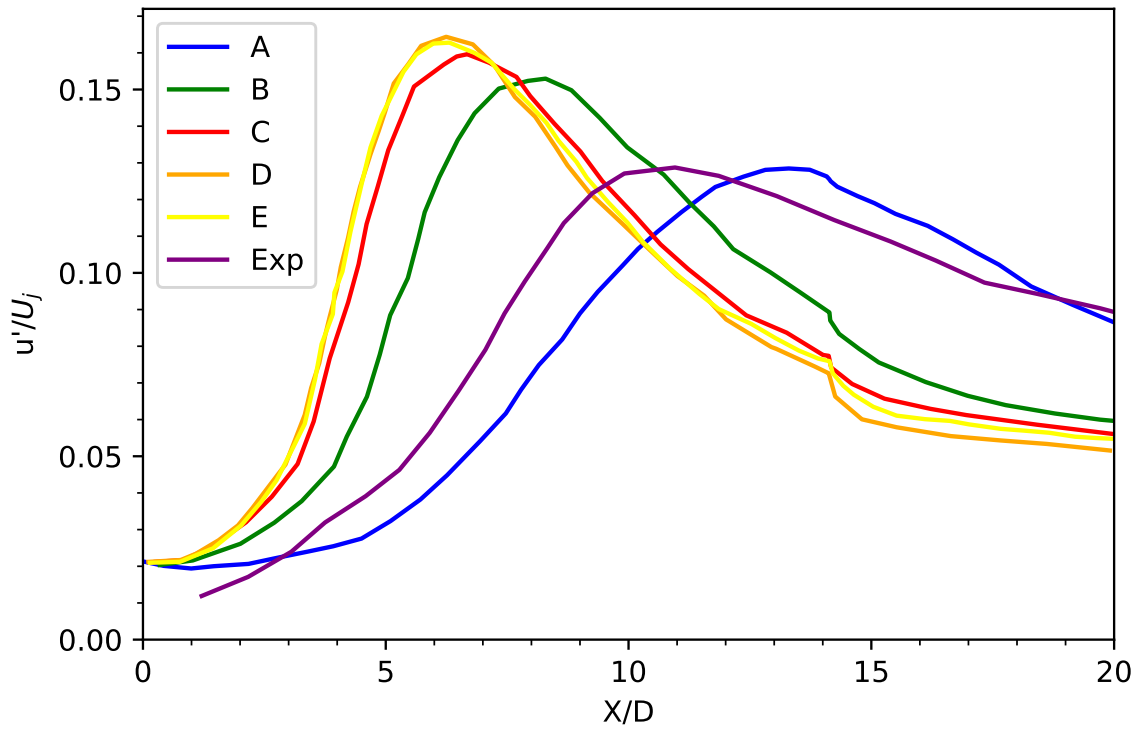

Fig. 5.33 Time averaged velocity fluctuation profile along jet center line.

essentially equivalent (neglecting spectral differences arising from smooth filters etc.). While SGS refers to the scales removed by the grid, leaving behind the smallest possible structures that could *possibly* be resolved, SFS relates directly to scales removed by LES filtering. If the two are equivalent to each other ($\tilde{\Delta} = h$) or only slightly different, it will result in the integral length structures which remain post-filter being poorly resolved.

Case A essentially increases the sub-filter resolution ($\tilde{\Delta}/h$) by setting SFS greater than SGS, resulting in the integral length eddies being adequately captured across sufficient grid points. Of course this is not necessarily always a solution for a general configuration as increasing SFS without limit just to match an arbitrary grid could potentially result in a cut-off wavenumber outside the inertial range. However in the context of relatively few refinement levels as employed here the approach seems to work better with improved sub-filter resolution being one of the potential contributors. This is similar to the approach (Bull and Jameson, 2016) of explicit filtering that shifts scales resolved by the grid to higher wave numbers to limit numerical/aliasing errors , albeit without an actual reconstruction for the explicit SFS term.

Returning to Figure 5.33, an additional pitfall of the alternative approaches is seen at the point of intersection between levels, where recall that the flow crosses from Level 4 (upstream) to Level 3 (downstream). Consider first Case E where the filter width is local, the flow experiences a drastic increase in filter size going from Levels 4 to 3. The steepness of the rate of increase results in a much stronger violation of commutativity between gradient and filtering operators than when compared to the smoother changes found in gradually stretched grids. The result is essentially the nonphysical and sudden addition of scales and with it spurious noise at the interface. Perhaps this is not too surprising as the approach is essentially solving for two different filtered solutions and associated turbulent cascades, for either side of the interface with no attempt at reconciling them. Resulting in a large kink that can be seen in Figure 5.33 at the interface, which is expected to be even further exaggerated for cases where the flow is passing more than the just single level jump being considered here.

Case D employs a constant filter width based on the finest grid (i.e. Level 4) and can be seen to have just as severe a kink as before if not even slightly worse. The setup is essentially a poorer imitation of Case E. To arrive at this interpretation consider the scenario as a combination of two classes of filtering, namely one at the prescribed level (i.e. same as the one incorporated into the SGS model) and one at the inherent grid level (i.e. true implicit filtering). By basing the filter width on Level 4, as the flow moves downstream it ends up in a situation where the filter size is actually smaller than the grid size. However as scales of the grid size will be removed anyway, the prescription of a smaller filter is irrelevant. The

combined effect reverts back to the previous case, where the filtering of scales is essentially based on the local grid, however it is slightly worse as the SGS model downstream does not take this into account and still assumes the existence of a smaller filter width than the grid size.

Judging from the remaining cases it can be seen that increasing the filter width further brings about a large reduction in the interface kink. This is to expected due to the reduction in commutativity violations that arise from varying the filter width as discussed in Chapter 2. Despite this the transition is never *perfectly* smooth , likely due to the fact that the Smagorinsky model of Equation 2.33 depends not only on the filter size but also the deformation tensor. There will inevitably be some numerical discrepancy in computing the latter by evaluation of gradients at the interface due to interpolation approximations between levels. However the net detriment on the SGS model is severely limited by using a larger filter width, which also helps to remove undue build up of energy in the energy scales further upstream leading to the over-predictions that can be seen in the time averaged velocity fluctuation.

At this point a short aside may be necessary. Earlier the idea of implicit filtering was put forward as a means to avoid the requirement of an additional explicit filtering operation and indeed the latter although beneficial can be rather costly (Denaro, 2011; Lund, 2003). So far it has been suggested that implicit filtering can be achieved via the inherent properties of numerically discretising derivatives, yet in this section the idea of using a filter width larger than the local mesh size is made use of which may seem contradictory initially. The notion of increasing the filter width in the expression for SGS viscosity corresponding to solving for a solution at a larger filter width is founded on the concept of SGS models having built in filtering characteristics. This idea has been developed in many previous works such as Mason and Callen (1986); Mason (1994); Muschinski (1996), that considered the relationship between eddy viscosity models and the kinetic energy spectrum in order to attempt controlling the filtering process directly via LES models only. This effectively relegates the notion of *actually filtering* to little more than a formalism in the act of writing the governing equations at the continuous level, while at the numerical level one solves directly for the filtered solution. Indeed Magnient et al. (2001) also expands on this avenue by controlling the filter length directly through the SGS model and conducting grid-independent filtering larger than the mesh size. This was then used to try to determine the specific shape of built in filters for two difference SGS closures, namely the Smagorinsky and Schumann models (Schumann, 1975). In summary for the former, changing the subfilter viscosity amplitude is equivalent to changing the filter width (Magnient et al., 2001) and this is the approach used here. Albeit this may not be quite as true for all models, such as when additional transport equations are involved in the SGS closure, potentially influencing the

shape of any built-in filter as well. Even if the numerical filter built into the grid discretisation scheme still remains, Magnient et al. (2001) report that for large values of subfilter resolution (i.e. $\tilde{\Delta}/h > 2$), the effective overall filter has quasi-universal behaviour and is almost entirely determined by the SGS model.

Returning now to the debate between using a local or constant filter width, Figure 5.35 displays the respective instantaneous dilatation fields. Dilatation can be shown (Colonius et al., 1997) to be directly related to the acoustic pressure and is often used as a more visually intuitive illustration of the sound distribution instead of pressure fields (Haghiri et al., 2018). A sharp change in the acoustic distribution is observed when comparing both sides of the interface for Case E, demonstrating the strong influence of having a sharp jump in filter width in terms of spurious noise. Meanwhile Case A presents a much more uniform distribution across the interface, with some local hot-spots close to the zone where the jet breaks.

Case E clearly contains a lot more noise generating structures compared to Case A. However just because there are more numerous features of acoustic source/sinks does not necessarily mean they are physical. This is not only supported by the time averaged statistics earlier but also in Figure 5.36 which displays dilatation extracted along the center-line at the same times as Figure 5.35. It can be seen that Case E is significantly noisier upstream, likely to the wide range of poorly resolved wave numbers but after the interface collapses to a state very similar to Case A. Meanwhile the latter exhibits consistent behaviour throughout the domain without any drastic and sudden shift at the interface.

In order to better understand the nature of these differences, Figure 5.37 illustrates the instantaneous vorticity contours for the same two approaches as above. Case E contains a region of significantly higher vorticity in the upstream region. It is difficult to differentiate between how much of this is due to (poorly resolved) fine structures and how much is from the knock on effect of these structures triggering earlier jet breakage. More importantly, in addition to these downsides the steep change in vorticity contours at the interface is obviously not physical and could have significant consequences in the neighbourhood of a flame front. Case A is comparatively much more consistent throughout. Even if some of the finest scales have been filtered out and replaced with a SGS model, the overall jet performs well and avoids the potential pitfall observed by Magnient et al. (2001) of too high a gap between SFS and SGS leading to potential inhibition of transition from excessive damping.

Figure 5.38 displays the Q-criterion for all proposed approaches in an effort to visualise the impact modelling choices have on the coherent structures themselves. Closer inspection near the inlet around the outer edge shows that vortical structures entering the domain here appear slightly stretched in the axial direction. Likely due to not enough unsteadiness in the region of the turbulent boundary layer leading to shedding of large, almost laminar-like

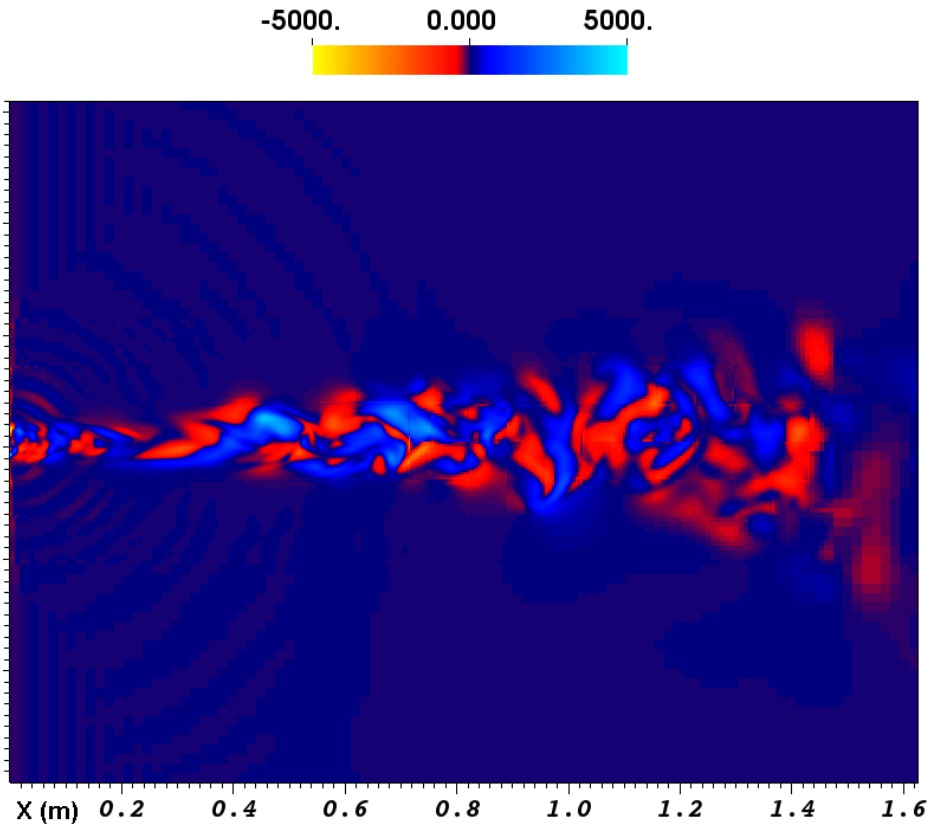

Fig. 5.34 Instantaneous dilatation field for Case A (i.e. $\tilde{\Delta} = h^{coarse}$)

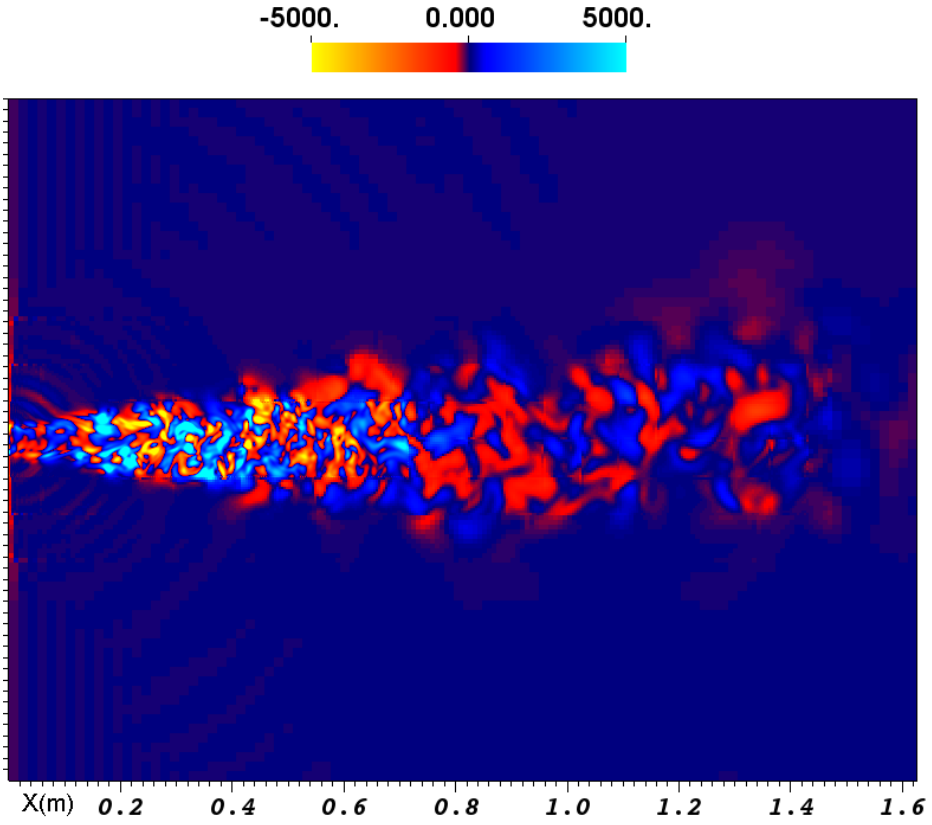

Fig. 5.35 Instantaneous dilatation field for Case E (i.e. $\tilde{\Delta} = h^{local}$)

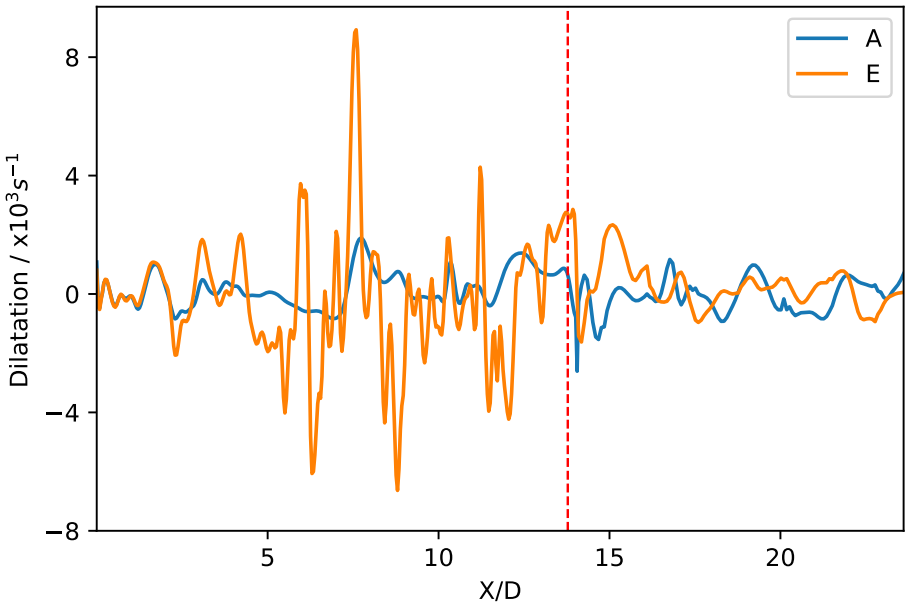

Fig. 5.36 Line-out of instantaneous dilatation sampled along the center line.

vortical structures. This has been reported in similar studies (Ingraham and Bridges, 2017) and suggested to be a cause of discrepancy between simulations and experiments in this region. Yet the overall effect is small and agreement with other numerical studies still reasonable, as will be shown shortly.

It is evident from Figure 5.38 that using a smaller filter width leads to the manifestation of a greater number of small structures. Cases E and D look fairly identical upstream of the interface while both show a large jump in structure size at the interface. As discussed earlier the only practical difference between these two will be an under-prediction in the SGS viscosity for Case D, which although hard to pinpoint directly is somewhat alluded to by the prolonged survival of some of the smaller structures downstream. Moving forwards it is seen how progressively increasing the filter width leads to a smoother transition over the level interface but at the cost of losing smaller structures. Note that even if the first few diameters near the inlet for Case A seems to be lacking in small turbulent structures, this is not necessarily incorrect or a result of over damping. In fact this is to be expected as the experiments suggest a very stable potential core in this region. Also with inlet turbulence limited mostly to the boundary layer by virtue of hyperbolic tangent smoothing, coupled with not enough unsteadiness in the generator patch, the result is large almost ring-like structures in the outer periphery.

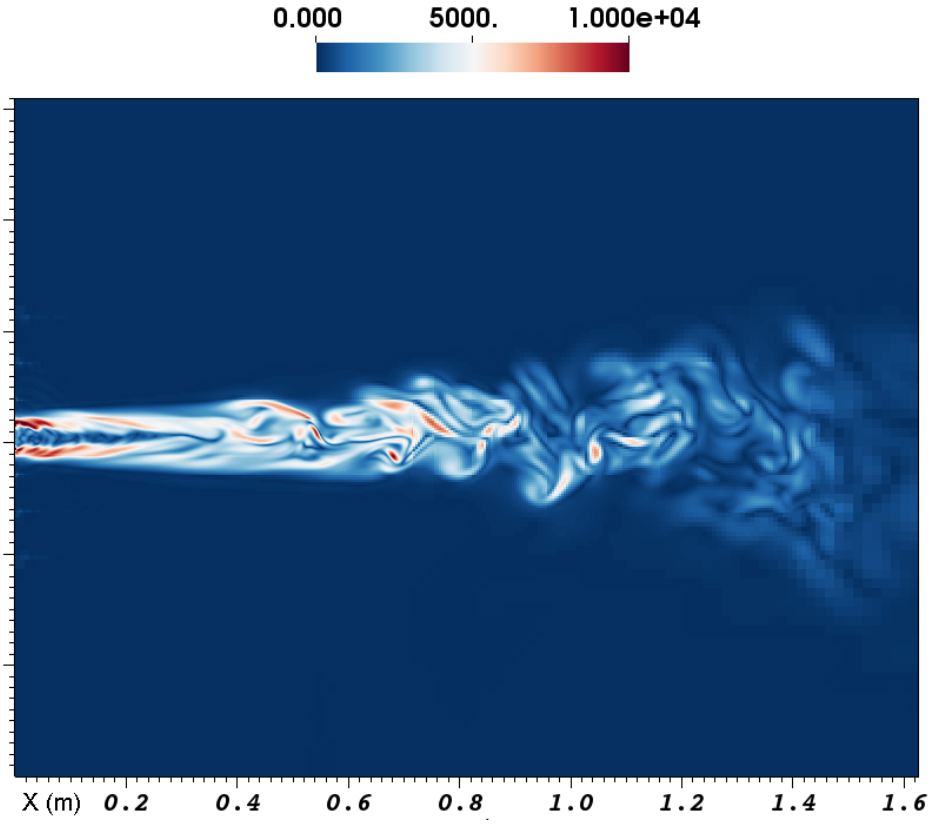

Instantaneous vorticity field for Case A (i.e. $\tilde{\Delta} = h^{coarse}$)

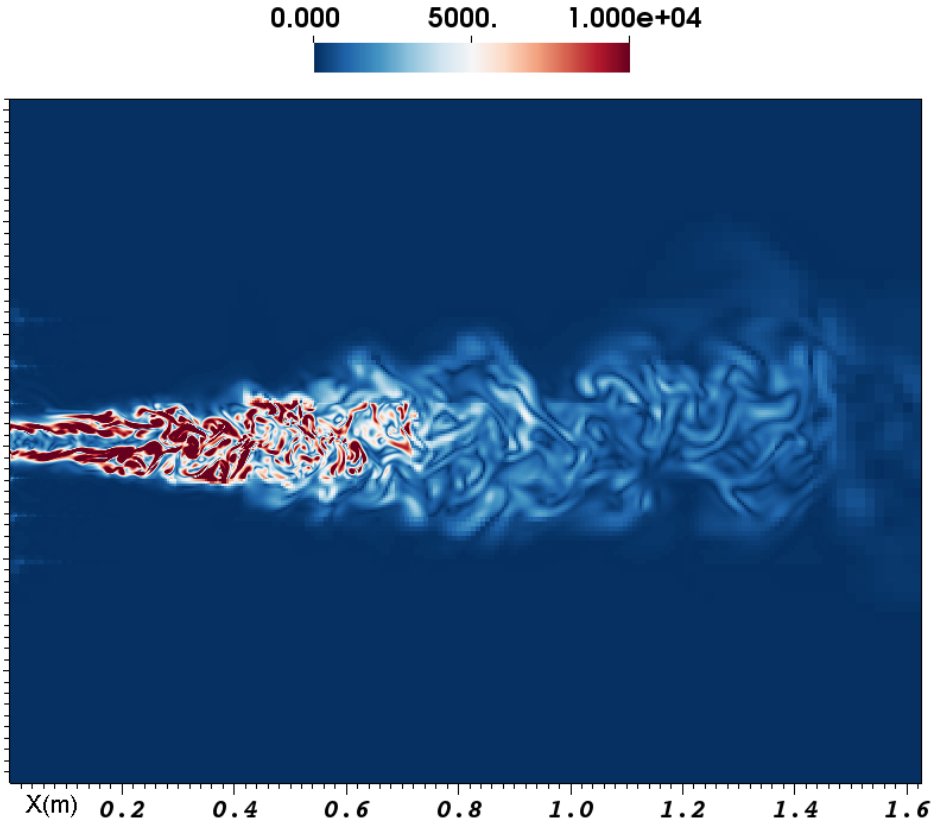

Fig. 5.37 Instantaneous vorticity field for Case E (i.e. $\tilde{\Delta} = h^{local}$)

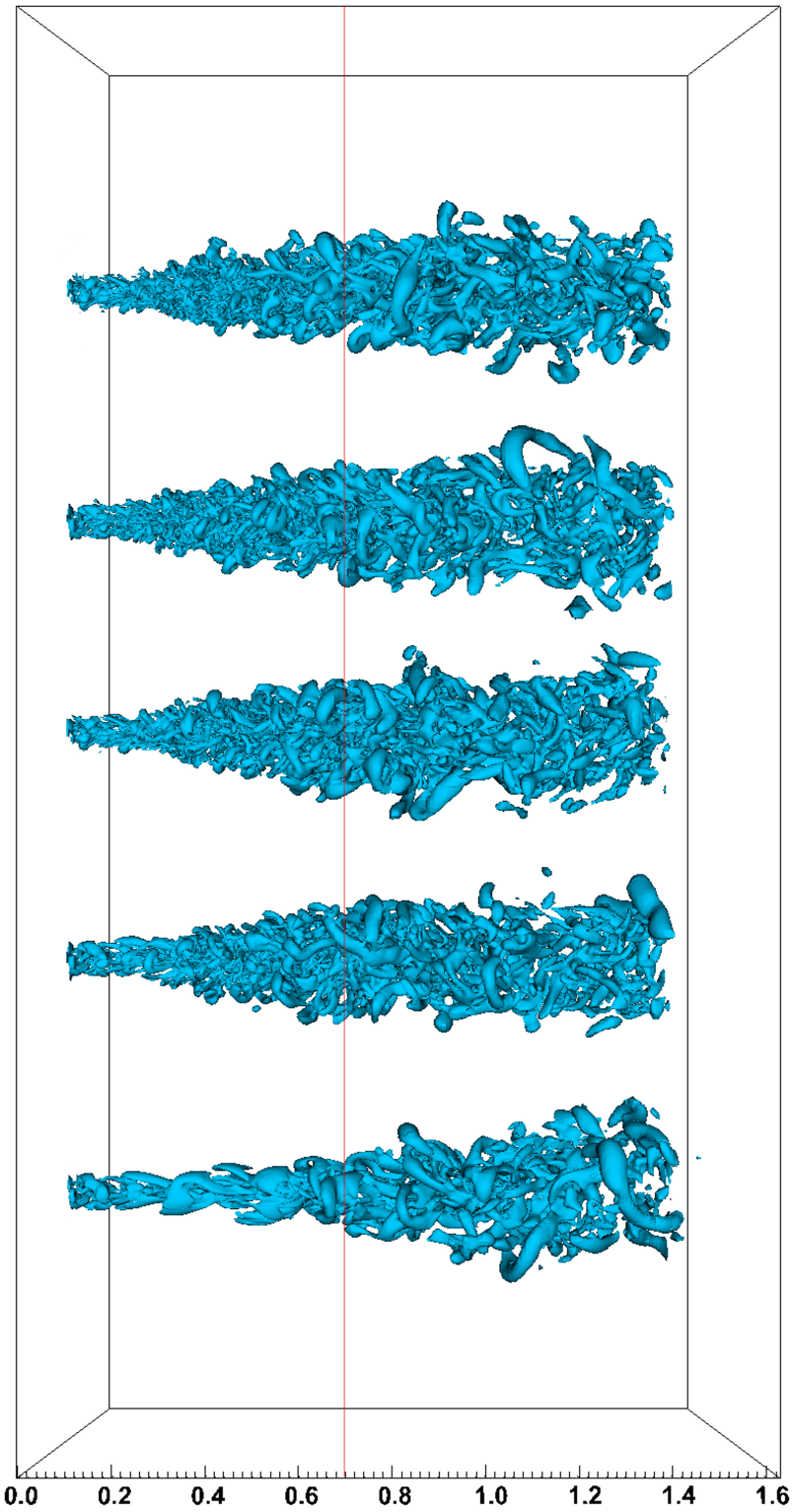

Fig. 5.38 Instantaneous Q-criterion iso-surfaces. From bottom to top: decreasing filter width culminating in the local approach (i.e.Vertically ascending as per Case A $\rightarrow$ Case B $\rightarrow$ Case C $\rightarrow$ Case D $\rightarrow$ Case E)

In summary out of the tested methods, Case A which corresponds to using a constant filter width directly related to the mesh resolution at the coarsest level seems to perform best. Note that the preceding results considered implications of violating commutativity between the filtering operator and *spatial derivatives* only. In practice as the grid dynamically adapts on the fly, using localised filter widths or indeed anything smaller than the coarsest level, would also introduce commutation errors with the temporal derivative and filter operator (Leonard et al., 2007).

In order to better appreciate the accuracy of Case A within a wider numerical context, results are now compared to other LES studies of the same jet found in literature. The comparison simulations were carried out by an unstructured LES solver (Kailasanath et al., 2014) using a second order Taylor-Galerkin scheme and are detailed in Ingraham and Bridges (2017). Note that the aforementioned work employs Monotonically Integrated LES (MILES), where the numerical dissipation inherent to the code's discretisation scheme is used to represent unresolved scales in lieu of an explicit SGS model (Grinstein and Fureby, 2005). The meshes incorporate nozzle geometry into the domain and have a resolution of 0.005D near the inlet which gradually increases to 0.04D at a distance of 25D downstream. Results from two such meshes are presented below, namely PW1 which uses around 27 million nodes and GM0 which has a much more gradual decrease in resolution in the downstream direction and employs around 55 million nodes. Both meshes are therefore significantly finer than the one employed here as described in Table 5.4.

Figure 5.39 contains the mean center line velocity profiles, where good agreement is seen throughout the near-field region and all solutions show reasonably accurate prediction of the potential core length. Case A shows even closer agreement with experiments than PW1/GM0 in the middle region of $5-12$D, before under predicting velocity further downstream. Considering that the mesh here is even coarser due to the early truncation of Level 4, some degree of mismatch is not too surprising. Despite this the general trends are in agreement with other LES studies, where the experimental data is shadowed closely at first and slightly under-predicted downstream. Furthermore the degree of mismatch is not too unreasonable when comparing with how even the finer PW1/GM0 meshes show similar differences in the zones of $11-15$D for example.

Figure 5.40 illustrates profiles for the RMS fluctuating velocity where it can be seen that in the first few diameters PW1/GM0 agree slightly better with experiments than Case A. This is likely due to their incorporation of the actual nozzle geometry without the reliance on an artificial turbulence generator. However even then the improvements are marginal and washed away further downstream. All simulations predict the peak magnitude accurately although based on the point to point differences for PW1/GM0 it is argued that differences

between Case A and experiments are well within expected limits. Moreover Case A shows significantly better behaviour at regions beyond about 15D where MILES seems to exhibit excessive dissipation even when using finer meshes.

The profiles for mean velocity along the lip-line of the jet (i.e. $D/2$) is shown in Figure 5.41. All simulations under-predict experiments which the greatest differences manifesting near the inlet. This is attributed to a combination of difficulty in creating enough local unsteadiness in the boundary layer as well as not having enough resolution to actually resolve the sharp gradients within the latter unlike in DNS. Furthermore although hyperbolic tangent smoothing is used to approximate the boundary layer for Case A, the final result is a balance between minimising artificial smoothing while also maintaining numerical stability so is likely to introduce approximation errors. Despite under-predicting experiments somewhat along the lip line, Case A still shows remarkable agreement with other LES studies for a range of statistics and lays the groundwork for the unified LES-AMR-ATF framework discussed next.

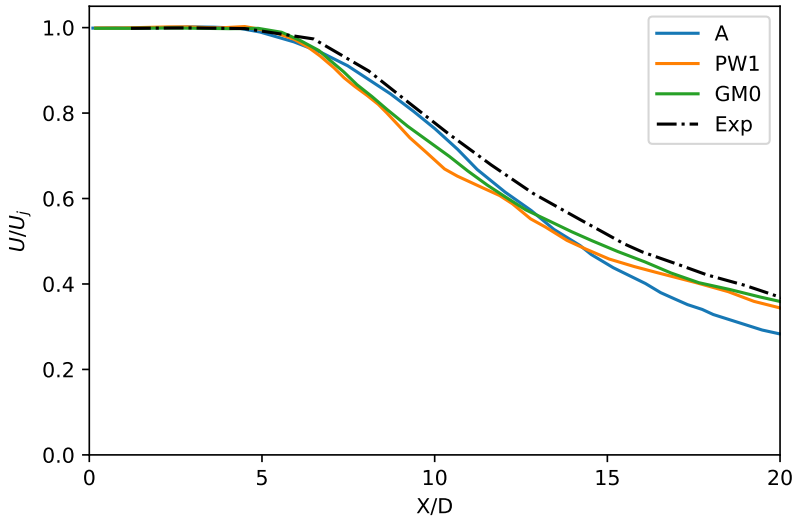

Fig. 5.39 Time averaged mean velocity profiles along the center line.

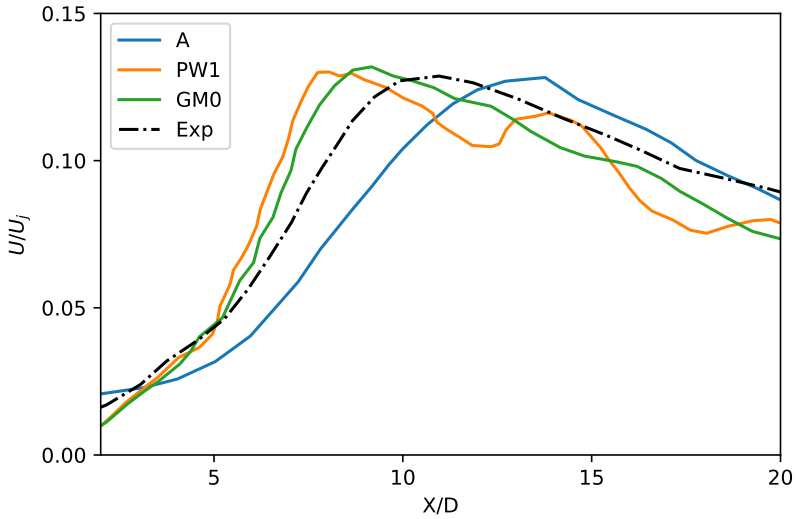

Fig. 5.40 Time averaged velocity fluctuation profiles along the center line.

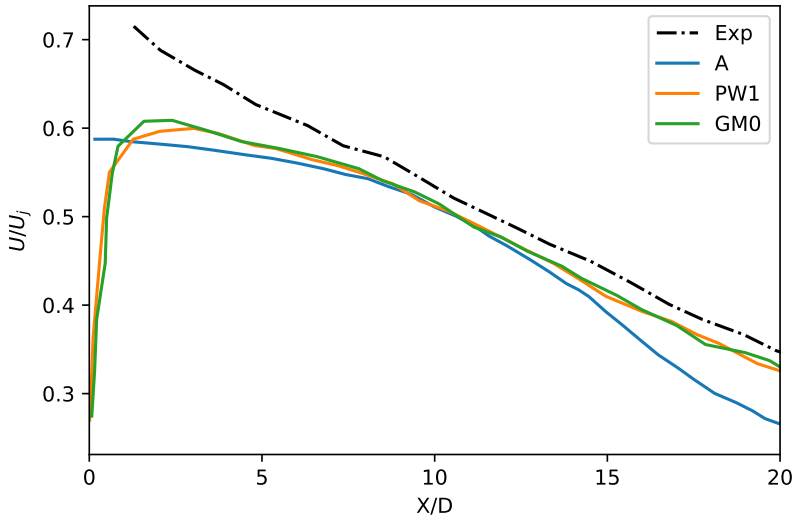

Fig. 5.41 Time averaged mean velocity profiles along the lip-line.

5.4 Turbulent Bunsen Flame

The previous section laid important groundwork for a AMR-LES coupling that balances computational complexity and cost with the desired degree of accuracy. This is now extended to also include the modified ATF model to form a comprehensive reactive flow solver. In theory the proposed ATF model is uniquely poised to take advantage of AMR as the filter width does not directly appear in the combustion model and instead *all* scales are transformed implicitly. Many alternatives require an explicit representation for unresolved scales which may not always be obvious or ideally cast in the context of AMR and many levels of refinement.

In order to evaluate performance of the unified framework being proposed in a reactive context, the laboratory scale burner of Yuen and Gülder (2009) was simulated in CompReal. This burner has been the focus of several experimental (G$\dot{v}$ider and Smallwood, 2000; Gülder et al., 2000; Yuen and Gülder, 2009) as well as numerical campaigns (Hernández-Pérez et al., 2011, 2014; Pérez and Emanuel, 2011; Shahbazian, 2015) and is well suited for the purposes envisioned here. Particularly so due to the availability of experimental curvature, a quantity forming much of the groundwork for the next chapter, but also in light of Hernández-Pérez et al. (2011) who carried out a comparative study while using AMR on the same burner for different LES models, including the conventional ATF approach.

5.4.1 Computational Setup

A lean, perfectly premixed methane-air mixture at equivalence ratio 0.7 is issued from an axisymmetric Bunsen type burner into a computational domain of $0.1 \times 0.05 \times 0.05$m as shown in Figure 5.42 The burner itself has an inner diameter of 11.2mm and feeds a reactant mixture at 300K into the system with a velocity of 15.58m/s. Turbulence is artificially generated and superimposed at the inlet with characteristic parameters from experiments collated in Table 5.5, in terms of the integral, Taylor micro and Kolomogorov length scales ($\Lambda_T/\lambda_T/\eta$ respectively). This corresponds to Case M14 in the full data matrix of Yuen (2009) and is one of the most turbulent configurations considered. The resultant flame lies in the thin reaction zone of the turbulent combustion diagram with a turbulent Reynolds number of 324. The Damköhler and Karlovitz numbers are 1.2 and 13.4, suggesting significant impact of turbulence on the flame.

The experimental flame is stabilised with annular pilot flames which were approximated using a uniform inflow of hot combustion products at 16.81m/s as done in Yuen and Gülder (2009). The 4-step Jones-Lindstedt mechanism was initially employed but found to result in an inflated flame speed resulting in the fresh mixture burning too fast in the current

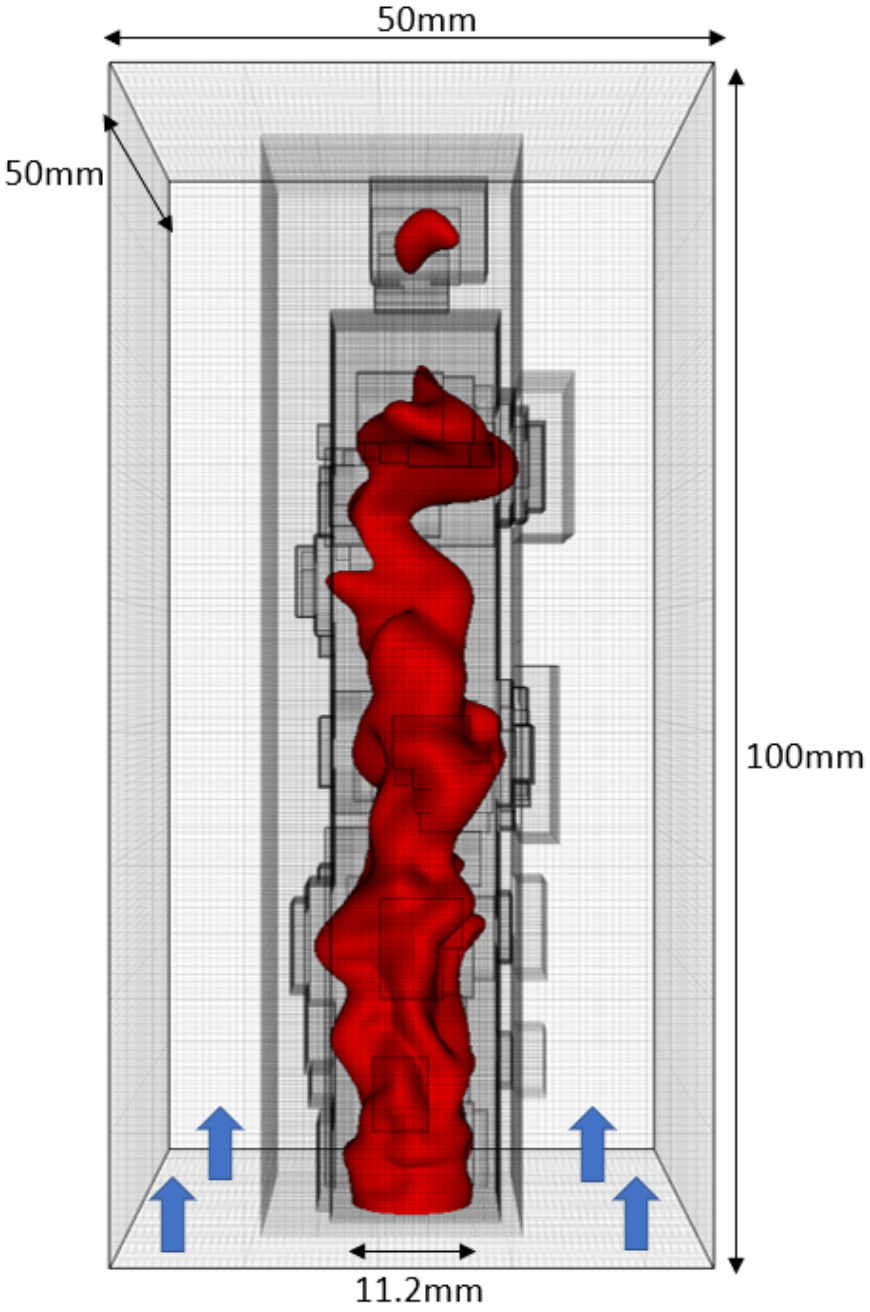

Fig. 5.42 Domain configuration for lean Bunsen flame. Flame surface iso-contours shown in red are encapsulated by AMR boxes at the finest level at all times. With blue arrows indicating the co-flow of hot products surrounding the central region.

Table 5.5 Turbulence Characteristics for lean methane-air Bunsen flame. Source Yuen (2009).

Λ_T (mm)	λ_T (mm)	η (mm)	δ_f^0 (mm)	s_l^o (m/s)	u'/s_l^0	Λ/δ_f^0
1.79	0.46	0.03	0.11	0.201	14.4	16.64

configuration. Similar findings have been reported in literature previously with Truffin (2005) showing how some of the pre-exponential constants can be modified to better adapt the scheme for different lean operating conditions. Franzelli (2011) expands on this to form a modified scheme (referred to as JONES*) which was also implemented into CompReal. Modest improvement was observed but the coefficients were not directly tailored to the particular conditions being used here and required further optimisation. As a compromise the 2-step BFER scheme (see Table 3.3 earlier) was employed and showed reasonable stability which coupled with computational savings justified its use.

Four different simulations were run and are briefly summarised in Table 5.6 with the sensor referring to either the symmetric implementation of Durand and Polifke (2007) or the asymmetric formulation developed as part of this work (see Chapter 2). The filter width is identified in terms of the level of refinement with the equivalent mesh resolution. Two different meshes were used, both with 3 levels of refinement coupled with heuristically tuned tagging conditions on variations in density. In conjunction with a regrid every 100 time steps this ensured the flame front was always resolved on the finest level. The coarse and fine meshes differ from the very first level with the latter being twice as fine as noted in Table 5.7. With approximate values for how many points lie within the thickened flame when using the thickening factor of 5 employed in all simulations here also indicated. Despite the moniker of "fine" both meshes are significantly below the threshold of DNS with the coarse mesh having a grid spacing of the order of laminar flame thickness or even slightly larger.

The motivation behind simulating cases A and B is clearly to compare the influence of the sensor, particularly for transforming curvatures as will be shown shortly. However Case C was designed with the specific intention to differentiate between sources of improvement in Case D. As the latter is based on a finer grid the primary driver for increased accuracy is expected to be better *a priori* resolution of scales to be transformed by the thickening procedure. However indirectly the configuration also involves a smaller filter width as the first level is twice as fine as the corresponding first level on the coarse mesh. Therefore Case

Table 5.6 Simulation parameters for lean premixed methane-air Bunsen flame.

Case	Mesh	Sensor	Filter Width
A	Coarse	Symmetric	Level 1
B	Coarse	Asymmetric	Level 1
C	Coarse	Asymmetric	Level 2
D	Fine	Asymmetric	Level 1

Table 5.7 AMR grid spacing at coarsest/finest levels and approximate flame resolution.

Mesh	Level 1 [mm]	Level 3 [mm]	δ_f^0/Δ_3	$\hat{\delta}_f^0/\Delta_3$
Coarse	0.69	0.17	~ 1	~ 4
Fine	0.35	0.08	~ 2	~ 8

C is designed to have the same filter-width as Case D, differing only in mesh resolution in order to isolate its relative contribution.

5.4.2 Results

Figure 5.43 presents slices across the center-plane of the domain in order to provide a qualitative comparison of flame behaviour. Case A seems to exhibit a greater degree of wrinkling observed along the outer edge than Case B. Furthermore several hot, locally burning pockets of mixture are seen to be forming even in the central fresh region. This is indicative of localised self flame interaction leading to phenomena such as pocket formation, tunnel closure etc. which was observed in experiments (Yuen and Gülder, 2009) but is not comparably reproduced in Case B. Hence suggesting modest possible improvements to be gained with the modified flame sensor.

Case C overall performs similarly to A, implying little impact of reducing the filter width alone. Although there is a small increase in localised wrinkling near the base this quickly disappears further downstream and is not significant. Suggesting that even if more scales are included by reducing the cutoff, subfilter resolution is too poor to provide a meaningful reduction to SGS turbulence. In summary although minor differences may be

observed between A-C, the mesh resolution is the primary limiting factor making it difficult to segregate impact of secondary forces. Recall that this mesh is of the order of laminar flame thickness and challenging for any ATF approach.

Case D showcases the ability of the modified model to resolve flame wrinkling remarkably well despite relatively modest improvements in mesh criteria. Significant wrinkling is observed and across a larger range of scales upon tracing the flame front. Furthermore prominent self-interaction events leading to tunnel formation are readily identified. These improvements likely stem from the finer mesh having better a priori resolution of turbulent scales prior to the thickening transformation. The model is not without any limitation whatsoever in terms of mesh criteria but clearly still has the potential to offer significant computational savings.

Figure 5.44 displays the complete 3D structure of the flame for the same instants in time. Aside from the obvious changes in wrinkling of flame surface, it is noted that the overall size of the flame envelopes is fairly similar. Furthermore the highly corrugated flame wrinkling coupled with inherent curved nature of a small diameter Bunsen flame clearly manifests in a complex structure that spans all three spatial dimensions. As will be seen shortly this can have implications on the use of two dimensional curvature data which for the cases here might have significant out of plane contributions.

Following on from the topic of flame envelopes, Figure 5.45 contains the time averaged profiles for a progress variable contour of 0.5 for simulations and the experimental counterpart. All approaches used here show excellent agreement and reliably reproduce global flame behaviour. Although some small differences are observed, they are minor and readily explained by thickening potentially displacing a particular contour in space within the larger flame zone. The main point to be made is that even the coarser mesh simulations capture the overall quasi-steady state very well. Whether this directly translates to a well resolved internal flame structure remains to be seen and is discussed next.

First however consider Figure 5.46 which contains the same time averaged profiles for a variety of alternative modelling approaches sourced from literature. Included is the conventional thickened flame model with an efficiency function (TF3). Care is warranted in making strict comparisons with simulations run here as although cases in Figure 5.46 were also run with AMR, they employ a different numerical discretisation (Riemann solvers) and single step chemistry. More importantly the precise regrid parameters and subsequent resolution in the flame front is not known. Although based on the value of thickening factor of 3 employed in TF3, it is taken to be reasonable to assume a resolution similar if not finer to the mesh used in Case D was employed. As such MATF seems to have outperformed

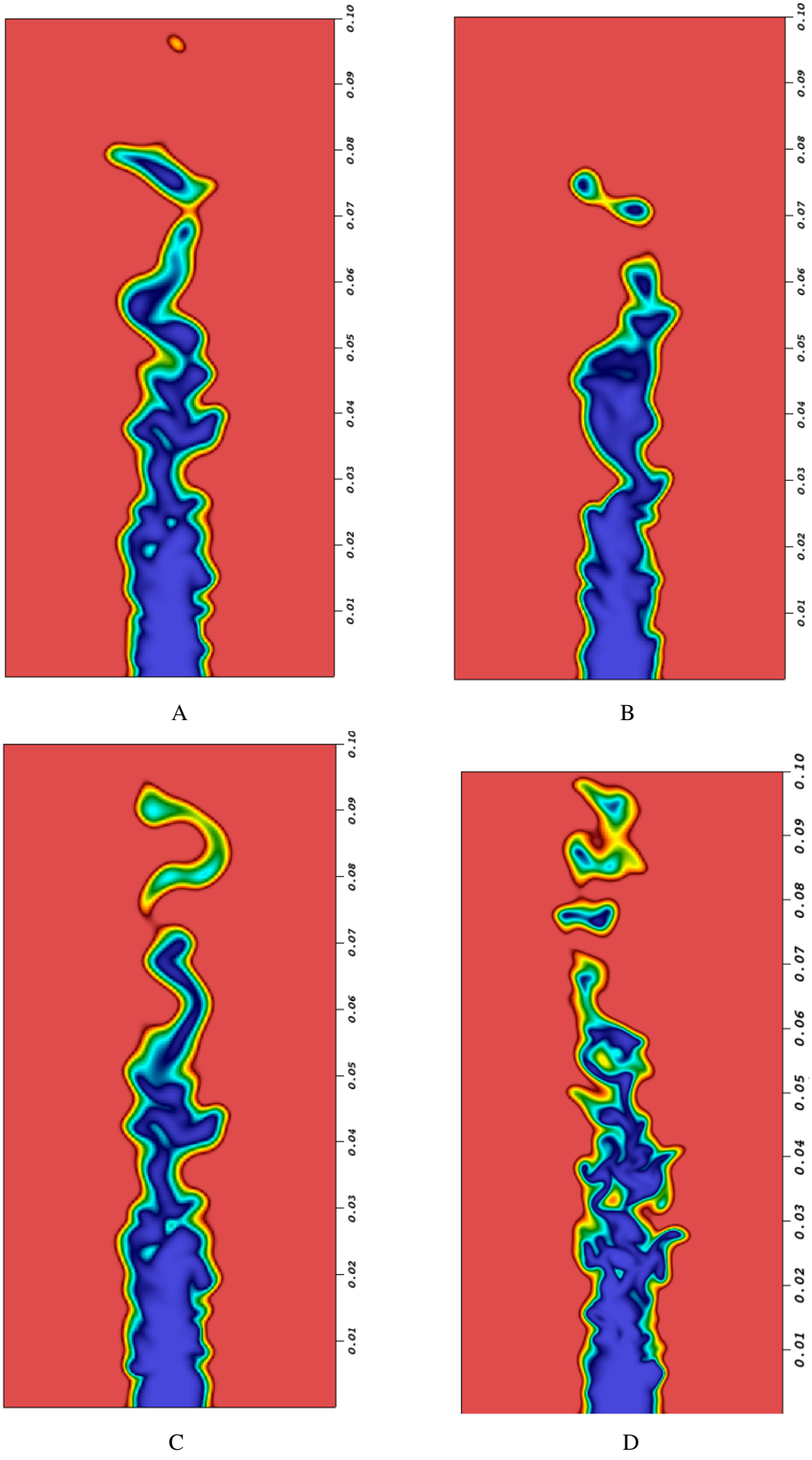

Fig. 5.43 Instantaneous progress variable for test cases described in Table 5.6.

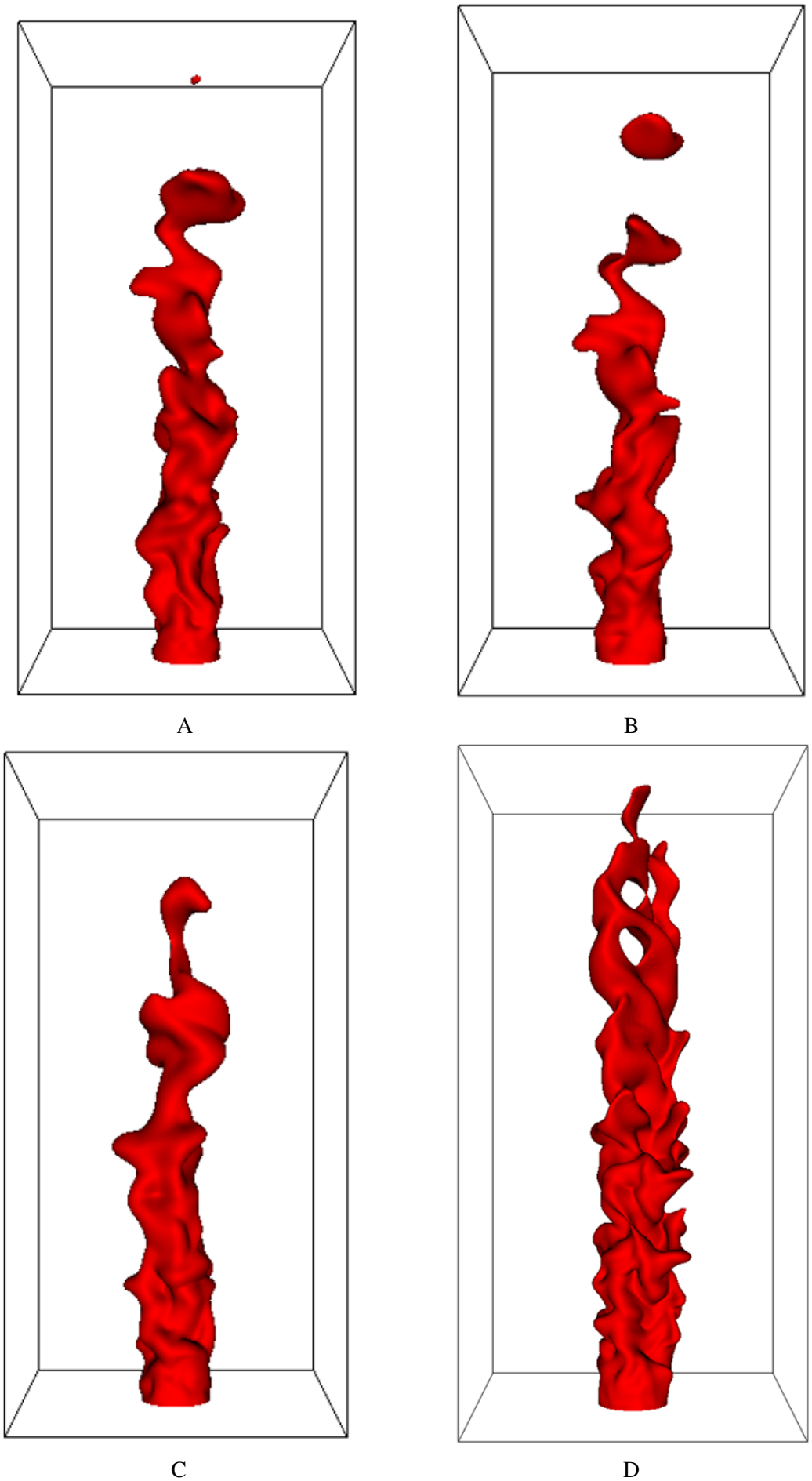

Fig. 5.44 Instantaneous 3D progress variable for test cases described in Table 5.6.

many of its alternatives both in terms of cost/complexity but also in predicting global flame behaviour such as the mean flame length.

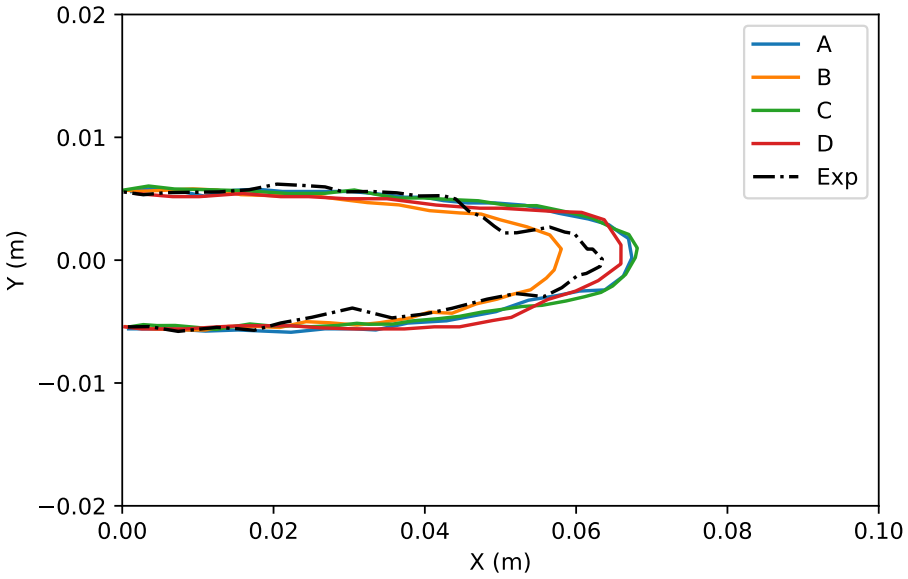

Fig. 5.45 Time averaged distribution of progress variable iso-contour of 0.5 for MATF. Experiment sourced from Hernández-Pérez et al. (2011).

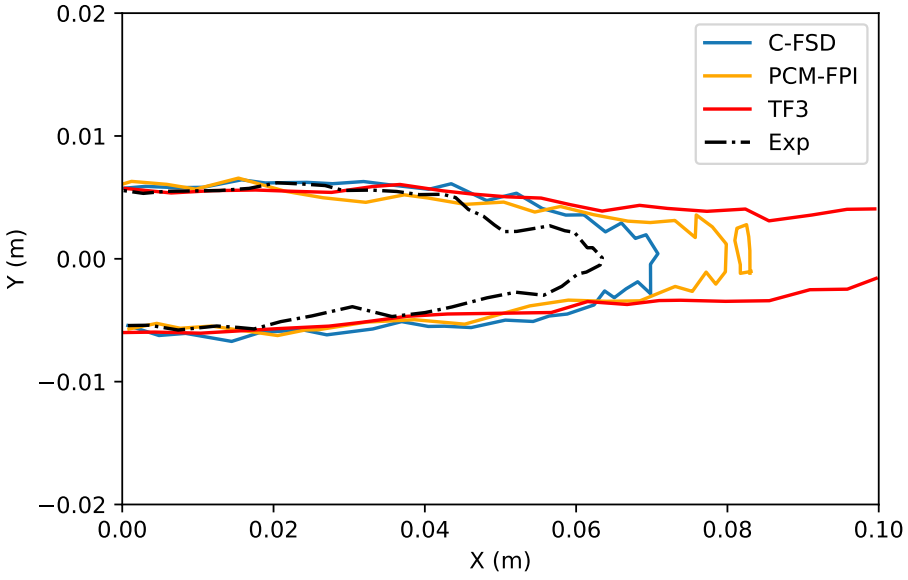

Fig. 5.46 Time averaged distribution of progress variable iso-contour of 0.5 for conventional LES methodologies. Adapted from Hernández-Pérez et al. (2011).

In order to evaluate resolution of the internal flame structure Figure 5.47 illustrates the mean curvature distributions for all cases compared with experiments at 0.5 progress variable. Note that there are some uncertainties with respect to the filtered data as this was obtained from Hernández-Pérez et al. (2011) where the finer details of the filtering procedure are not specified. Cases A-C at this stage seem to misrepresent the experimental distribution by showing an exaggerated preferential bias towards negative values. Even if the values on the left branch are relatively close to experimental data the mean appears to have shifted and positive values considerably under-predicted. Potential causes for the latter include differences between 3D and inherently 2D curvatures supplied from simulations and experiments respectively. It has been suggested (Chen et al., 2007; Yuen, 2009) that this difference is small. However such an assumption is questionable for the particular geometry used here in light of the significant out of plane wrinkling observed in Figure 5.44 as discussed in Appendix C. Moreover it seems that due to mesh resolution prior to thickening being the primary limiting factor, there is little benefit to the resolved flame structure of using a particular sensor or filter width, at least along this particular iso-contour.

Case D however shows much better qualitative behaviour in terms of location of the mean and slope profiles and does capture the relative preferences reasonably well. The results essentially lie in between a filtered and experimental solution which perhaps is not too surprising. One potential explanation for this is that although theoretically MATF solutions should tend towards an approximate DNS since there is no filtering in the flame, in practical context this is difficult. Particularly so as the model is implemented into an LES framework therefore the filter is active upstream in the fresh mixture. Essentially any input turbulence does see some implicit filtering prior to arriving at the actual flame zone and some of the turbulent scales may have been removed , although its effects on the flow remain. However it is generally easier to resolve these than the flame itself, so solutions include better grid resolution even away from the flame or more sophisticated LES models than the Smagorinsky approach applied here.

The choice of progress variable iso-surface for evaluation of curvature data is also important. Figure 5.48 contains the same experimental data but simulation values for a value of progress variable shifted more towards the fresh side. Improvement is observed for all simulations but markedly more so for ones runs on the coarser mesh. Of course this is not a strict comparison as it is hard to isolate the individual reasons for this change. However as the greatest change occurs for Cases A-C it is possible that the sensor dependant term in the curvature scaling law which was developed in Appendix B might not necessarily be negligible for such extremely coarse meshes where sensor space is not smoothly resolved. Lastly the degree of unsteadiness at the turbulent inflow (i.e. the characteristic turbulent time

scale numerically used to determine how quickly to vary the inflow patch and thus determine the axial shape of incoming eddies) can be very difficult to obtain experimental values for. A more detailed discussion is shown in the next section to have a significant effect on curvature distributions.

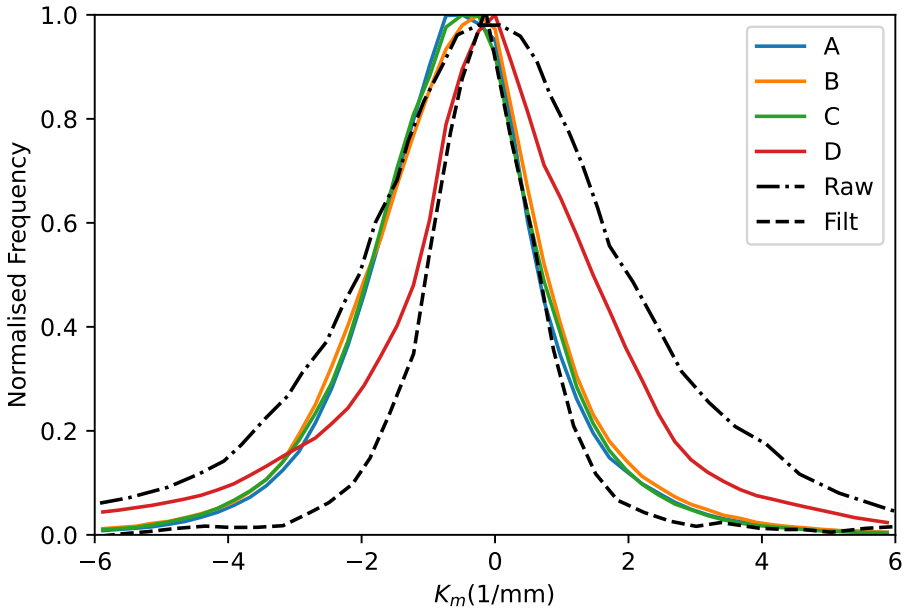

Fig. 5.47 Mean curvature distributions at progress variable of 0.5. Raw and filtered experimental data sourced from Yuen (2009) and Hernández-Pérez et al. (2011) respectively.

Despite all of the above the curvature distribution is approximated much better than with several of the alternative LES methodologies as shown in Figure 5.49. Of particular note is the poor performance of TF3 where despite using an efficiency function large degrees of flame wrinkling remain unaccounted for. Indeed the scaling of curvatures approach developed as part of this work is one of the main suggested advantages of the modified model and is only made possible due to the approach not being reliant on an efficiency function.

Another subtle benefit of the approach is rooted in the practicalities of numerical schemes as opposed to combustion modelling principles. On LES meshes flames appear as very sharp discontinuities which are naturally difficult to capture with a numerical scheme without taking specific measures. As detailed earlier, in the flux-skew conservative formulation employed here this is taken care of by a sensor based diffusive flux. However it is noted that locally in the flame zone, this essentially acts as a poorer imitation of thickening. Figure 5.50 demonstrates this by showing what happens when an originally thickened solution ($\mathcal{F} = 5$) is restarted in different configurations in terms of progress variable. Each of the subsequent

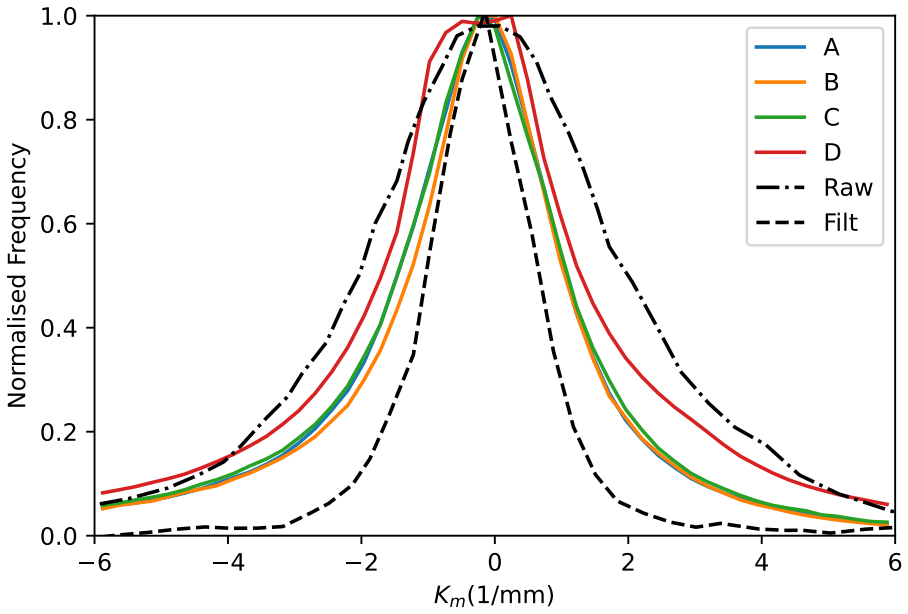

Fig. 5.48 Mean curvature distribution at progress variable of 0.1. Raw and filtered experimental data sourced from Yuen (2009) and Hernández-Pérez et al. (2011) respectively.

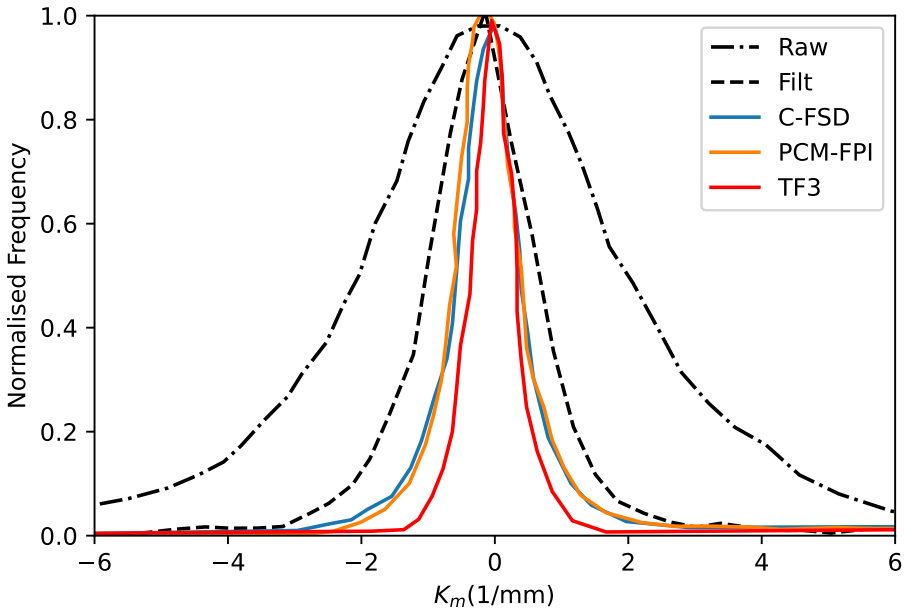

Fig. 5.49 Mean curvature distributions for different LES methodologies. Adapted from Hernández-Pérez et al. (2011).

snapshots was taken a very short time delay after restarting and the only object of concern is the thickness profile along the flame front. The first case is a continuation with the same model and as expected there is no change. Next is the no model approach (NM) where the effect of thickening previously is made obvious as the flame zone shrinks and gradients reestablish their original forms. However this new form the flame tries to approach is so sharp that for such a coarse grid the simulation crashes. The alternative then to make the no model approach feasible is inclusion of the diffusive flux (DF) originally designed for shock capturing as done in the final picture. The simulation stabilises but the flame is obviously thicker than the NM case even without the use of an ATF model.

Thickening in a simulation can be thought of as two components: firstly there is thickening from a numerical point of view without which sharp gradients present in a flame cannot be solved on LES grids (at least for many schemes). Secondly there is thickening brought on by the ATF transformation of scales itself. The former is almost entirely nonphysical and needed just to ensure stability while the latter in an MATF framework is grounded in physical principles of transforming scales. By employing MATF the reliance on artificial dissipation terms is reduced since the transformed flame is smoother by nature, hence going further towards providing numerical stability without tainting the solution by introducing uncontrolled and somewhat arbitrary alternative measures.

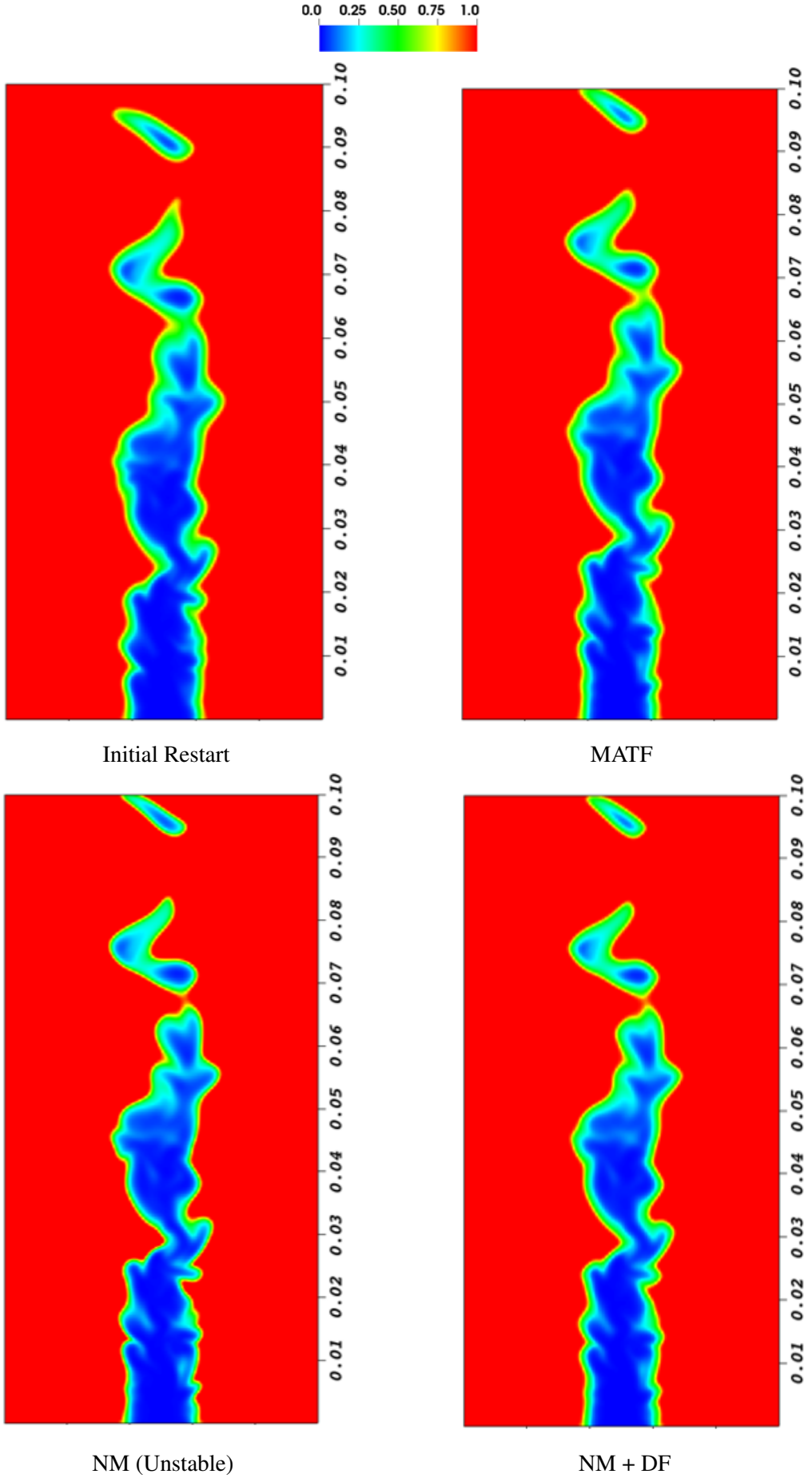

Fig. 5.50 A comparison between induced thickening for the case of MATF, no model (NM) and no model but inclusion of diffusive flux terms (NM+DF).

5.5 Summary

Flame-vortex interaction is commonly used as a simplified representation of turbulence induced flame wrinkling. The vortex size was chosen as such to ensure that the flame always appears *thick* in comparison as this is a well known weakness of ATF methods in general. Whereby conventionally, smaller vortices are no longer able to wrinkle the larger flame front and have traditionally relied upon efficiency functions. However the proposed modifications made to the standard ATF model were shown to be able to qualitatively capture the full range of behaviour even in strain dominated regions without requiring an efficiency function.

This was accompanied with excellent quantitative agreement in heat release rates, indicative of resolved total flame surface.Moreover since the model directly resolves scalar gradients in thickened regions it is possible to derive curvature statistics which otherwise would not have been viable with conventional LES alternatives. Most conventional LES alternatives would have either not directly resolved the gradients needed to evaluate curvature in the first place, or resulted in a smearing of the physical gradients via model parameters (such as an efficiency function for example). Close alignment of curvature distributions suggests it is feasible to extract meaningful conclusions regarding scalar structures (i.e. as they are identified based on curvature statistics) which in the past has been limited to DNS.

Very large thickening factors produced a qualitative change in some cases where the vortex was no longer able to induce local quenching and net heat release rate showed unexpected increases. By considering each reaction constituting the chemical scheme it is put forward that the latter is an unforeseen consequence of using multi-step chemistry, which has not been thoroughly reported in ATF literature. The changes in quenching behaviour are likely due to a complex balance of transients that are slightly distorted by the ATF model. Indeed the time to quench has been suggested to be in dependant of vortex strain (Meneveau and Poinsot, 1991), and by changing the time spent under quenching conditions the thickened solution fail to produce pocket pinch off. However this only happens at very large values of thickening factor that are well outside the recommended range of use.

The proposed model works well even for weaker vortices, suggestive of mitigating common weaknesses associated with classical ATF. Furthermore even if there are some instantaneous discrepancies these are for phenomena ocurring at very fast and very small scales. Thus do not preclude the methods application to a wide range of quasi-steady flames of relevance. The modified sensor was also shown to provide better agreements in heat release stemming from improved flame surface resolution.

Acoustically forced Bunsen flame exhibit strong local transients embedded into a globally periodic state. In light of a recent study in literature that demonstrated failure of classic ATF methods to capture flame dynamics even in simple configurations this was chosen as the next

validation case. Simulation parameters ensured that flow scales were well resolved but the internal flame structure was not. The proposed model performed exceptionally well across a range of dynamic scales, capturing the nature of acoustic-induced vortex roll-up of flame sheets accurately. Furthermore the method was shown to achieve grid independent solutions on coarser meshes than for DNS and also outperformed its classical ATF counterpart in both flame shape and heat release.

A novel transform is presented to map solutions from a thickened to unthickened state using a coordinate transformation. This technique holds immense relevance not just for an improved qualitative understanding of the flame state, but also in providing corrected statistics conditioned on progress variable or space for comparison with reference data. The method is cheap, can be performed *a posteriori* and very general in nature.

Following isolated model validation, focus is shifted towards incorporating the modified ATF approach into a unified LES-AMR-ATF framework to deliver a comprehensive computational tool. Specification of a filter width in LES-AMR poses substantial uncertainty due to multiple levels of refinement in the same simulation resulting in multiple simultaneous local energy cascades. Several simple approaches are proposed and subsequently tested using a subsonic jet configuration. Improper handling of the filter width was shown to generate spurious numerical artifacts and large mismatches in jet statistics.

For simulations employing a small number of levels, the most optimal out of proposed approaches was specifying a constant filter width based on grid size at the finest level. Benefits of this are two fold, firstly mitigation of commutation errors at the interface. These were noticeable even for the case of a single level jump and expected to be much more relevant in realistic configurations where the flow can cross multiple levels and also experiences temporal commutation errors. The second advantage of a larger filter width was improved jet statistics which are thought to be caused by an increased subfilter resolution. Where essentially the smallest scales that persist post-filtering are better resolved on the grid.

Using this to justify a more informed choice of filter width, the unified LES-AMR-ATF framework was tested by simulating an experimental turbulent Bunsen burner. General flame envelopes were well predicted even for the coarsest meshes which had a grid spacing slightly larger than laminar flame thickness. A small increase in mesh quality was soon to result in large improvements in resolving internal flame structure in a way that would be inaccessible for many other LES methods such as the mean curvature distribution.

Lastly the contributions to thickening in a simulation are decomposed into that induced by numerics or by MATF. It is shown that artificial flux terms designed to ensure stability of the numerical scheme can effectively introduce a numerical thickening of the flame front. Use of the MATF model reduces reliance on such arbitrary measures by inherently smoothing

out the regions of sharp gradients in a flame. In doing so replacing the otherwise arbitrary, difficult to estimate numerical thickening with an alternative that has a firm grounding in physical transformation of scales.

Chapter 6

Flame-Flame Interaction

Interactions between turbulent flames occur in wide array of practical applications, including land-based and aircraft gas turbines, rocket engines, boilers and furnaces. These interactions can influence the overall system by changing stability, flame structure,dynamics and attachment characteristics, blow-off limits, distribution of heat release and subsequent thermoacoustic response (Dawson and Worth, 2014; Samarasinghe et al., 2013; Worth and Dawson, 2012a,b). Staffelbach et al. (2009) conducted one of the first large scale LES of a complete annular helicopter engine with multiple burners. Showing for a particular configuration that several flames can be approximated with the same reduced order models used for an isolated flame (Wolf et al., 2009). However this conclusion in general cannot be extended to other configurations (Aguilar et al., 2015; Fanaca et al., 2010; Kwong and Steinberg, 2019; Smith et al., 2018; Wolf et al., 2012). As the flames or nozzles cluster closer together, merging of flow fields and preheat zones can drastically amplify interaction between neighbours thereby rendering models designed for isolated flames as lacking.

Adopting a macroscopic frame of view towards flame-flame interaction and its impact on system parameters is an important cornerstone for optimising device operation and understanding dynamic flame behaviour. However there exist a class of interactions that manifest at much smaller scales and play a crucial role in determining the local flame topology. Previously described as normal or counter-normal flame-flame interactions, these events are commonly observed in premixed flames and can have an additive effect on the global system across a much larger range of scales. Such flame-flame interactions can drastically impact local flame structure due to interplay between the preheat zone, inner layer and oxidation layer (Ranganath and Echekki, 2005, 2006). Where changes to heat and species distributions in the region lead to altered flame speed and propagation (Chen and Sohrab, 1995; Chen et al., 1999; Sun and Law, 1998), hence system dynamics.

LES is commonly used to simulate laboratory or industrial scale reactive systems, however many of these models require knowledge of flame behaviour at the subgrid scale. For example a family of methods rely on transport equations for the flame surface density (FSD) (Chakraborty and Cant, 2007, 2009; Hawkes and Cant, 2000; Ma et al., 2014), where the FSD correlates directly with turbulent flame speed (Filatyev et al., 2005). However appropriate modelling of subgrid FSD requires an understanding of mechanisms driving flame surface generation and destruction. A key element for the latter has been identified as mutual flame-flame interaction and quenching Meneveau and Poinsot (1991) and several models have been proposed (Duclos et al., 1993) to account for this despite limited experimental measurements and validation (Skiba et al., 2017; Tyagi et al., 2019b).

Therefore the work described in this chapter is motivated by the desire to better understand the nature of these small scale interactions. This is envisioned to be of significance not just for multi-burner scenarios found in modern devices but also for improved fundamental LES modelling by providing a statistical description of relevant events. The case also highlights the ability of the modified ATF model to provide meaningful inferences that would not be possible with alternatives LES methods.

Moreover to the author's knowledge there are no other LES studies currently in literature of scalar structures and how they relate to small scale flow topologies in the context of flame-flame interaction with multiple burners.

6.1 Simulation of Experimental Slot Flame

This section draws much of its motivation from the experimental campaigns of Tyagi et al. (2019a,b, 2018) that aim to quantify statistics for flame-flame interaction in the context of neighbouring slot flames. This was done using a flexible test rig containing two neighbouring high aspect ratio slot burners as shown in Figure 6.1, where the separation distance could be adjusted and the operating conditions varied. In conjunction with an automatic feature extraction algorithm (Ranganath and Echekki, 2006; Tyagi et al., 2019b) that compared subsequent OH-PLIF images to map the flame front transformation by local convection, the authors attempt to quantify interaction events.

Tyagi et al. (2019a) consider the effects of a neighbouring flow on self flame-flame interactions by igniting only one burner and having the second issue inert gas. Having a high shear mean flow on one side of a flame was found to cause inwards bending due to increased entertainment in the downstream section. In the near field differences were noted in frequency of interaction events between the branch of the flame on the side of the inert flow and the outer side exposed to semi-quiescent conditions, highlighting the impact of coflow

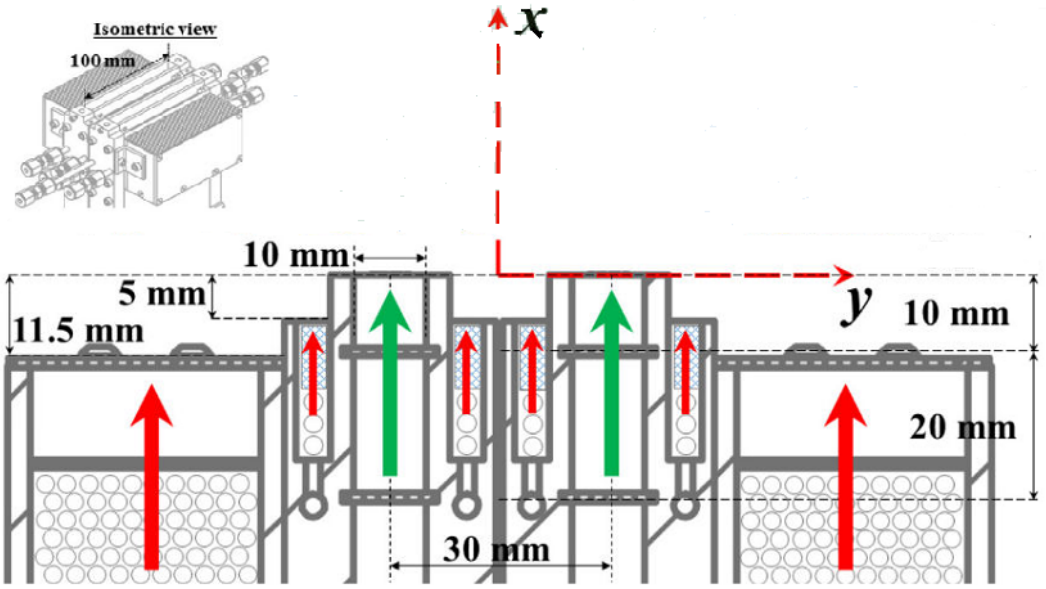

Fig. 6.1 Illustration of experimental test rig for dual slot flames. Green arrows represent fresh mixture while red arrows stand for hot co-flow products used to stabilise the flame. Adapted from Tyagi et al. (2019a).

dynamics. However these differences between sides of the flame were seen to diminish when traversing downstream as vortical structures from the base gradually decayed and flame elements merge at the tip. Negative biases in curvatures were found and suggested to be caused by a prevalence of cusping interactions which then decrease downstream.

Tyagi et al. (2019b) extend the latter on the same test rig to consider the case of two active flames next to each other when compared to an isolated burner. Comparing for a range of bulk flow velocities it was found that all flames bend away from the experimental center line and this was most pronounced at lower inflow velocities. Furthermore locally compressive strains were suggested to be a driving force for flame annihilation events. The addition of a second flame increased the amount of counter-normal interactions when compared to an isolated burner and vice versa for normal interactions. However for all cases normal interactions were found to be more likely and exhibited flame annihilation at comparatively larger scales than counter-normal interactions.

6.1.1 Computational Setup

In order to evaluate the proposed modified ATF model's capability to resolve internal flame structure in a realistic turbulent context, the full scale laboratory flame is simulated for

the case of an isolated burner. The general domain configuration is as as shown in Figure 6.2 which includes a progress variable iso-surface to illustrate significant resolved flame wrinkling. Grid stretching is employed with approximately 23 million points for a uniform mesh in the near field which progressively coarsens towards the boundaries (see Figure 6.3). Spatial limits of the fine region were determined primarily by the region from which experiments were able to extract measurements. The uniform zone has a resolution roughly of the order of the laminar flame thickness and is coupled with a thickening factor of $\mathcal{F} = 5$ and the proposed asymmetric flame sensor (see Chapter 2).

The inflow consists of a perfectly premixed methane-air mixture at unity equivalence ratio, 300K and 1 atmosphere. The experimental co-flows are approximated by a mixture containing the fully burnt products evaluated at chemical equilibrium. The bulk flow velocity is 12m/s with turbulent fluctuations superimposed at the inlet using an artificial turbulence generator. The corresponding hydraulic diameter based Reynolds number, turbulent velocity fluctuation, integral length scale, Taylor micro-scale, turbulent Reynolds number, and non-dimensional numbers of interest are summarised in Table 6.1. This constitutes a challenging case of particular relevance to the modified ATF model as the large flow scales are relatively well resolved based on experimental values of Λ_T/λ_T but the internal flame structure is not. Moreover this collection of parameters leads to a flame operating in the thin-reactions regime of the Borghi-Peters diagram. The two step BFER mechanism was used to model reactive chemistry and the ATF model was coupled with a standard Smagorinsky turbulent viscosity model with a filter width based on the local mesh. Due to smooth variations in grid size that occur only in regions away from the area of interest the impact of the latter is expected to be small (see Chapter 3).

6.1.2 Results

The proposed model qualitatively captures flame-flame interaction as evidenced by Figures 6.4-6.5 which facilitate a direct comparison between simulations and experiments. The nature

Table 6.1 Turbulence characteristics for experimental slot flame. Source Tyagi et al. (2019b)

Re_h	u' (m/s)	Λ_T (mm)	λ_T (mm)	Re_T	u'/ s_l^0	Λ_T/δ_f^0
15000	2.2	2.1	1.4	325	5.5	11.1

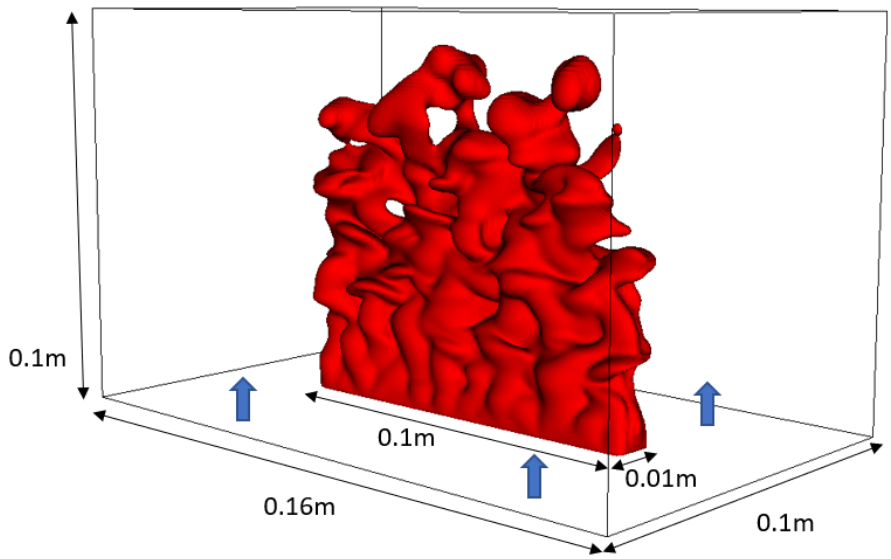

Fig. 6.2 General computational domain configuration for isolated slot flame. Red iso-surface of progress variable illustrates instantaneous flame wrinkling and blue arrows refer to coflows.

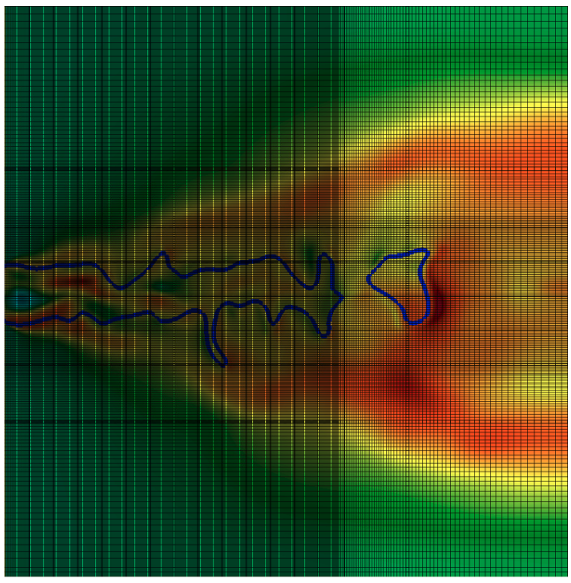

Fig. 6.3 Grid stretching progressively coarsens mesh away from the flame zone. Overlay of instantaneous velocity field and flame position (blue contours) are included.

and behaviour of both normal and counter-normal flame-flame interactions is accurately reproduced even in the thickened state. The normal interaction shown in Figure 6.4 represents the meeting of two flame elements along their natural direction of propagation followed by their annihilation. Depending on the size of the interaction there may or may not be subsequent pocket formation and an associated reallocation of flame surface. These events can occur across a wide range of scales and have complex three dimensional topologies.

A canonical counter-normal interaction is depicted in Figure 6.5 where a flame surface is brought into contact with another against its normal direction of propagation due to surrounding turbulence. In this case two flame elements merge and the process consists mostly of flame surface annihilation rather than generation. The latter is also possible whereby a product pocket is formed due to encircling of a small amount of product by surrounding mixture. In which case a secondary ignition source spreads through the mixture. However this is less likely than normal pocket formation as stronger local compressive strains (Tyagi et al., 2019b) are needed for large scale counter-normal interactions.

Figure 6.6 displays the same counter-normal interaction but with a vector overlay of the flow velocity. The interaction is a result of consecutive folds of flame surface propagating at different speeds and directions which coupled with significant wrinkling allows contact between elements on the product side. These interactions tend to occur in regions with large curvature and strong velocity fields as discussed in Dunstan et al. (2013a); making prominent counter normal interactions unlikely.

These interactions naturally may have complex three dimensional topologies. As illustrated in Figure 6.7 even if there is no interaction in 2D, there is the possibility of the flame colliding with an out of plane neighbour. Moving further downstream towards the tip region the flame pattern becomes highly three dimensional due to the large scale pocket formation and cavities in the reactive front. Figure 6.8 illustrates complex topological structures here as well as easily identifiable canonical tunnel closure and formation events. The general structure suggests that any progress variable conditioned statistics are likely to show a strong dependency on the actual iso-surface chosen even in the thin reaction regime. Depending on how deep tunnel formation events have penetrated into the flame thickness for example, samples data might vary significantly from iso-surface to iso-surface. The assumption of quasi-2D statistics due to the high aspect ratio of these burners might also be too optimistic here as pocket formation is inherently a fully three dimensional phenomena.

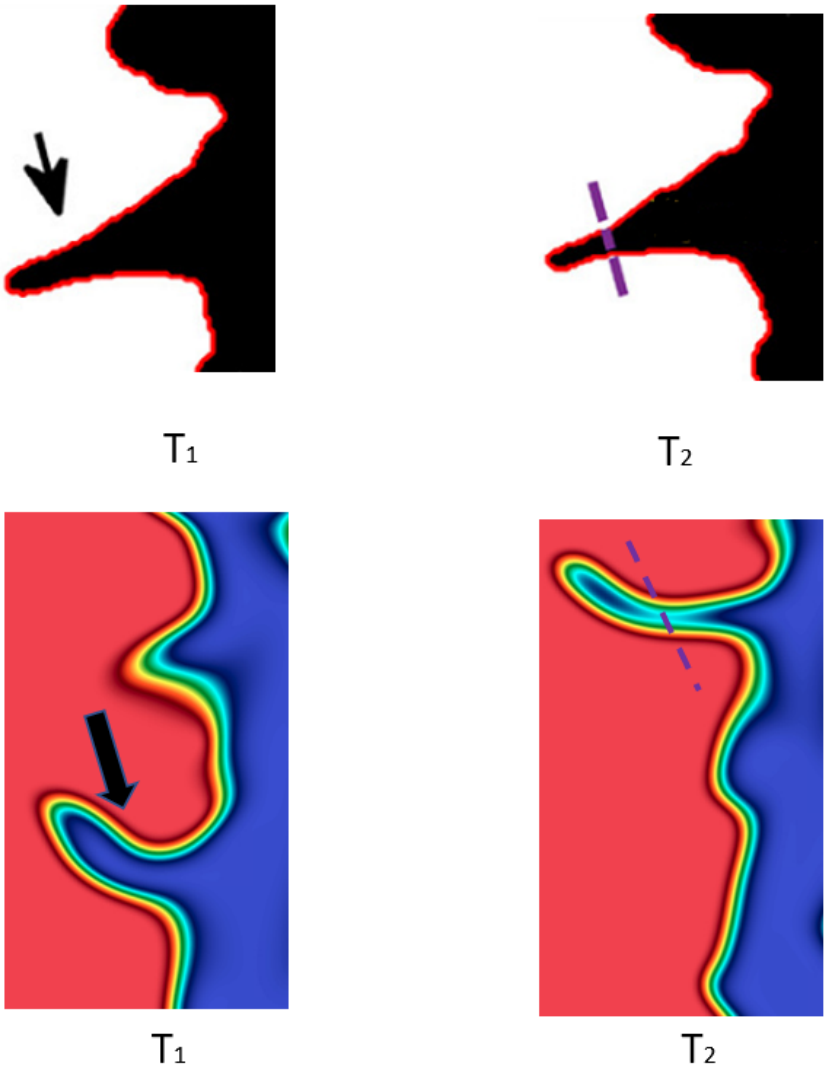

Fig. 6.4 **Normal flame-flame** interaction with dotted line indicating interaction zone. Experiments (top) use black for reactants and white for products with a red line to show flame surface (Tyagi et al., 2019b). Simulations (bottom) use blue for reactants, red for products and a color scale for the resolved flame structure.

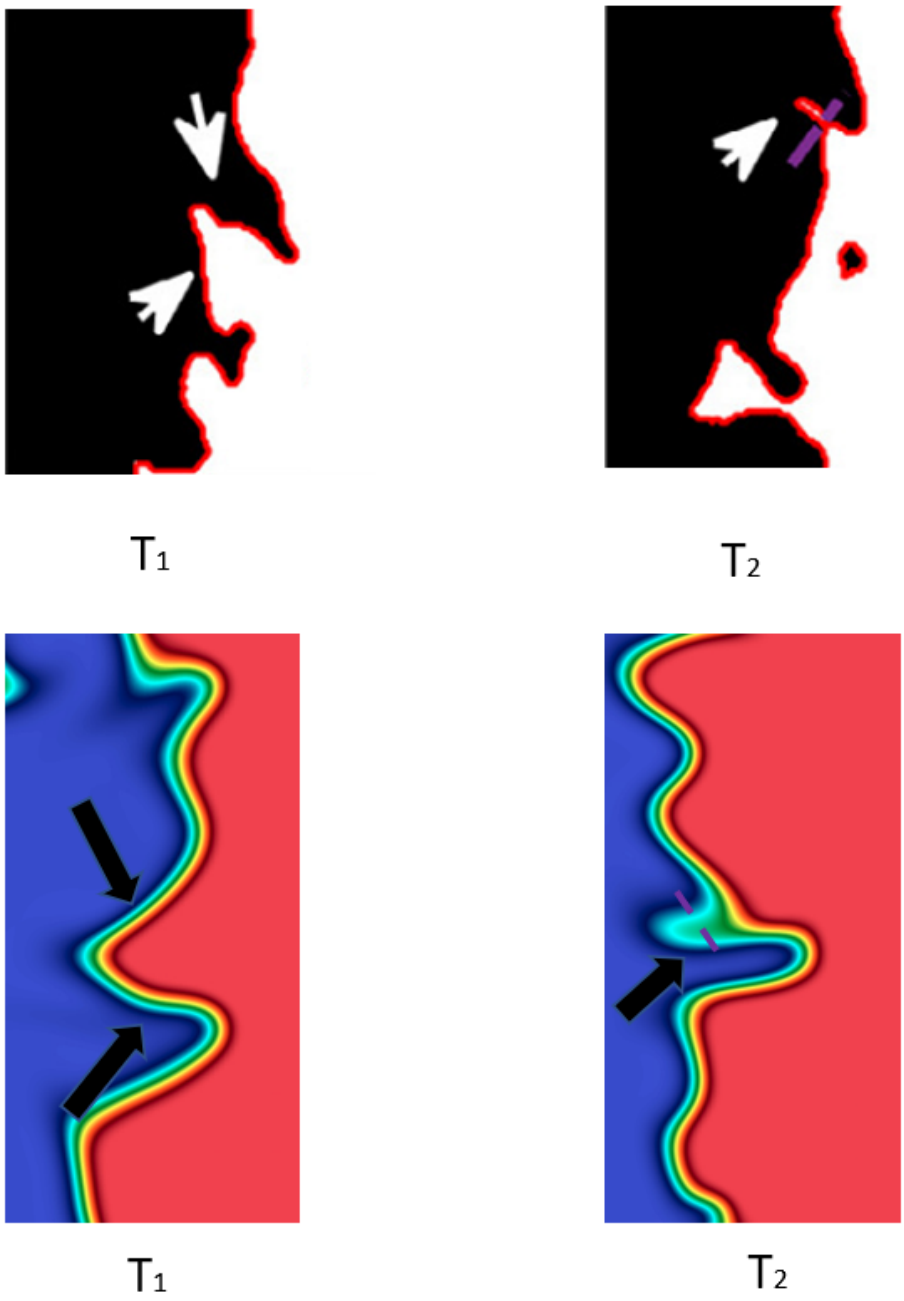

Fig. 6.5 **Counter-normal** flame-flame interaction with dotted line indicating interaction zone. Experiments (top) use black for reactants and white for products with a red line to show flame surface (Tyagi et al., 2019b). Simulations (bottom) use blue for reactants, red for products and a color scale for the resolved flame structure.

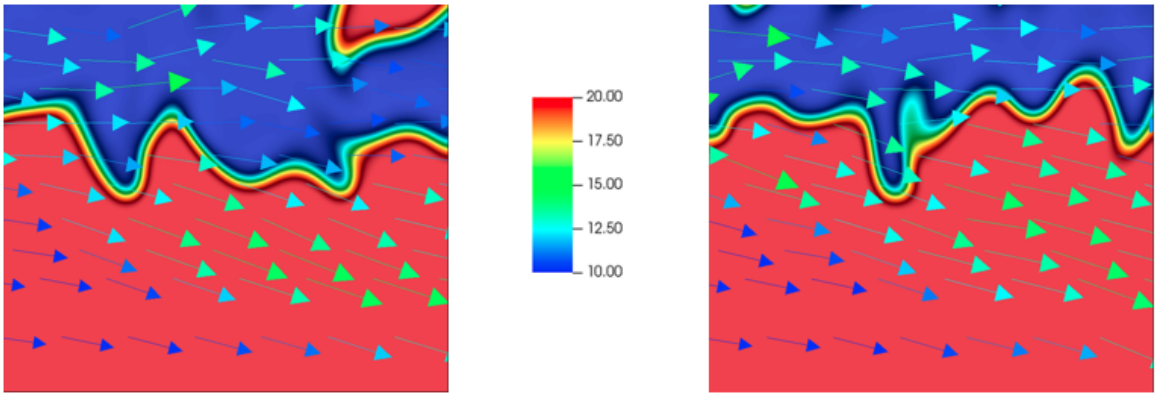

Fig. 6.6 Vector overlay of the velocity field during a counter-normal interaction as the flow pushes one flame fold into another due to local turbulence.

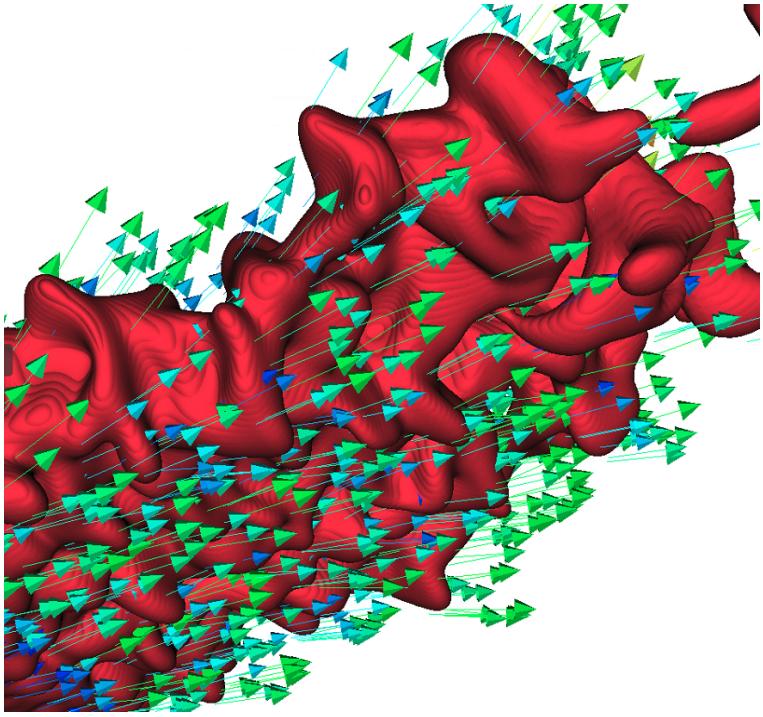

Fig. 6.7 Illustration of the three dimensional structure of both flame folds and the underlying flow field. Interaction events do not always occur in the same plane.

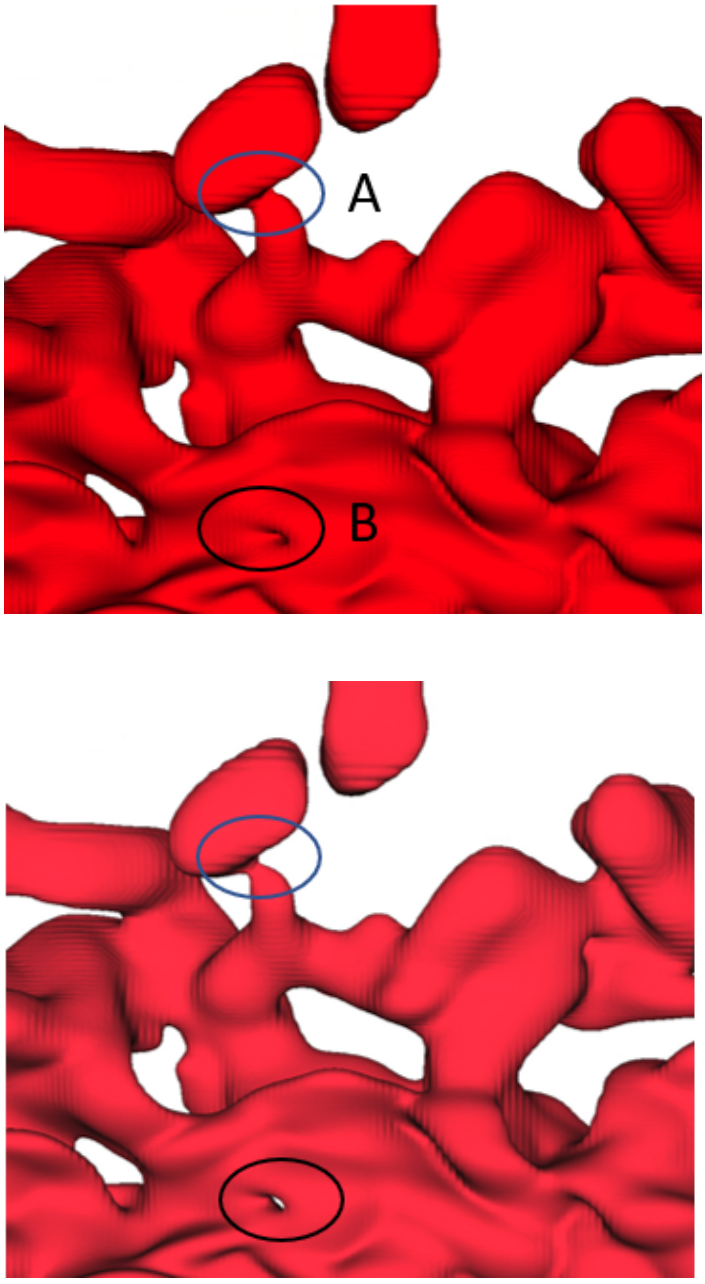

Fig. 6.8 Focus view near the flame tip illustrating a highly broken flame front with significant out of plane interaction. Tunnel closure (A) leading to subsequent pocket formation and tunnel formation (B) leading to a broken flame front are readily identified. The region is a complex mixture of flame surface annihilation and generation events.

6.1.3 Curvature

In order to investigate whether the relative distribution frequencies are preserved the subsequent figures present curvature statistics as a measure of the internal flame structure. Figure 6.9 contains the curvature statistics sampled in the near-field close to the inlet and its experimental counterpart. Overall excellent agreement is observed with the negative bias in the mean captured very well. There is some disagreement at the very tails of the distribution, however as this corresponds to very small radii of curvature this is not unexpected. Furthermore Appendix D discusses additional uncertainties related to experimental data such as co-flow parameters and degree of unsteadiness for the input turbulence that could help explain this.

Figure 6.10 also contains curvature statistics but is sampled further downstream where in general the results still agree reasonably well. The experimental mean shifts further back to zero which is reportedly due to decay of the strong vortical motions which modulate the flame surface further upstream (Tyagi et al., 2018). The simulation mean also exhibits a shift but not quite to the same extent. In addition to parametric dependencies shown in Appendix C, a suggested explanation for these discrepancies is dimensionality of the system. It has been suggested that these experimental flames are quasi-2D in order to justify experimental curvature measurements (Chen et al., 2007; Tyagi et al., 2019a; Yuen, 2009). Indeed the close agreement in Figure 6.9 suggests this to be a reasonable assumption. However in the downstream region the flame has been shown to accrue an increasing amount of inherently 3D phenomena such as pocket formation, tunnelling events and burnout.

Figure 6.11 therefore shows the same experimental data but compared to a 2D evaluation of simulation curvature where excellent agreement is reached once again. This suggests that the assumption of quasi-2D may not be valid across the entirety of the flame front which highlights the potential impact of interaction events on flame structure. In doing so demonstrating why a better understanding of interaction events is needed for more robust combustion modelling.

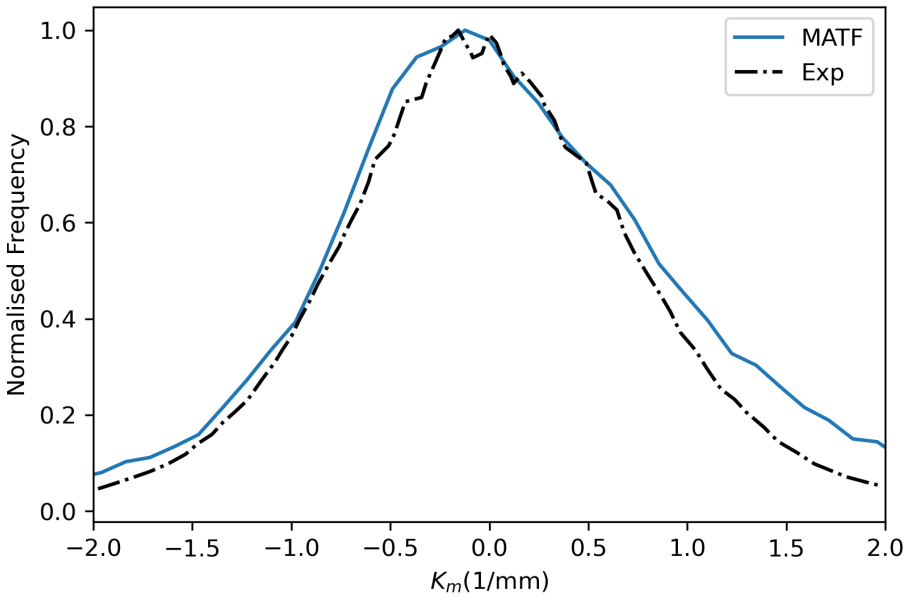

Fig. 6.9 Curvature statistics samples in the field of view close to the inlet.

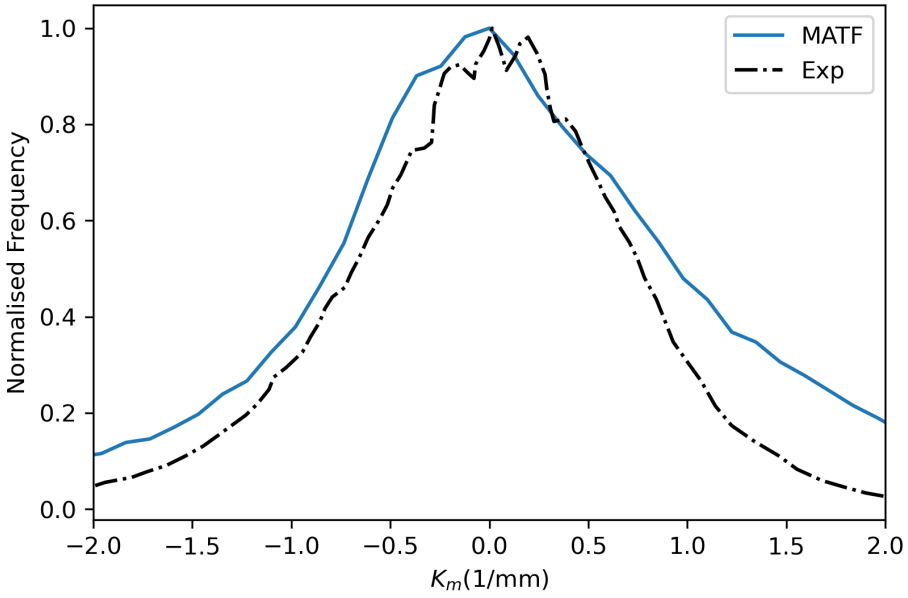

Fig. 6.10 Curvature statistics sampled in the field of view downstream.

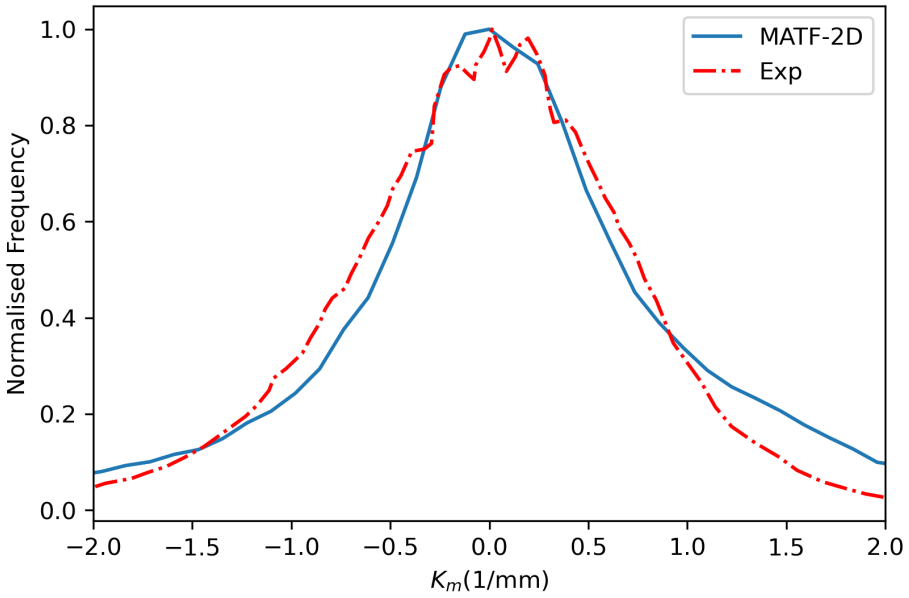

Fig. 6.11 Curvature statistics sampled in the field of view downstream

6.2 Dual Flames

The experimental slot flames have a high aspect ratio (10 : 1) in order to limit out of plane boundary effects for data sampled at a cross-sectional slice. One such flame has been simulated in the previous section to demonstrate the proposed approach and its modelling capabilities, however inclusion of a second burner with the same mesh quality results in a doubling of required grid points. In order to mitigate computation costs a model problem is now proposed which takes inspiration from the experimental setup. Whereas the general configuration remains as reported in Tyagi et al. (2019b, 2018) however the burner aspect ratio is halved to (5 : 1). Impact of this modification is assessed by repeating the isolated flame simulations once again for the new geometries before comparisons with a dual setup.

6.2.1 Computational Setup

System parameters remain identical to Section 6.1.1 with changes limited to the mesh and inflow configuration. By halving the burner out of plane dimension the required mesh points to maintain the same resolution is reduced to around 11 million per flame i.e. approximately 22 million total for dual burner simulations. A uniform mesh is ensured across the flame region with gradual stretching/compression in between burners and progressive coarsening towards the boundaries to provide computational domains shown in Figure 6.2. The burner

separation distance is varied from 30mm which corresponds to the closest experimental case (Tyagi et al., 2018) to 20mm along with two different bulk velocities of 12m/s and 20m/s as summarised in Table 6.2.

Table 6.2 Parameters for model dual flame simulations.

Simulation	Burners	Inlet velocity (m/s)	Separation distance (mm)	u' (m/s)	Λ_T (mm)
A	single	12	-	2.2	2.1
B	dual	12	30	2.2	2.1
C	dual	20	30	3.6	2.3
D	dual	12	20	2.2	2.1

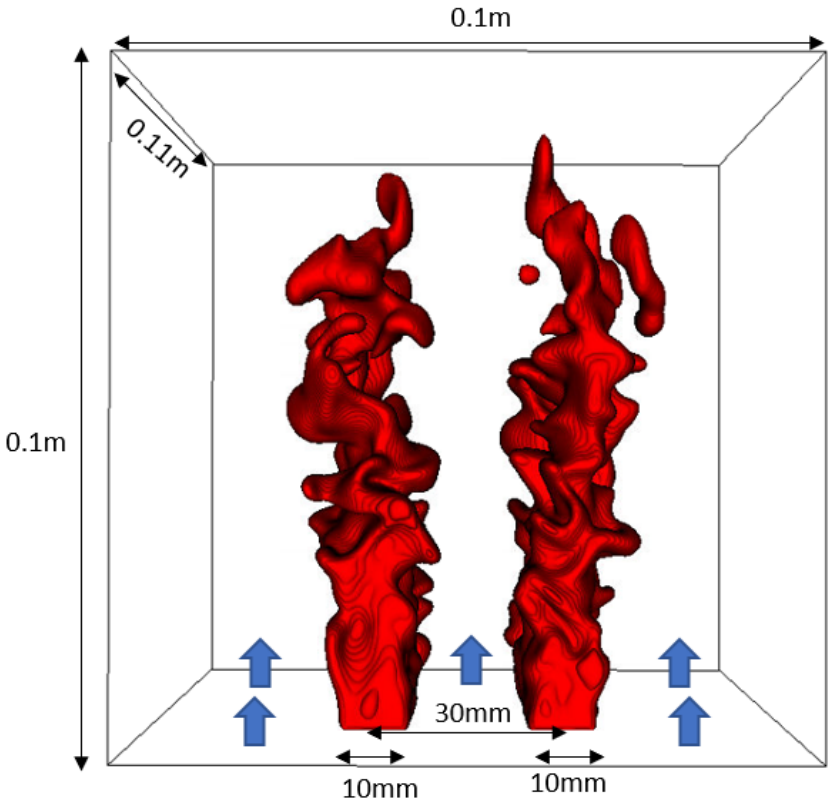

Burner configuration for Cases A-C.

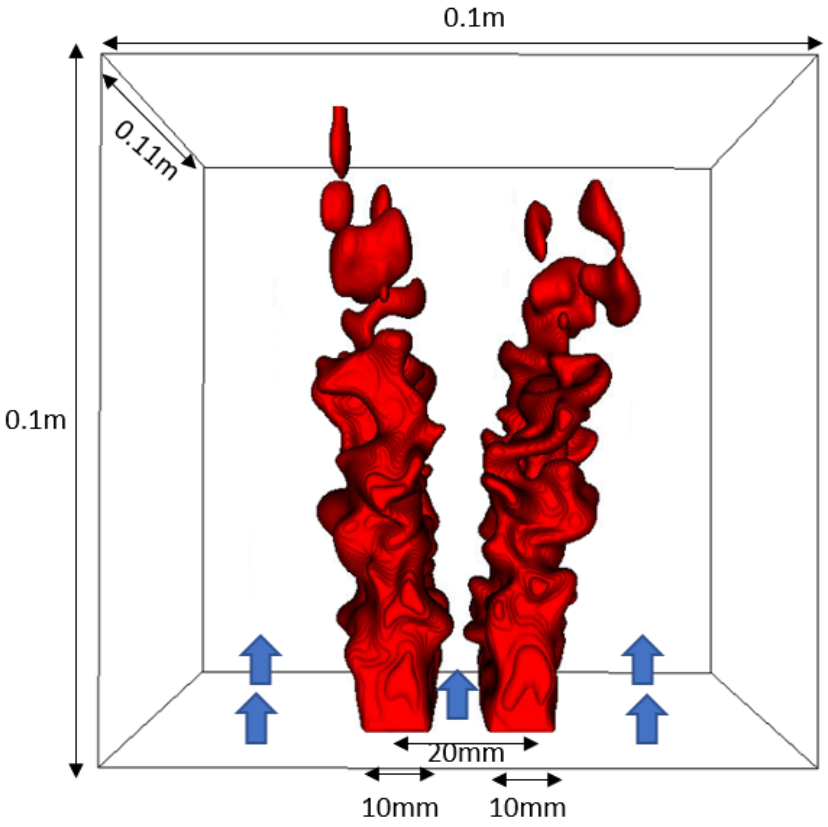

Burner configuration for Case D. Note increased flame spreading away from center-line.

Fig. 6.12 Flame iso-surface illustrated using progress variable for different burner spacing. Blue arrows indicate coflows of burnt products.

6.2.2 Results

To appreciate the implications of a reduced aspect ratio, Figure 6.13 compares the curvature distribution from an isolated, smaller flame to the isolated, larger experimental flame. Excellent agreement is observed across both fields of view, and the shift in mean away from a negative bias downstream reproduced accurately. The slightly wider distribution downstream is a likely consequence of uncertainty in turbulence specification at the inlet as expanded on in Appendix D. Therefore it is expected that the trends inferred from this model problem are readily extendable to the experimental configuration and subsequently many areas of practical interest.

Figure 6.14 illustrates the scalar topologies using the joint curvature PDFs where the scaling relation discussed earlier for curvatures has not been applied as the topic of interest is simply the trend and not actual values. The negative bias observed in both experimental and simulation mean curvatures for an isolated flame previously seems to correspond to the upper left instead of lower right quadrant predominantly. Recall these sectors represent elliptic concave and saddle concave structures. This corresponds well with the previous visual inspections where significant elliptic flame wrinkling was observable. The high density region at the center is also slightly elongated along the horizontal axis suggesting a notable present of weakly tiled structure for the case of an isolated flame.

The addition of a second flame brings with it several prominent changes to the previous distribution however the left quadrants still remains the most likely overall. Based on the topography of concave structures described in Figure 2.4, they are intuitively understood to have a high likelihood of flame elements coming into contact in the direction of normal propagation. Therefore their preference is a good indication of normal interactions remaining the most likely with agrees well with experimental observations.

Despite this Case B also exhibits a clear reduction in concave (see Chapter 2) structures when compared to Case A. Furthermore there is an increased presence in mostly the top but also bottom right quadrants, indicative of elliptic convex and saddle convex topologies. With the former being a readily identifiable precursor to the canonical counter-normal interaction shown in Figure 6.5 for example, these findings suggest a relative increase in counter-normal interactions upon inserting a neighbouring flame. This once again concurs well with experimental findings while also adding to it by isolating which particular scalar structures might be the relevant causes.

Figure 6.15 displays two supplementary dual flame configurations in order to better understanding impact of burner spacing and flow speed. Increasing the flow speed seems to spread the distribution further out, implying the formation of structures across a wider range of scales. It is likely this is a key precursor to the more frequent flame-flame interactions

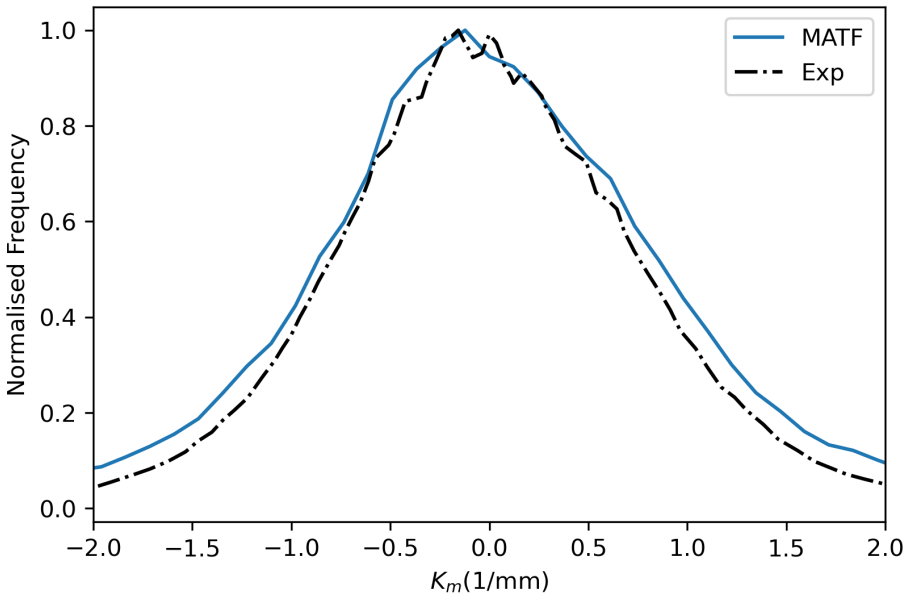

Upstream field of view.

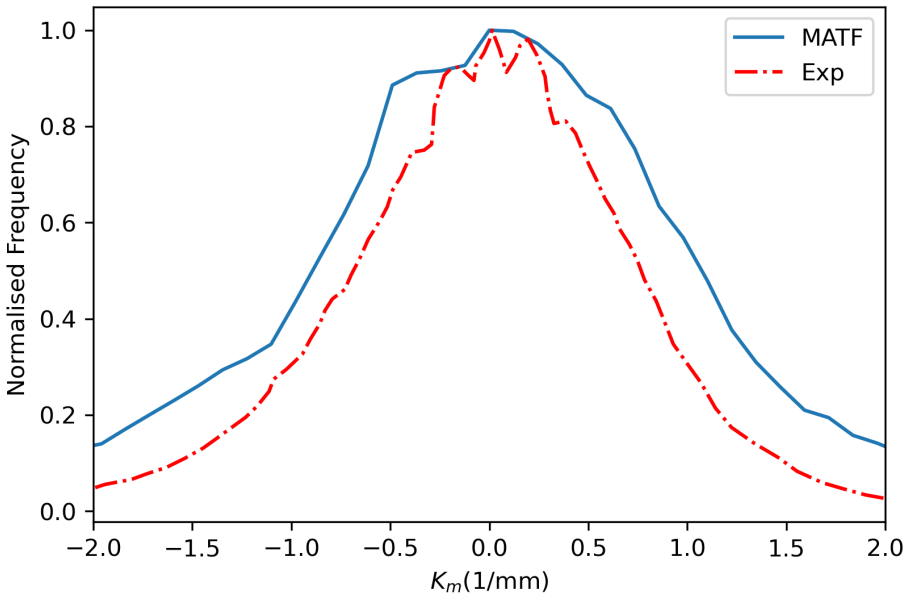

Downstream field of view.

Fig. 6.13 Curvature distributions for the model case compared with the experimental configuration.

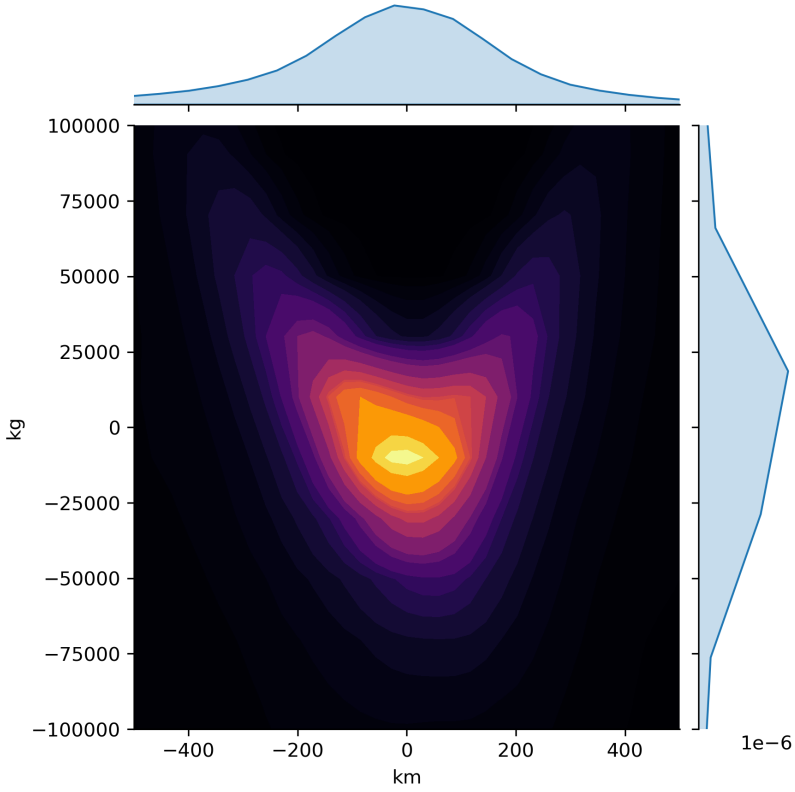

Case A - Single flame at 12m/s.

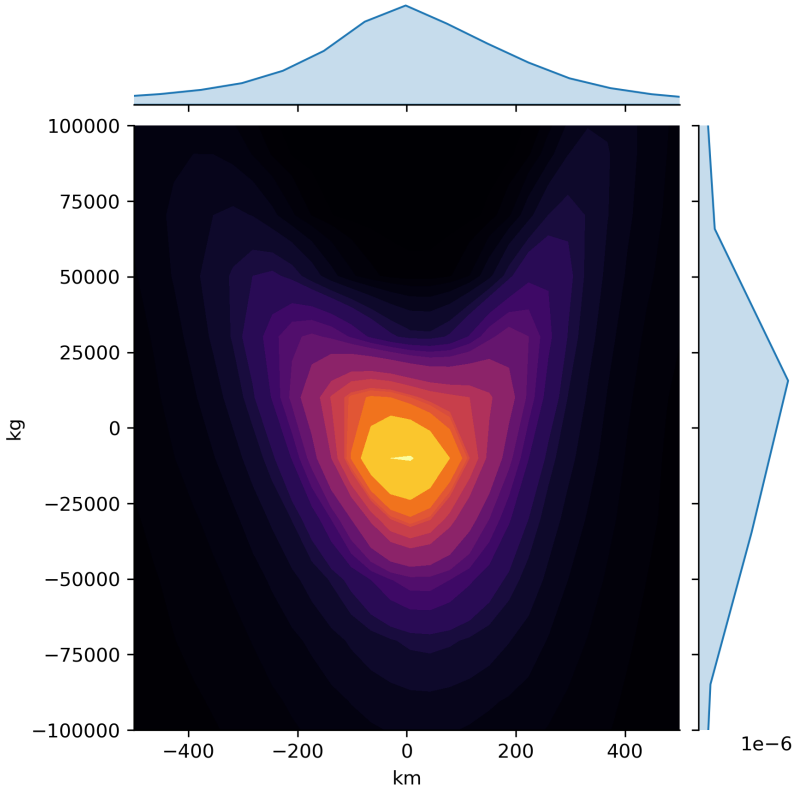

Case B- Dual flames at 12m/s.

Fig. 6.14 Scalar topology distributions mapped in curvature space.

for faster flames reported experimentally. This spreading occurs in all directions, therefore a strong presence is still retained in the top left quadrant making it difficult to speculate on the individual impacts of a second burner and higher flow speeds when compared to Case A.

The degree of axial elongation for the central regions does slightly decrease, suggesting more elliptic/saddle like structures rather than weakly curved tiles. Furthermore compared to Case B there is also an extension into the right quadrants which suggests the stronger flow fields help increase likelihood of counter-normal interactions as expected. Unlike previous simulations Case D is close to showing a slight preference for convex over concave structures. This suggests a significantly increase chance of counter-normal interactions which is well explained by the merging flow fields and proximity of neighbouring burners. Some of the wrinkles were close to impacting folds on its neighbouring burner after all as seen in Figure 6.12 near the base. Furthermore the flames were also seen to open up more away from the center-line at such close spacing, this implies increased stretch on the inner flame side but also increased compression on the outer branch. With the latter having already been discussed as a key component for facilitating larger scale counter-normal interactions. It is of note that all the experimental flames found a preference for normal interactions. However such a small spacing is beyond the minimum recorded in corresponding experiments, these findings thus demonstrate the global shift of behaviour away from expected trends as flame-flame interactions intensify.

In summary it appears that a second flame tends to increase counter-normal interactions by creating more convex topologies. While concave do remain relatively more likely unless for very small burner spacing. With the impact of higher bulk velocity primarily being an increase in interaction events across all scales.

To better understand causes for these structural changes in the flame iso-surface, Figure 6.16 shows the different flow topologies observed across the flame for each case. General trends are in close alignment with literature (Cifuentes et al., 2016, 2014) in that the flow is mostly dominated by S2 which is characteristic of premixed flames. Focal topologies are expected to disappear in favour of nodal alternatives due to destruction of vorticity by positive dilatation and increased temperature. Indeed this is is clearly observed for S1,S4 and S7 across all cases whereby they mostly exist on the fresh ($Y < 0.5$) side. Compressive topologies such as S1 i.e. Unstable Focus Compressing (UFC) and S5 i.e. Stable Focus Compressing (SFC) are very rarely seen in premixed flames as they usually occur in regions of negative dilatation. There is a considerable amount of S1 observed however and this is the likely case of flame folds interactions with each other as well as bending away from center-line cause the flow to experience local compression. The unstable nature of this is adequately represented by the favourability of UFC and almost complete absence of SFC.

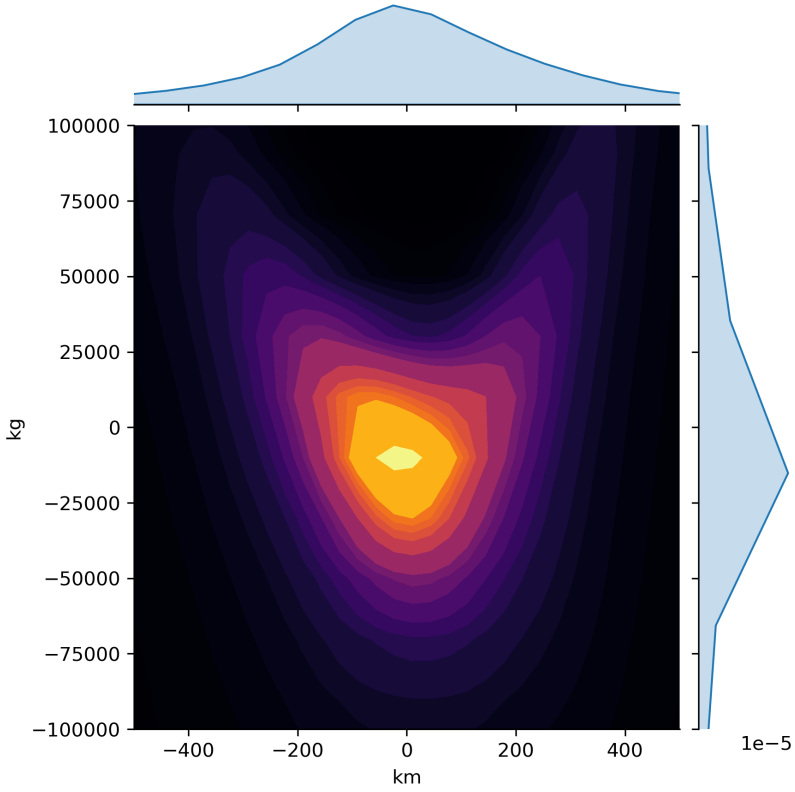

Case C - Dual flames at 20m/s.

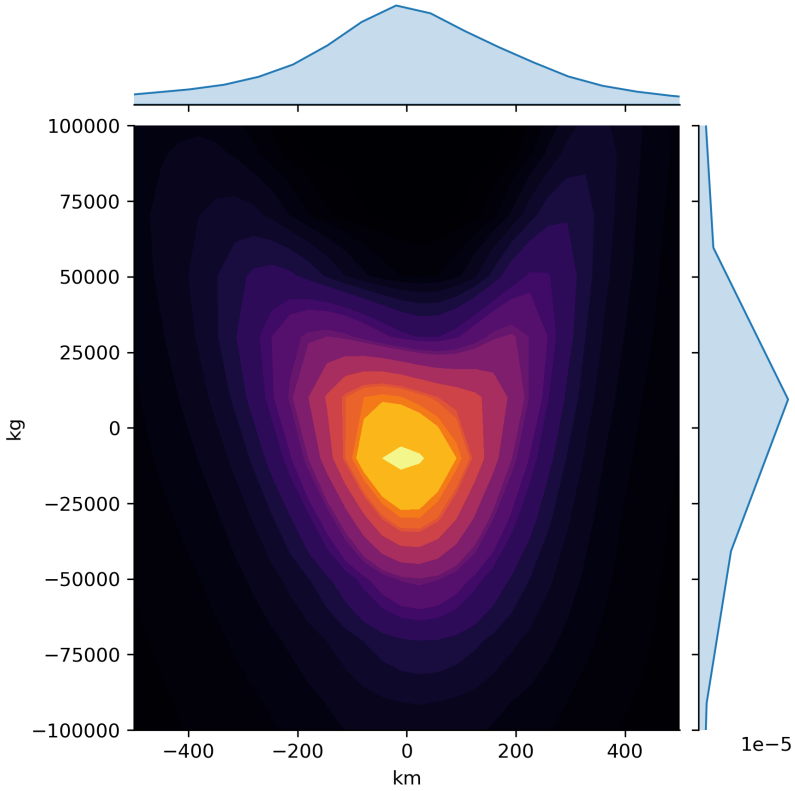

Case D- Dual flames at 12m/s and 20mm separation.

Fig. 6.15 Scalar topology distributions mapped in curvature space.

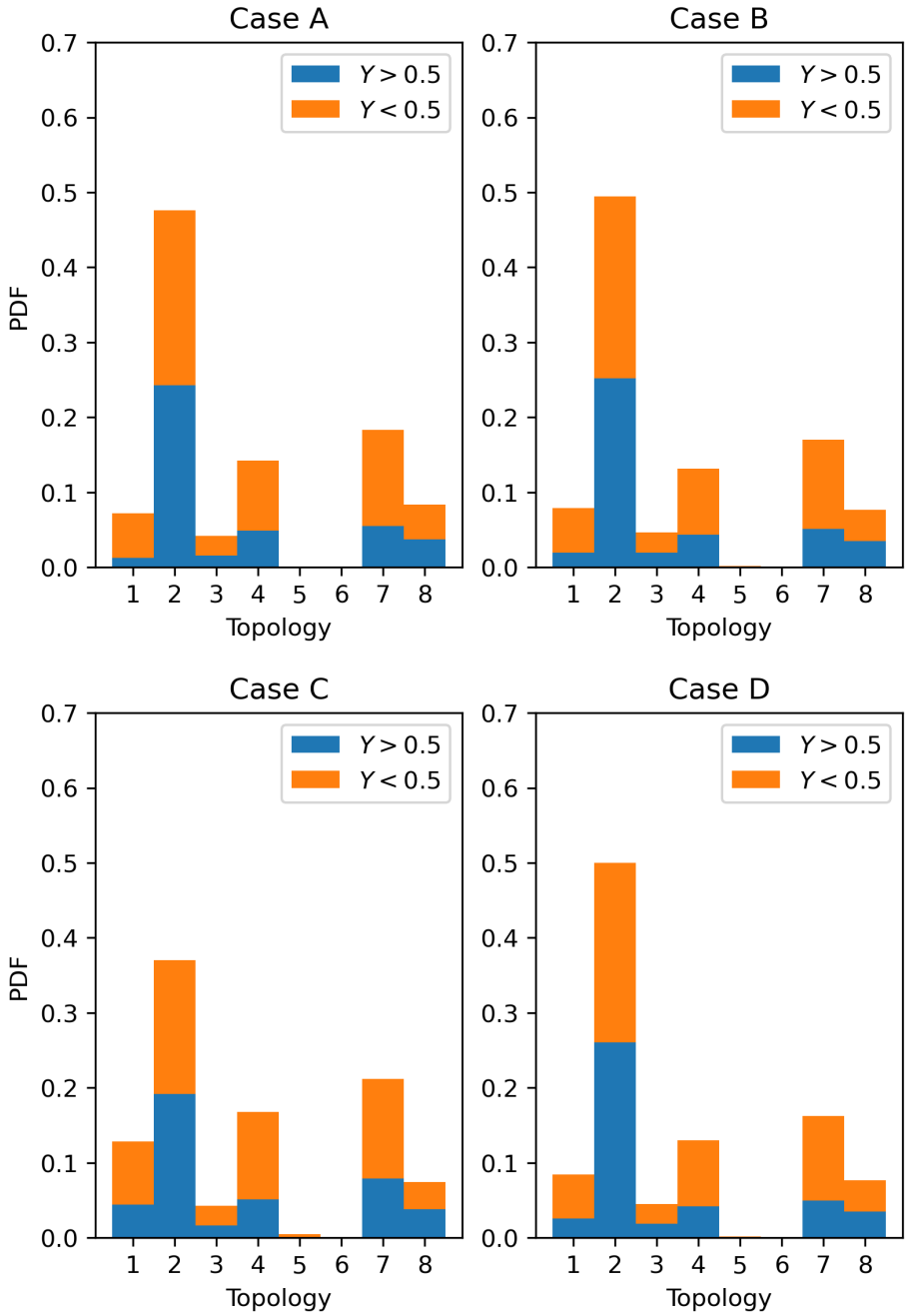

Fig. 6.16 Local flow topologies within the flame zone. Split in terms of progress variable to highlight impact of flame front.

In order to correlate the flow topologies for each burner with corresponding scalar structures, Figure 6.18 first presents a conditioning of the former on the latter. The cases for both a single and dual flame are presented just to highlight that even if the values differ the following trends still apply to either, suggesting some degree of generality. Moreover concave structures seem to have a higher correlation with S2 than convex ones. Since S2 is dominant in all the cases of Figure 6.16 this helps explain the higher likelihood for concave structures and subsequently normal flame-flame interactions.

However convex structures show a stronger correlation with compressive topologies such as S1, which were shown to increase for the cases of a second flame. Therefore increased S1 brought upon by outward bending and compression is a likely pathway for the increase in counter-normal flame-flame interactions observed in dual flames. The largest increases in compressive topologies came with the case of a second flame coupled with higher velocity. It is difficult to isolate how much of this was due to bending compared to increased turbulence born mixing. As the rise was larger than Case D where the flames spread out more the latter is a likely candidate.

Elliptic convex structures also have a stronger correlation with compressive flow topologies such as S1 and S5 than saddle convex as shown in Figure 6.19. Which explains why the majority of increased precursors to counter-normal interactions were observed in the top right quadrant as opposed to bottom right when a second flame was added.

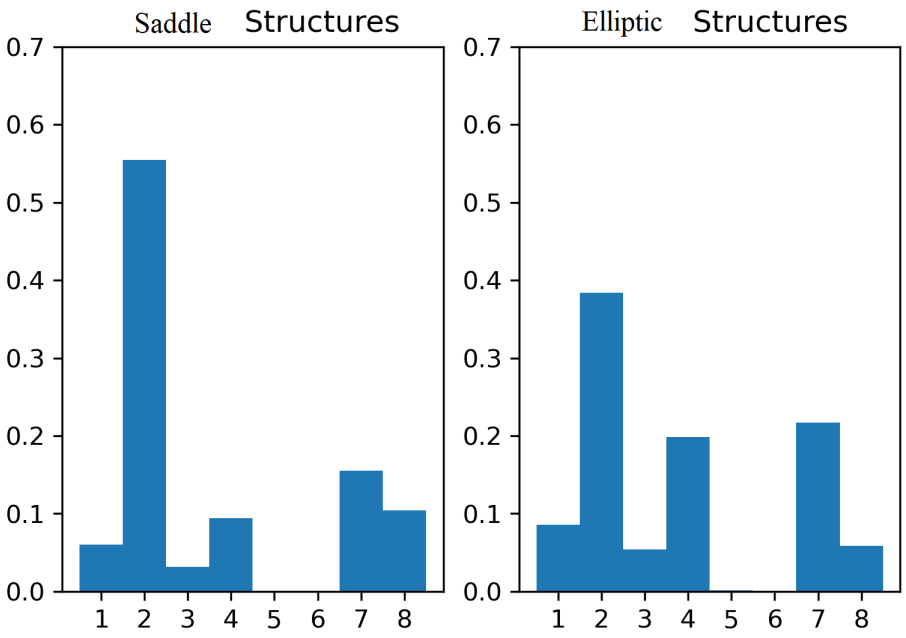

Case A- Single Flame

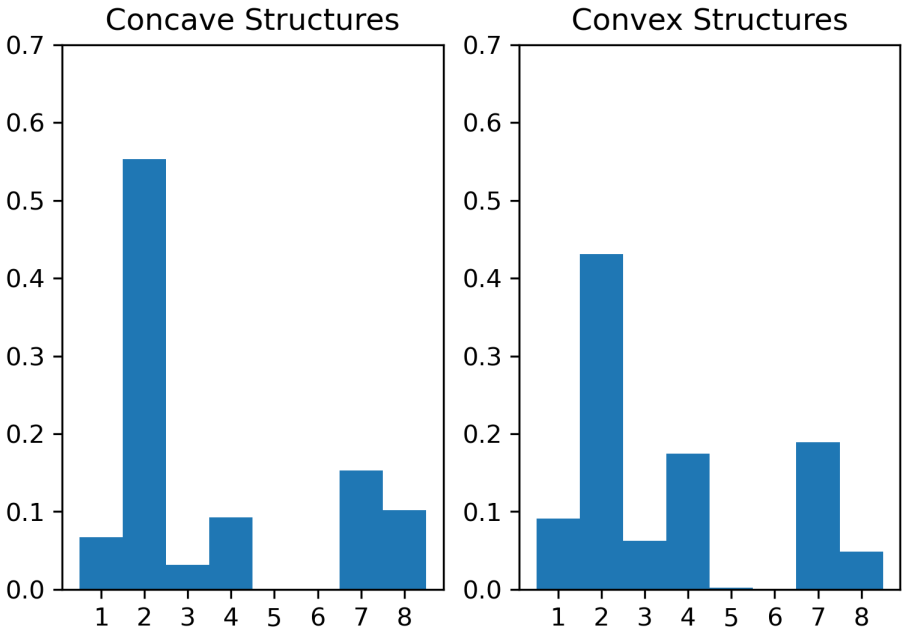

Fig. 6.17 Case B- Dual Flame

Fig. 6.18 Local flow topologies conditioned on type of scalar structure.

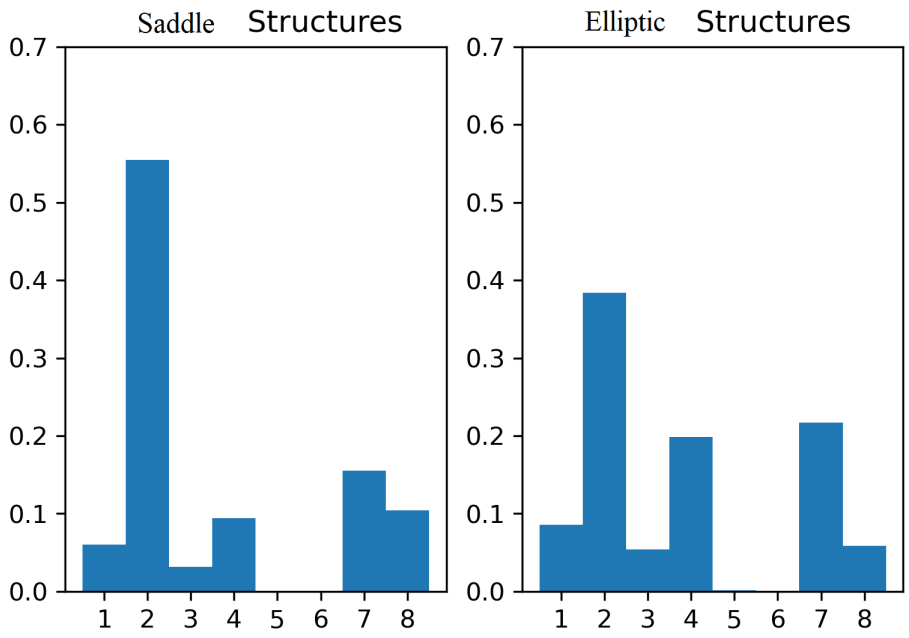

Fig. 6.19 Local flow topologies conditioned on type of convex structure.

6.3 Summary

A full scale turbulent experimental was simulated using the modified ATF model being proposed. This was done on realistic LES meshes that resolve large turbulent scales but not internal flame structure. Flame-flame interactions were captured for a range of canonical configurations. Including tunnel closure events leading to fully 3D large scale pocket formation which is often difficult to capture experimentally due to limited optical access. In general, modelling approaches are optimised to work best within specific combustion regimes and can have compromised performance outside of established regions of validity. However interactions were shown to result in a locally broken and complex topological flame front, highlighting the need for a better understanding of their dynamics for improved combustion modelling.

Close alignment of statistical curvature was demonstrated, suggesting the potential of the approach to make meaningful inferences about small scalar structures, with the method providing a means for comparison with experiments that would otherwise be restricted to the realm of DNS due to a dependency on resolved gradients within the flame front. The influence of uncertainties at the inlet were also presented and include the impact of quantifying unsteadiness in turbulence generators and approximating experimental coflows.

Note this could not have been done with the conventional ATF approach due to artificial smearing of gradients by the efficiency function

Following this the effects of adding a second flame on local scalar and flow topologies was investigated. A second flame was shown to increase compressive flow topologies which correlate more towards convex scalar structures. The latter corroborates experimental findings of increased counter-normal flame interactions upon addition of a second flame. Moreover by exploring the fundamental driving forces behind this increase, in terms of flow and scalar topologies, important groundwork has been laid for better understanding how to predict their occurrence and impact on global system parameters. Indeed the large difference in recovery times between counter-normal and normal interactions might be of significant importance for multi-burner configurations undergoing thermoacoustic instability.

Chapter 7

Conclusions

This thesis has contributed to wide array of research directions and delved into many different facets relevant to the LES of compressible reactive systems. In summary, outcomes can be classified into one of three categories namely the study of boundary conditions and general code development, combustion modelling and study of flame-flame interaction. Key findings and achievements with respect to each are summarised below.

7.1 Development of an in-house flow solver

- Various discretisation schemes were implemented into CompReal. Their corresponding strengths and weaknesses were evaluated prior to choosing the option most suited for envisioned research goals.
- Adaptive Mesh Refinement functionality was incorporated into the code.
- Navier-Stokes Characteristic Boundary Conditions were reviewed and both temperature and pressure based versions implemented.
- Retention of chemical source terms was found to provide little benefit in contrast to previous findings in literature.
- The standard NSCBC formulation was extended to axisymmetric configurations by proposing an additional source term. Inclusion of which was found to reduce spurious noise generation by up to $\approx 50\%$ in such configurations.
- Lingering open questions in the realm of NSCBCs were highlighted and possible solutions suggested. These include choice of relaxation parameters, inflows decoupled from the outflow and reversed flow in the presence of compositional inhomgeneities.

7.2 Combustion Modelling

- A modified artificially thickened flame model (MATF) coupled with a novel flame sensor was proposed (Rathore and Navarro-Martinez, 2023). The method does not require an efficiency function which can be difficult to determine, impact accuracy and has limited regimes of validity.
- The formulation was tested across a variety of configurations and demonstrated to better preserve flame-turbulence interaction than many alternatives.
- Similar to the approach adopted for classical ATF by Colin et al. (2000), the canonical case of flame-vortex interaction was used to investigate if the thickened flame *a priori* is less prone to wrinkling. The proposed approach showed good agreement with DNS for even the most challenging cases i.e. small and weak vortices.
- An acoustically modulated flame was used to demonstrate the ability of the model to handle large flame dynamics where there is significant movement of the flame front. Even the convection of disturbances in the flame front through a shear layer was reproduced with reasonable accuracy, suggesting a wide range of potential applicability.
- The approach is accompanied by the proposal of novel scaling laws for curvature and a simple reverse transform to obtain unthickened solutions which retains immense generality.
- Good prediction of flame curvatures suggest meaningful inferences about small scale flame structures can be made. This is only viable because the modified ATF model can directly provide an approximation for resolved gradients in the flame front where the use of an efficiency function would create numerical smearing.
- The main limitation of the approach is the requirement of relatively well resolved flow scales prior to transformation. In theory this limitation can be overcome by refining the mesh around the flow since it is a much less stringent condition than DNS. In practice this restricts the method to regimes of low to medium Karlovitz numbers.
- Despite the latter, prudent application of MATF can provide significant computational savings over DNS while simultaneously providing information that may not be available via conventional LES. Consider the case presented earlier of a turbulent Bunsen flame where having just one or two grid points in the (unthickened) flame provided excellent agreement of global flame statistics. This is a computational saving of the order of 7-9 times when compared to DNS in *each dimension* for a total potential

reduction by a factor 343-728. Moreover this may further be enhanced in some cases by increasing the thickening factor.

- Furthermore the new method has been shown to achieve grid independence faster than DNS. Therefore is a promising bridge between coarse mesh LES methods and fine DNS grids.

- In practice how much parameters such as mesh resolution and thickening factor can best be leveraged to maximise computational savings depends on the objective. In general, global flame behaviour such as mean flame length/position will place a weaker emphasis on grid requirements compared to statistics such as curvature that require resolution of the internal flame structure. Albeit even then the method was shown to provide a good approximation at a fraction of the cost of DNS. Moreover if the system of interest is quasi-steady and differences in instantaneous transients can be neglected, there is much more leeway in terms of model restrictions that can be utilised.

- The method is uniquely well poised to take advantage of AMR since there is no explicit dependence on the local filter width for any tuning parameters. A unified LES-AMR-ATF framework was correspondingly implemented and evaluated.

- It could be argued that an efficiency function tries to account for all scales (up to a certain cut-off) including those below the filter width while the MATF approach requires flow features to be seen on the original mesh i.e. something that is not seen cannot be transformed. However this is really a irrelevant comparison, as the real strength of the model is being able to get accurate results *without* an efficiency function, thereby making the approach more general and simpler.

- It is true that there are limitations on how well flow dynamics are preserved as the sensor implies a localized transformation This effect applies to the entire family of ATF models (both CATF and MATF), where spreading the heat release across a large flame area affects the thermal expansion is reduced, with its subsequent impact in the flow field. However, the impact of MATF is smaller than the CATF as Damköhler number is preserved and the maximum thickening occurs in a very thin region within the center of the flame as determined by the sensor. For progress variables outside 0.1-0.9, the sensor value is $\Omega < 0.12$ (for a symmetric sensors, less for asymmetric) and thickening would be $\mathcal{F} = 0.88 + 0.12\mathcal{F}_0$, which implies a very modest modification of the flow field and impact of incoming vortices. This thickening would be smaller than the ”numerical thickening” associated with numerical schemes in the neighbourhood of the flame. Nevertheless, the choice of sensor will obviously impact dynamics, however

it is difficult to suggest an optimal choice for all cases which may depend on the flow/conditions. For example, it is unclear if the slope of an ideal sensor transition should be steeper or more gradual. While the latter implies a greater transition area with associated uncertainties it is possible that the former may distort the physical system.

- The question of *how much space is thickened*, becomes even more poignant in the region close to walls. Especially if the direction of propagation is normal to the surface and the *thickened* flame is extinguished as the boundary layer is also thicker. This case has not been examined here and the potential pitfalls of the approach close to surfaces are shared with CATF and many other approaches to turbulent combustion. Local refinement and moderate thickening in this area are likely to be required.

7.3 Flame-Flame interaction

- The MATF method was shown to resolve canonical flame-flame interaction types and also associated curvature distributions. This opens doors to study of scalar/flow topologies primarily restricted to the realm of DNS in the past.
- Inclusion of a second burner results in an increase of convex scalar structures. These are suggested to be the underlying precursor to increased counter-normal interactions observed in experiments.
- The observed convex scalar structures have a strong correlation with compressive flow topologies.
- Compressive flow topologies increase upon addition of a second flame. Likely due greater bending away from the center-line for slot flames studied here.
- The implications of reducing flame spacing or increase flow velocity are discussed and both were found to increase structures across wider scales.
- The most common configuration for each simulation was concave structures and this helps explain the prevalence of normal flame-flame interactions observed experimentally.
- Being able to differentiate between normal and counter-normal interactions can be important due to differences in their impact on global system behaviour. Understanding their different recovery time scales, heat release fluctuations and local flow dynamics

can lead to better combustion modelling strategies and system design. Therefore by highlighting the fundamental driving forces behind their development in terms of scalar and flow structures, it is hoped a strong step has been taken towards providing a more universal modelling approach.

7.4 Outlook

A promising novel combustion model that leverages retention of physics with model complexity has been presented and its implications for flame-turbulence interaction assessed. However there is room for new research directions to build on the approach here and some of them are mentioned below :

- Recent studies have developed novel flame sensors that dynamically tract a flame front and would provide a useful coupling with MATF. The subsequent consequences for multi-step chemistry remain to be quantified however.
- In theory the proposed approach could be hybridised with conventional efficiency functions to extend range of validity to higher Karlovitz numbers.
- Effects of preferential diffusion at non-unity Lewis number for complex systems warrant further investigation, but in principle should be straightforward.
- Transient responses should be evaluated across a wider range of frequencies in order to gauge ability to handle faster dynamics despite being in thickened time.
- The method in principle should be extendable to non-premixed flames as well, although this requires further study.

The study of flame-flame interactions remains a rewarding field of study in its own right with important implications for next generation gas turbines even in simple configurations. Promising avenues of research include :

- Applying the MATF model in configurations with acoustic forcing, particularly in the transverse direction. This also raises the question of how best to create inflow perturbations representing an aziumthal mode, should it be done in the axial inlet or transverse boundaries?
- Combine the identification of scalar topologies done here with image registration techniques to quantify changes in flame surface. This can then be used to relate the

changes in flame surface during an interaction even with the corresponding heat release fluctuation. Expanding on this will allow a better understanding of the heat release perturbations during thermoacoustic excitiation of multiple neighbouring burners.

- Explore topology distributions for realistic gas turbines and compare with conventional DNS, in conjunction with studies across a wider parametric range that preferably includes unstable thermoacoustic modes. If using a LES model the impact of walls and surfaces will have a key role for such configurations. Indeed there is often the question of how best to specify the wall boundary condition itself, with some arguing that the wall boundary condition should also be updated in time.

References

Agostinelli, P., Laera, D., Boxx, I., Gicquel, L., and Poinsot, T. (2021). Impact of wall heat transfer in large eddy simulation of flame dynamics in a swirled combustion chamber. *Combustion and Flame*, 234:111728.

Aguilar, M., Malanoski, M., Adhitya, G., Emerson, B., Acharya, V., Noble, D., and Lieuwen, T. (2015). Helical flow disturbances in a multinozzle combustor. *Journal of Engineering for Gas Turbines and Power*, 137(9).

Ahn, B., Indlekofer, T., Dawson, J. R., and Worth, N. A. (2022). Heat release rate response of azimuthal thermoacoustic instabilities in a pressurized annular combustor with methane/hydrogen flames. *Combustion and Flame*, 244:112274.

Almeida, Y. and Navarro-Martinez, S. (2019). Large eddy simulation of supersonic combustion using the eulerian stochastic fields method. *Flow, Turbulence and Combustion*, 103(4):943–962.

Andersson, N., Eriksson, L.-E., and Davidson, L. (2005). Large-eddy simulation of subsonic turbulent jets and their radiated sound. *AIAA journal*, 43(9):1899–1912.

Andreopoulos, Y. and Honkan, A. (2001). An experimental study of the dissipative and vortical motion in turbulent boundary layers. *Journal of Fluid Mechanics*, 439:131–163.

Aris, R. (2012). *Vectors, tensors and the basic equations of fluid mechanics*. Courier Corporation.

Aspden, A., Nikiforakis, N., Dalziel, S., and Bell, J. (2009). Analysis of implicit les methods. *Communications in Applied Mathematics and Computational Science*, 3(1):103–126.

Auzillon, P., Fiorina, B., Vicquelin, R., Darabiha, N., Gicquel, O., and Veynante, D. (2011). Modeling chemical flame structure and combustion dynamics in les. *Proceedings of the Combustion Institute*, 33(1):1331–1338.

Badia, S., Martín, A. F., Neiva, E., and Verdugo, F. (2020). A generic finite element framework on parallel tree-based adaptive meshes. *SIAM Journal on Scientific Computing*, 42(6):C436–C468.

Baillot, F., Durox, D., and Prud'Homme, R. (1992). Experimental and theoretical study of a premixed vibrating flame. *Combustion and flame*, 88(2):149–168.

Bake, F., Gaetani, P., Persico, G., Neuhaus, L., and Knobloch, K. (2016). Indirect noise generation in a high pressure turbine stage. In *22nd AIAA/CEAS Aeroacoustics Conference*, page 3004.

Bake, F., Richter, C., Mühlbauer, B., Kings, N., Röhle, I., Thiele, F., and Noll, B. (2009). The entropy wave generator (ewg): a reference case on entropy noise. *Journal of Sound and Vibration*, 326(3-5):574–598.

Balachandran, R., Ayoola, B., Kaminski, C., Dowling, A., and Mastorakos, E. (2005). Experimental investigation of the nonlinear response of turbulent premixed flames to imposed inlet velocity oscillations. *Combustion and Flame*, 143(1-2):37–55.

Ball, C., Fellouah, H., and Pollard, A. (2012). The flow field in turbulent round free jets. *Progress in Aerospace Sciences*, 50:1–26.

Balusamy, S., Li, L. K., Han, Z., Juniper, M. P., and Hochgreb, S. (2015). Nonlinear dynamics of a self-excited thermoacoustic system subjected to acoustic forcing. *Proceedings of the Combustion Institute*, 35(3):3229–3236.

Batchelor, G. K. (1952). The effect of homogeneous turbulence on material lines and surfaces. *Proceedings of the Royal Society of London. Series A. Mathematical and Physical Sciences*, 213(1114):349–366.

Bauerheim, M., Nicoud, F., and Poinsot, T. (2016). Progress in analytical methods to predict and control azimuthal combustion instability modes in annular chambers. *Physics of Fluids*, 28(2):021303.

Baum, M., Poinsot, T., Haworth, D., and Darabiha, N. (1994). Direct numerical simulation of h2/o2/n2 flames with complex chemistry in two-dimensional turbulent flows. *Journal of Fluid Mechanics*, 281:1–32.

Baum, M., Poinsot, T., and Thévenin, D. (1995). Accurate boundary conditions for multicomponent reactive flows. *Journal of computational physics*, 116(2):247–261.

Bayliss, A. and Turkel, E. (1982). Far field boundary conditions for compressible flows. *Journal of Computational Physics*, 48(2):182–199.

Beita, J., Talibi, M., Sadasivuni, S., and Balachandran, R. (2021). Thermoacoustic instability considerations for high hydrogen combustion in lean premixed gas turbine combustors: A review. *Hydrogen*, 2(1):33–57.

Bell, J., Almgren, A., Beckner, V., Day, M., Lijewski, M., Nonaka, A., and Zhang, W. (2012). Boxlib user's guide. *github. com/BoxLib-Codes/BoxLib*.

Bellows, B. D., Hreiz, A., and Lieuwen, T. (2008). Nonlinear interactions between forced and self-excited acoustic oscillations in premixed combustor. *Journal of propulsion and power*, 24(3):628–631.

Bénard, P., Lartigue, G., Moureau, V., and Mercier, R. (2019). Large-eddy simulation of the lean-premixed preccinsta burner with wall heat loss. *Proceedings of the Combustion Institute*, 37(4):5233–5243.

Berger, M. J. and Oliger, J. (1984). Adaptive mesh refinement for hyperbolic partial differential equations. *Journal of computational Physics*, 53(3):484–512.

Berland, J., Bogey, C., Marsden, O., and Bailly, C. (2007). High-order, low dispersive and low dissipative explicit schemes for multiple-scale and boundary problems. *Journal of Computational Physics*, 224(2):637–662.

Betchov, R. (1956). An inequality concerning the production of vorticity in isotropic turbulence. *Journal of Fluid Mechanics*, 1(5):497–504.

Birbaud, A.-L., Durox, D., and Candel, S. (2006). Upstream flow dynamics of a laminar premixed conical flame submitted to acoustic modulations. *Combustion and flame*, 146(3):541–552.

Blackburn, H. M., Mansour, N. N., and Cantwell, B. J. (1996). Topology of fine-scale motions in turbulent channel flow. *Journal of Fluid Mechanics*, 310:269–292.

Blaisdell, G., Spyropoulos, E., and Qin, J. (1996). The effect of the formulation of nonlinear terms on aliasing errors in spectral methods. *Applied Numerical Mathematics*, 21(3):207–219.

Blanchard, M., Schuller, T., Sipp, D., and Schmid, P. (2015). Response analysis of a laminar premixed m-flame to flow perturbations using a linearized compressible navier-stokes solver. *Physics of Fluids*, 27(4):043602.

Bodony, D. J. and Lele, S. K. (2005). On using large-eddy simulation for the prediction of noise from cold and heated turbulent jets. *Physics of Fluids*, 17(8):085103.

Bodony, D. J. and Lele, S. K. (2008). Current status of jet noise predictions using large-eddy simulation. *AIAA journal*, 46(2):364–380.

Boger, M., Veynante, D., Boughanem, H., and Trouvé, A. (1998). Direct numerical simulation analysis of flame surface density concept for large eddy simulation of turbulent premixed combustion. In *Symposium (International) on Combustion*, volume 27, pages 917–925. Elsevier.

Bogey, C. and Bailly, C. (2004). Investigation of subsonic jet noise using les: Mach and reynolds number effects. In *10th AIAA/CEAS aeroacoustics conference*, page 3023.

Bogey, C., Bailly, C., and Juve, D. (2000). Computation of the sound radiated by a 3-d jet using large eddy simulation. In *6th Aeroacoustics Conference and Exhibit*, page 2009.

Bogey, C., Bailly, C., and Juve, D. (2001). Noise computation using lighthill's equation with inclusion of mean flow-acoustics interactions. In *7th AIAA/CEAS Aeroacoustics Conference and Exhibit*, page 2255.

Bose, S. T., Moin, P., and You, D. (2010). Grid-independent large-eddy simulation using explicit filtering. *Physics of Fluids*, 22(10):105103.

Boughanem, H. and Trouvé, A. (1998). The domain of influence of flame instabilities in turbulent premixed combustion. In *Symposium (International) on Combustion*, volume 27, pages 971–978. Elsevier.

Bouheraoua, L. (2014). *Simulation aux grandes échelles et modélisation de la combustion supersonique*. PhD thesis, Rouen, INSA.

Bourehla, A. and Baillot, F. (1998). Appearance and stability of a laminar conical premixed flame subjected to an acoustic perturbation. *Combustion and flame*, 114(3-4):303–318.

Brès, G. A., Ham, F. E., Nichols, J. W., and Lele, S. K. (2017). Unstructured large-eddy simulations of supersonic jets. *AIAA journal*, 55(4):1164–1184.

Bres, G. A., Jaunet, V., Le Rallic, M., Jordan, P., Colonius, T., and Lele, S. K. (2015). Large eddy simulation for jet noise: the importance of getting the boundary layer right. In *21st AIAA/CEAS aeroacoustics conference*, page 2535.

Brès, G. A. and Lele, S. K. (2019). Modelling of jet noise: a perspective from large-eddy simulations. *Philosophical Transactions of the Royal Society A*, 377(2159):20190081.

Bridges, J. and Wernet, M. P. (2011). The nasa subsonic jet particle image velocimetry (piv) dataset. Technical report.

Brouwer, J., Reiss, J., and Sesterhenn, J. (2014). Conservative time integrators of arbitrary order for skew-symmetric finite-difference discretizations of compressible flow. *Computers & Fluids*, 100:1–12.

Brouzet, D., Haghiri, A., Talei, M., and Brear, M. J. (2019). Annihilation events topology and their generated sound in turbulent premixed flames. *Combustion and Flame*, 204:268–277.

Bull, J. R. and Jameson, A. (2016). Explicit filtering and exact reconstruction of the sub-filter stresses in large eddy simulation. *Journal of Computational Physics*, 306:117–136.

Butler, T. and O'rourke, P. (1977). A numerical method for two dimensional unsteady reacting flows. In *Symposium (international) on combustion*, volume 16, pages 1503–1515. Elsevier.

Candel, S., Durox, D., Ducruix, S., Birbaud, A.-L., Noiray, N., and Schuller, T. (2009). Flame dynamics and combustion noise: progress and challenges. *International Journal of Aeroacoustics*, 8(1):1–56.

Candel, S., Durox, D., and Schuller, T. (2004). Flame interactions as a source of noise and combustion instabilities. In *10th AIAA/CEAS Aeroacoustics Conference*, page 2928.

Candel, S., Durox, D., Schuller, T., Bourgouin, J.-F., and Moeck, J. P. (2014). Dynamics of swirling flames. *Annual review of fluid mechanics*, 46:147–173.

Candel, S., Durox, D., Schuller, T., Palies, P., Bourgouin, J.-F., and Moeck, J. P. (2012). Progress and challenges in swirling flame dynamics. *Comptes rendus mecanique*, 340(11-12):758–768.

Candel, S. M. and Poinsot, T. J. (1990). Flame stretch and the balance equation for the flame area. *Combustion Science and Technology*, 70(1-3):1–15.

Cant, R., Ahmed, U., Fang, J., Chakarborty, N., Nivarti, G., Moulinec, C., and Emerson, D. (2022). An unstructured adaptive mesh refinement approach for computational fluid dynamics of reacting flows. *Journal of Computational Physics*, page 111480.

Cant, R. and Bray, K. (1989). Strained laminar flamelet calculations of premixed turbulent combustion in a closed vessel. In *Symposium (International) on Combustion*, volume 22, pages 791–799. Elsevier.

Chacin, J. M. and Cantwell, B. J. (2000). Dynamics of a low reynolds number turbulent boundary layer. *Journal of Fluid Mechanics*, 404:87–115.

Chakraborty, N. and Cant, R. S. (2007). A priori analysis of the curvature and propagation terms of the flame surface density transport equation for large eddy simulation. *Physics of Fluids*, 19(10):105101.

Chakraborty, N. and Cant, R. S. (2009). Direct numerical simulation analysis of the flame surface density transport equation in the context of large eddy simulation. *Proceedings of the Combustion Institute*, 32(1):1445–1453.

Chan, C. P., Bachan, J. D., Kenny, J. P., Wilke, J. J., Beckner, V. E., Almgren, A. S., and Bell, J. B. (2016). Topology-aware performance optimization and modeling of adaptive mesh refinement codes for exascale. In *2016 First International Workshop on Communication Optimizations in HPC (COMHPC)*, pages 17–28. IEEE.

Charlette, F., Meneveau, C., and Veynante, D. (2002). A power-law flame wrinkling model for les of premixed turbulent combustion part i: non-dynamic formulation and initial tests. *Combustion and Flame*, 131(1-2):159–180.

Chen, C. and Sohrab, S. (1995). Upstream interactions between planar symmetric laminar methane premixed flames. *Combustion and flame*, 101(3):360–370.

Chen, J. H., Cantwell, B. J., and Mansour, N. N. (1989). The topology and vorticity dynamics of a three-dimensional plane compressible wake. In *Australasian Fluid Mechanics Conference*.

Chen, J. H., Echekki, T., and Kollmann, W. (1999). The mechanism of two-dimensional pocket formation in lean premixed methane-air flames with implications to turbulent combustion. *Combustion and flame*, 116(1-2):15–48.

Chen, Y.-C., Kim, M., Han, J., Yun, S., and Yoon, Y. (2007). Analysis of flame surface normal and curvature measured in turbulent premixed stagnation-point flames with crossed-plane tomography. *Proceedings of the Combustion Institute*, 31(1):1327–1335.

Chong, M. S., Perry, A. E., and Cantwell, B. J. (1990). A general classification of three-dimensional flow fields. *Physics of Fluids A: Fluid Dynamics*, 2(5):765–777.

Chong, M. S., Soria, J., Perry, A., Chacin, J., Cantwell, B., and Na, Y. (1998). Turbulence structures of wall-bounded shear flows found using dns data. *Journal of Fluid Mechanics*, 357:225–247.

Chow, F. K. and Moin, P. (2003). A further study of numerical errors in large-eddy simulations. *Journal of Computational Physics*, 184(2):366–380.

Christodoulou, L., Kabiraj, L., Saurabh, A., and Karimi, N. (2016). Characterizing the signature of flame flashback precursor through recurrence analysis. *Chaos: An Interdisciplinary Journal of Nonlinear Science*, 26(1):013110.

Cifuentes, L., Dopazo, C., Martin, J., Domingo, P., and Vervisch, L. (2016). Effects of the local flow topologies upon the structure of a premixed methane-air turbulent jet flame. *Flow, Turbulence and Combustion*, 96(2):535–546.

Cifuentes, L., Dopazo, C., Martin, J., and Jimenez, C. (2014). Local flow topologies and scalar structures in a turbulent premixed flame. *Physics of Fluids*, 26(6):065108.

Clavin, P. and Williams, F. (1982). Effects of molecular diffusion and of thermal expansion on the structure and dynamics of premixed flames in turbulent flows of large scale and low intensity. *Journal of fluid mechanics*, 116:251–282.

Cohen, J., Hagen, G., Banaszuk, A., Becz, S., and Mehta, P. (2011). Attenuation of gas turbine combustor pressure oscillations using symmetry breaking. In *49th AIAA Aerospace Sciences Meeting including the New Horizons Forum and Aerospace Exposition*, page 60.

Colin, O., Ducros, F., Veynante, D., and Poinsot, T. (2000). A thickened flame model for large eddy simulations of turbulent premixed combustion. *Physics of fluids*, 12(7):1843–1863.

Colonius, T. and Lele, S. K. (2004). Computational aeroacoustics: progress on nonlinear problems of sound generation. *Progress in Aerospace sciences*, 40(6):345–416.

Colonius, T., Lele, S. K., and Moin, P. (1991). The free compressible viscous vortex. *Journal of Fluid Mechanics*, 230:45–73.

Colonius, T., Lele, S. K., and Moin, P. (1993). Boundary conditions for direct computation of aerodynamic sound generation. *AIAA journal*, 31(9):1574–1582.

Colonius, T., Lele, S. K., and Moin, P. (1997). Sound generation in a mixing layer. *Journal of Fluid Mechanics*, 330:375–409.

Ćosić, B., Bobusch, B. C., Moeck, J. P., and Paschereit, C. O. (2012). Open-loop control of combustion instabilities and the role of the flame response to two-frequency forcing. *Journal of engineering for gas turbines and power*, 134(6).

Ćosić, B., Terhaar, S., Moeck, J. P., and Paschereit, C. O. (2015). Response of a swirl-stabilized flame to simultaneous perturbations in equivalence ratio and velocity at high oscillation amplitudes. *Combustion and Flame*, 162(4):1046–1062.

Coussement, A., Gicquel, O., Caudal, J., Fiorina, B., and Degrez, G. (2012). Three-dimensional boundary conditions for numerical simulations of reactive compressible flows with complex thermochemistry. *Journal of computational physics*, 231(17):5571–5611.

Crocco, L. (1969). Research on combustion instability in liquid propellant rockets. In *Symposium (International) on Combustion*, volume 12, pages 85–99. Elsevier.

Crocco, L. and Cheng, S.-I. (1956). Theory of combustion instability in liquid propellant rocket motors. Technical report, Princeton Univ Nj.

Cuenot, B., Shum-Kivan, F., and Blanchard, S. (2021). The thickened flame approach for non-premixed combustion: Principles and implications for turbulent combustion modeling. *Combustion and Flame*, page 111702.

Cuquel, A., Durox, D., and Schuller, T. (2011). Theoretical and experimental determination of the flame transfer function of confined premixed conical flames. In *7th Mediterranean Combustion Symposium*, volume 36, pages 58–64. Chia Laguna, Cagliari, Sardinia, Italy.

Cuquel, A., Durox, D., and Schuller, T. (2013). Impact of flame base dynamics on the non-linear frequency response of conical flames. *Comptes Rendus Mécanique*, 341(1-2):171–180.

da Silva, C. B. and Pereira, J. C. (2008). Invariants of the velocity-gradient, rate-of-strain, and rate-of-rotation tensors across the turbulent/nonturbulent interface in jets. *Physics of fluids*, 20(5):055101.

Danaila, I., Kaplanski, F., and Sazhin, S. (2015). Modelling of confined vortex rings. *Journal of Fluid Mechanics*, 774:267–297.

Dawson, J. R. and Worth, N. A. (2014). Flame dynamics and unsteady heat release rate of self-excited azimuthal modes in an annular combustor. *Combustion and Flame*, 161(10):2565–2578.

De, A. and Acharya, S. (2009). Large eddy simulation of a premixed bunsen flame using a modified thickened-flame model at two reynolds number. *Combustion science and technology*, 181(10):1231–1272.

Denaro, F. M. (2011). What does finite volume-based implicit filtering really resolve in large-eddy simulations? *Journal of Computational Physics*, 230(10):3849–3883.

Diskin, B. and Thomas, J. L. (2008). Accuracy of gradient reconstruction on grids with high aspect ratio. *NIA report*, 12:2008.

Dopazo, C., Martín, J., and Hierro, J. (2006). Iso-scalar surfaces, mixing and reaction in turbulent flows. *Comptes Rendus Mécanique*, 334(8-9):483–492.

Dopazo, C., Martín, J., and Hierro, J. (2007). Local geometry of isoscalar surfaces. *Physical Review E*, 76(5):056316.

Dowling, A. P. (1997). Nonlinear self-excited oscillations of a ducted flame. *Journal of fluid mechanics*, 346:271–290.

Dowling, A. P. (1999). A kinematic model of a ducted flame. *Journal of fluid mechanics*, 394:51–72.

Drennan, S. A., Kumar, G., and Liu, S. (2017). Developing grid-convergent les simulations of augmentor combustion with automatic meshing and adaptive mesh refinement. In *55th AIAA Aerospace Sciences Meeting*, page 1574.

Driscoll, J. F. (2008). Turbulent premixed combustion: Flamelet structure and its effect on turbulent burning velocities. *Progress in Energy and Combustion Science*, 34(1):91–134.

Du, Y. (2019). Generalized boundary equations for conservative navier–stokes equations. *Aerospace Science and Technology*, 86:836–849.

Du, Y. and Cai, J. (2022). Amplitudes of characteristic waves and non-reflecting outflow conditions for high-fidelity numerical simulations. *Proceedings of the Institution of Mechanical Engineers, Part G: Journal of Aerospace Engineering*, 236(4):636–644.

Dubey, A., Almgren, A., Bell, J., Berzins, M., Brandt, S., Bryan, G., Colella, P., Graves, D., Lijewski, M., Löffler, F., et al. (2014). A survey of high level frameworks in block-structured adaptive mesh refinement packages. *Journal of Parallel and Distributed Computing*, 74(12):3217–3227.

Duclos, J., Veynante, D., and Poinsot, T. (1993). A comparison of flamelet models for premixed turbulent combustion. *Combustion and flame*, 95(1-2):101–117.

Ducros, F., Ferrand, V., Nicoud, F., Weber, C., Darracq, D., Gacherieu, C., and Poinsot, T. (1999). Large-eddy simulation of the shock/turbulence interaction. *Journal of Computational Physics*, 152(2):517–549.

Ducros, F., Laporte, F., Soulères, T., Guinot, V., Moinat, P., and Caruelle, B. (2000). High-order fluxes for conservative skew-symmetric-like schemes in structured meshes: application to compressible flows. *Journal of Computational Physics*, 161(1):114–139.

Ducruix, S., Durox, D., and Candel, S. (2000). Theoretical and experimental determinations of the transfer function of a laminar premixed flame. *Proceedings of the combustion institute*, 28(1):765–773.

Dunstan, T., Swaminathan, N., Bray, K., and Kingsbury, N. (2013a). The effects of non-unity lewis numbers on turbulent premixed flame interactions in a twin v-flame configuration. *Combustion science and technology*, 185(6):874–897.

Dunstan, T., Swaminathan, N., Bray, K., and Kingsbury, N. (2013b). Flame interactions in turbulent premixed twin v-flames. *Combustion science and technology*, 185(1):134–159.

Durand, L. and Polifke, W. (2007). Implementation of the thickened flame model for large eddy simulation of turbulent premixed combustion in a commercial solver. In *ASME Turbo Expo 2007: Power for Land, Sea, and Air*, pages 869–878.

Durox, D., Schuller, T., and Candel, S. (2005). Combustion dynamics of inverted conical flames. *Proceedings of the combustion Institute*, 30(2):1717–1724.

Durox, D., Schuller, T., Noiray, N., and Candel, S. (2009). Experimental analysis of nonlinear flame transfer functions for different flame geometries. *Proceedings of the Combustion Institute*, 32(1):1391–1398.

Echekki, T. and Chen, J. H. (1996). Unsteady strain rate and curvature effects in turbulent premixed methane-air flames. *Combustion and Flame*, 106(1-2):184–202.

Elsinga, G. and Marusic, I. (2010a). Evolution and lifetimes of flow topology in a turbulent boundary layer. *Physics of Fluids*, 22(1):015102.

Elsinga, G. and Marusic, I. (2010b). Universal aspects of small-scale motions in turbulence. *Journal of Fluid Mechanics*, 662:514–539.

Emami, S., Mazaheri, K., Shamooni, A., and Mahmoudi, Y. (2015). Les of flame acceleration and ddt in hydrogen–air mixture using artificially thickened flame approach and detailed chemical kinetics. *international journal of hydrogen energy*, 40(23):7395–7408.

Erlebacher, G., Hussaini, M. Y., Speziale, C. G., and Zang, T. A. (1992). Toward the large-eddy simulation of compressible turbulent flows. *Journal of fluid mechanics*, 238:155–185.

Fanaca, D., Alemela, P., Hirsch, C., and Sattelmayer, T. (2010). Comparison of the flow field of a swirl stabilized premixed burner in an annular and a single burner combustion chamber. *Journal of Engineering for Gas Turbines and Power*, 132(7).

Fang, Y., Yang, Y., Hu, K., Wang, G., Li, J., and Zheng, Y. (2021). Experimental study on self-excited thermoacoustic instabilities and intermittent switching of azimuthal and longitudinal modes in an annular combustor. *Physics of Fluids*, 33(8):084104.

Farisco, F., Panek, L., and Kok, J. B. (2017). Thermo-acoustic cross-talk between cans in a can-annular combustor. *International journal of spray and combustion dynamics*, 9(4):452–469.

Ferrer, P. (2013). *Simulation numérique directe dans la combustion turbulente sur une couche de cisaillement*. PhD thesis, Ph. D. Thesis, Ecole Nationale Supérieure de Mécanique et d'Aérotechique ....

Filatyev, S. A., Driscoll, J. F., Carter, C. D., and Donbar, J. M. (2005). Measured properties of turbulent premixed flames for model assessment, including burning velocities, stretch rates, and surface densities. *Combustion and Flame*, 141(1-2):1–21.

Fleifil, M., Annaswamy, A. M., Ghoneim, Z., and Ghoniem, A. F. (1996). Response of a laminar premixed flame to flow oscillations: A kinematic model and thermoacoustic instability results. *Combustion and flame*, 106(4):487–510.

Franzelli, B., Riber, E., Sanjosé, M., and Poinsot, T. (2010). A two-step chemical scheme for kerosene–air premixed flames. *Combustion and Flame*, 157(7):1364–1373.

Franzelli, B. G. (2011). *Impact of the chemical description on direct numerical simulations and large eddy simulations of turbulent combustion in industrial aero-engines*. PhD thesis.

Fredrich, D. (2019). A numerical method for the prediction of combustion instabilities.

Freitag, M. and Klein, M. (2006). An improved method to assess the quality of large eddy simulations in the context of implicit filtering. *Journal of Turbulence*, (7):N40.

Freund, J. B., Lele, S. K., and Moin, P. (1996). Calculation of the radiated sound field using an open kirchhoff surface. *AIAA journal*, 34(5):909–916.

Fureby, C. (2009). Large eddy simulation modelling of combustion for propulsion applications. *Philosophical Transactions of the Royal Society A: Mathematical, Physical and Engineering Sciences*, 367(1899):2957–2969.

Garby, R., Selle, L., and Poinsot, T. (2013). Large-eddy simulation of combustion instabilities in a variable-length combustor. *Comptes Rendus Mécanique*, 341(1-2):220–229.

Garnier, E., Adams, N., and Sagaut, P. (2009). *Large eddy simulation for compressible flows*. Springer Science & Business Media.

G̈vider, Ö. L. and Smallwood, G. J. (2000). Do turbulent premixed flame fronts in spark-ignition engines behave like passive surfaces? *SAE transactions*, pages 1823–1832.

Génin, F. and Menon, S. (2010). Simulation of turbulent mixing behind a strut injector in supersonic flow. *AIAA journal*, 48(3):526–539.

Germano, M., Piomelli, U., Moin, P., and Cabot, W. H. (1991). A dynamic subgrid-scale eddy viscosity model. *Physics of Fluids A: Fluid Dynamics*, 3(7):1760–1765.

Geurts, B. J. and Fröhlich, J. (2002). A framework for predicting accuracy limitations in large-eddy simulation. *Physics of fluids*, 14(6):L41–L44.

Ghosal, S. and Moin, P. (1995). The basic equations for the large eddy simulation of turbulent flows in complex geometry. *Journal of Computational Physics*, 118(1):24–37.

Giacomazzi, E., Giulietti, E., Stringola, C., Cassani, S., Pagliari, L., and Chiocchini, S. (2014). Combustion monitoring in gas turbines and enhanced stability at very lean conditions. In *Turbo Expo: Power for Land, Sea, and Air*, volume 45684, page V04AT04A036. American Society of Mechanical Engineers.

Gibson, C. H. (1968). Fine structure of scalar fields mixed by turbulence. i. zero-gradient points and minimal gradient surfaces. *The Physics of Fluids*, 11(11):2305–2315.

Gicquel, L. Y., Staffelbach, G., and Poinsot, T. (2012). Large eddy simulations of gaseous flames in gas turbine combustion chambers. *Progress in energy and combustion science*, 38(6):782–817.

Giles, M. B. (1990). Nonreflecting boundary conditions for euler equation calculations. *AIAA journal*, 28(12):2050–2058.

Giusti, A. and Mastorakos, E. (2019). Turbulent combustion modelling and experiments: Recent trends and developments. *Flow, Turbulence and Combustion*, 103(4):847–869.

Givoli, D. (1991). Non-reflecting boundary conditions. *Journal of computational physics*, 94(1):1–29.

Global, E. (2020). Hydrogen gas turbines: The path towards a zero-carbon gas turbine. *ETN Global*, page 2.

Godunov, S. and Bohachevsky, I. (1959). Finite difference method for numerical computation of discontinuous solutions of the equations of fluid dynamics. *Matematičeskij sbornik*, 47(3):271–306.

Gong, C., Jangi, M., Bai, X.-S., Liang, J.-H., and Sun, M.-B. (2017). Large eddy simulation of hydrogen combustion in supersonic flows using an eulerian stochastic fields method. *international journal of hydrogen energy*, 42(2):1264–1275.

Gonzalez-Juez, E. D., Kerstein, A. R., Ranjan, R., and Menon, S. (2017). Advances and challenges in modeling high-speed turbulent combustion in propulsion systems. *Progress in Energy and Combustion Science*, 60:26–67.

Gran, I. R., Echekki, T., and Chen, J. H. (1996). Negative flame speed in an unsteady 2-d premixed flame: A computational study. In *Symposium (International) on Combustion*, volume 26, pages 323–329. Elsevier.

Griffiths, J. (1995). Reduced kinetic models and their application to practical combustion systems. *Progress in energy and combustion science*, 21(1):25–107.

Griffiths, R., Chen, J., Kolla, H., Cant, R., and Kollmann, W. (2015). Three-dimensional topology of turbulent premixed flame interaction. *Proceedings of the Combustion Institute*, 35(2):1341–1348.

Grinstein, F. F. and Fureby, C. (2005). On monotonically integrated large eddy simulation of turbulent flows based on fct algorithms. In *Flux-Corrected Transport*, pages 79–104. Springer.

Grout, R., Gruber, A., Yoo, C. S., and Chen, J. (2011). Direct numerical simulation of flame stabilization downstream of a transverse fuel jet in cross-flow. *Proceedings of the Combustion Institute*, 33(1):1629–1637.

Gruhlke, P., Inanc, E., Mercier, R., Fiorina, B., and Kempf, A. M. (2021). A simple post-processing method to correct species predictions in artificially thickened turbulent flames. *Proceedings of the Combustion Institute*, 38(2):2977–2984.

Gülder, Ö., Smallwood, G. J., Wong, R., Snelling, D., Smith, R., Deschamps, B., and Sautet, J.-C. (2000). Flame front surface characteristics in turbulent premixed propane/air combustion. *Combustion and Flame*, 120(4):407–416.

Haghiri, A., Talei, M., Brear, M. J., and Hawkes, E. R. (2018). Sound generation by turbulent premixed flames. *Journal of Fluid Mechanics*, 843:29–52.

Hagstrom, T., Hariharan, S., and Thompson, D. (2003). High-order radiation boundary conditions for the convective wave equation in exterior domains. *SIAM Journal on Scientific Computing*, 25(3):1088–1101.

Haldenwang, P. and Pignol, D. (2002). Dynamically adapted mesh refinement for combustion front tracking. *Computers & fluids*, 31(4-7):589–606.

Han, X., Li, J., and Morgans, A. S. (2015). Prediction of combustion instability limit cycle oscillations by combining flame describing function simulations with a thermoacoustic network model. *Combustion and Flame*, 162(10):3632–3647.

Han, X., Yang, J., and Mao, J. (2016). Les investigation of two frequency effects on acoustically forced premixed flame. *Fuel*, 185:449–459.

Harten, A., Lax, P. D., and Leer, B. v. (1983). On upstream differencing and godunov-type schemes for hyperbolic conservation laws. *SIAM review*, 25(1):35–61.

Hawkes, E. R. and Cant, R. (2000). A flame surface density approach to large-eddy simulation of premixed turbulent combustion. *Proceedings of the Combustion Institute*, 28(1):51–58.

Hawkes, E. R. and Cant, R. S. (2001). Implications of a flame surface density approach to large eddy simulation of premixed turbulent combustion. *Combustion and Flame*, 126(3):1617–1629.

Hawkes, E. R. and Chen, J. H. (2004). Direct numerical simulation of hydrogen-enriched lean premixed methane–air flames. *Combustion and Flame*, 138(3):242–258.

Hawkes, E. R., Sankaran, R., and Chen, J. H. (2011). Estimates of the three-dimensional flame surface density and every term in its transport equation from two-dimensional measurements. *Proceedings of the combustion institute*, 33(1):1447–1454.

Heinberg, R. (2015). *Afterburn: society beyond fossil fuels*. New Society Publishers.

Hernández-Pérez, F., Yuen, F., Groth, C., and Gülder, Ö. (2011). Les of a laboratory-scale turbulent premixed bunsen flame using fsd, pcm-fpi and thickened flame models. *Proceedings of the Combustion Institute*, 33(1):1365–1371.

Hernández-Pérez, F. E., Groth, C. P., and Gülder, Ö. L. (2014). Large-eddy simulation of lean hydrogen–methane turbulent premixed flames in the methane-dominated regime. *international journal of hydrogen energy*, 39(13):7147–7157.

Hickel, S., Adams, N. A., and Domaradzki, J. A. (2006). An adaptive local deconvolution method for implicit les. *Journal of Computational Physics*, 213(1):413–436.

Hield, P. A. and Brear, M. J. (2008). Comparison of open and choked premixed combustor exits during thermoacoustic limit cycle. *AIAA journal*, 46(2):517–526.

Hield, P. A., Brear, M. J., and Jin, S. H. (2009). Thermoacoustic limit cycles in a premixed laboratory combustor with open and choked exits. *Combustion and Flame*, 156(9):1683–1697.

Holke, J. (2018). Scalable algorithms for parallel tree-based adaptive mesh refinement with general element types. *arXiv preprint arXiv:1803.04970*.

Hornung, R. D., Wissink, A. M., and Kohn, S. R. (2006). Managing complex data and geometry in parallel structured amr applications. *Engineering with Computers*, 22(3):181–195.

Indlekofer, T., Faure-Beaulieu, A., Noiray, N., and Dawson, J. (2021). The effect of dynamic operating conditions on the thermoacoustic response of hydrogen rich flames in an annular combustor. *Combustion and Flame*, 223:284–294.

Ingraham, D. and Bridges, J. E. (2017). Validating a monotonically-integrated large eddy simulation code for subsonic jet acoustics. In *55th AIAA Aerospace Sciences Meeting*, page 0456.

Jacques, M. and Wilk, O. (2021). High-order absorbing boundary condition, domain decomposition method and stratified dispersive wave model. *Wave Motion*, 106:102806.

Jameson, A. (2008). Formulation of kinetic energy preserving conservative schemes for gas dynamics and direct numerical simulation of one-dimensional viscous compressible flow in a shock tube using entropy and kinetic energy preserving schemes. *Journal of Scientific Computing*, 34(2):188–208.

Jameson, A., Schmidt, W., and Turkel, E. (1981). Numerical solution of the euler equations by finite volume methods using runge kutta time stepping schemes. In *14th fluid and plasma dynamics conference*, page 1259.

Jiménez, J., Wray, A. A., Saffman, P. G., and Rogallo, R. S. (1993). The structure of intense vorticity in isotropic turbulence. *Journal of Fluid Mechanics*, 255:65–90.

Jones, W. and Lindstedt, R. (1988). Global reaction schemes for hydrocarbon combustion. *Combustion and flame*, 73(3):233–249.

Jost, A., Zhang, J., and Jackson, T. L. (2016). Incompressible flow solver with ghost-cell immersed boundary method and adaptive mesh refinement. In *46th AIAA Fluid Dynamics Conference*, page 3328.

Juniper, M. P. and Sujith, R. I. (2018). Sensitivity and nonlinearity of thermoacoustic oscillations. *Annual Review of Fluid Mechanics*, 50:661–689.

Kailasanath, K., Corrigan, A. T., Liu, J., and Ramamurti, R. (2014). Efficient supersonic jet noise simulations using jenre. In *50th AIAA/ASME/SAE/ASEE Joint Propulsion Conference*, page 3740.

Karimi, N. (2014). Response of a conical, laminar premixed flame to low amplitude acoustic forcing–a comparison between experiment and kinematic theories. *Energy*, 78:490–500.

Karimi, N., Brear, M. J., Jin, S.-H., and Monty, J. P. (2009). Linear and non-linear forced response of a conical, ducted, laminar premixed flame. *Combustion and flame*, 156(11):2201–2212.

Karimi, N., Brear, M. J., and Moase, W. H. (2008). Acoustic and disturbance energy analysis of a flow with heat communication. *Journal of Fluid Mechanics*, 597:67–89.

Karimi, N., Brear, M. J., and Moase, W. H. (2010). On the interaction of sound with steady heat communicating flows. *Journal of sound and vibration*, 329(22):4705–4718.

Kartheekeyan, S. and Chakravarthy, S. (2006). An experimental investigation of an acoustically excited laminar premixed flame. *Combustion and flame*, 146(3):513–529.

Kashinath, K., Hemchandra, S., and Juniper, M. P. (2013). Nonlinear thermoacoustics of ducted premixed flames: the influence of perturbation convection speed. *Combustion and Flame*, 160(12):2856–2865.

Kasthuri, P., Pawar, S. A., Gejji, R., Anderson, W., and Sujith, R. I. (2022). Coupled interaction between acoustics and unsteady flame dynamics during the transition to thermoacoustic instability in a multi-element rocket combustor. *Combustion and Flame*, 240:112047.

Katz, A. and Sankaran, V. (2012). High aspect ratio grid effects on the accuracy of navier–stokes solutions on unstructured meshes. *Computers & fluids*, 65:66–79.

Kazmouz, S. J., Haworth, D. C., Lillo, P., and Sick, V. (2022). Extension of a thickened flame model to highly stratified combustion—application to a spark-ignition engine. *Combustion and Flame*, 236:111798.

Kee, R. J., Rupley, F. M., and Miller, J. A. (1989). Chemkin-ii: A fortran chemical kinetics package for the analysis of gas-phase chemical kinetics. Technical report, Sandia National Lab.(SNL-CA), Livermore, CA (United States).

Keller, J. J. (1995). Thermoacoustic oscillations in combustion chambers of gas turbines. *AIAA journal*, 33(12):2280–2287.

Kerr, R. M. (1985). Higher-order derivative correlations and the alignment of small-scale structures in isotropic numerical turbulence. *Journal of Fluid Mechanics*, 153:31–58.

Khashehchi, M., Elsinga, G. E., Ooi, A., Soria, J., and Marusic, I. (2010). Studying invariants of the velocity gradient tensor of a round turbulent jet across the turbulent/nonturbulent interface using tomo-piv. In *15th Int Symp on Applications of Laser Techniques to Fluid Mechanics Lisbon, Portugal*, pages 05–08.

Kim, J., John, T., Adhikari, S., Wu, D., Emerson, B., Acharya, V., Isono, M., Saito, T., and Lieuwen, T. (2022). Nonlinear dynamics of combustor azimuthal modes: Experiments and modeling. *Combustion and Flame*, 238:111931.

Kim, J. W. and Lee, D. J. (1997). Implementation of boundary conditions for optimized high-order compact schemes. *Journal of Computational Acoustics*, 5(02):177–191.

Kim, K. T., Lee, J. G., Lee, H. J., Quay, B. D., and Santavicca, D. A. (2010). Characterization of forced flame response of swirl-stabilized turbulent lean-premixed flames in a gas turbine combustor. *Journal of engineering for gas turbines and power*, 132(4).

Kings, N. and Bake, F. (2010). Indirect combustion noise: noise generation by accelerated vorticity in a nozzle flow. *International Journal of spray and combustion dynamics*, 2(3):253–266.

Kollmann, W. and Chen, J. H. (1998). Pocket formation and the flame surface density equation. In *Symposium (International) on Combustion*, volume 27, pages 927–934. Elsevier.

Koplow, D. and Dernbach, J. (2001). Federal fossil fuel subsidies and greenhouse gas emissions: a case study of increasing transparency for fiscal policy. *Annual review of Energy and the Environment*, 26(1):361–389.

Kostiuk, L., Bray, K., and Cheng, R. (1993). Experimental study of premixed turbulent combustion in opposed streams. part i—nonreacting flow field. *Combustion and flame*, 92(4):377–395.

Kraus, C., Selle, L., and Poinsot, T. (2018). Coupling heat transfer and large eddy simulation for combustion instability prediction in a swirl burner. 191:239–251.

Kravchenko, A. and Moin, P. (1997). On the effect of numerical errors in large eddy simulations of turbulent flows. *Journal of computational physics*, 131(2):310–322.

Kravchenko, A. G. and Moin, P. (2000). Numerical studies of flow over a circular cylinder at re d= 3900. *Physics of fluids*, 12(2):403–417.

Kuenne, G., Ketelheun, A., and Janicka, J. (2011). LES modeling of premixed combustion using a thickened flame approach coupled with FGM tabulated chemistry. 158(9):1750–1767.

Kuhlmann, J., Lampmann, A., Pfitzner, M., and Polifke, W. (2022). Assessing accuracy, reliability and efficieny of combustion models for prediction of flame dynamics with large eddy simulation. *Physics of Fluids*.

Kuo, A. Y.-S. and Corrsin, S. (1972). Experiment on the geometry of the fine-structure regions in fully turbulent fluid. *Journal of Fluid Mechanics*, 56(3):447–479.

Kuo, K. K. (1986). Principles of combustion.

Kuo, K. K.-y. and Acharya, R. (2012). *Fundamentals of turbulent and multiphase combustion*. John Wiley & Sons.

Kwong, W. Y. and Steinberg, A. M. (2019). Blowoff and reattachment dynamics of a linear multinozzle combustor. *Journal of Engineering for Gas Turbines and Power*, 141(1):011015.

Law, C. K. (2007). Combustion at a crossroads: Status and prospects. *Proceedings of the Combustion Institute*, 31(1):1–29.

Lax, P. (1959). Systems of conservation laws. Technical report, LOS ALAMOS NATIONAL LAB NM.

Lee, T. and Kim, K. T. (2022). High-frequency transverse combustion instabilities of lean-premixed multislit hydrogen-air flames. *Combustion and Flame*, 238:111899.

Lefebvre, A. H. and Ballal, D. R. (2010). *Gas turbine combustion: alternative fuels and emissions*. CRC press.

Légier, J., Poinsot, T., Varoquié, B., Lacas, F., and Veynante, D. (2002). Large eddy simulation of a non-premixed turbulent burner using a dynamically thickened flame model. In *IUTAM symposium on turbulent mixing and combustion*, pages 315–326. Springer.

Leonard, S., Terracol, M., and Sagaut, P. (2007). Commutation error in les with time-dependent filter width. *Computers & fluids*, 36(3):513–519.

Lesieur, M., Métais, O., Comte, P., et al. (2005). *Large-eddy simulations of turbulence*. Cambridge university press.

Li, L. K. and Juniper, M. P. (2013). Lock-in and quasiperiodicity in hydrodynamically self-excited flames: experiments and modelling. *Proceedings of the Combustion Institute*, 34(1):947–954.

Lieuwen, T., Neumeier, Y., and Zinn, B. T. (1998). The role of unmixedness and chemical kinetics in driving combustion instabilities in lean premixed combustors. *Combustion Science and Technology*, 135(1-6):193–211.

Lieuwen, T. C. and Yang, V. (2005). *Combustion instabilities in gas turbine engines: operational experience, fundamental mechanisms, and modeling*. American Institute of Aeronautics and Astronautics.

Lilly, D. K. (1965). On the computational stability of numerical solutions of time-dependent non-linear geophysical fluid dynamics problems. *Monthly Weather Review*, 93(1):11–25.

Lilly, D. K. (1967). The representation of small-scale turbulence in numerical simulation experiments. *IBM Form*, pages 195–210.

Lodato, G. (2008). *Tridimensional Boundary Conditions for Direct and Large-Eddy Simulation of Turbulent Flows. Sub-Grid Scale Modeling for Near-Wall Region Turbulence*. PhD thesis, INSA de Rouen.

Lodato, G., Domingo, P., and Vervisch, L. (2008). Three-dimensional boundary conditions for direct and large-eddy simulation of compressible viscous flows. *Journal of computational physics*, 227(10):5105–5143.

Louch, D. and Bray, K. (2001). Vorticity in unsteady premixed flames: vortex pair–premixed flame interactions under imposed body forces and various degrees of heat release and laminar flame thickness. *Combustion and flame*, 125(4):1279–1309.

Lourier, J.-M., Huber, A., Noll, B., and Aigner, M. (2014). Numerical analysis of indirect combustion noise generation within a subsonic nozzle. *AIAA Journal*, 52(10):2114–2126.

Lund, T. (2003). The use of explicit filters in large eddy simulation. *Computers & Mathematics with Applications*, 46(4):603–616.

Ma, T., Stein, O. T., Chakraborty, N., and Kempf, A. (2014). A posteriori testing of the flame surface density transport equation for les. *Combustion Theory and Modelling*, 18(1):32–64.

Maekawa, H., Hiyama, T., and Matsuo, Y. (1999). Study of the geometry of flow patterns in compressible isotropic turbulence. *JSME International Journal Series B Fluids and Thermal Engineering*, 42(3):336–343.

Magnient, J.-C., Sagaut, P., and Deville, M. (2001). A study of built-in filter for some eddy viscosity models in large-eddy simulation. *Physics of Fluids*, 13(5):1440–1449.

Maio, G., Cailler, M., Mercier, R., and Fiorina, B. (2019). Virtual chemistry for temperature and co prediction in les of non-adiabatic turbulent flames. *Proceedings of the Combustion Institute*, 37(2):2591–2599.

Manco, J. A. A. and de Mendonca, M. T. (2019). Comparative study of different non-reflecting boundary conditions for compressible flows. *Journal of the Brazilian Society of Mechanical Sciences and Engineering*, 41(10):1–16.

Mankbadi, R. (1999). Review of computational aeroacoustics in propulsion systems. *Journal of propulsion and power*, 15(4):504–512.

Marchner, P., Antoine, X., Geuzaine, C., and Bériot, H. (2022). Construction and numerical assessment of local absorbing boundary conditions for heterogeneous time-harmonic acoustic problems. *SIAM Journal on Applied Mathematics*, 82(2):476–501.

Mason, P. and Callen, N. (1986). On the magnitude of the subgrid-scale eddy coefficient in large-eddy simulations of turbulent channel flow. *Journal of Fluid Mechanics*, 162:439–462.

Mason, P. J. (1994). Large-eddy simulation: A critical review of the technique. *Quarterly Journal of the Royal Meteorological Society*, 120(515):1–26.

McMurtry, P., Riley, J. J., and Metcalfe, R. (1989). Effects of heat release on the large-scale structure in turbulent mixing layers. *Journal of Fluid Mechanics*, 199:297–332.

McMurtry, P. A., Jou, W.-H., Riley, J., and Metcalfe, R. (1986). Direct numerical simulations of a reacting mixing layer with chemical heat release. *AIAA journal*, 24(6):962–970.

Mehl, C., Liu, S., and Colin, O. (2021). A strategy to couple thickened flame model and adaptive mesh refinement for the les of turbulent premixed combustion. *Flow, Turbulence and Combustion*, 107(4):1003–1034.

Mehl, C., Liu, S., See, Y. C., and Colin, O. (2018). Les of a stratified turbulent burner with a thickened flame model coupled to adaptive mesh refinement and detailed chemistry. In *2018 Joint Propulsion Conference*, page 4563.

Meneveau, C. and Poinsot, T. (1991). Stretching and quenching of flamelets in premixed turbulent combustion. *Combustion and Flame*, 86(4):311–332.

Meyers, J. and Sagaut, P. (2007). Is plane-channel flow a friendly case for the testing of large-eddy simulation subgrid-scale models? *Physics of Fluids*, 19(4):048105.

Mittal, R. and Iaccarino, G. (2005). Immersed boundary methods. *Annu. Rev. Fluid Mech.*, 37:239–261.

Moëll, D., Lörstad, D., and Bai, X.-S. (2015). Numerical investigation of hydrogen enriched natural gas in the sgt-800 burner. In *Turbo Expo: Power for Land, Sea, and Air*, volume 56697, page V04BT04A064. American Society of Mechanical Engineers.

Moëll, D., Lörstad, D., and Bai, X.-S. (2018). Les of hydrogen enriched methane/air combustion in the sgt-800 burner at real engine conditions. In *Turbo Expo: Power for Land, Sea, and Air*, volume 51067, page V04BT04A023. American Society of Mechanical Engineers.

Moffat, H. (2003). *New trends in turbulence. Turbulence: nouveaux aspects: Les Houches Session LXXIV 31 July-1 September 2000*, volume 74. Springer Science & Business Media.

Moin, P. and Kim, J. (1982). Numerical investigation of turbulent channel flow. *Journal of fluid mechanics*, 118:341–377.

Moin, P. and Mahesh, K. (1998). Direct numerical simulation: a tool in turbulence research. *Annual review of fluid mechanics*, 30(1):539–578.

Moin, P., Squires, K., Cabot, W., and Lee, S. (1991). A dynamic subgrid-scale model for compressible turbulence and scalar transport. *Physics of Fluids A: Fluid Dynamics*, 3(11):2746–2757.

Moore, M. (1997). Nox emission control in gas turbines for combined cycle gas turbine plant. *Proceedings of the Institution of Mechanical Engineers, Part A: Journal of Power and Energy*, 211(1):43–52.

Moreau, S. and Duran, I. (2011). Analytical and numerical study of the entropy wave generator experiment on indirect combustion noise. In *17th AIAA/CEAS Aeroacoustics Conference (32nd AIAA Aeroacoustics Conference)*, page 2829.

Morgans, A. S. and Dowling, A. P. (2007). Model-based control of combustion instabilities. *Journal of Sound and Vibration*, 299(1-2):261–282.

Morinishi, Y. (1995). Conservative properties of finite difference schemes for incompressible flow. *Center for Turbulence Research Annual Research Briefs: 1995*.

Moule, Y., Sabelnikov, V., and Mura, A. (2014). Highly resolved numerical simulation of combustion in supersonic hydrogen–air coflowing jets. *Combustion and Flame*, 161(10):2647–2668.

Müller, J.-D. and Giles, M. (2001). Solution adaptive mesh refinement using adjoint error analysis. In *15th AIAA Computational Fluid Dynamics Conference*, page 2550.

Muschinski, A. (1996). A similarity theory of locally homogeneous and isotropic turbulence generated by a smagorinsky-type les. *Journal of Fluid Mechanics*, 325:239–260.

Noiray, N., Bothien, M., and Schuermans, B. (2011). Investigation of azimuthal staging concepts in annular gas turbines. *Combustion Theory and Modelling*, 15(5):585–606.

Noiray, N. and Schuermans, B. (2013). On the dynamic nature of azimuthal thermoacoustic modes in annular gas turbine combustion chambers. *Proceedings of the Royal Society A: Mathematical, Physical and Engineering Sciences*, 469(2151):20120535.

O'Brien, J., Towery, C. A., Hamlington, P. E., Ihme, M., Poludnenko, A. Y., and Urzay, J. (2017). The cross-scale physical-space transfer of kinetic energy in turbulent premixed flames. *Proceedings of the Combustion Institute*, 36(2):1967–1975.

Odier, N., Sanjosé, M., Gicquel, L., Poinsot, T., Moreau, S., and Duchaine, F. (2019). A characteristic inlet boundary condition for compressible, turbulent, multispecies turbomachinery flows. *Computers & Fluids*, 178:41–55.

Okong'o, N. and Bellan, J. (2002). Consistent boundary conditions for multicomponent real gas mixtures based on characteristic waves. *Journal of Computational Physics*, 176(2):330–344.

Ozturkmen, M. O. and Ozyoruk, Y. (2022). Investigation of a solution approach to quadratic eigenvalue problem for thermoacoustic instabilities. In *AIAA SCITECH 2022 Forum*, page 1855.

Pal, P., Kumar, G., Drennan, S. A., Rankin, B. A., and Som, S. (2021). Multidimensional numerical modeling of combustion dynamics in a non-premixed rotating detonation engine with adaptive mesh refinement. *Journal of Energy Resources Technology*, 143(11).

Pérez, F. E. H. and Emanuel, F. (2011). *Subfilter scale modelling for large eddy simulation of lean hydrogen-enriched turbulent premixed combustion*, volume 73.

Perry, A. E. and Chong, M. S. (1987). A description of eddying motions and flow patterns using critical-point concepts. *Annual Review of Fluid Mechanics*, 19(1):125–155.

Peskin, C. S. (2002). The immersed boundary method. *Acta numerica*, 11:479–517.

Peters, N. (1988). Laminar flamelet concepts in turbulent combustion. In *Symposium (international) on combustion*, volume 21, pages 1231–1250. Elsevier.

Peters, N. (2001). Turbulent combustion.

Pfadler, S., Kerl, J., Beyrau, F., Leipertz, A., Sadiki, A., Scheuerlein, J., and Dinkelacker, F. (2009). Direct evaluation of the subgrid scale scalar flux in turbulent premixed flames with conditioned dual-plane stereo piv. *Proceedings of the Combustion Institute*, 32(2):1723–1730.

Picciani, M., Richardson, E., and Navarro-Martinez, S. (2018a). Resolution requirements in stochastic field simulation of turbulent premixed flames. *Flow, Turbulence and Combustion*, 101(4):1103–1118.

Picciani, M., Richardson, E., and Navarro-Martinez, S. (2018b). A thickened stochastic fields approach for turbulent combustion simulation. *Flow, Turbulence and Combustion*, 101(4):1119–1136.

Piomelli, U. (1999). Large-eddy simulation: achievements and challenges. *Progress in aerospace sciences*, 35(4):335–362.

Piomelli, U., Cabot, W. H., Moin, P., and Lee, S. (1991). Subgrid-scale backscatter in turbulent and transitional flows. *Physics of Fluids A: Fluid Dynamics*, 3(7):1766–1771.

Piomelli, U., Zang, T. A., Speziale, C. G., and Hussaini, M. Y. (1990). On the large-eddy simulation of transitional wall-bounded flows. *Physics of Fluids A: Fluid Dynamics*, 2(2):257–265.

Pirozzoli, S. (2011). Numerical methods for high-speed flows. *Annual review of fluid mechanics*, 43:163–194.

Pitsch, H. (2006). Large-eddy simulation of turbulent combustion. *Annu. Rev. Fluid Mech.*, 38:453–482.

Pitsch, H. and Attili, A. (2020). *Data Analysis for Direct Numerical Simulations of Turbulent Combustion*. Springer.

Poinsot, T. and Veynante, D. (2005). *Theoretical and numerical combustion*. RT Edwards, Inc.

Poinsot, T., Veynante, D., and Candel, S. (1991). Quenching processes and premixed turbulent combustion diagrams. *Journal of Fluid mechanics*, 228:561–606.

Poinsot, T. J. and Lele, S. (1992). Boundary conditions for direct simulations of compressible viscous flows. *Journal of computational physics*, 101(1):104–129.

Polifke, W., Wall, C., and Moin, P. (2006). Partially reflecting and non-reflecting boundary conditions for simulation of compressible viscous flow. *Journal of Computational Physics*, 213(1):437–449.

Pope, S. (1988). The evolution of surfaces in turbulence. *International journal of engineering science*, 26(5):445–469.

Pope, S. B. (1985). Pdf methods for turbulent reactive flows. *Progress in energy and combustion science*, 11(2):119–192.

Pope, S. B. (2004). Ten questions concerning the large-eddy simulation of turbulent flows. *New journal of Physics*, 6(1):35.

Pope, S. B. and Pope, S. B. (2000). *Turbulent flows*. Cambridge university press.

Popinet, S. (2003). Gerris: a tree-based adaptive solver for the incompressible euler equations in complex geometries. *Journal of computational physics*, 190(2):572–600.

Popp, S., Kuenne, G., Janicka, J., and Hasse, C. (2019). An extended artificial thickening approach for strained premixed flames. 206:252–265.

Potgieter, J., Lombaard, L., Hannay, J., Moghimi, M., Valluri, P., and Meyer, J. (2021). Adaptive mesh refinement method for the reduction of computational costs while simulating slug flow. *International Communications in Heat and Mass Transfer*, 129:105702.

Preetham, Santosh, H., and Lieuwen, T. (2008). Dynamics of laminar premixed flames forced by harmonic velocity disturbances. *Journal of Propulsion and Power*, 24(6):1390–1402.

Proch, F. and Kempf, A. M. (2014). Numerical analysis of the cambridge stratified flame series using artificial thickened flame les with tabulated premixed flame chemistry. *Combustion and Flame*, 161(10):2627–2646.

Prosser, R. (2005). Improved boundary conditions for the direct numerical simulation of turbulent subsonic flows. i. inviscid flows. *Journal of Computational Physics*, 207(2):736–768.

Qian, Y., Sun, S., Ju, D., Shan, X., and Lu, X. (2017). Review of the state-of-the-art of biogas combustion mechanisms and applications in internal combustion engines. *Renewable and Sustainable Energy Reviews*, 69:50–58.

Ranadive, H. D., Wang, H., Savard, B., and Hawkes, E. R. (2019). Assessment of artificial fluid properties for high-order accurate large-eddy simulations of shock-free compressible turbulent flows with strong temperature gradients. *Computers & Fluids*, 190:274–293.

Ranganath, B. and Echekki, T. (2005). Effects of preferential and differential diffusion on the mutual annihilation of two premixed hydrogen–air flames. *Combustion Theory and Modelling*, 9(4):659–672.

Ranganath, B. and Echekki, T. (2006). On the role of heat and mass transport during the mutual annihilation of two premixed propane–air flames. *International journal of heat and mass transfer*, 49(25-26):5075–5080.

Rathore, O. and Navarro-Martinez, S. (2023). Flame dynamics modelling using artificially thickened models. *Flow, Turbulence and Combustion*, pages 1–31.

Rayleigh, J. (1877). The theory of sound, macmillan and co.

Rayleigh, L. (1878). The explanation of certain acoustical phenomena. *Roy. Inst. Proc.*, 8:536–542.

Reiss, J. and Sesterhenn, J. (2014). A conservative, skew-symmetric finite difference scheme for the compressible navier–stokes equations. *Computers & Fluids*, 101:208–219.

Rendleman, C. A., Beckner, V. E., Lijewski, M., Crutchfield, W., and Bell, J. B. (2000). Parallelization of structured, hierarchical adaptive mesh refinement algorithms. *Computing and Visualization in Science*, 3(3):147–157.

Renou, B., Boukhalfa, A., Puechberty, D., and Trinité, M. (1998). Effects of stretch on the local structure of preely propagating premixed low-turbulent flames with various lewis numbers. In *Symposium (International) on Combustion*, volume 27, pages 841–847. Elsevier.

Ribert, G., Petit, X., and Domingo, P. (2017). High-pressure methane-oxygen flames. analysis of sub-grid scale contributions in filtered equations of state. *The Journal of Supercritical Fluids*, 121:78–88.

Rochette, B., Collin-Bastiani, F., Gicquel, L., Vermorel, O., Veynante, D., and Poinsot, T. (2018). Influence of chemical schemes, numerical method and dynamic turbulent combustion modeling on les of premixed turbulent flames. *Combustion and Flame*, 191:417–430.

Rochette, B., Riber, E., Cuenot, B., and Vermorel, O. (2020). A generic and self-adapting method for flame detection and thickening in the thickened flame model. *Combustion and Flame*, 212:448–458.

Rogallo, R. S. and Moin, P. (1984). Numerical simulation of turbulent flows. *Annual review of fluid mechanics*, 16(1):99–137.

Rolland, E. O., De Domenico, F., and Hochgreb, S. (2018). Direct and indirect noise generated by entropic and compositional inhomogeneities. *Journal of Engineering for Gas Turbines and Power*, 140(8).

Rudy, D. H. and Strikwerda, J. C. (1980). A nonreflecting outflow boundary condition for subsonic navier-stokes calculations. *Journal of Computational Physics*, 36(1):55–70.

Ruetsch, G. and Maxey, M. (1991). Small-scale features of vorticity and passive scalar fields in homogeneous isotropic turbulence. *Physics of Fluids A: Fluid Dynamics*, 3(6):1587–1597.

Rutland, C. J., Ferziger, J. H., and El Tahry, S. H. (1991). Full numerical simulations and modeling of turbulent premixed flames. In *Symposium (International) on Combustion*, volume 23, pages 621–627. Elsevier.

Sagaut, P. (2006). *Large eddy simulation for incompressible flows: an introduction*. Springer Science & Business Media.

Samarasinghe, J., Peluso, S., Szedlmayer, M., De Rosa, A., Quay, B., and Santavicca, D. (2013). Three-dimensional chemiluminescence imaging of unforced and forced swirl-stabilized flames in a lean premixed multi-nozzle can combustor. *Journal of Engineering for Gas Turbines and Power*, 135(10).

Sankaran, V. and Menon, S. (2005). Les of scalar mixing in supersonic mixing layers. *Proceedings of the combustion Institute*, 30(2):2835–2842.

Sankaran, V. and Merkle, C. (2014). Fundamental physics and model assumptions in turbulent combustion models for aerospace propulsion. In *50th AIAA/ASME/SAE/ASEE Joint Propulsion Conference*, page 3941.

Schlimpert, S., Meinke, M., and Schröder, W. (2016). Nonlinear analysis of an acoustically excited laminar premixed flame. *Combustion and Flame*, 163:337–357.

Schoder, S. and Kaltenbacher, M. (2019). Hybrid aeroacoustic computations: State of art and new achievements. *Journal of Theoretical and Computational Acoustics*, 27(04):1950020.

Schuller, T., Ducruix, S., Durox, D., and Candel, S. (2002a). Modeling tools for the prediction of premixed flame transfer functions. *Proceedings of the Combustion Institute*, 29(1):107–113.

Schuller, T., Durox, D., and Candel, S. (2002b). Dynamics of and noise radiated by a perturbed impinging premixed jet flame. *Combustion and flame*, 128(1-2):88–110.

Schumann, U. (1975). Subgrid scale model for finite difference simulations of turbulent flows in plane channels and annuli. *Journal of computational physics*, 18(4):376–404.

Schwarz, K. (1990). Evidence for organized small-scale structure in fully developed turbulence. *Physical review letters*, 64(4):415.

Sengupta, U., Waxenegger-Wilfing, G., Martin, J., Hardi, J., and Juniper, M. P. (2021). Forecasting thermoacoustic instabilities in liquid propellant rocket engines using multimodal bayesian deep learning. *arXiv preprint arXiv:2107.06396*.

Sezen, S. and Atlar, M. (2022). An alternative vorticity based adaptive mesh refinement (v-amr) technique for tip vortex cavitation modelling of propellers using cfd methods. *Ship Technology Research*, 69(1):1–21.

Shahbazian, N. (2015). *Subfilter scale combustion modelling for large eddy simulation of turbulent premixed flames*. University of Toronto (Canada).

She, Z.-S., Jackson, E., and Orszag, S. A. (1990). Intermittent vortex structures in homogeneous isotropic turbulence. *Nature*, 344(6263):226–228.

Shehadi, E. and van der Weide, E. (2021). Ongoing development of non-reflective boundary conditions for euler and navier-stokes equations via the discontinuous galerkin framework. In *AIAA Scitech 2021 Forum*, page 1660.

Shin, D.-H. and Lieuwen, T. (2013). Flame wrinkle destruction processes in harmonically forced, turbulent premixed flames. *Journal of Fluid Mechanics*, 721:484–513.

Shur, M. L., Spalart, P. R., and Strelets, M. K. (2005). Noise prediction for increasingly complex jets. part i: Methods and tests. *International journal of aeroacoustics*, 4(3):213–245.

Sierra, J., Citro, V., and Fabre, D. (2019). On boundary conditions for compressible flow simulations. In *Symposium on Fluid-Structure-Sound Interactions and Control*, pages 335–340. Springer.

Siggia, E. D. (1981). Numerical study of small-scale intermittency in three-dimensional turbulence. *Journal of Fluid Mechanics*, 107:375–406.

Sitaraman, H., Yellapantula, S., de Frahan, M. T. H., Perry, B., Rood, J., Grout, R., and Day, M. (2021). Adaptive mesh based combustion simulations of direct fuel injection effects in a supersonic cavity flame-holder. *Combustion and Flame*, 232:111531.

Sjögreen, B. and Yee, H. C. (2017). Accuracy consideration by drp schemes for dns and les of compressible flow computations. *Computers & fluids*, 159:123–136.

Skiba, A. W., Wabel, T. M., Carter, C. D., Hammack, S. D., Temme, J. E., Lee, T., and Driscoll, J. F. (2017). Reaction layer visualization: A comparison of two plif techniques and advantages of khz-imaging. *Proceedings of the Combustion Institute*, 36(3):4593–4601.

Smagorinsky, J. (1963). General circulation experiments with the primitive equations: I. the basic experiment. *Monthly weather review*, 91(3):99–164.

Smith, T. E., Chterev, I. P., Emerson, B. L., Noble, D. R., and Lieuwen, T. C. (2018). Comparison of single-and multinozzle reacting swirl flow dynamics. *Journal of Propulsion and Power*, 34(2):384–394.

Sohrab, S., Ye, Z., and Law, C. (1985). An experimental investigation on flame interaction and the existence of negative flame speeds. In *Symposium (International) on Combustion*, volume 20, pages 1957–1965. Elsevier.

Sondergaard, R., Chen, J., Soria, J., and Cantwell, B. (1991). Local topology of small scale motions in turbulent shear flows. In *8th Symposium on Turbulent Shear Flows, Volume 1*, volume 1, pages 16_1_1–16_1_6.

Soria, J., Sondergaard, R., Cantwell, B., Chong, M., and Perry, A. (1994). A study of the fine-scale motions of incompressible time-developing mixing layers. *Physics of Fluids*, 6(2):871–884.

Speziale, C. G., Erlebacher, G., Zang, T., and Hussaini, M. (1988). The subgrid-scale modeling of compressible turbulence. *The Physics of fluids*, 31(4):940–942.

Staffelbach, G., Gicquel, L., Boudier, G., and Poinsot, T. (2009). Large eddy simulation of self excited azimuthal modes in annular combustors. *Proceedings of the Combustion Institute*, 32(2):2909–2916.

Stöhr, M., Yin, Z., and Meier, W. (2017). Interaction between velocity fluctuations and equivalence ratio fluctuations during thermoacoustic oscillations in a partially premixed swirl combustor. *Proceedings of the Combustion Institute*, 36(3):3907–3915.

Stokes, G. G. (1845). On the theories of the internal friction of fluids in motion, and of the equilibrium and motion of elastic solids. *Transactions of the Cambridge Philosophical Society*.

Stow, S. R. and Dowling, A. P. (2004). Low-order modelling of thermoacoustic limit cycles. In *Turbo Expo: Power for Land, Sea, and Air*, volume 41669, pages 775–786.

Strakey, P. A. and Eggenspieler, G. (2010). Development and validation of a thickened flame modeling approach for large eddy simulation of premixed combustion. *Journal of Engineering for Gas Turbines and Power*, 132(7).

Straub, C., Kronenburg, A., Stein, O. T., Kuenne, G., Janicka, J., Barlow, R. S., and Geyer, D. (2018). Multiple mapping conditioning coupled with an artificially thickened flame model for turbulent premixed combustion. *Combustion and Flame*, 196:325–336.

Stull, D. R. (1965). *JANAF Thermochemical Tables...*, volume 1. Clearinghouse.

Suman, S. and Girimaji, S. S. (2010). Velocity gradient invariants and local flow-field topology in compressible turbulence. *Journal of Turbulence*, (11):N2.

Sun, C. and Law, C. (1998). On the consumption of fuel pockets via inwardly propagating flames. In *Symposium (International) on Combustion*, volume 27, pages 963–970. Elsevier.

Sutherland, J. C. and Kennedy, C. A. (2003). Improved boundary conditions for viscous, reacting, compressible flows. *Journal of computational physics*, 191(2):502–524.

Swanson, R. C. and Turkel, E. (1992). On central-difference and upwind schemes. *Journal of computational physics*, 101(2):292–306.

Talei, M., Brear, M. J., and Hawkes, E. R. (2011). Sound generation by laminar premixed flame annihilation. *Journal of Fluid Mechanics*, 679:194–218.

Talei, M., Brear, M. J., and Hawkes, E. R. (2012). A parametric study of sound generation by premixed laminar flame annihilation. *Combustion and Flame*, 159(2):757–769.

Talei, M., Hawkes, E. R., and Brear, M. J. (2013). A direct numerical simulation study of frequency and lewis number effects on sound generation by two-dimensional forced laminar premixed flames. *Proceedings of the Combustion Institute*, 34(1):1093–1100.

Tam, C. K. and Parrish, S. A. (2018). The physical processes of indirect combustion noise generation. *International Journal of Aeroacoustics*, 17(1-2):22–35.

Tam, C. K. and Webb, J. C. (1993). Dispersion-relation-preserving finite difference schemes for computational acoustics. *Journal of computational physics*, 107(2):262–281.

Tanahashi, M., Fujimura, M., and Miyauchi, T. (2000). Coherent fine-scale eddies in turbulent premixed flames. *Proceedings of the Combustion Institute*, 28(1):529–535.

Tanna, H. (1977). An experimental study of jet noise part i: Turbulent mixing noise. *Journal of sound and Vibration*, 50(3):405–428.

Tatsumi, S., Martinelli, L., and Jameson, A. (1995). Flux-limited schemes for the compressible navier-stokes equations. *AIAA journal*, 33(2):252–261.

Thibaut, D. and Candel, S. (1998). Numerical study of unsteady turbulent premixed combustion: Application to flashback simulation. *Combustion and Flame*, 113(1-2):53–65.

Thompson, K. W. (1987). Time dependent boundary conditions for hyperbolic systems. *Journal of computational physics*, 68(1):1–24.

Thompson, K. W. (1990). Time-dependent boundary conditions for hyperbolic systems, ii. *Journal of computational physics*, 89(2):439–461.

Toro, E. F., Spruce, M., and Speares, W. (1994). Restoration of the contact surface in the hll-riemann solver. *Shock waves*, 4(1):25–34.

Truffin, K. (2005). *Simulation aux grandes échelles et identification acoustique des turbines à gaz en régime partiellement prémélangé*. PhD thesis.

Turns, S. R. et al. (1996). *Introduction to combustion*, volume 287. McGraw-Hill Companies New York, NY, USA.

Tyagi, A., Boxx, I., Peluso, S., and O'Connor, J. (2019a). The role of flow interaction in flame–flame interaction events in a dual burner experiment. *Proceedings of the Combustion Institute*, 37(2):2485–2491.

Tyagi, A., Boxx, I., Peluso, S., and O'Connor, J. (2019b). Statistics and topology of local flame–flame interactions in turbulent flames. *Combustion and Flame*, 203:92–104.

Tyagi, A., Boxx, I. G., Peluso, S. J., Shupp, R., and O'Connor, J. (2018). Structure of flames in flame interaction zones. In *2018 AIAA Aerospace Sciences Meeting*, page 0161.

Valera-Medina, A., Marsh, R., Runyon, J., Pugh, D., Beasley, P., Hughes, T., and Bowen, P. (2017). Ammonia–methane combustion in tangential swirl burners for gas turbine power generation. *Applied Energy*, 185:1362–1371.

Valera-Medina, A., Morris, S., Runyon, J., Pugh, D. G., Marsh, R., Beasley, P., and Hughes, T. (2015). Ammonia, methane and hydrogen for gas turbines. *Energy Procedia*, 75:118–123.

Van Oijen, J. and De Goey, L. (2000). Modelling of premixed laminar flames using flamelet-generated manifolds. *Combustion Science and Technology*, 161(1):113–137.

Van Oijen, J., Donini, A., Bastiaans, R., ten Thije Boonkkamp, J., and De Goey, L. (2016). State-of-the-art in premixed combustion modeling using flamelet generated manifolds. *Progress in Energy and Combustion Science*, 57:30–74.

Vermorel, O., Quillatre, P., and Poinsot, T. (2017). LES of explosions in venting chamber: A test case for premixed turbulent combustion models. 183:207–223.

Verstappen, R. and Veldman, A. (1997). A comparison of low-order dns, high-order dns and les. In *Direct and Large-Eddy Simulation II*, pages 93–102. Springer.

Vervisch, L. and Poinsot, T. (1998). Direct numerical simulation of non-premixed turbulent flames. *Annual review of fluid mechanics*, 30(1):655–691.

Vincent, A. and Meneguzzi, M. (1991). The spatial structure and statistical properties of homogeneous turbulence. *Journal of Fluid Mechanics*, 225:1–20.

von Saldern, J. G., Moeck, J. P., and Orchini, A. (2021). Nonlinear interaction between clustered unstable thermoacoustic modes in can-annular combustors. *Proceedings of the Combustion Institute*, 38(4):6145–6153.

Vuorinen, V., Wehrfritz, A., Yu, J., Kaario, O., Larmi, M., and Boersma, B. J. (2011). Large-eddy simulation of subsonic jets. In *Journal of Physics: Conference Series*, volume 318, page 032052. IOP Publishing.

Wang, G., Boileau, M., and Veynante, D. (2011). Implementation of a dynamic thickened flame model for large eddy simulations of turbulent premixed combustion. *Combustion and Flame*, 158(11):2199–2213.

Wang, L. and Lu, X.-Y. (2012). Flow topology in compressible turbulent boundary layer. *Journal of Fluid Mechanics*, 703:255–278.

Wang, L. and Peters, N. (2006). The length-scale distribution function of the distance between extremal points in passive scalar turbulence. *Journal of Fluid Mechanics*, 554:457–475.

Wang, Z. J., Fidkowski, K., Abgrall, R., Bassi, F., Caraeni, D., Cary, A., Deconinck, H., Hartmann, R., Hillewaert, K., Huynh, H. T., et al. (2013). High-order cfd methods: current status and perspective. *International Journal for Numerical Methods in Fluids*, 72(8):811–845.

Warnatz, J., Maas, U., Dibble, R. W., and Warnatz, J. (2006). *Combustion*. Springer.

Wasistho, B., Geurts, B. J., and Kuerten, J. G. (1997). Simulation techniques for spatially evolving instabilities in compressible flow over a flat plate. *Computers & fluids*, 26(7):713–739.

Weber, G. H., Childs, H., and Meredith, J. S. (2012). Efficient parallel extraction of crack-free isosurfaces from adaptive mesh refinement (amr) data. In *IEEE Symposium on Large Data Analysis and Visualization (LDAV)*, pages 31–38. IEEE.

Wee, D., Park, S., Yi, T., Annaswamy, A., and Ghoniem, A. (2002). Reduced order modeling of reacting shear flow. In *40th AIAA Aerospace Sciences Meeting & Exhibit*, page 478.

Weller, H., Tabor, G., Gosman, A., and Fureby, C. (1998). Application of a flame-wrinkling les combustion model to a turbulent mixing layer. In *Symposium (International) on Combustion*, volume 27, pages 899–907. Elsevier.

Williams, F. A. (2018). *Combustion theory*. CRC Press.

Wolf, P., Staffelbach, G., Gicquel, L. Y., Müller, J.-D., and Poinsot, T. (2012). Acoustic and large eddy simulation studies of azimuthal modes in annular combustion chambers. *Combustion and Flame*, 159(11):3398–3413.

Wolf, P., Staffelbach, G., Roux, A., Gicquel, L., Poinsot, T., and Moureau, V. (2009). Massively parallel les of azimuthal thermo-acoustic instabilities in annular gas turbines. *Comptes Rendus Mecanique*, 337(6-7):385–394.

Worth, N. A. and Dawson, J. R. (2012a). Cinematographic oh-plif measurements of two interacting turbulent premixed flames with and without acoustic forcing. *Combustion and Flame*, 159(3):1109–1126.

Worth, N. A. and Dawson, J. R. (2012b). Tomographic reconstruction of oh* chemiluminescence in two interacting turbulent flames. *Measurement Science and Technology*, 24(2):024013.

Wright, M. R. (2005). *Introduction to chemical kinetics*. John Wiley & Sons.

Wu, J., Vakili, A., and Wu, J. (1991). Review of the physics of enhancing vortex lift by unsteady excitation. *Progress in Aerospace Sciences*, 28(2):73–131.

Xia, Y., Morgans, A., Jones, W., Rogerson, J., Bulat, G., and Han, X. (2017). Predicting thermoacoustic instability in an industrial gas turbine combustor: combining a low order network model with flame les. In *Turbo Expo: Power for Land, Sea, and Air*, volume 50848, page V04AT04A017. American Society of Mechanical Engineers.

Xu, L., Bo, S., Hongde, Y., and Lei, W. (2015). Evolution of rolls-royce air-cooled turbine blades and feature analysis. *Procedia Engineering*, 99:1482–1491.

Yang, Y., Fang, Y., Zhong, L., Xia, Y., Jin, T., Li, J., and Wang, G. (2021). Dmd analysis for velocity fields of a laminar premixed flame with external acoustic excitation. *Experimental Thermal and Fluid Science*, 123:110318.

Yee, H. and Sjögreen, B. (2018). Recent developments in accuracy and stability improvement of nonlinear filter methods for dns and les of compressible flows. *Computers & Fluids*, 169:331–348.

Yetter, R., Dryer, F., and Rabitz, H. (1991). A comprehensive reaction mechanism for carbon monoxide/hydrogen/oxygen kinetics. *Combustion Science and Technology*, 79(1-3):97–128.

Yoo, C. S. and Im, H. G. (2007). Characteristic boundary conditions for simulations of compressible reacting flows with multi-dimensional, viscous and reaction effects. *Combustion Theory and Modelling*, 11(2):259–286.

Yoo, C. S., Wang, Y., Trouvé, A., and Im, H. G. (2005). Characteristic boundary conditions for direct simulations of turbulent counterflow flames. *Combustion Theory and Modelling*, 9(4):617–646.

Yoon, M. (2021). Thermoacoustics and combustion instability analysis for multi-burner combustors. *Journal of Sound and Vibration*, 492:115774.

Yoon, M. (2022). Thermoacoustics of multi-burner combustors with plenum and chamber cross-talk. *Journal of Sound and Vibration*, 520:116623.

Yoshizawa, A. and Horiuti, K. (1985). A statistically-derived subgrid-scale kinetic energy model for the large-eddy simulation of turbulent flows. *Journal of the Physical Society of Japan*, 54(8):2834–2839.

Yu, S. and Navarro-Martinez, S. (2015). Modelling of deflagration to detonation transition using flame thickening. *Proceedings of the combustion institute*, 35(2):1955–1961.

Yuan, L. and Tang, T. (2007). Resolving the shock-induced combustion by an adaptive mesh redistribution method. *Journal of Computational Physics*, 224(2):587–600.

Yuen, F. T. and Gülder, Ö. L. (2009). Premixed turbulent flame front structure investigation by rayleigh scattering in the thin reaction zone regime. *Proceedings of the Combustion Institute*, 32(2):1747–1754.

Yuen, F. T. C. (2009). *Experimental investigation of the dynamics and structure of lean-premixed turbulent combustion*.

Zhang, P., Park, J.-W., Wu, B., and Zhao, X. (2021). Large eddy simulation/thickened flame model simulations of a lean partially premixed gas turbine model combustor. *Combustion Theory and Modelling*, 25(7):1296–1323.

Zhao, D., Ji, C., Li, S., and Li, J. (2014). Thermodynamic measurement and analysis of dual-temperature thermoacoustic oscillations for energy harvesting application. *Energy*, 65:517–526.

Zhen, H., Liu, H., Wei, Z., Liu, Z., Liu, X., and Huang, Z. (2022). A study on acoustically modulated bunsen flame and its impingement heat transfer. *International Journal of Hydrogen Energy*, 47(26):13168–13177.

Zhiyin, Y. (2015). Large-eddy simulation: Past, present and the future. *Chinese journal of Aeronautics*, 28(1):11–24.

Zhou, Y., Zhang, C., Han, X., and Lin, Y. (2021). Monitoring combustion instabilities of stratified swirl flames by feature extractions of time-averaged flame images using deep learning method. *Aerospace Science and Technology*, 109:106443.

Appendix A

Conservative and Primitive Forms

The governing equations in conservative form :

$$\frac{\partial \boldsymbol{U}}{\partial t} + \frac{\partial \boldsymbol{F}_i}{\partial x_i} + \boldsymbol{\Omega} = \boldsymbol{0} \qquad i = 1,2,3 \tag{A.1}$$

with

$$\boldsymbol{U} = [\rho, \rho u, \rho v, \rho w, \rho e, \rho Y_1 ... \rho Y_N]$$
$$\rho e = \frac{1}{2}\rho u_i u_i + \rho \sum_{k=1}^{N} (h_k - \frac{R}{W_k} T) Y_k$$

And

$$\boldsymbol{F}_i = \begin{bmatrix} \rho u_i \\ \rho u u_i + \delta_{1i} p \\ \rho v u_i + \delta_{2i} p \\ \rho w u_i + \delta_{3i} p \\ (\rho e + P) u_i \\ \rho u_i Y_1 \\ \vdots \\ \rho u_i Y_n \end{bmatrix}, \quad \boldsymbol{\Omega} = \begin{bmatrix} 0 \\ 0 \\ 0 \\ 0 \\ 0 \\ W_1 \dot{\omega}_1 \\ \vdots \\ W_n \dot{\omega}_n \end{bmatrix}$$

can be recast into primitive form to give

$$\frac{\partial \boldsymbol{U}^p}{\partial t} + \boldsymbol{A}_i \frac{\partial \boldsymbol{U}^p}{\partial x_i} + \boldsymbol{\Omega}^p = \boldsymbol{0} \tag{A.2}$$

With:

$$\boldsymbol{U}^p = [\rho, u, v, w, T, Y_1, \ldots, Y_n], \boldsymbol{\Omega}^p = [0,0,0,0,0, \frac{1}{\rho} W_1 \dot{\omega}_1 \ldots \frac{1}{\rho} W_N \dot{\omega}_N]$$

$$\boldsymbol{A}_i = \begin{bmatrix} u_1 & \delta_{1i}\rho & \delta_{2i}\rho & \delta_{3i}\rho & 0 & 0 & \ldots & 0 \\ \delta_{1i}\frac{RT}{\overline{W}\rho} & u_i & 0 & 0 & \delta_{1i}R/\overline{W} & \delta_{1i}RT/W_1 & \ldots & \delta_{1i}RT/W_N \\ \delta_{2i}\frac{RT}{\overline{W}\rho} & 0 & u_i & 0 & \delta_{2i}R/\overline{W} & \delta_{2i}RT/W_1 & \ldots & \delta_{2i}RT/W_N \\ \delta_{3i}\frac{RT}{\overline{W}\rho} & 0 & 0 & u_i & \delta_{3i}R/\overline{W} & \delta_{3i}RT/W_1 & \ldots & \delta_{3i}RT/W_N \\ 0 & \delta_{1i}\frac{RT}{\overline{W}c_v} & \delta_{2i}\frac{RT}{\overline{W}c_v} & \delta_{3i}\frac{RT}{\overline{W}c_v} & u_i & 0 & \ldots & 0 \\ 0 & 0 & 0 & 0 & 0 & u_i & \ldots & 0 \\ \vdots & \vdots & \vdots & \vdots & \vdots & \vdots & \vdots & \\ 0 & 0 & 0 & 0 & 0 & 0 & \ldots & u_i \end{bmatrix} \tag{A.3}$$

One can move freely between conservative and primitive forms using the relation below, where $\boldsymbol{P}$ is the transformation matrix as defined in Equation (A.5). The transformation is actually used in obtaining the above coefficient matrix as well since $A_i = P^{-1}\frac{\partial F_i}{\partial U}P$.

$$\frac{\partial \boldsymbol{U}^p}{\partial t} = \boldsymbol{P}^{-1}\frac{\partial \boldsymbol{U}}{\partial t} \tag{A.4}$$

$$\boldsymbol{P} = \frac{\partial \boldsymbol{U}}{\partial \boldsymbol{U}^p} = \begin{bmatrix} 1 & 0 & 0 & 0 & 0 & 0 & \dots & 0 \\ u_1 & \rho & 0 & 0 & 0 & 0 & \dots & 0 \\ u_2 & 0 & \rho & 0 & 0 & 0 & \dots & 0 \\ u_3 & 0 & 0 & \rho & 0 & 0 & \dots & 0 \\ e & \rho u_1 & \rho u_2 & \rho u_3 & \rho c_v & \rho(h_1 - RT/W_1) & \dots & \rho(h_N - RT/W_N) \\ Y_1 & 0 & 0 & 0 & 0 & \rho & \dots & 0 \\ \vdots & \vdots & \vdots & \vdots & \vdots & \vdots & \vdots & \\ Y_N & 0 & 0 & 0 & 0 & 0 & \dots & \rho \end{bmatrix} \tag{A.5}$$

Appendix B

Scaling of Curvatures

Assuming a simplified approximation of curvature as the divergence of gradient of suitable reduced mass fraction and applying the generic thickening transformation it can be shown :

$$\kappa = \frac{\frac{\partial^2 \phi}{\partial x^2}}{\sqrt{\left(\frac{\partial \phi}{\partial x}\right)^2 + \left(\frac{\partial \phi}{\partial y}\right)^2}} = \frac{\mathcal{F}^2 \frac{\partial^2 \phi}{\partial \xi^2} + \mathcal{F} \frac{\partial \phi}{\partial \xi} \frac{\partial \mathcal{F}}{\partial c} \frac{\partial c}{\partial \xi}}{\mathcal{F}\sqrt{\left(\frac{\partial \phi}{\partial \xi}\right)^2 + \left(\frac{\partial \phi}{\partial \eta}\right)^2}} \tag{B.1}$$

$$\frac{\kappa}{\mathcal{F}} = \frac{\frac{\partial^2 \phi}{\partial \xi^2} + \frac{\partial \phi}{\partial \xi} \frac{\partial \mathcal{F}}{\partial c} \frac{\partial c}{\partial \xi}}{\sqrt{\left(\frac{\partial \phi}{\partial \xi}\right)^2 + \left(\frac{\partial \phi}{\partial \eta}\right)^2}} = \kappa_t + \frac{\frac{\partial \phi}{\partial \xi} \frac{\partial \mathcal{F}}{\partial c} \frac{\partial c}{\partial \xi}}{\sqrt{\left(\frac{\partial \phi}{\partial \xi}\right)^2 + \left(\frac{\partial \phi}{\partial \eta}\right)^2}} \tag{B.2}$$

$$\frac{\kappa}{\mathcal{F}} \approx \kappa_t + \frac{\partial c}{\partial \xi} \frac{\partial \mathcal{F}}{\partial c} = \kappa_t + \frac{\partial \mathcal{F}}{\partial \xi} \tag{B.3}$$

The last term on the RHS is dependant on the sensor function used. For constant thickening it would simply disappear. It is assumed that if sufficient thickening is applies than this term is small due to relative smooth evaluation of $\mathcal{F}$ in progress progress variable space and of progress variable in thickened space. This assumption is likely to be strong in buffer regions near the start of the thickening region but should give reasonable estimates within the flame front. As a result the physical curvature is obtained by multiplying its thickened counterpart with the corresponding thickening factor.

Note that recently (and independently) Gruhlke et al. (2021) suggest a scaling for post processing of intermediate species in thickened flame simulations. The method and origin of their work is different to what is being suggested here but it does support the notion of *a posteriori* scaling applied to ATF results.

Appendix C

Dimensionality of Curvature Data

Experiments usually rely on binarised images to identify the flame front prior to image post processing to determine curvature. Although estimates for out of plane components can be made these techniques are inherently two dimensional in nature. Unless otherwise stated simulation results are presenting using the full 3D curvature as these are the ones used for topology classification later. Hawkes et al. (2011) present a useful method among others for estimating the difference between 2D and 3D dimensional measurements. However the approach does not extend well to low Reynolds numbers and general configurations. This makes direct comparison between 3D measurements and experiments difficult.

Many studies have argued that the difference is negligible, with relevant references provided in the main body of this text. However for the context of cylindrical turbulent flames this is unlike due to the prevalence of a consistent cylindrical curvature. This is exemplified in Figure C.1 below where using 2D curvatures result in much better alignment with experimental data even on the coarse mesh which was significantly different before. The goal of this illustration is jsut to highlight dimensionality of the data as a potential source of uncertainty when validating curvature data.

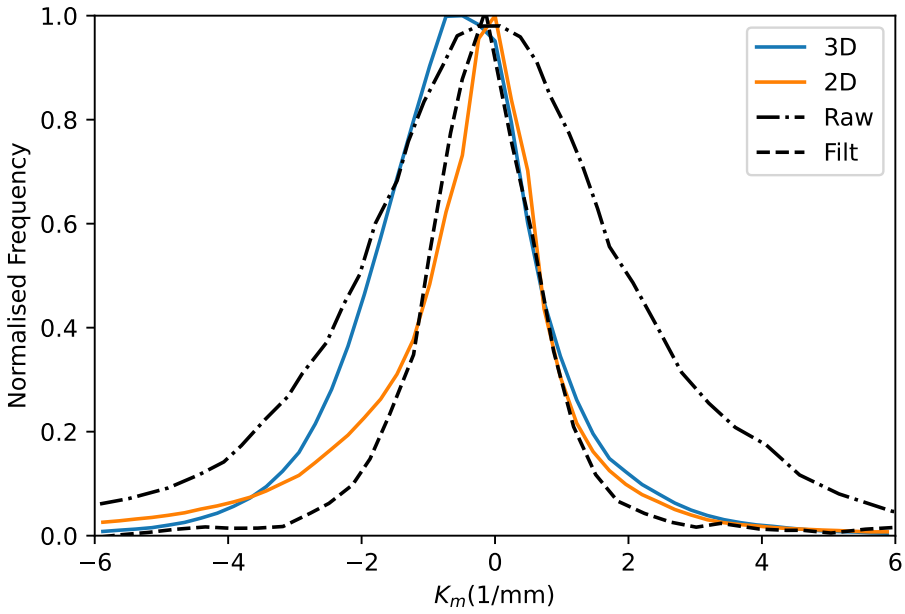

Fig. C.1 Comparison between 2D and 3D curvatures for lean turbulent Bunsen flame.

Appendix D

Slot Curvatures

Two main potential causes of uncertainty for the slot flames of Chapter 6 are briefly presented here. Firstly the artificial turbulence generator requires a characteristic time for degree of unsteadiness. Figure D.1 highlights how this parameter can have a drastic impact on curvature statistics. The legend is organised in terms of a base estimate for characteristic time (1) and subsequent reduction factors. i.e. 3 corresponds to the characteristic time of 1 but divided by 3 and so on.

The coflow parameters are also unknown. For starters the experiments use pilot flames which are actually burning and not simply burnt products. They also may or may not even share a turbulent feed with the main burners. Therefore it is very difficult to predict a single uniform coflow velocity a priori. This becomes a variable of uncertainty for the slot flame and two options were simulated with comparisons in curvature shown in Figure D.2. The take away point is that the exact coflow velocity was unclear from experiments and can influence curvature.

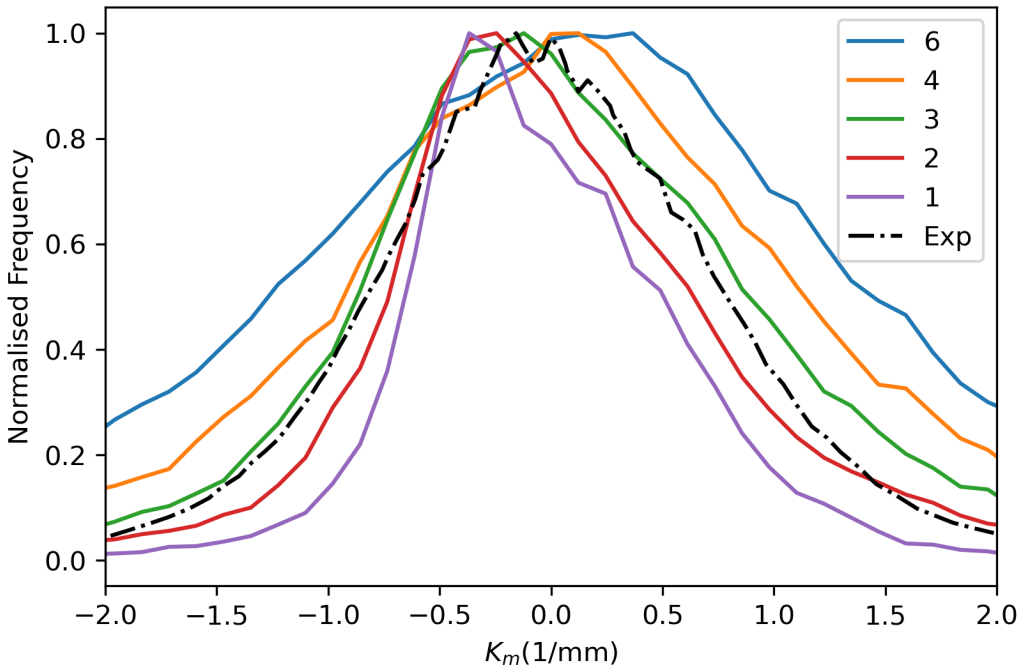

Fig. D.1 Impact of different degrees of unsteadiness in the artificial turbulent generator on flame curvature .

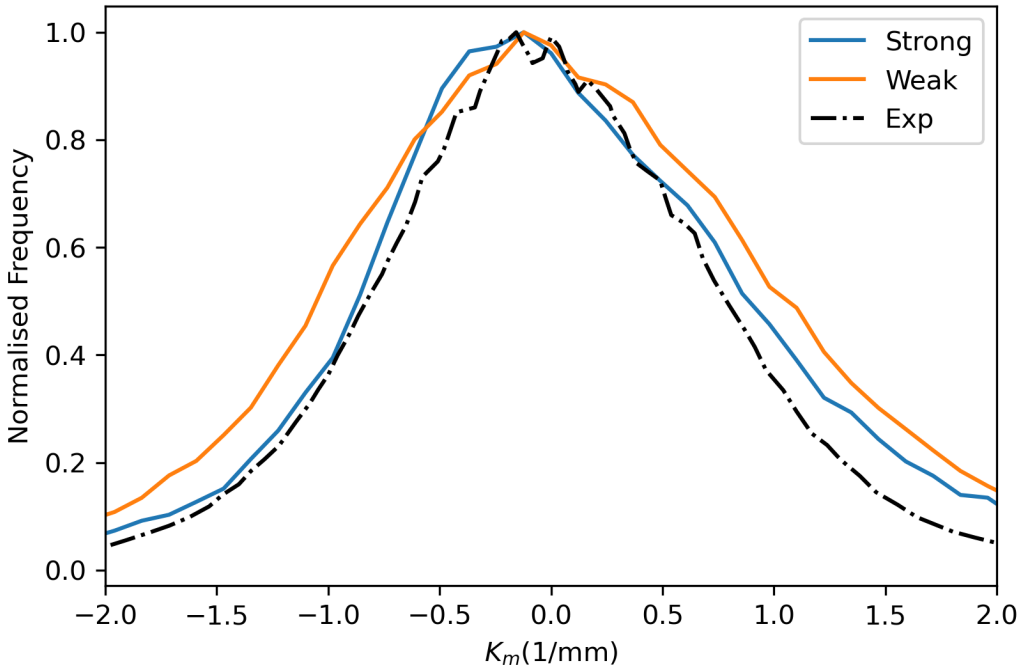

Fig. D.2 Impact of different degrees of uncertainties in coflow on flame curvature.